Transverse momentum dependence in double parton scattering

Dissertation
zur Erlangung des Doktorgrades
an der Fakultät für Mathematik, Informatik und Naturwissenschaften
Fachbereich Physik
der Universität Hamburg

vorgelegt von

Oskar Mateusz Grocholski

Hamburg
2024

Gutachter/innen der Dissertation:	Dr. Markus Diehl Prof. Dr. Sven-Olaf Moch
Zusammensetzung der Prüfungskommission:	 Dr. Markus Diehl Prof. Dr. Sven-Olaf Moch Prof. Dr. Elisabetta Gallo Prof. Dr. Jürgen Reuter Prof. Dr. Dieter Horns
Vorsitzende/r der Prüfungskommission:	Prof. Dr. Dieter Horns
Datum der Disputation:	16.10.2024
Vorsitzender des Fach-Promotionsausschusses PHYSIK:	Prof. Dr. Markus Drescher
Leiter des Fachbereichs PHYSIK:	Prof. Dr. Wolfgang J. Parak
Dekan der Fakultät MIN:	Prof. Dr.-Ing. Norbert Ritter

Summary

Double parton scattering (DPS) is a mechanism in which two hard parton-level processes take place in a single hadron-hadron collision. This can yield important contributions to search processes at the LHC, a prominent channel being like-sign lepton pair production via the production of two W bosons of equal charge in a double Drell-Yan process.

The factorization theorems allow to write the DPDs cross-section in terms of perturbatively computable hard scattering part, and non-perturbative objects called double parton distributions (DPDs), which contain a lot of new information about hadron structure at the quantum level, such as correlations between partons in polarization, color, and momentum.

In this thesis, we describe transverse-momentum dependence in the process of production of two W bosons in proton-proton collision via double parton scattering. This requires so-called transverse momentum-dependent double parton distributions (DTMDs). In the first part of the work, we express DTMDs in the transverse-position space, Fourier conjugate to the transverse momenta, and discuss their structure and evolution equations – the renormalization group- and rapidity evolution (Collins-Soper) equation.

After that, we identify the regions, where perturbative methods can be used to connect DTMDs to simpler objects, such as collinear double parton distributions (DPDFs) and single parton distributions (PDFs). These are called the "large-$\mathbf{y}$", and "short-distance" regions, and are described in the later part of the work. We describe the initial conditions for DPDs in both regions and the corresponding form of the Collins-Soper equation. We analyze the position-space dependence of DTMDs in both approximations and their corresponding uncertainties due to the perturbative matching to either DPDFs or PDFs.

Later, we discuss the non-perturbative input required in the computation and present a scheme needed to i) extrapolate the perturbatively computed approximation of DPDs to non-perturbative distances, and ii) interpolate between the two approximations valid in different subregions of the phase space. In the final part, we compute the contribution to the differential cross-section of the considered process in each region independently, identify the most important contributions, and discuss their uncertainties due to the modeling of DTMDs and the rapidity evolution kernels. Finally, we combine all of the contributions and discuss the final results for the differential cross-sections.

Zusammenfassung

Die Doppel-Parton Streuung (Double parton scattering, DPS) ist ein Mechanismus, bei dem zwei harte Parton-Prozesse in einer einzelnen Hadron-Hadron-Kollision stattfinden. Dies kann wichtige Beiträge zu Suchprozessen am LHC liefern, Ein prominentes Beispiel ist die Produktion von Leptonenpaaren durch die Erzeugung von zwei W-Bosonen mit gleicher Ladung im Doppel Drell-Yan-Prozess.

Die Faktorisierungssätze (Factorization theorems) erlauben es, den Wirkungsquerschnitt der DPS durch einen perturbativ berechenbaren harten Streuteil und nicht-perturbative Objekte, sogenannte Doppelpartonverteilungen (Double Parton Distribution, DPDs), beschreiben. Diese enthalten viele neue Informationen über die Struktur von Hadronen auf Quantenebene, wie zum Beispiel Korrelationen zwischen Partonen in Polarisation, Farbe und Impuls.

In dieser Arbeit beschreiben wir die transversale Impulsabhängigkeit bei der Erzeugung von zwei W-Bosonen in Proton-Proton-Kollisionen durch DPS. Dies erfordert sogenannte transversale impulsabhängige Doppelpartonverteilungen (transverse momentum dependent double parton distributions, DTMDs). Im ersten Teil der Arbeit drücken wir die DTMDs im Ortsraum aus, der Fourier-konjugiert zu den transversalen Impulsen ist, und diskutieren deren Struktur und Skalen Evolution, einschließlich der Renormierungsgruppen- und Collins-Soper-Gleichung.

Anschließend identifizieren wir die Bereiche, in denen perturbative Methoden verwendet werden können, um DTMDs durch einfacheren Objekten, wie Kollinearen Doppelpartonverteilungen (DPDFs) und Partonverteilungen (PDFs), zu beschreiben. Diese werden als die "large-$\mathbf{y}$" und "short-distance" Bereiche bezeichnet und im späteren Teil der Arbeit beschrieben. Wir beschreiben die Anfangsbedingungen für DPDs in beiden Bereichen und die entsprechende Form der Collins-Soper-Gleichung. Wir analysieren die Abhängigkeit der DTMDs im Ortsraum in beiden "large-$\mathbf{y}$" und "short-distance" Näherungen und deren entsprechende Unsicherheiten aufgrund der perturbativen Matching an entweder DPDFs oder PDFs.

Später diskutieren wir den nicht-perturbativen Input, der für die Berechnung erforderlich ist, und präsentieren ein Schema, das notwendig ist, um i) die perturbativ berechnete Näherung von DPDs auf nicht-perturbative Distanzen zu extrapolieren, und ii) zwischen den beiden Näherungen zu interpolieren, die in verschiedenen Teilbereichen des Phasenraums gültig sind. Im letzten Teil berechnen wir den Beitrag zum differentiellen Wirkungsquerschnitt des betrachteten Prozesses in beiden "large-$\mathbf{y}$" und "short-distance" Bereichen. Wir identifizieren die wichtigsten Beiträge und diskutieren deren Unsicherheiten aufgrund der Modellierung der DTMDs und der Collins-Soper-Kerne. Schließlich fassen wir alle Beiträge zusammen und diskutieren die Endergebnisse für die differentiellen Wirkungsquerschnitte.

Declaration on oath

I hereby declare and affirm that this doctoral dissertation is my own work and that I have not used any aids and sources other than those indicated.

If electronic resources based on generative artificial intelligence (gAI) were used in the course of writing this dissertation, I confirm that my own work was the main and value-adding contribution and that complete documentation of all resources used is available in accordance with good scientific practice. I am responsible for any erroneous or distorted content, incorrect references, violations of data protection and copyright law or plagiarism that may have been generated by the gAI.

03.09.2024 Oskar Grochalski

Date Signature of doctoral candidate

Acknowledgements

First and foremost, I would like to express my deep gratitude to Markus for his invaluable support and guidance over the past three years.

I am also grateful to Frank Tackmann, Peter Plößl, and Florian Fabry for many insightful discussions about my work.

I would like to thank Florian, Rebecca, and Giulia for the time spent together working in our office, as well as everyone on the third floor of building 1b for creating a great atmosphere at work.

Finally, I would like to thank for the support of the German Academic Scholarship Foundation.

Contents

Chapter 1

Introduction

Deep inelastic scattering experiments [2], explained by Feynman in the so-called parton model [3], followed by a more formal description in the language of the collinear factorization formalism allowed to study of hadrons at the level of their elementary constituents, now identified with quarks and gluons. Later works allowed for an all-order QCD description of parton distributions with the help of factorization theorems and introduced more general objects such as transverse momentum-dependent parton distributions (TMDs) as well as off-forward parton distributions (GPDs), which enable more detailed study of internal structure of nucleons [4–11]. Already in the 80's it was realized that in the appropriate kinematics the multiparton processes may also be significant [12–18]. In the last years, the theoretical description of multiparton scattering has been further developed, and a factorization theorem for a Drell-Yan production of color-neutral states in double-parton scattering has been established, [19–25]. The study of double-parton distributions is worthwhile for two main reasons. First, they encode information about the structure of hadrons which is inaccessible with the help of ordinary single-parton distributions, such as the correlation between the partons (color, polarization, energy). Moreover, they may be important in future precision measurements at high energies, in which accounting for contributions stemming from multiparton interactions might be crucial to minimize theoretical uncertainties. Already multiple studies of the contribution from double-parton scattering to various processes have been performed, for example in multijet- [26–30], and dijtet-processes [31–33], J/ψ production [34–38], four-lepton production [39, 40], BSM searches [41–44], or the like-sign W boson pair production [45–48], which is the main topic of this work.

The production of like-sign W pair in proton-proton collision has been studied intensively for many years [49–57]. It is of particular interest, since in this process the single-parton scattering (SPS) process is suppressed by two orders in strong or weak coupling with respect to the DPS channel. Moreover, the diagrammatic analysis shows that the SPS channel involves ≥ 2 jets, as opposed to the DPS, which can occur

without jets. Finally, it is expected that at the corresponding kinematics, the DPS will be enhanced compared to the SPS process since at high energies, partons carrying a small fraction of the proton's energy are probed – in that region, the densities of partons become large so that multiple parton processes are more likely to occur. Indeed, in one of the recent works on this process [48], the CMS Collaboration reported the observation of the double parton scattering with 6σ confidence level.

In the following part, we give a brief introduction to the theory of double-parton scattering. In Section 2.1 we present the power-counting argument to explain in what kind of observables the DPS process has that same power behavior as single parton scattering (SPS). Furthermore, we argue that in the case of like-sign W boson pair production, the DPS contribution acquires additional enhancement compared to SPS. Next, we give the formal definition of double-parton distributions, and discuss the factorization formalism and the evolution equations in Section 2.3. We present the cross-section formula and outline the problem of the double-counting between SPS and DPS in Section 2.4. In Section 2.5 we discuss the most important aspects in the numerical computation.

In the next chapters we show the regions of the phase-space where one can improve the description of transverse momentum-dependent double-parton distributions (DTMDs) with the help of perturbative methods. In Chapter 3 we focus on the case where one can apply the operator product expansion in order to relate DTMDs to the collinear double-parton distributions (DPDFs). In Chapter 4 we examine the regime where all of the relevant distances are perturbatively small. In both cases we identify the region of validity for each approximation, present the evolution equations, and discuss the extrapolation of double-parton distributions.

In Chapter 5 we present the individual contributions to the differential cross-section of W pair production from the two discussed approximations. We show how these are combined to form the total result and outline the approach used to estimate prediction uncertainties, assessing the relative significance of different error sources.

Finally, in Chapter 6, we summarize the work and present the conclusions.

Chapter 2

Double Parton Scattering

2.1 Power-counting for double parton scattering

The starting point of the analysis should be the following question: since in the single parton case, the factorization formalism depends on neglecting the terms suppressed by the powers of the hard scale, then is the expected scaling behavior of the double parton scattering process smaller or larger than those neglected terms?

The analysis at the level of simple power-counting suggests that in the case of transverse momentum-dependent observables the DPS process can indeed give contributions that are not negligible compared with SPS. In the following part, we recapitulate the results obtained in Section 2.4 in [22]. For a process involving the production of two states characterized by hard scales collectively denoted Q, and transverse momenta $\mathbf{q}_{1,2}$, the single-parton transverse momentum-dependent differential cross section can be written as

$$\frac{d\sigma^{\mathrm{SPS}}}{dx\,d\bar{x}\prod_{i=1,2}d^2\mathbf{q}_i} \;=\; \hat{\sigma}\int d^2\mathbf{k}\int d^2\bar{\mathbf{k}}\,\delta^{(2)}\big(\mathbf{q}_1+\mathbf{q}_2-\mathbf{k}-\bar{\mathbf{k}}\big)\,f(x,\mathbf{k})\bar{f}(\bar{x},\bar{\mathbf{k}})\,, \tag{2.1}$$

where the hard-scattering cross-section $\hat{\sigma}$ scales like Q^{-4}, and transverse momentum-dependent single parton distributions (TMDs) $f, \bar{f}$ scale like Λ^{-2} each, where Λ is the scale of non-perturbative interactions. The integration over transverse momenta of the partons $d^2\mathbf{k}\,d^2\bar{\mathbf{k}}$ with two-dimensional delta distributions gives scaling a factor of Λ^2. In total, one obtains scaling behavior

$$\frac{d\sigma^{\mathrm{SPS}}}{dx\,d\bar{x}\prod_{i=1,2}d^2\mathbf{q}_i} \;\sim\; \frac{1}{Q^4\Lambda^2}\,. \tag{2.2}$$

x ($\bar{x}$) is the longitudinal momentum fraction of the active parton in the right-moving (left-moving) hadron.

In the case of double-parton scattering, one can write

$$\frac{d\sigma^{\mathrm{DPS}}}{\prod_{i=1,2} dx_i d\bar{x}_i d^2\mathbf{q}_i} = \hat{\sigma}_1\hat{\sigma}_2\Big(\prod_{j=1,2}\int d^2\mathbf{k}_j \int d^2\bar{\mathbf{k}}_j\, \delta^{(2)}\big(\mathbf{q}_j - \mathbf{k}_j - \bar{\mathbf{k}}_j\big)\Big) \int d^2\mathbf{y}\, F(x_i,\mathbf{k}_i,\mathbf{y})\bar{F}(\bar{x}_i,\bar{\mathbf{k}}_i,\mathbf{y})\,. \quad (2.3)$$

Double-parton distributions (DPDs), denoted as F and $\bar{F}$, scale like Λ^{-2}. Integration over the transverse distance between partons 1 and 2, denoted as $\mathbf{y}$, gives scaling Λ^2, and each hard scattering cross-section $\hat{\sigma}_{1,2}$ scales like Q^{-2}. In total

$$\frac{d\sigma^{\mathrm{DPS}}}{\prod_{i=1,2} dx_i d\bar{x}_i d^2\mathbf{q}_i} \sim \frac{1}{Q^4\Lambda^2}\,, \quad (2.4)$$

which is the same power behavior as the SPS. The formal definition of the DPDs will be given in Section 2.3. However, when integrating over the transverse momenta one has the following phase-space bounds:

$$|\mathbf{q}_1 + \mathbf{q}_2| \sim \Lambda\,, \quad |\mathbf{q}_{1,2}| \gtrsim Q \qquad \text{for SPS}, \quad (2.5)$$

$$|\mathbf{q}_{1,2}| \sim \Lambda \qquad \text{for DPS}\,. \quad (2.6)$$

In double-parton scattering, each transverse momentum $\mathbf{q}_i$ is the sum of the parton momenta, hence it is bound by the soft scales. However, for SPS the sum of the transverse momenta of the active partons is $\mathbf{q}_1 + \mathbf{q}_2$, so only this combination is bound in the latter case, while the individual momentum can be as large as the hard scale. It implies that integration over the transverse momenta gives a different power behavior in these two cases:

$$\int d^2\mathbf{q}_1\, d^2\mathbf{q}_1 \to Q^2\Lambda^2 \qquad \text{for SPS}, \quad (2.7)$$

$$\int d^2\mathbf{q}_1\, d^2\mathbf{q}_1 \to \Lambda^4 \qquad \text{for DPS}. \quad (2.8)$$

This means that the cross sections integrated over transverse momenta have different scaling behavior:

$$\frac{d\sigma^{\mathrm{SPS}}}{dx d\bar{x}} \sim \frac{1}{Q^2}\,, \qquad \frac{d\sigma^{\mathrm{DPS}}}{\prod_{i=1,2} dx_i d\bar{x}_i} \sim \frac{\Lambda^2}{Q^4}\,. \quad (2.9)$$

It implies that the double-parton scattering should be best visible in observables that depend on the transverse momentum of the produced states. In the following part of this work, we will study a single class of such processes.

2.2 Like-sign W boson pair production

In the previous part it was argued that for observables differential with respect to transverse momenta of produced particles, the DPS channel has the same power-law scaling as SPS. However, one still can expect that in many cases the SPS dominates over the multiparton scattering, so the experimental observation of the double parton scattering will still be a difficult task. Here we will discuss an example of a process, in which the double parton scattering acquires an additional advantage over the single parton case, and which will serve as an important motivation for the presented study.

Let us consider a process of production of two like-sign W bosons in a proton-proton collision:

$$pp \longrightarrow W^{\pm}W^{\pm} + X \,. \tag{2.10}$$

X denotes unobserved hadronic states that are summed over. W bosons decay into leptons and neutrinos. Examples of the leading-order diagrams for single- and double-parton scattering channels at the parton level for this process are shown in Fig. 2.1.

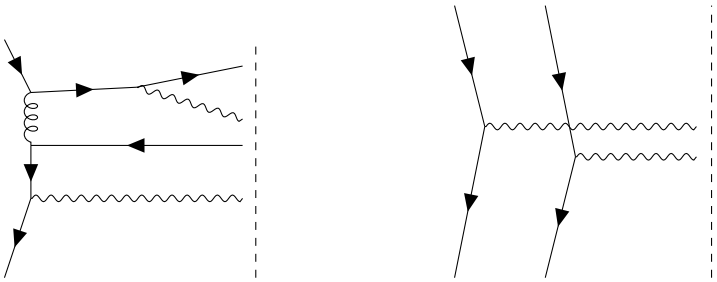

Figure 2.1: Single- and double Drell-Yan production of $W^{\pm}W^{\pm}$ pair.

Remarkably, the SPS channel is suppressed in coupling by α_S^2, and involves two parton lines that cross the cut, which means the emission of at least 2 jets in this channel. Therefore, by considering the processes with ≤ 1 jets one can study the double-parton scattering.

2.3 Double-parton distributions

In this Section, we give a brief overview of the theory of double-parton scattering, introduce the operator definitions of double-parton distributions depending on the parton polarizations and color representations. We recall the most important points in the derivation of factorization theorems for DPS, and show the evolution equation of DPDs.

Parton distributions are commonly studied using the lightcone coordinates, sometimes referred to as the Sudakov frame, cf. Appendix B of [10], in which the four-vectors are

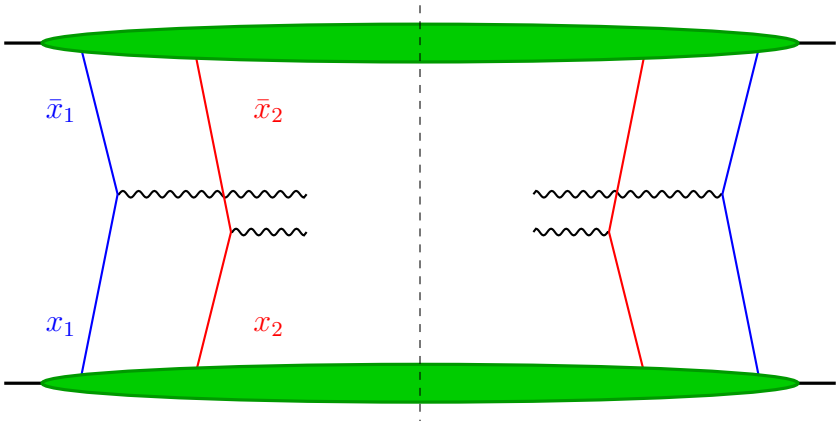

Figure 2.2: Leading-order graph representing the W boson pair production via double parton scattering (DPS).

decomposed using two light-cone coordinates

$$v^{\pm} = \frac{1}{\sqrt{2}}\left(v^0 \pm v^3\right) , \tag{2.11}$$

and the transverse components $\mathbf{v}$. In this setting, the momentum of a right-moving proton is approximated by

$$p^{\mu} = (p^+, 0, \mathbf{0}) , \tag{2.12}$$

where we neglect the transverse momentum $\mathbf{p}$, and the proton mass.

2.3.1 Tree-level analysis

Before giving the all-orders definition of double-parton distributions, let us explain how they appear at the lowest order of perturbation theory, and describe briefly each component that appears at higher orders. The leading-order diagram for the process of W boson pair via the double parton scattering (DPS) is presented in Fig. 2.2. Instead of using parton distributions in the transverse momentum space as in Eq. (2.3), it is more convenient to express the differential cross-section in terms of DPDs in the transverse position space:

$$\frac{d\sigma^{\mathrm{DPS}}}{\prod_{i=1,2} dx_i d\bar{x}_i d^2\mathbf{q}_i} = \sum_{a_1,a_2,b_1,b_2} H_{a_1b_1} H_{a_2b_2} \int \frac{d^2\mathbf{z}_1}{(2\pi)^2} e^{-i\mathbf{q}_1\mathbf{z}_1} \int \frac{d^2\mathbf{z}_2}{(2\pi)^2} e^{-i\mathbf{q}_2\mathbf{z}_2}$$
$$\int d^2\mathbf{y}\, F^{\underline{r}_1\underline{r}_2}_{a_1a_2}\left(x_i, \mathbf{z}_i, \mathbf{y}\right) \bar{F}^{\underline{r}_1\underline{r}_2}_{b_1b_2}\left(\bar{x}_i, \mathbf{z}_i, \mathbf{y},\right) . \tag{2.13}$$

H is the perturbatively computed hard part. a_i, b_i denotes parton species (at LO only quarks). $\underline{r}_i$ denotes a pair of color indices:

$$\underline{r}_i = r_i, r_i' . \tag{2.14}$$

Double parton distributions are denoted as F. Both the hard part H, and F carry spinor indices, which are summed over – this is done using the usual Fierz decomposition, and for simplicity, we suppress the spinor indices in the presented formula. At leading-order, quark DTMDs F are given by the matrix elements:

$$F^{r_1 r_2}_{a_1 a_2}\big(x_i, \mathbf{y}, \mathbf{z}_i\big) = 2p^+ \int dy^- \int \frac{dz_1^-}{2\pi}\frac{dz_2^-}{2\pi} e^{i(x_1 z_1^- + x_2 z_2^-)p^+} \\ \langle p| \left(\bar{q}_{a_1,r_1}(y - z_1/2) q_{a_1,r_1'}(y + z_1/2)\right)\left(\bar{q}_{a_2,r_2}(-z_2/2) q_{a_2,r_2'}(z_2/2)\right)|p\rangle \Big|_{y^+ = z_1^+ = z_2^+ = 0}. \tag{2.15}$$

As noted in various works [22, 54, 58], there exist also so-called 'interference' DPDs, which describe the interference in fermion number and quark flavor. They are expected to be negligible at small x, as explained in Section 2.5 in [22], and will not be considered in this work. Using the Fierz decomposition one obtains parton distributions for definite parton polarizations:

$$\begin{aligned} \Gamma_q &= \frac{1}{2}\gamma^+ && \text{unpolarized,} \\ \Gamma_{\Delta q} &= \frac{1}{2}\gamma^+\gamma_5 && \text{longitudinally polarized,} \\ \Gamma^j_{\delta q} &= \frac{1}{2} i\sigma^{+j}\gamma_5 && \text{transversally polarized,} \end{aligned} \tag{2.16}$$

for quarks. For antiquarks one has $\Gamma_{\Delta\bar{q}} = -\Gamma_{\Delta q}$; for two remaining polarizations the matrices are identical.

2.3.2 All-order description

At higher orders, apart from the perturbative corrections to the hard parton scattering, one has two kinds of interactions that do not introduce power-suppression:

- Longitudinally polarized gluons with momenta collinear to the incoming/outgoing partons connecting the collinear and the hard part.
- Soft gluons connecting the collinear parts.

The most general form of a leading-power diagram representing the process of production of 2 bosons via DPS is presented in Fig. 2.3. The factorization theorem states that the effects of collinear and soft gluons decouple, and are independent of the hard part. Let us shortly recall, how the factorization is established.
Let Q denote the hard scale, and Λ is the typical scale of non-perturbative interactions.

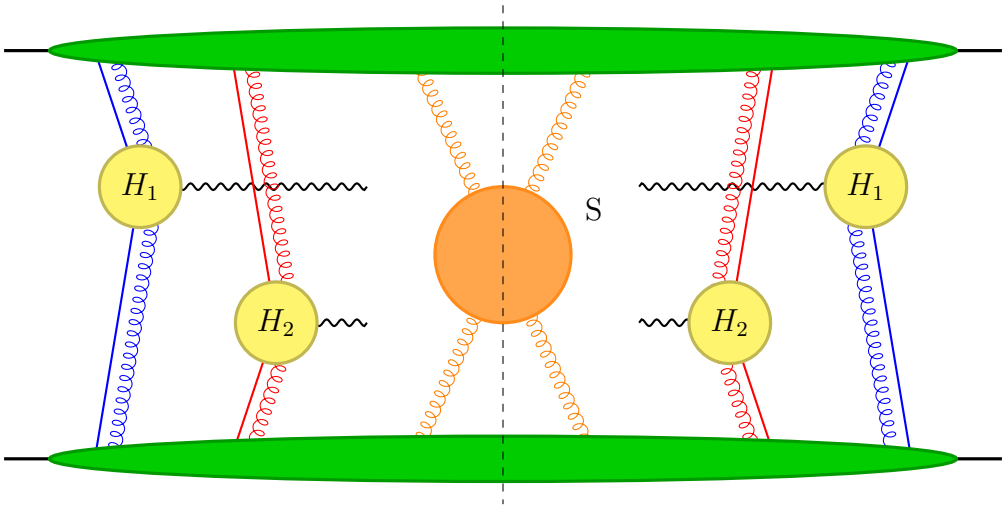

Figure 2.3: General leading-power graph representing the double-parton scattering. Each parton, represented by straight red and blue lines, enters the corresponding hard part H_i. An arbitrary number of collinear, longitudinally polarized gluons may connect the hadronic part (green blob) with the hard parts. Moreover, both hadronic parts can exchange an arbitrary number of soft gluons. Definitions of the collinear and soft momenta are given in Eq. (2.17).

Using the lightcone coordinates $v^\mu = (v^+, v^-, \mathbf{v})$ we define

$$\begin{aligned}
&\bullet \quad \text{All components of order } Q && \Longrightarrow \quad \text{hard momenta.} \\
&\bullet \quad (Q, \Lambda^2/Q, \Lambda) && \Longrightarrow \quad \text{collinear, right-moving.} \\
&\bullet \quad (\Lambda^2/Q, Q, \Lambda) && \Longrightarrow \quad \text{collinear, left-moving.} \\
&\bullet \quad \text{Components of order } \Lambda \text{ or } \Lambda^2/Q. && \Longrightarrow \quad \text{soft.}
\end{aligned} \tag{2.17}$$

The insertion of collinear longitudinally polarized gluons into the hard parts leads to quark fields in the definition of DPDs being multiplied by the Wilson lines. Take a fixed hard diagram H without the insertion of collinear gluons. Consider all of the attachments of n collinear, longitudinally polarized gluons to such a diagram.

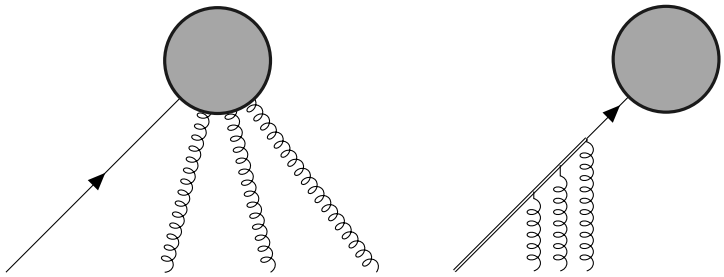

Figure 2.4: Graphical representation of the application of Slavnov-Taylor identities to decouple the collinear gluons from the inside of the hard part represented by a gray circle.

Using Slavnov-Taylor identities one can show that the sum over all attachments of the collinear gluons to the hard part gives the original hard part H with gluons attached to the quark line before it enters H, as shown schematically in Fig. 2.4. Using the Grammer-Yennie approximation one applies the following replacements for the coupling and quark propagators:

$$-igt^a\gamma_\mu \quad \longrightarrow \quad -gt^a v_\mu \,, \tag{2.18}$$

$$\frac{i}{\gamma\cdot k + i0} \quad \longrightarrow \quad \frac{i}{v\cdot k + i0} \,, \tag{2.19}$$

This allows to resum the effects of the soft- and collinear gluons into so-called Wilson lines, which in the case of gluons attached to the quark lines, are given by

$$W\big(\mathbf{b}, v\big) = \mathcal{P}\exp\Big[igt^a\int_{-\infty}^{0} ds\, v\cdot A^a(\mathbf{b}+sv)\Big] \,. \tag{2.20}$$

$\mathcal{P}$ denotes the standard path-ordering, so that fields $A^a(\mathbf{b}+sv)$ with larger values of s stand further to the right in the expanded exponential. We take different vectors v_L, v_R for right- and left-moving hadrons:

$$v_L^- \gg v_L^+ > 0 \,, \qquad v_R^+ \gg v_R^- > 0 \,. \tag{2.21}$$

Rapidity of the vector is defined as

$$Y = \frac{1}{2}\log\left|\frac{v^+}{v^-}\right| \tag{2.22}$$

It turns out that for transverse-momentum dependent factorization one cannot take vanishing $+/-$ components for vectors $v_{L/R}$ making them lightlike, since infinite rapidites would lead to ill-defined objects at the intermediate steps of the computation. In the later part, we will discuss how to apply the appropriate subtractions and express

the observables in terms of quantities that are well-defined in the limit of infinite rapidities. For right/left-moving hadron one takes $v_{L/R}$ such that the corresponding rapidity $Y_{L/R}$:

$$Y_L \ll 0\,, \qquad Y_R \gg 0\,. \tag{2.23}$$

The effects of the soft gluon exchanged between the hadrons, shown in Fig. 2.3 in orange, can be expressed in terms of the soft factor S multiplying double parton distributions, which is shown in the same way as in the case of collinear gluons, that is by using Slavnov-Taylor identities and the Grammer-Yennie approximation one proves that the effect of the exchange of the soft gluons is expressed in terms of the so-called soft factor multiplying DPDs in the cross-section formula. In the so-called Glauber region, where the gluon momenta $(k^+, k^-, \mathbf{k})$ are such that

$$|\mathbf{k}| \sim \Lambda \gg |k^+|, \quad |k^-| \sim \Lambda^2/Q\,, \tag{2.24}$$

one can see that in this region the Grammer-Yennie approximation breaks down. The crucial point in the proof of factorization is to show that in this region the gluons do not contribute at the leading power, as was shown in the case of the production of color-less states in [23].

The soft factor is defined as a vacuum expectation value of a product of Wilson lines. For processes involving two quarks, it is given by

$$\begin{aligned}&\big[S_{qq}\big]_{r_1r_1',r_2r_2',r_3r_3',r_4r_4'}(\mathbf{z}_i,\mathbf{y};v_L,v_R)\\ &\quad=\langle 0|\,\big[O_{S,q}(\mathbf{y},\mathbf{z}_1;v_L,v_R)\big]_{r_1r_1',r_3r_3'}\big[O_{S,q}(\mathbf{0},\mathbf{z}_2;v_L,v_R)\big]_{r_2r_2',r_4r_4'}\,|0\rangle\ .\end{aligned} \tag{2.25}$$

where

$$\begin{aligned}&\big[O_{S,q}(\mathbf{y},\mathbf{z};v_L,v_R)\big]_{r_1r_1',r_3r_3'}\\ &\quad=\big[W(\mathbf{y}+\tfrac{1}{2}\mathbf{z};v_L)W^\dagger(\mathbf{y}+\tfrac{1}{2}\mathbf{z};v_R)\big]_{r_1r_3}\big[W(\mathbf{y}-\tfrac{1}{2}\mathbf{z};v_L)W^\dagger(\mathbf{y}-\tfrac{1}{2}\mathbf{z};v_R)\big]_{r_1'r_3'}\,.\end{aligned} \tag{2.26}$$

For antiquarks instead of quarks, one replaces the corresponding W_{ij} with $W^\dagger_{ji}$. Soft factors for processes involving gluons, as well as the symmetry properties of S can be found for example in Section 3.2 in [56].

Subtraction of soft gluons

The collinear gluons, represented by red and blue lines in Fig. 2.3, are resummed into the Wilson lines multiplying the parton fields appearing in the definitions of parton distributions. As will be discussed shortly, since the Wilson lines include also the gluons with soft momenta, relevant to the soft factor, a consistent definition requires

subtraction of these soft gluons from the matrix elements of parton fields and Wilson lines. For now, let us focus on the unsubtracted DPDs, defined as

$$F^{r_1 r_2}_{us,a_1 a_2}\big(x_i, \mathbf{z}_i, \mathbf{y}; v_L\big) \;=\; 2p^+ (x_1 p)^{-n_1} (x_2 p)^{-n_2} \int dy^- \int \frac{dz_1^-}{2\pi} \frac{dz_2^-}{2\pi} e^{i(x_1 z_1^- + x_2 z_2^-)p^+} \\ \langle p| \, \mathcal{O}^{r_1}_{a_1}\big(y, z_1; v_L\big) \mathcal{O}^{r_2}_{a_2}\big(0, z_2; v_L\big) \, |p\rangle \;, \quad (2.27)$$

where $n_i = 1$ if parton 'a_i' is a gluon, and 0 otherwise. For parton 'a' being quark, the operator $\mathcal{O}$ is defined by

$$\mathcal{O}^r_a(y, z; v_L) = \bar{q}_{s'}\big(y - \tfrac{1}{2}z\big) W^\dagger_{s'r'}\big(y - \tfrac{1}{2}z; v_L\big) \Gamma_a W_{rs}\big(y + \tfrac{1}{2}z; v_L\big) q_s\big(y + \tfrac{1}{2}z\big) \;. \quad (2.28)$$

For antiquarks one exchanges the position arguments $\mathbf{y} + \frac{1}{2}z$ and $\mathbf{y} - \frac{1}{2}\mathbf{z}$, multiplies by -1, and uses spin projection matrices for antiquarks, as discussed below of Eq. (2.16). Summation over color indices s, s' is assumed. Definitions for the gluon DPDs can be found in Section 3.1 in [56].

Since the Wilson lines appearing in the definitions above include all collinear gluon momenta, they lead to a double-counting with the soft gluons – the quark DPDs with the soft gluons subtracted are given by

$$F_{sub} = S^{-1} F_{us} \;, \quad (2.29)$$

so that in the differential cross-section one has the following product of the unsubtracted DPDs and soft factors:

$$F^T_{us}(v_R) S^{-1}_{qq}(v_L, v_R) S_{qq}(v_L, v_R) S^{-1}_{qq}(v_L, v_R) F_{us}(v_L) \;. \quad (2.30)$$

The transposition in the first term pertains to the color indices. Lorentz invariance implies that the soft factors depend on the vectors v_L, v_R only via the difference of rapidities $Y_L - Y_R$:

$$S(v_L, v_R) = S(Y_R - Y_L) \;. \quad (2.31)$$

According to Section 3.2 in [56], one postulates the existence of a nonsingular matrix $s(Y)$ in color space such that

- It fulfills the equation

$$\frac{\partial}{\partial Y} s(Y) = s(Y) K \;, \quad K = K^\dagger, \quad K \text{ is } Y\text{-independent} \;, \quad (2.32)$$

- One can write the soft factor S as:

$$S(Y) = s(Y - Y_0) s^\dagger(Y_0) \;, \quad \text{for } Y \gg 1 \text{ and arbitrary } Y_0 \;. \quad (2.33)$$

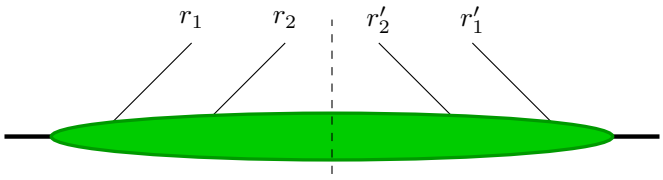

Figure 2.5: Color indices of DPDs. Projecting on definite representations in the t-channel one contracts indices r_i with their conjugate partners r_i' on the right side of the cut. In the s-channel, one contracts indices (r_1, r_2) and (r_1', r_2') on each side of the cut.

Using the second property, one can write the product of soft factors in Eq. (2.30) as

$$S_{qq}^{-1}(v_L, v_R) S_{qq}(v_L, v_R) S_{qq}^{-1}(v_L, v_R) = s^{\dagger\,-1}(Y_R - Y_C) s^{-1}(Y_C - Y_L)$$
$$\text{for } Y_L \ll Y_C \ll Y_R \,. \tag{2.34}$$

There exists a theoretical support for existence of s, see [24], however, a general proof does not exist. That allows to define DPDs as the limits of $|Y_{L/R}| \to \infty$:

$$F_{a_1 a_2}(Y_C) = \lim_{Y_L \to -\infty} s^{-1}_{a_1 a_2}(Y_C - Y_L) F_{us, a_1 a_2}(Y_L) \,,$$
$$\bar{F}_{b_1 b_2}(Y_C) = \lim_{Y_R \to \infty} s^{-1}_{b_1 b_2}(Y_R - Y_C) \bar{F}_{us, b_1 b_2}(Y_R) \,. \tag{2.35}$$

2.3.3 Projecting on definite color representation

In the remaining part of the work we shall work with DTMDs in a definite color representation. Notice that for DPD with free indices $F^{r_1 r_1' r_2 r_2'}$ one can either project with respect to the pairs $(r_1 r_1'), (r_2, r_2)$, or $(r_1, r_2), (r_1', r_2')$, see Fig. 2.5. The first decomposition, referred to as the "t-channel" allows to decouple color channels under RGE evolutions, and therefore will be used in this work. The decomposition in the "t-channel" is

$$\begin{aligned} &3 \otimes \bar{3} = 1 \oplus 8 && \text{quark-antiquark} \,, \\ &8 \otimes 8 = 1 \oplus A \oplus S \oplus 10 \oplus \bar{10} \oplus 27 && \text{gluon-gluon} \,. \end{aligned} \tag{2.36}$$

In the second decomposition, called the "s-channel", one couples the color indices on the left- and right-side of the cut, $(r_1, r_2), (r_1', r_2')$ respectively. Before renormalization, the collinear DPDs (DPDFs) in this representation can be interpreted as probability densities [58]. The application of this representation will become apparent in Section 3.3, and a more detailed description is provided in App. A. Let us denote the color representation of parton i by R_i. DTMDs decomposed in the t-channel are given by

$${}^{R_1 R_2}F_{a_1 a_2} = \varepsilon_{a_1}(R_1) \varepsilon_{a_2}(R_2) \frac{1}{\mathcal{N}_{a_1} \mathcal{N}_{a_2}} \frac{1}{\sqrt{m(R_1)}} P^{s_1 s_2}_{R_1 R_2} F^{s_1 s_2}_{a_1 a_2} \,, \tag{2.37}$$

where

$$\mathcal{N}_q = \mathcal{N}_{\bar{q}} = \sqrt{N}\,, \qquad \mathcal{N}_g = \sqrt{N^2-1}\,, \tag{2.38}$$

$$\varepsilon_{a_i} = \begin{cases} i & \text{if } R_i = A\,, \\ 1 & \text{otherwise} \end{cases}\,. \tag{2.39}$$

$N = 3$ is the number of colors, and $m(R)$ is the multiplicity of R. We notice that non-vanishing terms must have $m(R_1) = m(R_2)$. The color projectors $P^{s_1 s_2}_{R_1 R_2}$ are given in App. A.
One can also project the operators defining DPDs on the definite representation:

$${}^{R}\mathcal{O}^{r}_{a} = \varepsilon_a(R)\,\mathcal{N}_a\,P^{rs}_{R}\,\mathcal{O}^{s}_{a}\,. \tag{2.40}$$

In the later part, it will useful to define the operators integrated over the distances:

$${}^{R}O_a(x,\mathbf{z},\mathbf{y};v_L) = 2p^+\big(xp^+\big)^{-n}\int\frac{dz^-}{2\pi}\int dy^- e^{ixz^-p^+}\,{}^{R}\mathcal{O}_a(y,z;v_L)\,. \tag{2.41}$$

Unsubtracted DTMDs are then given by

$$\begin{aligned} &2\pi\delta(p^+-p'^+)\,2p^+\,{}^{R_1R_2}F_{us,a_1a_2}\big(z_i,\mathbf{z}_i,\mathbf{y};v_L\big) \\ &\quad= \langle p'|\,{}^{R_1}O_{a_1}(x_1,\mathbf{z}_1,\mathbf{y};v_L)\;{}^{R_2}O_{a_2}(x_2,\mathbf{z}_2,\mathbf{0};v_L)\,|p\rangle\,\Big|_{|\mathbf{p}|=|\mathbf{p}'|=0}\,. \end{aligned} \tag{2.42}$$

The corresponding collinear DPDF is obtained by setting $\mathbf{z}_i$ to 0.

2.3.4 Evolution equations of DTMDs

After discussion of the soft gluon subtraction, which led to the definition of DTMDs in the limit of lightlike vectors $v_{L/R}$ appearing in the Wilson lines, we are ready to present the evolution equation of DTMDs.

In the case of the rapidity dependence, it will be more convenient to introduce the rapidity parameter ζ for the left- and $\bar{\zeta}$ for the right-moving hadron:

$$\zeta = 2(p^+)^2\,e^{-2Y_C}\,, \qquad \bar{\zeta} = 2(\bar{p}^-)^2\,e^{2Y_C}\,. \tag{2.43}$$

Notice that the product of these two rapidity parameters is equal to the center-of-mass-system energy squared

$$\zeta\bar{\zeta} = 4\big(p^+\bar{p}^-\big)^2 = s^2\,. \tag{2.44}$$

From Eq. (2.32) we get that

$$\frac{d}{dY_C}F_{a_1a_2}(x_i,\mathbf{z}_i,\mathbf{y};\mu_i,Y_C) = -K_{a_1a_2}(\mathbf{z}_i,\mathbf{y};\mu_i)F_{a_1a_2}(x_i,\mathbf{z}_i,\mathbf{y};\mu_i,Y_C)(Y_C)\,, \tag{2.45}$$

where the kernel $K_{a_1a_2}$ depends on the type of partons a_i, but not on quark (antiquark) flavor. Using the relation $d/dY_C = -2d/d\log\zeta$, we get the rapidity evolution equation of DTMD:

$$\frac{d}{d\log\zeta}F_{a_1a_2}(\zeta) = \frac{1}{2}K_{a_1a_2}F_{a_1a_2}(\zeta)\,. \tag{2.46}$$

The Collins-Soper kernel $K_{a_1a_2}$ obeys the RGE equation

$$\frac{d}{d\log\mu_i}K_{a_1a_2}(\mathbf{z}_i,\mathbf{y};\mu_1,\mu_2) = -\gamma_{K,a_i}(\mu_i)\,\mathbb{I}\,. \tag{2.47}$$

$\mathbb{I}$ is a unit matrix in color space, and the cusp-anomalous dimension $\gamma_{K,a}(\mu_i)$ is rapidity-independent.
Projecting on definite representations, we can rewrite Eq. (2.46) as:

$$\frac{d}{d\log\zeta}{}^{R_1R_2}F_{a_1a_2} = \frac{1}{2}\sum_{R_1'R_2'}{}^{R_1R_2,\bar R_1'\bar R_2'}K_{a_1a_2}{}^{R_1'R_2'}F_{a_1a_2}\,, \tag{2.48}$$

The solution of Eq. (2.48) is

$$\begin{aligned}&{}^{R_1R_2}F_{a_1a_2}\big(x_i,\mathbf{z}_i,\mathbf{y};\mu_i,\zeta\big)\\ &\quad=\sum_{R_1'R_2'}{}^{R_1R_2,\bar R_1'\bar R_2'}\Big[\exp\Big(\tfrac{1}{2}K_{a_1a_2}\big(\mathbf{z}_i,\mathbf{y};\mu_i\big)\log\frac{\zeta}{\zeta_0}\Big)\Big]\;\times\;{}^{R_1'R_2'}F_{a_1a_2}\big(x_i,\mathbf{z}_i,\mathbf{y};\mu_i,\zeta_0\big)\,,\end{aligned} \tag{2.49}$$

where ${}^{R_1R_2,\bar R_1'\bar R_2'}\big[\exp(...)\big]$ is the exponentiated matrix.
Subtracted DTMDs are renormalized multiplicatively:

$$F_{a_1a_2}\big(\mu_1,\mu_2,Y_C\big) = Z_{F,a_1}(\mu_1,Y_C,x_1p^+)Z_{F,a_2}(\mu_2,Y_C,x_2p^+)F_{B,a_1a_2}(Y_C)\,, \tag{2.50}$$

where renormalization constants Z_F are independent of the polarization and color representation, but they are different for quarks and gluons. They are given in Section 3.4 in [56]. The renormalization group equation of DTMDs reads

$$\frac{d}{d\log\mu_i}{}^{R_1R_2}F_{a_1a_2}\big(x_i,\mathbf{z}_i,\mathbf{y};\mu_1,\mu_2,\zeta\big) = \gamma_F(\mu_i,x_i^2\zeta)\,{}^{R_1R_2}F_{a_1a_2}\big(x_i,\mathbf{z}_i,\mathbf{y};\mu_1,\mu_2,\zeta\big)\,, \tag{2.51}$$

where the anomalous dimension γ_F does not depend on the color representation or parton polarization. It is given by

$$\gamma_{F,a_i}(\mu_i,x_i^2\zeta) = \gamma_{a_i}(\mu_i) - \gamma_{K,a_i}(\mu_i)\log\frac{x_i\sqrt{\zeta}}{\mu_i}\,. \tag{2.52}$$

The kernel $\gamma_{K,a}$ is defined in Eq. (2.47), and

$$\gamma_{a_i}(\mu_i) = \gamma_{F,a_i}(\mu_i,\mu_i^2)\,. \tag{2.53}$$

The solution of the RGE reads

$$
\begin{aligned}
&{}^{R_1R_2}F_{a_1a_2}\big(x_i,\mathbf{z}_i,\mathbf{y};\mu_1,\mu_2,\zeta\big) \\
&\quad = \exp\Big(S_q\big(\mu_{01},\mu_1,x_1\sqrt{\zeta}\big)\Big) \times {}^{R_1R_2}F_{a_1a_2}\big(x_i,\mathbf{z}_i,\mathbf{y};\mu_{01},\mu_2,\zeta\big)\,,
\end{aligned}
\tag{2.54}
$$

where

$$
\exp\Big(S_{a_1}\big(\mu_{01},\mu_1,x_1\sqrt{\zeta}\big)\Big) = \exp\left(\int_{\mu_{01}}^{\mu_1}\frac{d\mu}{\mu}\Big(\gamma_{a_1}(\mu)-\gamma_{K,a_1}\log\frac{x_1\sqrt{\zeta}}{\mu}\Big)\right),
\tag{2.55}
$$

analogously for the second scale μ_2. The exponential in Eq. (2.54) is often called the Sudakov factor.

2.3.5 The case of collinear double parton distributions

This work deals mostly with transverse-momentum dependence, but for completeness let us also briefly discuss the evolution of collinear double parton distributions (DPDFs).

Also in that case one needs to subtract the double-counted soft gluons, as this was done previously for transverse momentum-dependent DPDs, but here the corresponding soft factor turns out to be diagonal in color representation after projecting on the t-channel, see Section 2.3.3. This allows for a simpler definition of the matrix s:

$$
{}^{RR}s(Y) = \sqrt{{}^{RR}S(2Y)}\,,
\tag{2.56}
$$

which leads to the following definition of subtracted DPDFs:

$$
{}^{R_1R_2}F^{coll.}_{a_1a_2}(Y_C) = \lim_{Y_L\to-\infty} {}^{RR}s^{-1}(Y_C-Y_L)F^{coll.}_{us,a_1a_2}(Y_L)\,.
\tag{2.57}
$$

The resulting rapidity evolution equation reads

$$
\frac{d}{d\log\zeta}{}^{R_1R_2}F^{coll.}_{a_1a_2}(x_i,\mathbf{y};\mu_1,\mu_2,\zeta) = \frac{1}{2}\,{}^{R_1}J(\mu_1,\mu_2,\zeta)F^{coll.}_{a_1a_2}(x_i,\mathbf{y};\mu_1,\mu_2,\zeta)\,.
\tag{2.58}
$$

The kernel ${}^{R}J$ depends only on the dimension of the representation, hence we write it only with a single color representation index R. The RGE of the rapidity evolution kernel reads

$$
\frac{d}{d\log\mu_i}\,{}^{R}J(\mu_1,\mu_2) \;=\; -{}^{R}\gamma_J(\mu_i)\,.
\tag{2.59}
$$

To all orders, one has

$$
{}^{1}J = 0\,.
\tag{2.60}
$$

The solution of the Collins-Soper equation in this case has a simple form:

$$
{}^{R_1R_2}F^{coll.}_{a_1a_2}(x_i,\mathbf{y};\mu_1,\mu_2,\zeta) \;=\; \exp\Big(\tfrac{1}{2}\,{}^{R_1}J(\mathbf{y};\mu_i)\log\frac{\zeta}{\zeta_0}\Big) \times {}^{R_1R_2}F^{coll.}_{a_1a_2}(x_i,\mathbf{y};\mu_1,\mu_2,\zeta_0)\,.
\tag{2.61}
$$

Just as in the case of PDFs, the collinear double-parton distributions are not renormalized multiplicatively, but by a convolution:

$$\begin{aligned}\frac{d}{d\log\mu_1}\,&{}^{R_1R_2}F_{a_1a_2}(x_i,\mathbf{y};\mu_i,\zeta)\\ &= 2\sum_{b_1,R_1'}{}^{R_1\bar{R}_1'}P_{a_1b_1}(x_1',\mu_1,x_1^2\zeta)\overset{\otimes}{{}_{x_1}}{}^{R_1'R_2}F_{b_1a_2}(x_i,\mathbf{y};\mu_i,\zeta)\,.\end{aligned}\tag{2.62}$$

The color-singlet sector shares the DGLAP kernels with the single parton distributions [22, 56]. The corresponding kernels have been computed up to N^{3}LO [59–61], and partial N^{4}LO correction are available [62–65]. On the other hand, the DGLAP kernels for the color-nonsinglet channels only recently have been computed to NLO [66], and the DGLAP evolution in these channels was extensively studied in [67].

2.3.6 Modelling of the Collins-Soper kernel

The rapidity evolution kernel ${}^{R}J$ relevant in the evolution of DPDFs depends on the transverse distance $\mathbf{y}$, and in general, is a non-perturbative quantity. It will be modeled in the same way as Collins-Soper kernels for single parton TMDs, according to the method developed by Collins, Soper, and Sterman [68]. In this approach, one introduces a distance-dependent function with the following properties:

$$\begin{aligned}&b^*(\mathbf{b})\approx|\mathbf{b}| && \mathbf{b}\text{ perturbatively small}\,,\\ &b^*(\mathbf{b})\to b_{\max} && \text{as }\mathbf{b}\to\infty\,.\end{aligned}\tag{2.63}$$

In the TMD literature, it is often called the *-prescription. It will be further discussed in Section 3.2. At small distances, one can compute the perturbative expansion of the kernel, denoted as ${}^{R}J^{pt}$. At arbitrary $\mathbf{y}$ one uses the following decomposition:

$${}^{R}J(\mathbf{y};\mu_i)\;=\;{}^{R}J^{pt}(\mathbf{y}^*;\mu_i)\;+\;g_J(\mathbf{y})\,,\tag{2.64}$$

where $g_J(\mathbf{y})$ is a non-perturbative, scale-independent function. This approach has been discussed in [56], and applied in the numerical study in [67].

All of the other rapidity evolution kernels depending on only one tranvserse distance relevant to this work will be modeled in the same way. The extrapolation of the DTMD kernel ${}^{R_1R_2,R_3R_4}K_{a_1a_2}$, which depends on 3 transverse distances $(\mathbf{z}_1,\mathbf{z}_2,\mathbf{y})$, is more complicated, and will be discussed in Chapter 4.

2.4 Differential cross-section and double-counting

After introducing the formal definition of double parton distributions, and the discussion of their scale dependence and color decomposition, let us recapitulate the

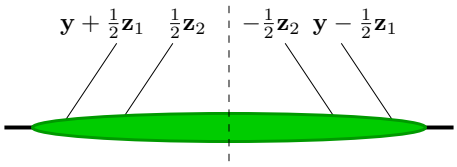

Figure 2.6: Transverse positions of partons on both sides of the cut.

general form of the cross-section formulas, and discuss the problem of double-counting between DPS and SPS.

For DTMDs in the transverse-position space, the distance between two partons on the left/right side of the cut is given by

$$\mathbf{y}_\pm = \mathbf{y} \pm \frac{1}{2}(\mathbf{z}_1 - \mathbf{z}_2)\,, \tag{2.65}$$

see Fig. 2.6. In the region where one of the distances becomes comparably small as the inverse of the hard scale Q^{-1}, the process should no longer be described as DPS, but rather an SPS/DPS interference, where the partons characterized by the small distance originate from the perturbative splitting of a single parton. Both distances $\mathbf{y}_\pm \lesssim Q^{-1}$ correspond to a single-parton scattering process.

Therefore, integration over the whole transverse-position space as in Eq. (2.13) introduces a double-counting of DPS, SPS, and interference terms. This is avoided using the Diehl-Gaunt-Schönwald scheme [69]. In that approach, one introduces the short-distance cut-offs $\Phi(y_\pm)$ on transverse distances $\mathbf{y}_\pm$ in the integrals defining DPS, and a single cut-off on either $\mathbf{y}_+$ ($\mathbf{y}_-$) for the SPS/DPS (DPS/SPS) interference term. The total SPS+DPS cross-section is then given by:

$$\begin{aligned}\sigma = \sigma_{\text{DPS}} &+ \Big[\sigma_{\text{DPD/SPS}} - \sigma_{\text{DPS},y_-\to 0} + \sigma_{\text{SPS/DPS}} - \sigma_{\text{DPS},y_+\to 0}\Big] \\ &+ \Big[\sigma_{\text{SPS}} - \sigma_{\text{DPD/SPS},y_+\to 0} - \sigma_{\text{SPD/DPS},y_-\to 0} + \sigma_{\text{DPS},y_\pm\to 0}\Big]\,.\end{aligned} \tag{2.66}$$

The subscript '$y_\pm \to 0$' denotes taking the limit of the vanishing relevant distance. Ideally, the dependence on the short-distance cut-off $\Phi(y_\pm)$ should be a subleading effect after including the subtractions. The inclusion of the subtractions, as well as the DPS/SPS interference, is beyond the scope of this work, and we will focus only on the DPS part. As will be shown in the following part of the work, for like-sign W pair production this is the only non-vanishing term at the considered order of perturbative QCD.

For transverse-momentum dependent observables we have

$$\begin{aligned}
&\frac{d\sigma^{\mathrm{DPS}}}{\prod_{i=1,2} dx_i d\bar{x}_i d^2\mathbf{q}_i} \\
&\quad = \frac{1}{C} \sum_{a_1,a_2,b_1,b_2} \sum_{R_1,R_2} \hat{\sigma}_{a_1b_1}(Q_1,\mu_1)\, \hat{\sigma}_{a_2b_2}(Q_2,\mu_2) \\
&\qquad \times \int \frac{d^2\mathbf{z}_1}{(2\pi)^2} e^{-i\mathbf{q}_1\mathbf{z}_1} \int \frac{d^2\mathbf{z}_2}{(2\pi)^2} e^{-i\mathbf{q}_2\mathbf{z}_2} \int d^2\mathbf{y}\; \Phi(y_+)\Phi(y_-) \\
&\qquad\quad \times {}^{R_1R_2}F_{a_1a_2}\big(x_i,\mathbf{z}_i,\mathbf{y};\mu_i,\zeta\big)\; {}^{R_1R_2}\bar{F}_{b_1b_2}\big(x_i,\mathbf{z}_i,\mathbf{y};\mu_i,\bar{\zeta}\big)\,.
\end{aligned} \tag{2.67}$$

The constant C is equal to 2 if the produced particles are identical, and 1 otherwise. The hard scattering cross-sections are connected to the functions H_{ab} in Eq. (2.13) by the relation

$$\hat{\sigma}_{ab} = \frac{H_{ab}}{\mathcal{N}_a \mathcal{N}_b}\,. \tag{2.68}$$

The rapidity parameters of the incoming hadrons are such that $\zeta\bar{\zeta} = s^2$, and the RGE scales μ_i are taken equal to the hard scales Q_i – in this case the mass of W boson. The typical momenta fractions of the active partons are given by

$$x \sim \frac{Q}{\sqrt{s}}\,. \tag{2.69}$$

For $Q = M_W = 80.377$ GeV, and $\sqrt{s} = 13$ TeV, x is about 6×10^{-3}.

2.5 Numerical set-up

In this section, we briefly describe the software used to obtain the results presented in the next Chapters. We describe the ChiliPDF framework, which provides us with the models and evolution of DPDFs and PDFs, and on which we developed the code needed to model and evolve the transverse momentum-dependent double parton densities, and compute physical observables.

In 2.5.2 we give an overview of the algorithm for the computation of integrals involving Bessel functions, which we have developed to compute the double Fourier transforms appearing in the cross-section formula discussed in the previous part.

2.5.1 ChiliPDF

The code developed to compute DTMDs and the differential cross-section of W pair production is a part of a C++ library ChiliPDF [70], which already implements the evolution of PDFs and collinear double parton distributions (DPDFs) [67, 71]. It is

based on expansion of parton densities and their evolution kernels using Chebyshev polynomials [72], allowing to discretize the evolution equations.

Single parton distributions (PDFs) used to construct DPDF and DTMD models used in this work are imported from LHAPDF [73].

2.5.2 Levin's integration method for Bessel transforms

As indicated in Eq. (2.67), the transverse momentum-dependent differential cross-section of double-parton scattering involves a double two-dimensional Fourier transform. As will be shown in the later parts, performing the angular integration in $d^2\mathbf{z}_i$ integrals allows to rewrite it as a double Hankel transform, also called a Bessel integral:

$$\int_0^\infty dz\, J_\mu(qz)\, f(z)\,, \tag{2.70}$$

where J_ν is a Bessel function of order ν. The precise and time-efficient computation of the Bessel integrals is a serious issue already at the level of single-parton TMD [74–76], where only a single integral is involved. Commonly used are quadrature methods [74–78], which, however, suffer from the necessity of taking the grid points in transverse-position space depending on the value of transverse momentum, while re-computing of DTMDs in the position space for each new pair of transverse momenta (q_1, q_2) would be extremely costly. There exist methods using grids with fixed points based on discrete Hankel transform [79,80], but we found them inefficient for the relevant class of transformed functions.

For this reason, we developed a method of computation of the Bessel integrals which allows to use the fixed grids in the position space in a wide range of q, and leads to typically a much faster convergence of the result with an increasing number of grid points. In the original version of the method presented in the work by D. Levin [81], one considers the integral

$$\int_{z_a}^{z_b} \left[\tilde{f}_1(z) J_\nu(qz) + \tilde{f}_2(z) J_{\nu+1}(qz)\right] dz\,, \tag{2.71}$$

with functions $\tilde{f}_{1,2}$ which do not oscillate rapidly. First, express (2.71) as a product of two vectors:

$$\int_{z_a}^{z_b} \tilde{\omega}\cdot\tilde{\mathbf{f}}\, dz\,, \tag{2.72}$$

where

$$\tilde{\omega}(z,q) = \begin{bmatrix} J_\nu(qz) \\ J_{\nu+1}(qz) \end{bmatrix}, \qquad \tilde{\mathbf{f}}(z) = \begin{bmatrix} \tilde{f}_1(z) \\ \tilde{f}_2(z) \end{bmatrix}. \tag{2.73}$$

The vector $\tilde{\omega}$ has the following property:

$$\frac{d}{dz}\tilde{\omega} = A^T\tilde{\omega}, \tag{2.74}$$

where A is a (z, q)-dependent matrix, which does not exhibit oscillatory behavior. Using integration by part, it can be shown that if one finds the solution of differential equation

$$\Big(\frac{d}{dz} + A\Big)\tilde{\mathbf{h}} = \tilde{\mathbf{f}}\,, \tag{2.75}$$

then the original integral is given by the boundary terms

$$\int_{z_a}^{z_b} \tilde{\omega} \cdot \tilde{\mathbf{f}}\, dz \;=\; \big(\tilde{\omega} \cdot \tilde{\mathbf{h}}\big)(z_b) - \big(\tilde{\omega} \cdot \tilde{\mathbf{h}}\big)(z_a)\,. \tag{2.76}$$

By discretizing the differential equation (2.75) on Chebyshev grid, one can construct its approximate solution using the Chebyshev spectral method. In our work [1], we modified the original method to allow for precise integration on interval $[0, \infty]$ by appropriately rescaling the vectors $\tilde{\omega}, \tilde{\mathbf{f}}$ and $\tilde{\mathbf{h}}$. Details are provided in Section 2 of the cited work. The algorithm was implemented in ChiliPDF , and in a publicly available C++ library BestLime [82].

Precision studies of the optimized Levin's method, discussed in Section 5 in [1] were our basic guidelines for the choice of interpolation grids used in the computation of double Bessel integrals, essential in evaluating the results presented in Chapter 5.

Chapter 3

DTMDs in the large y region

3.1 Small z expansion

For perturbatively small $|\mathbf{z}_i| \ll \Lambda^{-1}$, and $\mathbf{y}$ such that $|\mathbf{y}| \gg |\mathbf{z}_i|$, one can express the transverse position-dependent parton distributions (DTMDs) $F(\mathbf{z}_1, \mathbf{z}_2, \mathbf{y})$ in terms of collinear double-parton distribution (DPDFs), denoted as $F^{coll.}(\mathbf{y})$, using the operator product expansion, in a similar way to the case of single-parton distributions. This procedure, widely used in TMD physics, is commonly called "matching" [56, 68, 83–88].

The short-distance expansion of operators defining the unsubtracted DTMDs in a definite color representation, see Eq. (2.41), has the following form:

$$ {}^{R}O_a\big(x, \mathbf{z}, \mathbf{y}\big) = \sum_b \sum_{R'} {}^{RR'}C_{us,ab}(x', \mathbf{z}) \underset{x}{\otimes} {}^{R'}O_b\big(x', \mathbf{0}, \mathbf{y}\big) \,. \tag{3.1} $$

The symbol $\underset{x}{\otimes}$ denotes the convolution product defined as

$$ C(x') \underset{x}{\otimes} f(x') \;=\; \int_x^1 \frac{dx'}{x'}\, C(x')\, f\Big(\frac{x}{x'}\Big) \,. \tag{3.2} $$

Operators ${}^{R}O_b\big(x', \mathbf{0}, \mathbf{y}\big)$ define collinear double parton distributions. It should be noted that the matching kernels ${}^{RR'}C$ do not mix between color multiplicities, and kernels with $R \neq R'$ are non-zero only for matching between quarks in octet representation, and gluons in either symmetric- or antisymmetric octet representation, that is $R, R' \in \{8, S, A\}$.

The expansion of the soft factors given in Eq. (2.25), projected on definite color representations, has a multiplicative form:

$$ \begin{aligned} &{}^{R_1R_2, R_1'R_2'}S_{a_1a_2}(\mathbf{z}_i, \mathbf{y}) \\ &\quad = {}^{R_1R_2}C_{S,a_1}(\mathbf{z}_1)\, {}^{R_1R_2}C_{S,a_2}(\mathbf{z}_2)\, {}^{R_1R_2, R_1R_2}S_{a_1a_2}(\mathbf{z}_i = 0, \mathbf{y})\, \delta_{R_1R_2, R_1'R_2'} \,. \end{aligned} \tag{3.3} $$

This shows that in the large-$\mathbf{y}$ approximation the soft factor also does not mix between color representations – using the results of Section 2.3.5 for color-diagonal soft factor, one can write the matrix ${}^{R_1R_2,R_1'R_2'}s_{a_1a_2}$ in Eq. (2.33), in a simple form:

$$
\begin{aligned}
&{}^{R_1R_2,R_1'R_2'}s_{a_1a_2}\big(\mathbf{z}_i,\mathbf{y};\mu_i,Y\big)\\
&\quad=\sqrt{{}^{R_1R_2}C_{S,a_1}(\mathbf{z}_1;2Y)}\sqrt{{}^{R_1R_2}C_{S,a_2}(\mathbf{z}_2;2Y)}\;{}^{R_1R_2,R_1R_2}s_{a_1a_2}\big(\mathbf{y};\mu_i,Y\big)\;\delta_{R_1R_2,R_1'R_2'}\,.
\end{aligned}
\tag{3.4}
$$

The color-diagonal matrix $s(\mathbf{z}_i=0,\mathbf{y})$ appears in the soft gluons subtraction for collinear DPDFs as discussed in Section 2.3.5.

Using Eqs. (3.1), (3.4), and definitions of DPDs in Section 2.3 one finds that the subtracted DTMDs can be written in terms of collinear DPDFs convolved with subtracted matching kernels:

$$
\begin{aligned}
&{}^{R_1R_2}F_{a_1a_2}\big(x_i,\mathbf{z}_i,\mathbf{y};Y_C\big)\\
&\quad=\sum_{b_1b_2}\sum_{R_1',R_2'}{}^{R_1\bar{R}_1'}C_{a_1b_1}\big(x_1',\mathbf{z}_1;Y_C\big)\underset{x_1}{\otimes}\\
&\qquad\qquad{}^{R_2\bar{R}_2'}C_{a_2b_2}\big(x_2',\mathbf{z}_2;Y_C\big)\underset{x_2}{\otimes}{}^{R_1'R_2'}F^{coll.}_{b_1b_2}\big(x_i',\mathbf{y};Y_C\big)\,,
\end{aligned}
\tag{3.5}
$$

where subtracted matching kernels are defined according to

$$
{}^{R_1R_2}C_{ab}\big(x,\mathbf{z};\mu,Y_C\big)=\lim_{Y_L\to-\infty}\frac{{}^{R_1R_2}C_{us,ab}\big(x,\mathbf{z};\mu,Y_L\big)}{\sqrt{{}^{R_1R_2}C_{S,a}(\mathbf{z};\mu,2Y_C-2Y_L)}}
\tag{3.6}
$$

for the right-moving hadron. Recall from Eq. (2.57) that the subtracted collinear DPDF is defined as a limit

$$
{}^{R_1R_2}F^{coll.}_{a_1a_2}\big(x_i,\mathbf{y};Y_C\big)=\lim_{Y_L\to-\infty}{}^{R_1R_2,R_1R_2}s_{a_1a_2}\big(\mathbf{y};\mu_i,Y_C-Y_L\big)\;{}^{R_1R_2}F^{coll.}_{us,a_1a_2}\big(x_i,\mathbf{y};Y_L\big)\,.
\tag{3.7}
$$

Switching from the variable Y_C to ζ, where we recall

$$
\zeta=2(p^+)^2e^{-2Y_C}\,,
\tag{3.8}
$$

we obtain

$$
\begin{aligned}
&{}^{R_1R_2}F_{a_1a_2}\big(x_i,\mathbf{z}_i,\mathbf{y};\mu_i,\zeta\big)\\
&\quad=\sum_{b_1b_2}\sum_{R_1',R_2'}{}^{R_1\bar{R}_1'}C_{a_1b_1}\big(x_1',\mathbf{z}_1;\mu_1,x_1^2\zeta\big)\underset{x_1}{\otimes}\\
&\qquad\qquad{}^{R_2\bar{R}_2'}C_{a_2b_2}\big(x_2',\mathbf{z}_2;\mu_2,x_2^2\zeta\big)\underset{x_2}{\otimes}{}^{R_1'R_2'}F^{coll.}_{b_1b_2}\big(x_i',\mathbf{y};\mu_i,\zeta\big)\,.
\end{aligned}
\tag{3.9}
$$

Notice that the rapidity parameter enters the matching kernels for parton i $(= 1, 2)$ only in combinations $x_i^2\zeta$, which is because in a perturbative computation of the kernel the result depends on the momentum of a single parton, rather than the whole hadron. The exact form of the matching kernels is given in App. C, and the details of the matching procedure will be discussed in a later part.

Finally, using the formula for the subtracted kernels in Eq. (3.6), one obtains the Collins-Soper equation for the matching kernels:

$$\frac{d}{d\log\sqrt{\zeta}}\,{}^{R_1R_2}C_{ab}\big(x,\mathbf{z};\mu,\zeta\big) \;=\; {}^{R_1}K_a(\mathbf{z};\mu)\,. \tag{3.10}$$

For the color-singlet channel, the kernel ${}^1K_a$ is identical with the rapidity evolution kernel of single TMDs [56]. The rapidity evolution equation (3.10) will be used to resum logarithms of $x_i^2\zeta/\mu^2$ in the matching formula in Section 3.4.

Finally, the rapidity evolution equation of DTMDs obtained via perturbative matching reads

$$\begin{aligned}&\frac{d}{d\log\sqrt{\zeta}}\,{}^{R_1R_2}F_{a_1a_2}\big(x_i,\mathbf{z}_i,\mathbf{y};\mu_i,\zeta\big)\\ &\quad=\;\Big({}^{R_1}J(\mathbf{y};\mu_i)+{}^{R_1}K_{a_1}(\mathbf{z}_1;\mu_1)+{}^{R_2}K_{a_2}(\mathbf{z}_2;\mu_2)\Big)\,{}^{R_1R_2}F_{a_1a_2}\big(x_i,\mathbf{z}_i,\mathbf{y};\mu_i,\zeta\big)\,.\end{aligned} \tag{3.11}$$

Comparing with the general form of the Collins-Soper kernel for DTMDs in Eq. (2.48), one sees that in the large-**y** limit it becomes diagonal in color representations, and the solution of the rapidity equation in this case does not involve matrix exponentiation, cf. Eq. (2.49).

3.2 Intermediate scales

It turns out that the computation of double parton distributions via perturbative matching poses a multiscale problem – in the computation of observables one needs DTMDs at the scales of order of $M_W \approx 80$ GeV, whereas the natural choice of scales, at which one performs the matching is given by transverse distances $\mathbf{z}_i$, which are perturbatively small, but typically much larger than M_W^{-1}. Moreover, the scale at which one models the collinear parton distributions should depend only on the scale relevant to that distribution – that is $|\mathbf{y}|^{-1}$. In this Section, we discuss our choice of distance-dependent scales, and the evolution of the parton densities at intermediate steps of the computation.

Matching scales

The pair of the matching scales in Formula (3.9), which will be denoted as (μ_{01}, μ_{02}), is given by the distances $\mathbf{z}_i$, so that

$$\mu_{0i} \propto |\mathbf{z}_i|^{-1} \,. \tag{3.12}$$

The standard choice is

$$\mu_{0i} = \frac{b_0}{|\mathbf{z}_i|} \,, \qquad b_0 = 2e^{-\gamma_E} \approx 1.123 \,, \tag{3.13}$$

where γ_E is the Euler-Mascheroni constant. This choice makes the one-loop corrections to the TMD Collins-Soper kernel vanish.

Since the transverse momentum-dependent cross-section is expressed in terms of a double Fourier transform of $(\mathbf{z}_1, \mathbf{z}_2)$-dependent product of DTMDs, one may expect that the most relevant region of the phase space is characterized by the distance $|\mathbf{z}_i|$ of size of the inverse of the transverse momenta $\mathbf{q}_i$ of the produced W bosons: $|\mathbf{z}_i| \sim |\mathbf{q}_i|^{-1}$. To smoothly extrapolate to a region where either the perturbative calculation no longer makes sense (large $\mathbf{z}$), or where the inverse of $|\mathbf{z}|$ approaches the hard scale, we will apply the "*-prescription" to the transverse distances, as it is commonly done in TMD literature [68, 76, 86–88, 90]. It means that the perturbatively matched DTMD at the initial scales will be computed at regularized distances given by

$$\mathbf{b}^*(\mathbf{z}) \;\equiv\; \mathbf{z}^* \;=\; \mathbf{z}\left(\frac{1+\left(z_{\min}/|\mathbf{z}|\right)^4}{1+\left(|\mathbf{z}|/z_{\max}\right)^4}\right)^{1/4} \,, \tag{3.14}$$

where we choose

$$z_{\max} = \frac{b_0}{\mu_{\min}} \,, \qquad \mu_{\min} = 2\,\text{GeV}, \;\text{ and } \quad z_{\min} = \frac{b_0}{M_W} \,. \tag{3.15}$$

To have some indication of in which region the described *-prescription significantly modifies the transverse distances, it can be checked that the relative difference between $|\mathbf{b}^*(\mathbf{z})|$ and $|\mathbf{z}|$ is smaller than 5% for $0.021\,\text{GeV}^{-1} < |\mathbf{z}| < 0.38\,\text{GeV}^{-1}$. The powers in the definition are taken such that for perturbatively small, but also larger than the inverse of the hard scale distances $\mathbf{z}$: $Q^{-1} \ll |\mathbf{z}| \ll \Lambda^{-1}$, its regularized value differs from the unregularized ones by terms of 4-th power in $|\mathbf{z}|/b_{\max}, b_{\min}/|\mathbf{z}|$, allowing to achieve a smooth interpolation outside of the region of validity of the discussed approximation. A similar approach has been used by the MAP collaboration [87], while *-prescriptions considered in other works, e.g. [86, 88], are such that the difference between $|\mathbf{z}^*|$ and $|\mathbf{z}|$ is suppressed only by terms $\mathcal{O}\left(\mathbf{z}^2/b_{\max}^2\right)$, and $\mathbf{z}^*$ is not regularized from below.
Finally, our choice of the matching scales is given by

$$\mu_{0i} = \frac{b_0}{|\mathbf{z}_i^*|} \,, \tag{3.16}$$

This definition ensures that the matching scale used in the perturbative computation is much larger than the QCD scale, and does not exceed the hard scale. The latter ensures that one does not evolve DPDFs to scales larger than M_W in the region of very small $\mathbf{z}_i$, which is computationally costly, and gives a negligible contribution to the overall result. Moreover, the UV regularization avoids possible singularities of the Collins-Soper kernels when approaching the limit $|\mathbf{z}| \to 0$, as will be discussed in detail in Section 4.2.

Effects of quark masses

The number of active flavors n_f at the level of hard scattering is set by the hard scale – for W boson production it is $Q = M_W \approx 80.377$ GeV, so that in the considered kinematics one has DTMDs with $n_f = 5$ active quarks treated as massless. On the other hand, the initial scale of DPDFs, denoted as μ_y, is typically much smaller (but no smaller than 2 GeV), and the matching scales μ_{0i} are of order $|\mathbf{q}_T|$, so that neither of these scales is necessarily much larger than all of the active quark masses. We approach this problem in a similar way to that presented in [91], that is, after initializing the DPDF at a given number of active flavors, we either match to a higher number of flavors during the scale evolution, or match DPDF to DTMDs with different n_f using mass-dependent kernels.

For simplicity, let us assume that there is a single massive quark of mass m. Depending on the hierarchy between m and the remaining scales, one needs a different approach to including the quark mass effects in the computation. There are 4 possible configurations of the scales:

(a) $Q \gg |\mathbf{q}_T| \sim m$,

(b) $Q \gg |\mathbf{q}_T| \gg m$,

(c) $Q \sim m \gg |\mathbf{q}_T|$,

(d) $Q \gg m \gg |\mathbf{q}_T|$.

In the discussion of the scales hierarchy in the following part, we identify the matching scales μ_{0i} with the corresponding transverse momenta $|\mathbf{q}_T|$, thus focusing on the dominant region in the transverse position space. Instead of that, one can replace $|\mathbf{q}_T|$ with $b_0/|\mathbf{z}_i^*|$ in the considerations below, and pick the cases (a)-(d) depending on the value of $|\mathbf{z}_i|$. This approach, although more detailed, introduces two important drawbacks:

- Switching between the cases (a)-(d) would introduce a discontinuity in highly oscillatory z_i integrands, which can lead to artifacts in the numerical computation.

- Changing the number of active flavors $(n_{f,1}, n_{f,2})$ in DPDF depending on $(\mathbf{z}_1, \mathbf{z}_2)$, one needs to consider 4 different settings:

$$(n_l, n_l),\ (n_l+1, n_l),\ (n_l, n_l+1),\ (n_1+1, n_l+1).$$

  This would require computing DPDFs initially at n_l active flavors, and then evolving them from the region of the largest distances to the smallest, corresponding to scales at which there are n_l+1 active flavors. To achieve this, one would need to initialize two independent DPDF class instances, one for which one first passes the quark mass threshold for quark 1, matching $(n_l, n_l) \to (n_l+1, n_l)$ active flavors; and one instance where the matching is first performed for parton 2. Such an approach is possible to implement in our current framework, but it will be shown later that this is not necessary for the relevant scales.

It will be argued later that for the process considered in this work, based on the considered range of $\mathbf{q}_T$ values, it is justified to assume the scales hierarchy (a) for all $\mathbf{z}_i$. For this reason, we keep the treatment of the quark masses independent of transverse positions.

Case (d) is of little interest in this process since this would imply

$$|\mathbf{q}_T| \ll m_b \approx 4.18 \text{ GeV},$$

breaking the assumption of large transverse momenta. Cases (c) and (d) could be considered in the context of production of states with larger invariant mass, for example, a hypothetical heavy Z' boson or a two-boson state, where m would be the mass of the top quark.

For the W pair production process, the case (b) can be realized in a rather small region of the phase space, since it is questionable, whether one can treat any scale between m_b and M_W as much larger than the lower one, and much smaller than the upper one simultaneously – perhaps this can be justified for $|\mathbf{q}_T|$ close to the upper limit of the considered transverse momenta, which in this work we take equal to 20 GeV. However, we find that it is also reasonable to classify such scales as $m_b \sim |\mathbf{q}_T|$, hence in our numerical studies, we assume the case (a).

First, we will discuss the case (a) in detail. For completeness, we will also describe how to include the effect of quark masses in cases (b) and (c). By F_{n_f} we denote parton distributions F with n_f active quarks. Let n_l denote the number of light quarks (in our case $n_l = 4$). The collinear DPD is initialized at $\mathbf{y}$-dependent scale μ_{y^*}, and then evolved to the matching scales $\mu_{0i} \sim |\mathbf{q}_{T,i}| \sim m_b$. Since the mass of the charm quark is

$$m_c \approx 1.27 \,\text{GeV}\,, \tag{3.17}$$

and the initial scales of DPDFs are no smaller than

$$\mu_{\min} \;=\; \frac{b_0}{b_{\min}} \;=\; 2\,\mathrm{GeV}\,, \tag{3.18}$$

so that DPDFs are initialized at $n_f = 4$ light flavors at scale μ_{y^*}, and evolved with the corresponding DGLAP kernels to the matching scales. In the next step, one performs the matching of DPDFs with n_l active quarks onto DTMD with $n_l + 1$ active quarks, using the mass-dependent matching kernels for the bottom quark. Those are given in Appendix C. Finally, one evolves DTMD with $n_f = 5$ massless quarks to the hard scales.

In the case (b), for $|\mathbf{q}_T| \gg m$, one performs the threshold matching to DPDF_{n_l+1} before DPDF-DTMD matching if $m \gg \mu_{y^*}$, and then evolves DTMD_{n_l+1} to the final scales. If $m \sim \mu_{y^*}$, the DPDF is already initialized at $n_f + 1$ active quarks, and the mass effects are included only in the splitting formula for DPDFs.
In case c), for $Q \sim m$, one computes both DPDF and DTMD with n_l active flavors, and the quark mass dependence enters only via virtual corrections to the hard cross-section.

A schematic representation of the described procedure, in particular the scale evolution, matching between different number of flavors, and DPDF-DTMD matching in cases (a)-(c) is shown in Fig. 3.1.

Initial scales for DPDFs

For completeness, let us discuss the initial scales at which the model of collinear double parton distributions is formulated. Since the only relevant scale in the problem is $\mathbf{y}$, we take

$$\mu_{0,y} = \frac{b_0}{|\mathbf{y}^*|}\,. \tag{3.19}$$

The UV-regularization of the scale is, in this case, irrelevant, since one anyway imposes the cut-off $|\mathbf{y}| \geq M_W^{-1}$ in the computation of differential cross-section. The choice of the initial rapidity scale is less obvious and has been the object of discussion, see Erratum I.2 in [56]. In the perturbation theory, higher-order corrections may depend on rapidity via logarithms of the following products of ζ and the remaining scales:

$$\left(x_i\sqrt{\zeta_0}\right)|\mathbf{y}|\,, \qquad i = 1, 2\,.$$

Assuming that the correction involving $x_1\sqrt{\zeta_0}$ and $x_2\sqrt{\zeta_0}$ are the same, one can minimize the part linear in the logarithms by taking

$$\zeta_0 = \frac{\xi_0(\mathbf{y})}{x_1 x_2}\,. \tag{3.20}$$

where the scale ξ_0 depends only on the distance, and not on x_i, and is given by

$$\xi_0(\mathbf{y}) = \mu_{0,y}^2\,. \tag{3.21}$$

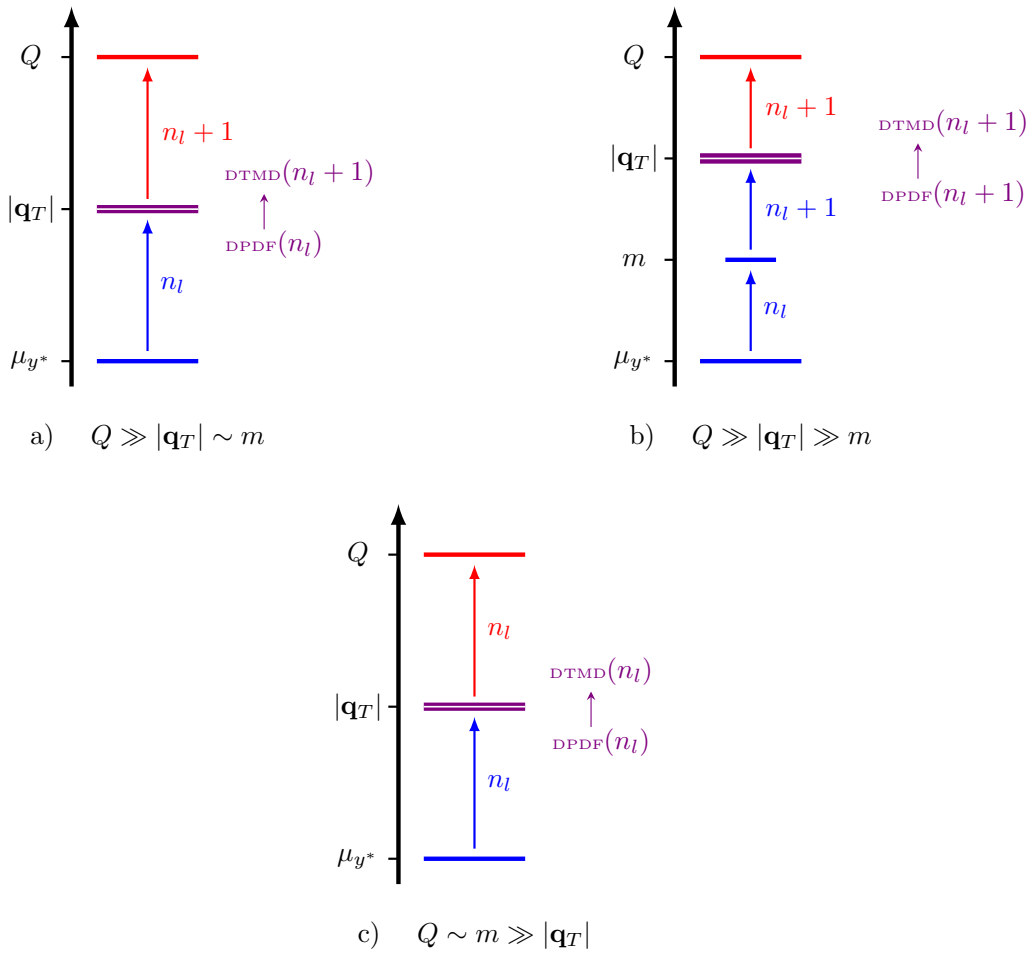

Figure 3.1: Representation of the evolution and matching of parton distributions between the intermediate scales for different hierarchies between Q, m, μ_0. Matching between DPDF and DTMD is represented by a double purple line. The corresponding number of active flavors (both partons) is indicated in parenthesis. Matching to collinear DPD with a higher number of active flavors is denoted by a short blue line. Next to the arrows representing the scale evolution, shown is the number of active parton flavors of a given DPD.

To avoid a potential confusion, we emphasize that in the whole work we use the notation where the rapidity is denoted by the letter ζ, and may depend on longitudinal momenta fractions x_i, while the scale ξ is the x-independent part, as given in Eq. (3.20). The exact form of DPDFs at the initial scales will be presented in Section 3.3.

3.3 Initial conditions for collinear DPDs

We use the DPD model described in [69, 92]. Double-parton distributions are decomposed into the "intrinsic" and "splitting" part, according to

$$ {}^{R_1R_2}F_{a_1a_2}\big(x_i,\mathbf{y};\mu_0,\zeta_0\big) = {}^{R_1R_2}F_{a_1a_2,int}\big(x_i,\mathbf{y};\mu_0,\zeta_0\big) + {}^{R_1R_2}F_{a_1a_2,spl}\big(x_i,\mathbf{y};\mu_0,\zeta_0\big)\,. \tag{3.22}$$

There is also a 'twist-three' part, obtained from a matrix element of a twist-3 operator [22,56,69]. However, the arguments presented at the end of Section 2 in [69] show that this is a subleading term, since the helicity of a single quark-antiquark pair (chiral odd) cannot be compensated by gluon helicity, and therefore such contribution to DPDFs does not obtain the contribution from mixing with gluons, which is the main source of enhancement at small x.

In the next part, we present the construction of both splitting and intrinsic parts.

3.3.1 Intrinsic part

The "intrinsic" part can be thought of as the contribution from the hadron's wave function. It will be approximated as a convolution of two impact parameter-dependent PDFs multiplied by some further factors that will be discussed later:

$$\begin{aligned} &{}^{R_1R_2}F_{a_1a_2,int}\big(x_i,\mathbf{y};\mu_0\big) \\ &\quad = n(a_1a_2)\, r_{a_1a_2}(R_1R_2)\, \rho_{a_1a_2}(x_1,x_2) \int d^2\mathbf{b}\, f_{a_1}(x_1,\mathbf{b};\mu_0) f_{a_2}(x_2,\mathbf{b}+\mathbf{y};\mu_0)\,. \end{aligned} \tag{3.23}$$

The impact-parameter dependence of PDFs is taken as

$$f_a(x_1,\mathbf{b};\mu_0) = \frac{1}{4h_a} f_a(x_1;\mu_0)\, e^{-\frac{\mathbf{b}^2}{4h_a}}\,. \tag{3.24}$$

The convolution simply produces another Gaussian factor:

$$\begin{aligned} &\int d^2\mathbf{b}\, f_{a_1}(x_1,\mathbf{b};\mu_0) f_{a_2}(x_2,\mathbf{b}+\mathbf{y};\mu_0) \\ &\quad = \frac{1}{4\pi(h_{a_1}+h_{a_2})} f_{a_1}(x_1;\mu_0) f_{a_2}(x_2;\mu_0)\, \exp\Big[-\frac{\mathbf{y}^2}{4(h_{a_1}+h_{a_2})}\Big]\,. \end{aligned} \tag{3.25}$$

In the later part we will denote

$$h_{a_1} + h_{a_2} = h_{a_1 a_2} \,. \tag{3.26}$$

The parameters h_a are taken from [69], and are equal to

$$h_a = \begin{cases} 2.33\ \mathrm{GeV}^{-2} & \text{for } a = g \\ 3.493\ \mathrm{GeV}^{-2} & \text{otherwise} \end{cases} \,. \tag{3.27}$$

Flavor number effects
To account for the fact that there are two up-quarks and one down-quark in the proton, we use the number factor $n(a_1 a_2)$ defined as

$$n(a_1 a_2) = \begin{cases} 0 & \text{if } (a_1, a_2) \;=\; (d^-, d^-) \\ \frac{1}{2} & \text{if } (a_1, a_2) \;=\; (u^-, u^-) \\ 1 & \text{otherwise} \end{cases} \,. \tag{3.28}$$

The 'minus' combinations for quark of flavor q are defined as a difference of quark and antiquark distributions:

$$q^- = q - \bar{q} \,. \tag{3.29}$$

To implement the presented number effects, the discussed DPD model is first formulated in the valence-sea basis, and later transformed to the parton basis.

Color non-singlet representations
The color factor $r_{a_1 a_2}(R_1 R_2)$ is taken equal 1 for the singlet representations $(R_1 R_2) = (1, 1)$. In the case of the non-singlet representation, we take such values that saturate the positivity bounds for DPDs [58]. As discussed in Section 2.3.3, we project the color indices on definite SU(3) representations in the t-channel. Projecting onto the s-channel one obtains distributions that mix representations under the evolution, but can be treated as probability densities at the lowest order. Using the matrices describing the transition from the s-channel to t-channel basis, one can find the maximal values of the non-singlet distributions that yield semi-positive distributions in the s-channel (in fact, one positive, and the rest equal to zero). The resulting values of $r_{a_1 a_2}(R_1 R_2)$ are given in App. A.3.

Parton momenta
The condition

$$x_1 + x_2 \leq 1 \tag{3.30}$$

is enforced by multiplying the distributions by a factor

$$\rho_{a_1 a_2}(x_1, x_2) = \begin{cases} \frac{(1-x_1-x_2)^2}{(1-x_1)^2 (1-x_2)^2} & x_1 + x_2 \leq 1 \\ 0 & x_1 + x_2 > 1 \end{cases} \,. \tag{3.31}$$

The factor $(1-x_1)^2(1-x_2)^2$ in the denominator is introduced to fulfill the sum rules for DPDs more accurately in the singlet sector [93].

Parton polarization
When specifying polarization, we shall use labels

- a for unpolarized,
- Δa for longitudinally polarized,
- $\delta^j a$ for transversely polarized in direction j.

Parton 'a' can be either quark, antiquark, or gluon. In this work we consider parton distributions only for combinations of a and Δa, since the transversely polarized partons do not contribute to the production of W boson pairs, see Section 2 in [53]. DPDs with only one parton longitudinally polarized are pseudoscalars – since one cannot construct a pseudoscalar using only a single vector $\mathbf{y}$, it follows that

$$F^{coll.}_{a\Delta b} = F^{coll.}_{\Delta a b} = 0 \qquad \text{for all } a, b\,. \tag{3.32}$$

In the case of DPDFs with both partons longitudinally polarized, a seemingly natural choice would be to construct it using a product of two polarized PDFs. One should however not take such an analogy too far, since the longitudinally polarized PDFs describe the correlation in polarization between parton and hadron, while longitudinally polarized DPDs describe the polarization correlations between two partons, see Section 4.3.1 in [22] and [94]. To account for longitudinal PDFs, instead of taking a polarized PDF fit, we take them equal to their unpolarized counter-parts at the initial scale of the fit, equal to 1 GeV [95], and evolve them to the scale μ_y using DGLAP for polarized PDFs. The identical approach was used in [67]. As will be shown later in Section 3.7, due to the evolution effects even so-constructed longitudinally polarized DTMDs are much smaller than the unpolarized ones.

Finally, the intrinsic part is given by

$$\begin{aligned} {}^{R_1R_2}F_{a_1a_2,int}\big(x_i, \mathbf{y}; \mu_0, \zeta_0\big) \\ &= n(a_1a_2)\, r_{a_1a_2}(R_1R_2)\, \rho_{a_1a_2}(x_1, x_2) \\ &\quad \times f_{a_1}(x_1;\mu_0) f_{a_2}(x_2;\mu_0)\, \frac{1}{4\pi h_{a_1a_2}} \exp\Big[-\frac{\mathbf{y}^2}{4h_{a_1a_2}}\Big]\,. \end{aligned} \tag{3.33}$$

3.3.2 Splitting part

The splitting part stems from a perturbative splitting of a single parton a_0 into a parton pair (a_1, a_2), as shown schematically in Fig. 3.3.2. The integration region where a_1 and

a_2 are nearly collinear with the parent parton a_0 describes double-parton scattering, whereas the region of the large transverse momenta corresponds to loop corrections to single-parton scattering. In this context, by 'large' momenta we understand those comparable with the hard scale Q, not determined by comparison with the fixed scale Λ.

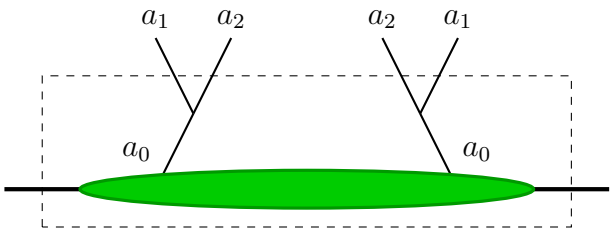

Figure 3.2: Splitting of a_0 into a_1+a_2. If the partons a_1 and a_2 are nearly collinear with a_0, then the considered hard process is described as double-parton scattering, and the perturbative splitting inside the box is treated as the splitting contribution to DPD.

The splitting part of DPDF is given by

$$ {}^{R_1R_2}F_{a_1a_2,spl}\big(x_i,\mathbf{y};\mu_0,\zeta_0\big) = {}^{R_1R_2}F_{a_1a_2,spl,pt}\big(x_i,\mathbf{y};\mu_0,\zeta_0\big)\ \exp\Big[-\frac{\mathbf{y}^2}{4h_{a_1a_2}}\Big]\,, \tag{3.34}$$

where $F_{a_1a_2,spl,pt}$ is the result obtained using the perturbation theory [22]:

$$ \begin{aligned} &{}^{R_1R_2}F_{a_1a_2,spl,pt}\big(x_i,\mathbf{y};\mu_0,\zeta_0\big) \\ &\quad= \frac{1}{\pi y^2}\frac{\alpha_s(\mu_0)}{2\pi}\sum_{a_0} {}^{R_1R_2}P_{a_0\to a_1a_2}\Big(\frac{x_1}{x_1+x_2}\Big)\frac{f_{a_0}(x_1+x_2;\mu_0)}{x_1+x_2}\,. \end{aligned} \tag{3.35}$$

The splitting kernels ${}^{R_1R_2}P_{a_0\to a_1a_2}$ are given in Appendix D. The Gaussian falloff factor is taken the same as in the intrinsic part. Finally, we emphasize that while we use the splitting scale μ_0 dependent on the regularized distance $\mathbf{y}^*$, in the denominator in the splitting formula we have the unregularized $\mathbf{y}^2$ rather than $(\mathbf{y}^*)^2$.

In this work, we use only the LO splitting formula for DPDFs. The reason behind this is that in the analysis of like-sign W pair production the contribution from this part turns out to be much smaller than the intrinsic part, while in the case of the opposite-sign W production, the splitting formula for PDF-DTMD splitting is known only at the leading accuracy, so that a full next-to-leading order analysis is not yet accessible for this channel. The NLO splitting formula in the collinear case, PDF→DPDF has been recently computed [97, 98].

3.4 Matching at perturbatively small z

As described in Section 3.1, to compute parton distributions at arbitrary scales and distances, one first computes their fully perturbative form at regularized, perturbatively small distances, and then extrapolates to larger distances at fixed scales. It is important to emphasize that in order to have a consistent extrapolation form, one needs to specify the rapidity scale at which the extrapolation is performed. We decide to extrapolate the DTMDs at the **y**-dependent initial rapidity of DPDFs defined in Eqs. (3.20)-(3.21).

Let us recall the matching formula for subtracted DTMDs:

$$\begin{aligned}
&{}^{R_1R_2}F_{a_1a_2}\big(x_i,\mathbf{z}_i,\mathbf{y};\mu_{0i},\xi_0/(x_1x_2)\big)\\
&\quad=\sum_{b_1b_2}\sum_{R_1',R_2'}{}^{R_1\bar{R}_1'}C_{a_1b_1}\big(x_1',\mathbf{z}_1;\mu_{01},x_1\xi_0/x_2\big)\underset{x_1}{\otimes}\\
&\qquad\qquad{}^{R_2\bar{R}_2'}C_{a_2b_2}\big(x_2',\mathbf{z}_2;\mu_{02},x_2\xi_0/x_1\big)\underset{x_2}{\otimes}{}^{R_1'R_2'}F^{coll.}_{b_1b_2}\big(x_i',\mathbf{y};\mu_{0i},\xi_0/(x_1x_2)\big)\,.
\end{aligned}\tag{3.36}$$

R_1R_2 denotes the color representation, the matching kernels ${}^{R\bar{R}'}C_{ab}$ are given in App. C. The mass-dependent kernels were obtained based on analogous results for TMD matching kernels [96]. Collinear double parton distributions are denoted as $F^{coll.}$. Notice that, since the matching kernel must depend on the kinematics of a given parton, and not on that of a hadron, the rapidity parameter in the kernel is $x_i\xi_0/x_j=x_i^2\big(\xi_0/x_ix_j\big)$.
As discussed in Section 3.2, the initial value of DPDF for momenta fractions (x_1',x_2') is computed at x'-dependent rapidity scale:

$$\zeta_{0,\mathrm{DPDF}}=\frac{\xi_0(y)}{x_1'x_2'}\,,\tag{3.37}$$

The label 'DPDF' is used to distinguish the rapidity scale at which the collinear parton density is initially modeled from the rapidity scale at which the matching is computed. Such choice is expected to minimize the higher-order logarithmic corrections at fixed scales and momenta fractions. To obtain DPDFs at rapidity $\xi_0/(x_1x_2)$, we use the solution of the Collins-Soper equation in Eq. (2.58), and obtain:

$$\begin{aligned}
&{}^{R_1'R_2'}F^{coll.}_{b_1b_2}\big(x_i',\mathbf{y};\mu_{0i},\xi_0/(x_1x_2)\big)\\
&\quad=\exp\Big(\frac{1}{2}{}^{R_1'}J(\mathbf{y};\mu_{01},\mu_{02})\log\frac{x_1'x_2'}{x_1x_2}\Big){}^{R_1'R_2'}F^{coll.}_{b_1b_2}\big(x_i',\mathbf{y};\mu_{0i},\xi_0/(x_1'x_2')\big)\,.
\end{aligned}\tag{3.38}$$

The value of the kernel ${}^{R}J$ depends only on the dimension of the representation R – since the matching formula does not mix the dimensions of the representation, one can use R_1 instead of R_1' in the formula above.

The matching kernels depend on rapidity multiplied by the momenta fractions $x_i\xi_0/x_j$. To minimize the effects of logarithmic higher order corrections, we first compute the kernel in fixed-order perturbation theory at rapidity equal to μ_{0i}^2, and then evolve them using the Collins-Soper equation for the kernels, which is given in Eq. (3.10). The resummed formula for the kernel reads

$$
\begin{aligned}
&{}^{R_1\bar{R}'_1}C_{a_1b_1}\left(x'_1,\mathbf{z}_1;\mu_{01},x_1\xi_0/x_2\right)\\
&\quad=\exp\left({}^{R_1}K^{pt}_{a_1}(\mathbf{z}_1;\mu_{01})\log\frac{\sqrt{x_1\xi_0/x_2}}{\mu_{01}}\right)\times{}^{R_1\bar{R}'_1}C_{a_1b_1}\left(x'_1,\mathbf{z}_1;\mu_{01},\mu_{01}^2\right),
\end{aligned}
\tag{3.39}
$$

and analogously for the kernel in variable x_2. The label $'pt'$ is used to denote that the **z**-dependent Collins-Soper kernels here are computed in perturbation theory, and there is no model-dependent nonperturbative input involved, cf. the discussion of the modeling of rapidity evolution kernels in Section 2.3.6.

Finally, the perturbative matching formula is given by:

$$
\begin{aligned}
&{}^{R_1R_2}F^{pt}_{a_1a_2}\left(x_i,\mathbf{z}_i,\mathbf{y};\mu_{0i},\xi_0/(x_1x_2)\right)\\
&\quad=\exp\left({}^{R_1}K^{pt}_{a_1}(\mathbf{z}_1;\mu_{01})\log\frac{\sqrt{x_1\xi_0/x_2}}{\mu_{01}}+{}^{R_2}K^{pt}_{a_2}(\mathbf{z}_2;\mu_{02})\log\frac{\sqrt{x_2\xi_0/x_1}}{\mu_{02}}\right)\\
&\qquad\times\sum_{b_1b_2}\sum_{R'_1,R'_2}{}^{R_1\bar{R}'_1}C_{a_1b_1}\left(x'_1,\mathbf{z}_1;\mu_{01},\mu_{01}^2\right)\underset{x_1}{\otimes}{}^{R_2\bar{R}'_2}C_{a_2b_2}\left(x'_2,\mathbf{z}_2;\mu_{02},\mu_{02}^2\right)\underset{x_2}{\otimes}\\
&\qquad\qquad{}^{R'_1R'_2}F^{coll.}_{b_1b_2}\left(x'_i,\mathbf{y};\mu_{0i},\xi_0/(x'_1x'_2)\right)\times\exp\left(\frac{1}{2}{}^{R_1}J(\mathbf{y};\mu_{0i})\log\frac{x'_1x'_2}{x_1x_2}\right).
\end{aligned}
\tag{3.40}
$$

It should be emphasized that while the z-dependent Collins-Soper kernels K are taken in a purely perturbative form here, this is not the case for the kernel $J(\mathbf{y};\mu_{0i})$, since one assumes $|\mathbf{y}|\gtrsim\Lambda^{-1}$, the full large-distance form of the kernel J is used from the beginning.

3.5 Extrapolation to large z

In analogy to TMD studies [68, 83–88] one models DTMDs at arbitrary $\mathbf{z}_i$ by first computing their perturbatively expanded form at regularized distances $\mathbf{z}_i^*$, and then

extrapolating at fixed rapidity scale $\zeta_0 = \xi_0(\mathbf{y})/(x_1 x_2)$:

$$ {}^{R_1R_2}F\big(x_i, \mathbf{z}_i, \mathbf{y}; \mu_i, \zeta_0\big) \;=\; {}^{R_1R_2}F^{pt}\big(x_i, \mathbf{z}_i^*, \mathbf{y}; \mu_i; \zeta_0\big)\; F_{\rm NP}\big(x_i, \mathbf{z}_i, \mathbf{y}\big)\,. \tag{3.41} $$

Recall that the superscript $'pt'$ denotes the perturbatively computed quantity.
$F_{\rm NP}\big(x_i, \mathbf{z}_i, \mathbf{y}\big)$ is a non-perturbative prefactor, which in general may depend on all transverse distances, momenta fractions, and parton species. Since the collinear DPDF used in the matching formula is assumed to be given for all distances, the argument $\mathbf{y}$ in Eq. (3.41) is not regularized. However, one can still allow for $\mathbf{y}$-dependence in the factor $F_{\rm NP}$.
In the next step, DPDs are evolved to arbitrary scales using the Collins-Soper kernels at large distances. We obtain:

$$ \begin{aligned} &{}^{R_1R_2}F_{a_1a_2}\big(x_i, \mathbf{z}_i, \mathbf{y}; \mu_i, \zeta\big) \\ &\quad= \exp\left(\frac{1}{2}\Big({}^{R_1}K_{a_1}(\mathbf{z}_1;\mu_1) + {}^{R_2}K_{a_2}(\mathbf{z}_2;\mu_2) + {}^{R_1}J(\mathbf{y};\mu_i)\Big)\log\frac{\zeta}{\zeta_0}\right) \\ &\qquad\times {}^{R_1R_2}F^{pt}_{a_1a_2}\big(x_i, \mathbf{z}_i^*, \mathbf{y}; \mu_i; \zeta_0\big)\; F_{\rm NP}\big(x_i, \mathbf{z}_i, \mathbf{y}\big)\,. \end{aligned} \tag{3.42} $$

Let us see, what would happen if one decided to extrapolate DTMDs using Eq. (3.41), at a different initial rapidity scale ζ_0'. Recall from Section 2.3.6 that the Collins-Soper kernels ${}^{R}K_a$ are decomposed as

$$ {}^{R}K_a(\mathbf{z};\mu) \;=\; {}^{R}K_a^{pt}(\mathbf{z}^*;\mu) \;+\; {}^{R}g_{K,a}(\mathbf{z})\,, \tag{3.43} $$

where ${}^{R}g_a$ is the non-perturbative part. As noted previously, perturbatively matched DTMDs in Eq. (3.4) are computed with ${}^{R}g_{K,a} = 0$. Demanding that DTMDs obtained using a new pair of the initial rapidity scale ζ_0' and a nonperturbative factor $F'_{\rm NP}$ applied to Eqs. (3.41)-(3.42) have the same value as the ones for the unprimed version, one finds

$$ F'_{\rm NP}(\mathbf{z}_i, \mathbf{y}) = F_{\rm NP}(\mathbf{z}_i, \mathbf{y})\; \exp\left(\frac{1}{2}\Big({}^{R_1}g_{K,a_1}(\mathbf{z}_1) + {}^{R_2}g_{K,a_2}(\mathbf{z}_2)\Big)\log\frac{\zeta_0}{\zeta_0'}\right). \tag{3.44} $$

It implies that one must carefully specify the rapidity scale at which the extrapolation to large distances is applied, in order to avoid mixing between the factor $F_{\rm NP}$ and extrapolation of the rapidity evolution kernels.

Therefore, the interpolation of double-parton distributions in our approach consists of the following steps:

1. Compute the perturbatively matched DTMD at regularized distances $\mathbf{z}_i^*$ given in Eq. (3.15). The initial scales (μ_{0i}, ζ_0) are given in Section 3.2.

2. Extrapolate to large $\mathbf{z}_i$ at the initial scales from the previous point according to

$$
\begin{aligned}
&{}^{R_1R_2}F_{a_1a_2}\big(x_i,\mathbf{z}_i,\mathbf{y};\mu_{0i},\xi_0/(x_1x_2)\big)\\
&\quad= {}^{R_1R_2}F^{pt}_{a_1a_2}\big(x_i,\mathbf{z}_i^*,\mathbf{y};\mu_{0i},\xi_0/(x_1x_2)\big)F_{\rm NP}\big(x_i,\mathbf{z}_i,\mathbf{y}\big)\,.
\end{aligned}
\tag{3.45}
$$

   The choice of $F_{\rm NP}$ will be discussed in the later part of this work.

3. Finally, evolve DTMDs to the final scales using the full Collins-Soper kernels. We emphasize that the parton distributions at regularized distance in Eq. (3.45) are computed using purely perturbative kernels K, and the full kernels that involve the non-perturbative part are used only to evolve them from the initial rapidity $\xi_0/(x_1x_2)$ to the final one.

Finally, after using the solutions of RGE and Collins-Soper equations discussed in Section 2.3.4, we obtain DTMDs in the large-$\mathbf{y}$ approximation at arbitrary scales:

$$
\begin{aligned}
&{}^{R_1R_2}F_{a_1a_2}\big(x_i,\mathbf{z}_i,\mathbf{y};\mu_i,\zeta\big)\\
&\quad= \exp\left(\int_{\mu_{01}}^{\mu_1}\frac{d\mu}{\mu}\Big(\gamma_{a_1}(\mu)-\gamma_{K,a_1}\log\frac{x_1\sqrt{\zeta}}{\mu}\Big)\;+\;\big(1\to 2\big)\right)\\
&\qquad\times\exp\left(\frac{1}{2}\Big({}^{R_1}J(\mathbf{y};\mu_{0i})+{}^{R_1}K(\mathbf{z}_1;\mu_{01})+{}^{R_2}K(\mathbf{z}_2;\mu_{02})\Big)\log\frac{\sqrt{x_1x_2\zeta}}{\xi_0}\right)\\
&\qquad\times F_{NP}\big(x_i,\mathbf{z}_i,\mathbf{y}\big)\,{}^{R_1R_2}F^{pt}_{a_1a_2}\big(x_i,\mathbf{z}_i^*,\mathbf{y};\mu_{0i},\xi_0/(x_1x_2)\big)\,,
\end{aligned}
\tag{3.46}
$$

.

with F^{pt} given in Eq. (3.4). The anomalous dimensions $\gamma_a,\gamma_{K,a}$ are given in App. B. Notice that for the typical scales in the problem $\sqrt{x_1x_2\zeta}\sim Q$, so that the logarithm in the exponential in the third line of Eq. (3.5) is positive and large for small value of ξ_0, associated with large distance $\mathbf{y}$. That, and the fact that the kernel ${}^RJ$ in the octet sector is positive, leads to strong suppression of the color-nonsinglet DPDs. Notice that this holds for both DTMDs and DPDFs, since the kernel ${}^RJ$ appears in the evolution equations for both DPDF and DTMD in large-$\mathbf{y}$ approximation.

3.6 Perturbative orders

Let us discuss the perturbative orders of the components used in the presented work. The choice is consistent with the DPDF study performed in [67], which in turn uses the conventions in line with [99, 100].

We start the discussion with the terms relevant to the resummation of large logarithms. The Collins-Soper kernels ${}^{R}K_a, {}^{R}J$, and non-cusp anomalous dimension γ_a $(a = q, g)$ appear in resummation of single logarithms, while the cusp anomalous dimensions γ_K, γ_J resum double logarithms. According to the conventions discussed in [99, 100], the perturbative order of the kernels and γ_a should be therefore taken one smaller than the one of γ_K, γ_J. Therefore, at $\mathrm{N^kLL}$ order corresponds to cusp anomalous dimensions computed at $\mathrm{N^kLO}$, and the kernels at one order lower. At LL the kernels and non-cusp anomalous dimensions γ_a are taken equal to 0, cf. Section 4.3 in [67].

In the next step, we consider the fixed-order expressions for the matching kernels $\hat{C}$, and the hard cross sections $\hat{\sigma}$, as well as the DGLAP kernels denoted as $\hat{P}$ – all of these components are taken at the same order: for a fixed-log accuracy $\mathrm{N^kLL}$ for $k \geq 1$ we take it at $\mathrm{N^{k-1}LO}$, and at LL we take it at LO. Primed accuracy $\mathrm{N^kLL'}$ implies that $\hat{P}, \hat{C}, \hat{\sigma}$ are taken at one order higher than in unprimed case, that is at $\mathrm{N^kLO}$. The perturbative order of the QCD β function expanded in powers of α_S should match the orders of the DGLAP kernels. For this reason, when referring to this set of quantities, we will refer to the 'order of DGLAP kernels'.

The perturbative expansion of the QCD beta function $\beta(\alpha_S)$ appears in the integrals involving cusp anomalous dimensions [101]

$$\begin{aligned}
\int \frac{d\mu}{\mu}\, \gamma_{K/J}(\mu) &= \int_{\alpha_S(\mu_0)}^{\alpha_S(\mu_1)} \frac{d\alpha}{\beta(\alpha)} \gamma_{K/J}\,, \\
\int \frac{d\mu}{\mu}\, \gamma_{K/J}(\mu)\, \log\frac{\mu}{\mu_0} &= \int_{\alpha_S(\mu_0)}^{\alpha_S(\mu_1)} \frac{d\alpha}{\beta(\alpha)} \gamma_{K/J} \int_{\alpha_S(\mu_0)}^{\alpha_S(\mu)} \frac{d\alpha'}{\beta(\alpha')}\,.
\end{aligned} \tag{3.47}$$

For consistency, the function $\beta(\alpha)$ in (3.47) should be expanded at the same order as $\gamma_{K/J}$. On the other hand, it was previously stated that the β-function of α_S used in the expansion of the fixed-order part should match the order of the DGLAP kernels. This leads to a discrepancy between the two consistency requirements for the order of the QCD β-function used in the computation. We make a compromise by taking it at different orders when applying it to different objects – in the perturbative expressions for the kernels and hard cross-sections, we shall refer to the order of α_S. On the other hand, when specifying the order of expansion of $\beta(\alpha)$ in Eq. (3.47), we will talk about the order of β, see Table 3.1. The same conventions have been applied in the previous work [67].

The perturbative order of the PDF fits used to model double parton distributions is chosen to be consistent with the DGLAP kernels order. We use the parametrizations of the MSHT [95] – at NLO we use the results for $\alpha_S(M_Z) = 0.118$. At LO we use the fits for $\alpha_S(M_Z) = 0.130$.

Finally, let us comment on the handling of the α_S expansion at the level of the computation of differential cross section. Since both the parton distributions F at the matching scale, and the hard scattering cross-sections $\hat{\sigma}$ are expanded in the strong coupling:

$$\hat{\sigma} = \sum_{n=0} \alpha_S^n \, \hat{\sigma}^{(n)} \,, \tag{3.48}$$

$$F = \sum_{n=0} \alpha_S^n \, F^{(n)} \,, \tag{3.49}$$

the product $F\bar{F}\hat{\sigma}_1\hat{\sigma}_2$ is expanded as

$$F\bar{F}\hat{\sigma}_1\hat{\sigma}_2 \;=\; \sum_{i,j,n,m} \alpha_S^{i+j+n+m} \, \hat{\sigma}_1^{(i)}\hat{\sigma}_2^{(j)} F^{(n)}\bar{F}^{(m)} \,, \tag{3.50}$$

where the superscript (n) denotes the n-th term in the perturbative expansion in α_S of a parton distribution or the hard factor. It should be noted that α_S in the matching expansion, and in the hard part are taken at different scales μ_{0i}, Q_j, but nonetheless are treated the same. To keep the fixed order in the α_S-expansion, we shall truncate this sum for powers $i+j+n+m$ larger than the considered perturbative order. Notice that already at NLO the expansion of DTMD in Eq. (3.49) contains α_S^2 terms from the product of two matching kernels computed at α_S – in the described scheme these terms are dropped at α_S order.

Accuracy	J,K	γ_a	$\hat{P}, \hat{C}, \hat{\sigma}, \alpha_S$	$\gamma_{J/K}, \beta$	PDF set
LL	—	—	LO	LO	LO
NLL	LO	LO	LO	NLO	LO
NLL'	LO	LO	NLO	NLO	NLO
NNLL	NLO	NLO	NLO	NNLO	NLO

Table 3.1: Perturbative orders at different accuracies.

3.7 Position-dependent DTMDs and the error estimation

The main goal of this Section is to study the most significant features of transverse position-dependent double-parton distributions obtained via perturbative matching to the collinear DPDFs in the kinematics relevant in the process of production of W pairs at

$$\sqrt{s} = 13 \text{ TeV}.$$

The hard scales are chosen as

$$\mu_i = M_W = 80.377 \text{ GeV}, \qquad \sqrt{\zeta\bar{\zeta}} = s \,. \tag{3.51}$$

We consider two values of the momenta fractions:

$$(x_1,\, x_2) \;=\; (x_0,\, x_0),\;\text{ and }\; (x_0 e^{Y},\, x_0 e^{-Y})\,, \quad Y = 3\,, \tag{3.52}$$

where x_0 corresponding to production of W at central rapidity is given by

$$x_0 = \frac{M_W}{\sqrt{s}} \approx 6.18 \times 10^{-3}\,, \tag{3.53}$$

so that

$$(x_0 e^{Y},\, x_0 e^{-Y}) \;\approx\; (0.124,\, 3.1 \times 10^{-4})\,. \tag{3.54}$$

The following analysis of DTMDs in the large-$\mathbf{y}$ region allows to address some important questions before the next part:

- In the case of intrinsic DPDFs, singlet distributions for longitudinally polarized partons are constructed by first saturating the positivity bounds of PDFs by taking the polarized distributions equal to their unpolarized counterparts at 1 GeV, and then evolving them with the single parton DGLAP to the initial scale of DPDFs μ_{y^*}. The color-nonsinglet sector of the intrinsic part is derived from the color-singlet double parton distributions by saturating the positivity bounds of DPDFs at the initial scale of μ_{y^*}. Do these distributions become enhanced by the effects of evolution and matching, so that in the relevant region of the phase space they dominate over the unpolarized color-singlet distributions, introducing a significant model dependence?

- It is expected that the relevant regions should be given by

  $$|\mathbf{z}_i| \;\sim\; |\mathbf{q}_i|^{-1} \;\sim\; \mathcal{O}(10)\,\text{GeV}, \qquad |\mathbf{y}| \gg |\mathbf{z}_i|\,. \tag{3.55}$$

  These assumptions would be challenged if in the described region DTMDs were strongly suppressed.

- For small $\mathbf{z}_i$ the relevant matching scales should be relatively large, which allows us to expect a rather quick convergence of the perturbative matching, given in powers of $\alpha_S(\mu_{0i})$. This needs, however, to be explicitly checked.

Since the result depends on the intermediate matching scales μ_{0i} by terms of order α_S^n higher than the currently known perturbative accuracy, we estimate the uncertainties due to the perturbative matching by varying the matching scales according to

$$\mu_0(\mathbf{z};\kappa) = \frac{\kappa b_0}{|\mathbf{z}^*|} + \big(1-\kappa\big)\,\mu_{\min}\,, \tag{3.56}$$

where $\mu_{\min} = 2$ GeV, and

$$\kappa \in \big\{0.5, 0.75,\, 1,\, 1.5,\, 2\big\}\,. \tag{3.57}$$

The variation of the scales is constructed in such a way that at small distances, corresponding to large values of μ_0, a fixed parameter implies a scale approximately scaled by κ. On the other hand, at large distances, all of the κ-dependent matching scales saturate at $\mu_{\min} = 2$ GeV. Instead of taking only 3 extreme values of κ, we also consider the intermediate ones: $0.75, 1.5$, since we observe that in some cases the value of the DTMD at the central scale is very close to one of the upper/lower estimates, effectively leading to an underestimation of the errors.

We will present uncertainty estimates obtained this way at 3 different accuracies, and verify that including the higher-order corrections indeed reduces the error bands obtained by this procedure. A comparison of the width of the error bands with the actual difference between different accuracies also provides guidance, on how accurate such an estimation is.

In Figs. 3.3-3.8 we present DTMDs as functions of $z_2 = |\mathbf{z}_2|$ for the following values of transverse distances:

$$|\mathbf{z}_2| \in [10^{-2}\,\text{GeV}^{-1},\, 0.5\,\text{GeV}^{-1}]\,, \qquad |\mathbf{z}_1| = 0.1\,\text{GeV}^{-1}\,, \qquad |\mathbf{y}| = 1\,\text{GeV}^{-1}\,. \tag{3.58}$$

Parton distributions were computed on a discrete grid in z_2 with 16 points and interpolated. For better interpolation precision, instead of taking a linear grid in z_2, we used the variable transformation

$$u \;=\; \log z_2\,. \tag{3.59}$$

The grids in x_i for color-singlet and color-nonsinglet representations are the same as in Eq. (C.2) in [67], that is:

$$\begin{aligned} &\big[10^{-5},\, 5\times10^{-3},\, 0.5,\, 1\big]_{(16,16,24)} && \text{for color singlet,}\\ &\big[10^{-5},\, 3\times10^{-4},\, 10^{-2},\, 0.5,\, 1\big]_{(16,16,24,24)} && \text{for color-nonsinglet.} \end{aligned}$$

The results are presented for small $\mathbf{z}$, so that the uncertainty due to the parametrization of the non-perturbative part of the Collins-Soper kernel is not analyzed at this stage. It should be noted that the non-perturbative part of the Collins-Soper kernel is not taken equal to zero in this analysis, since it significantly affects the $\mathbf{y}$-dependence of color non-singlet DTMDs. Therefore, here we will use our default choice of the kernel, which is defined in Eq. (5.53). Further discussion of the considered models for the Collins-Soper kernel will be given in Section 5.2.2.

Double parton distributions in the large-$\mathbf{y}$ approximation and their corresponding error bands are presented at 3 accuracies: NLL (green), NLL' (orange), and NNLL (blue). Since in the color-singlet sector the NLL' and NNLL results in all cases were found to be close to each other, and the error estimation for NLL' is typically of the same size, we show the results at the intermediate accuracy only in Fig. 3.3, and omit them in the remaining plots for the color-singlet sector in Figs. 3.4-3.6.

One can readily observe that the uncertainty estimation becomes smaller at higher accuracies. Interestingly, in many cases, the error estimates at NLL are several

times smaller than the actual difference between the two subsequent accuracies. To understand it, we recall that it was found that the result obtained using the extreme choices of μ_0 often are very close in value, see the discussion before Eq. (3.57). Therefore, we suspect that in some cases the DTMDs as a function of the parameter κ have a local minimum for $\kappa \in [0.5,\ 2]$ – despite the variation of the result being formally of one order in α_S higher than the perturbative expansion, we have no guarantee that the factor multiplying the higher power of α_S is not small. Whether this is a numerical coincidence at NLL, or the problem persists at higher accuracies would require the computation of higher-order corrections. The difference between NLL and NLL' is much more visible, than between NLL' and NNLL, which should not be surprising, given the change of the order of DGLAP, matching orders, and PDF fits between the first two accuracies.

Results presented here show that the longitudinally polarized DTMDs at the considered scales are several times smaller than their unpolarized counterparts, except the splitting form of DPDFs of quark and antiquark of identical flavor, see Fig. 3.5, where the distributions are of a similar size, but have opposite signs – this can be explained by the relative change of sign in the massless splitting formula of gluon into a quark-antiquark pair for unpolarized versus longitudinally polarized quarks, see Eq. (3.35), and the splitting kernels in Eq. (D.2). Since, as pointed out in the previous part, the considered model for intrinsic double parton distributions for longitudinally polarized partons is such that it saturates the positivity bounds at a scale equal to 1 GeV, one may expect the contributions from the polarized DTMDs to be even smaller in reality.

We observe no significant difference between the error bands and shapes of DTMDs at symmetric and asymmetric values of x_i, other than a shift of the maximum towards larger values of z_i in the latter case. On the other hand, the absolute values of DTMDs of non-valence partons strongly diminish if the corresponding x_i becomes large, which is to be expected from the behavior of single-parton distributions. Analogously, when $x_1 + x_2$ becomes large, also the splitting part of non-valence quarks gets smaller, due to the diminishing value of the parent single gluon density.

It is seen that singlet quark DTMDs diminish at larger z, while the nonsinglet distributions in some cases either vanish very slowly or even become enhanced, as in the case of the $(\Delta u, \Delta u)$ splitting part given in lower-right panel of Fig. 3.8. In general, we see that this effect is strong for longitudinally polarized quarks in both intrinsic and splitting parts and for unpolarized, charge-conjugate $q\bar{q}$ pairs in the splitting part. To understand it, let us first explain, why in most cases the matched DTMDs diminish with larger z_i. The matching consists of two evolution steps – DGLAP evolution from μ_y to the matching scales μ_{0i}, and then multiplicative DTMD evolution to the final scales. Typically, DGLAP evolution enhances DPDs more strongly than the evolution of DTMDs, so that a lower intermediate scale μ_{0i} corresponding to larger z_i results in a smaller value of DTMD. However, as found in [67], color-nonsinglet and longitudinally

polarized DPDFs evolve more slowly with DGLAP, resulting in the observed behavior. We also point out that based on Fig. G.1 in App. G, we see that the qualitative behavior of DTMDs may also change between the intrinsic and splitting form, meaning that also the initial conditions of the DGLAP evolution matter. We do not expect this effect to have a strong impact on the phenomenological results, since DTMDs exhibiting the described behavior tend to be small compared to the ones that diminish at large (but still perturbative) $\mathbf{z}$, and for this reason we did not pursue a further analysis of this behavior.

We observe that the color-nonsinglet distributions are strongly suppressed at larger $\mathbf{y}$ due to the Collins-Soper kernel J at large distances, which is consistent with results presented in [67]. The $\mathbf{y}$-dependence of DPDs is studied in more detail in the next part.

We verified that the discussed properties of DTMDs hold also at $|\mathbf{y}| = 0.5\,\mathrm{GeV}^{-1}$, where the rapidity evolution suppression of color-nonsinglet distributions is not yet that strong. This was checked on the same range in $|\mathbf{z}_2|$ as in Eq. (3.58), including $|\mathbf{z}_2|$ points which approach the value of $|\mathbf{y}|$ – this is beyond the region where the discussed approximation is valid, however, it still may be used when extrapolating to large $\mathbf{z}_i$.

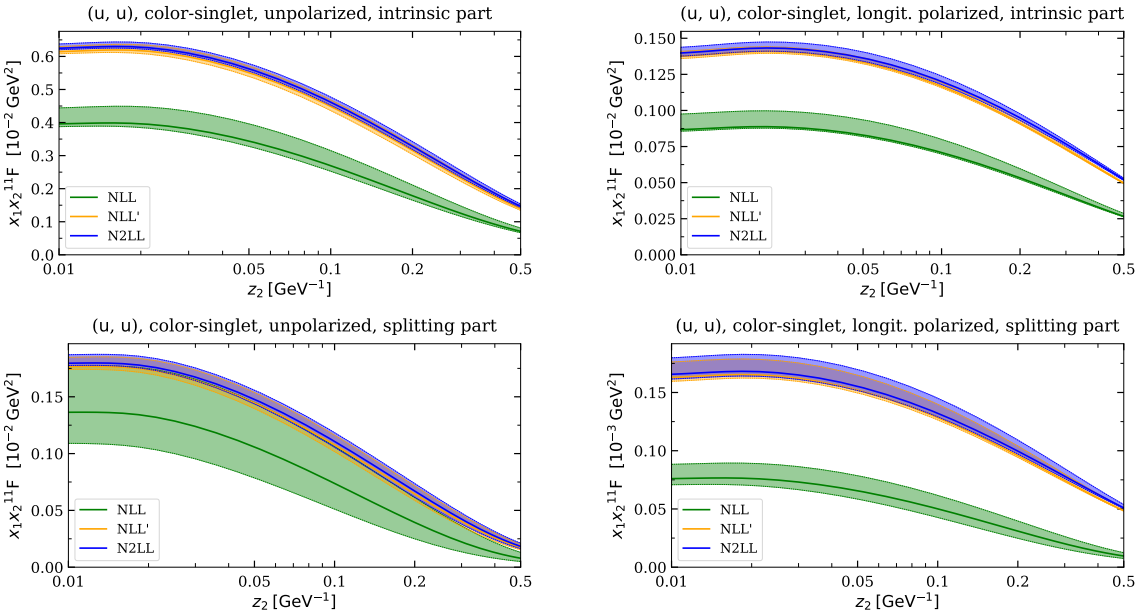

Figure 3.3: z_2-dependent color-singlet DTMDs for unpolarized (left) and longitudinally polarized (right) quarks (u, u) at fixed $y = 1\,\text{GeV}^{-1}$ and $z_1 = 0.1\,\text{GeV}^{-1}$ for intrinsic (upper) and splitting (lower) DPDF part at $(x_1, x_2) \approx (6.18 \times 10^{-3},\ 6.18 \times 10^{-3})$.

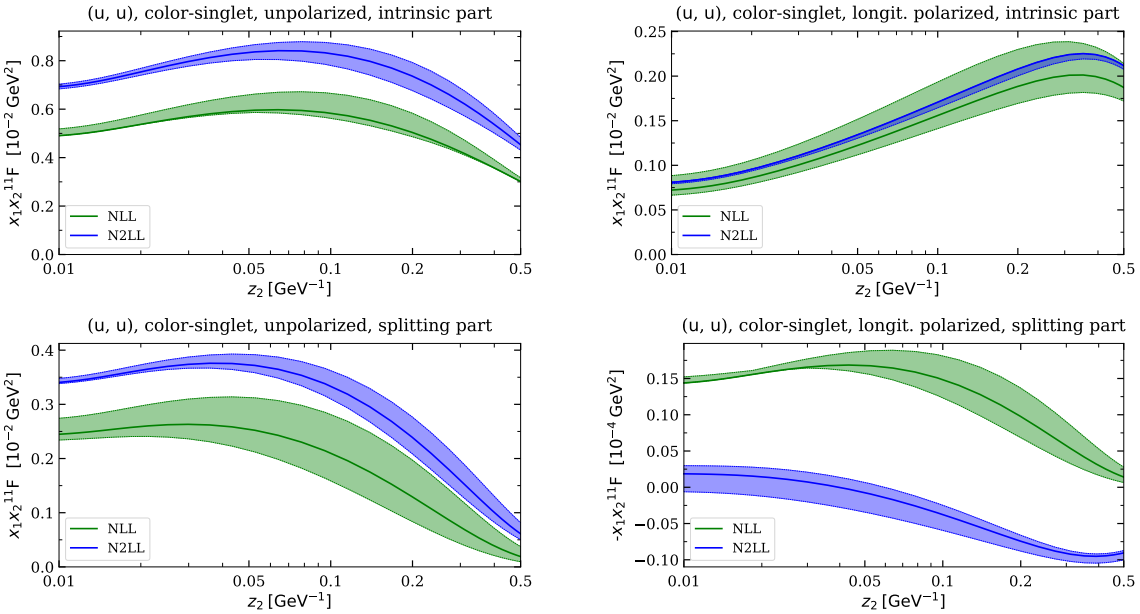

Figure 3.4: The same as in Fig. 3.3, but for $(x_1, x_2) \approx (0.124,\ 3.1 \times 10^{-4})$.

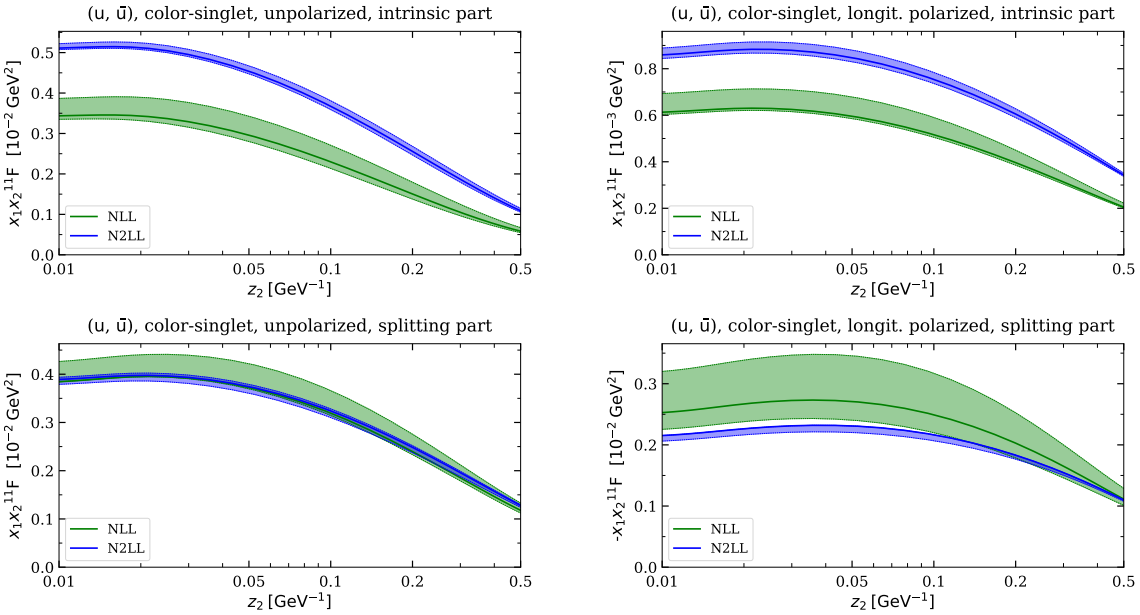

Figure 3.5: z_2-dependent color-singlet DTMDs for unpolarized (left) and longitudinally polarized (right) quarks $(u, \bar{u})$ at fixed $y = 1\,\text{GeV}^{-1}$ and $z_1 = 0.1\,\text{GeV}^{-1}$ for intrinsic (upper) and splitting (lower) DPDF part at $(x_1, x_2) \approx (6.18 \times 10^{-3},\ 6.18 \times 10^{-3})$.

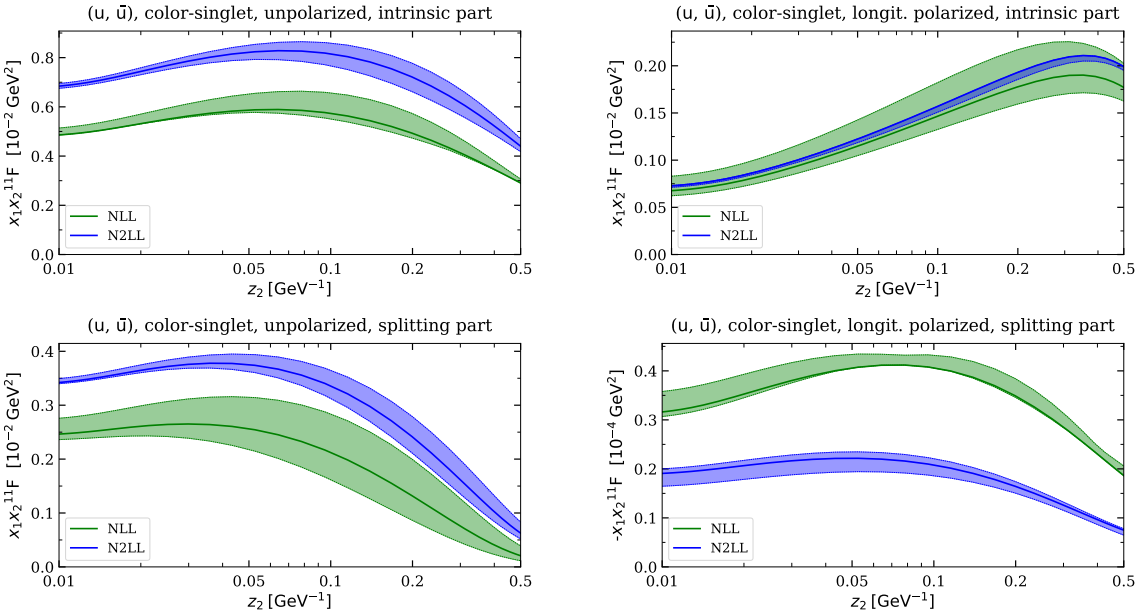

Figure 3.6: The same as in Fig. 3.5, but for $(x_1, x_2) \approx (0.124,\ 3.1 \times 10^{-4})$.

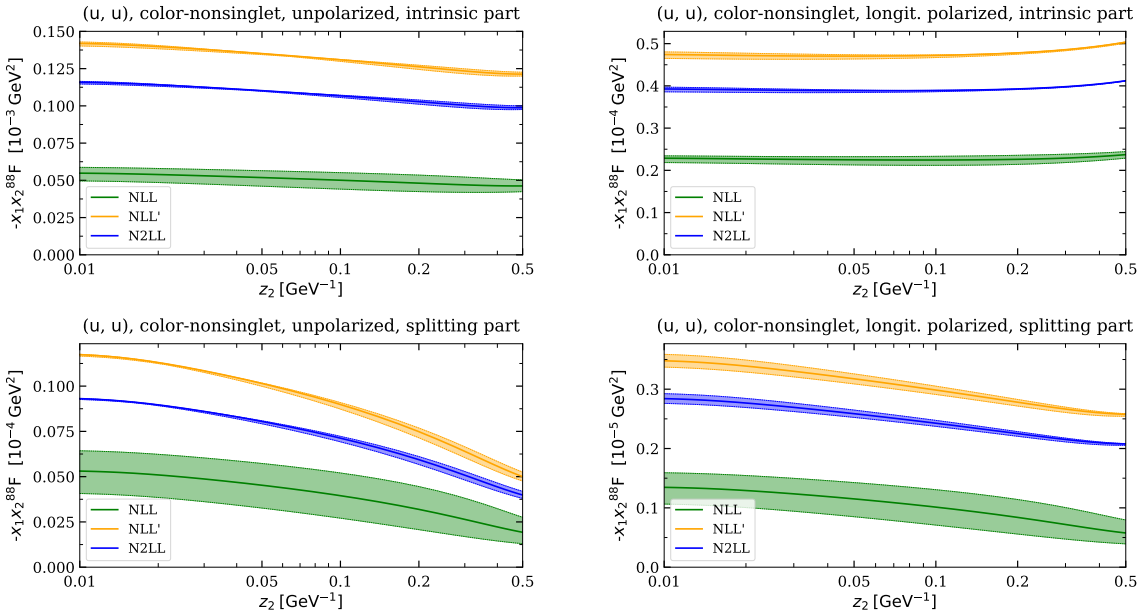

Figure 3.7: z_2-dependent color-nonsinglet DTMDs for unpolarized (left) and longitudinally polarized (right) quarks (u, u) at fixed $y = 1\,\mathrm{GeV}^{-1}$ and $z_1 = 0.1\,\mathrm{GeV}^{-1}$ for intrinsic (upper) and splitting (lower) DPDF part at $(x_1, x_2) \approx (6.18 \times 10^{-3}, 6.18 \times 10^{-3})$.

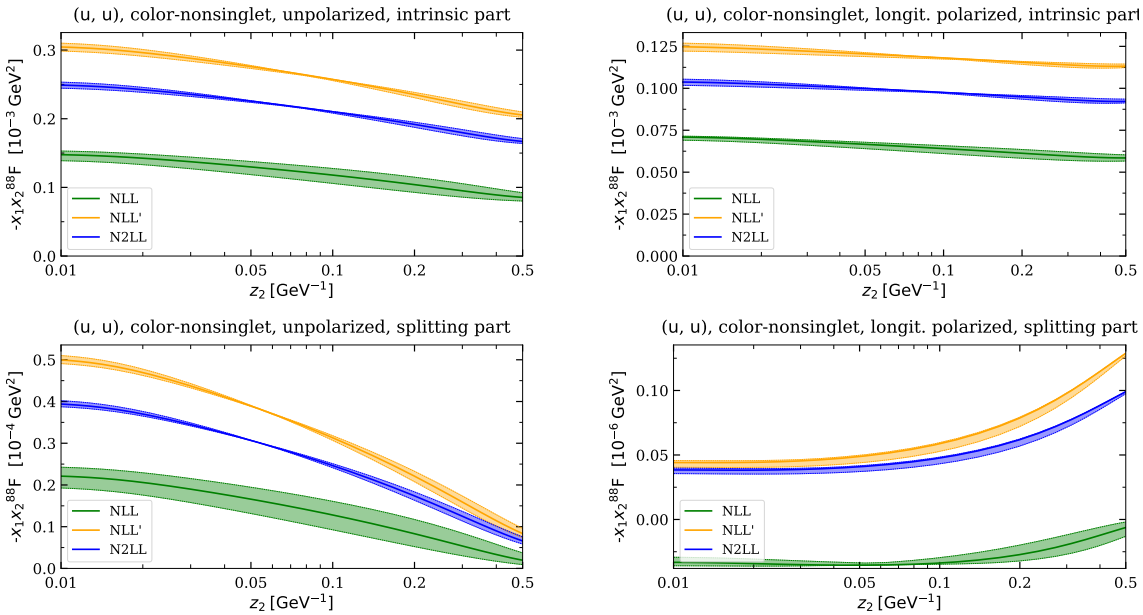

Figure 3.8: The same as in Fig. 3.7, but for $(x_1, x_2) \approx (0.124,\ 3.1 \times 10^{-4})$.

For completeness, let us present the comparison between $\mathbf{y}$-dependence of singlet and non-singlet parton distributions in Figs. 3.9 and 3.10 for

$$|\mathbf{z}_1| = |\mathbf{z}_2| = 0.1\,\mathrm{GeV}^{-1}\,, \tag{3.60}$$

for the same kinematics as in the previous part, at equal values of x_1, x_2, and for unpolarized distributions. The qualitative behavior of DPDs is analogous for asymmetric momenta fractions and longitudinal polarizations. For clarity of presentation, these are plotted on a logarithmic scale in $y = |\mathbf{y}|$, and multiplied by the measure factor[1] y. It is clearly seen that the singlet intrinsic part contributes mostly for non-perturbatively large $\mathbf{y}$. In the case of the splitting color-singlet contribution one observes that in the case parton pairs which are not generated by the leading-order PDF-DPDF splitting, but rather by the further DGLAP evolution, the regions of large- and small-$\mathbf{y}$ give comparable contributions. In the case of $q\bar{q}$ pairs produced directly by gluon splitting, the short-$\mathbf{y}$ region is the dominant one due to the $1/\mathbf{y}^2$ splitting factor. The color non-singlet parton distributions are mostly contained in the region of $|\mathbf{y}| < b_{\max}$ due to strong effects of rapidity evolution, as discussed at the end of Section 3.5.

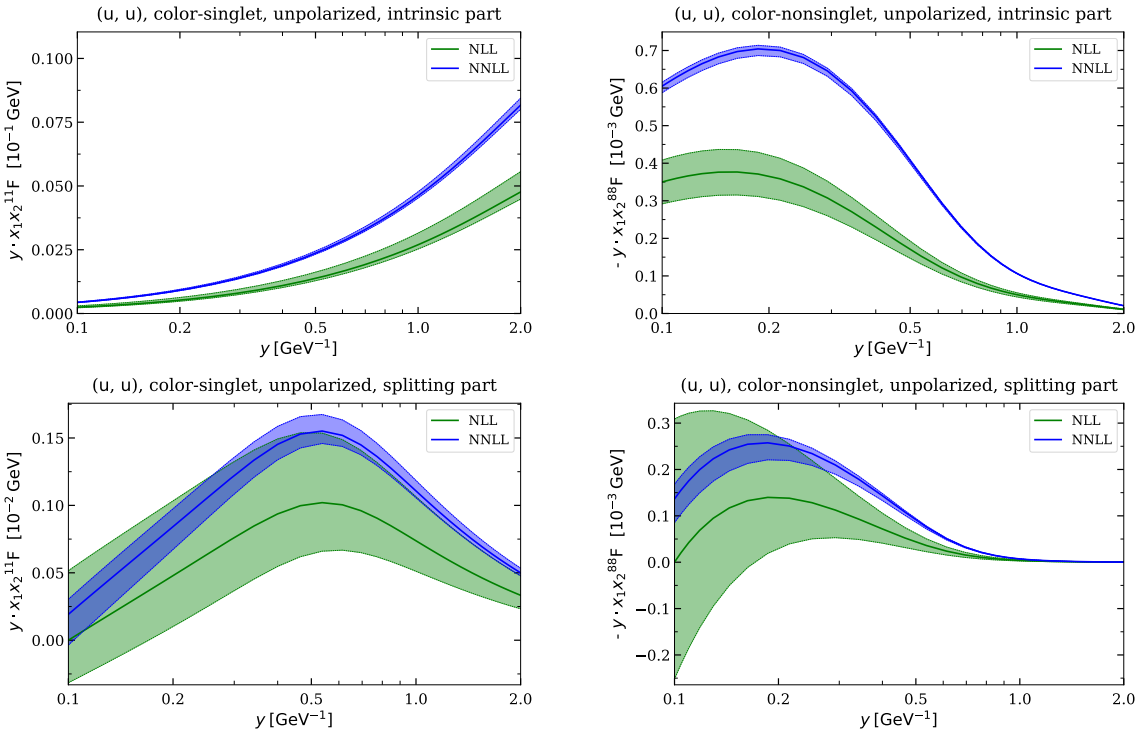

Figure 3.9: DTMD multiplied by y for parton pair (u, u) at fixed (z_1, z_2).

[1]Since $\int y\,dy\,F\bar{F} = \int d(\log y)(yF)(y\bar{F})$, we find such scaling on the logarithmic grid to give the best visual assessment of the relative size of the contribution to the cross-section from different regions in y.

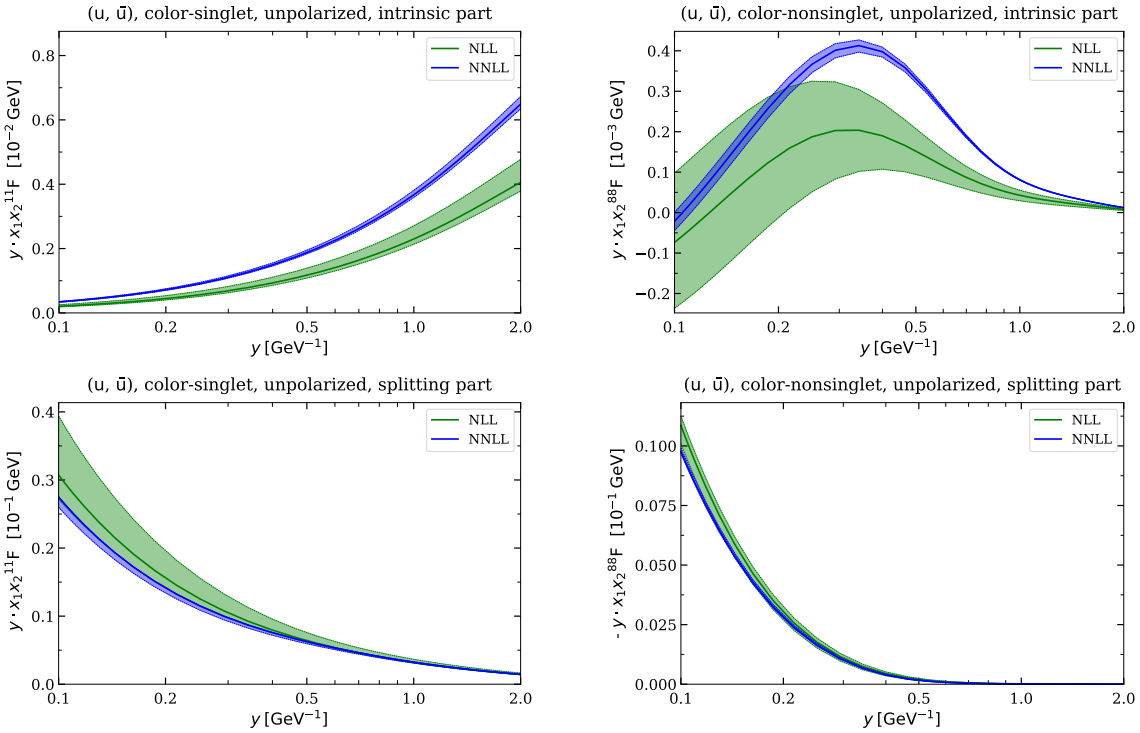

Figure 3.10: The same as in Figure 3.9, but for quarks $(u, \bar{u})$.

Chapter 4

DTMDs at small transverse distances

In this part, we discuss the description of double parton distributions in the region where all transverse distances are perturbatively small $|\mathbf{y}|, |\mathbf{z}_1|, |\mathbf{z}_2| \ll \Lambda^{-1}$. In Section 4.1 we present the decomposition of DTMDs at short distances as introduced in [69]. In Section 4.1.1 we describe the coordinate system used in the computation. We discuss the choice of the matching scales in Section 4.1.2, and in Section 4.2 we discuss the short-distance expansion of the Collins-Soper kernel. Numerical results together with the discussion of the scale choice and comparison with parton distributions obtained in the previous chapter are presented in Section 4.3. Finally, in Section 4.3.1 we address the problem of extrapolating DTMDs to large and small ($\lesssim Q^{-1}$) transverse distances, which will become crucial in the computation of cross-sections.

4.1 Short-distance expansion

According to [69], Section 3.3, transverse momentum-dependent DPDs in position space at small transverse distances can be expanded in 3 terms:

$$ {}^{R_1R_2}F = {}^{R_1R_2}F_{spl.} + {}^{R_1R_2}F_{tw.3} + {}^{R_1R_2}F_{intr.} \,, \tag{4.1} $$

constructed using matrix elements of twist-two, twist-three and twist-four operators respectively, just as in the case of the collinear distributions discussed in Section 3.3.

The first term described the perturbative splitting of a single parton a_0 into a pair a_1, a_2 – the leading-order graph for two quark distributions is presented in Fig. 4.1. The LO formulas for the splitting kernels can be found in Section 7.4 of [56]. For a detailed derivation see Section 5.2 in [22]. The new result of this work is a computation of the mass-dependent splitting formula for gluon to quarks splitting for the configurations of polarizations relevant to this work. Here we present the results for both massless- and

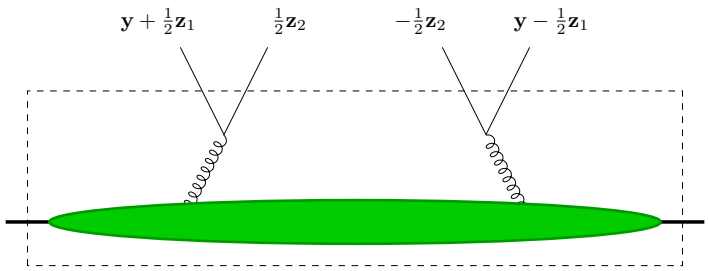

Figure 4.1: Leading-order contribution to the splitting part of DTMD. Shown are the transverse positions of the considered partons. The rectangular box indicates that the splitting is collinear and thus the presented graph contributes to double parton distribution.

mass-dependent cases. The mass-dependent splitting formula is derived by including the masses in quark propagators in the derivation presented in Section 5.2.2 in [22].

The splitting contribution for massless quarks reads:

$$ {}^{R_1R_2}F_{a_1a_2,\mathrm{spl}} = \frac{\mathbf{y}_+^l \mathbf{y}_-^{l'}}{\mathbf{y}_+^2 \mathbf{y}_-^2} \frac{\alpha_S(\mu)}{2\pi^2} {}^{R_1R_2}T^{ll'}_{g\to a_1a_2}\Big(\frac{x_1}{x_1+x_2}\Big) \frac{f_g(x_1+x_2;\mu)}{x_1+x_2} \,, \tag{4.2} $$

where

$$ \mathbf{y}_\pm = \mathbf{y} \pm \frac{1}{2}(\mathbf{z}_1 - \mathbf{z}_2) \,, \tag{4.3} $$

and the indices l, l' pertain to the tranvserse components: $l, l' \in \{1, 2\}$. Indices a_1, a_2 encode both the flavor of the pairs (a_1 and a_2 are charge-conjugate) and polarizations of each quark independently. f_g is the gluon PDF.

The quark splitting kernels for the scalar distributions are given by

$$ {}^{11}T^{ll'}_{g\to q\bar{q}}(u) = -{}^{11}T^{ll'}_{g\to \Delta q\Delta\bar{q}}(u) = T_F\big(u^2+\bar{u}^2\big)\delta^{ll'} \,, \qquad u = \frac{x_1}{x_1+x_2} \,. \tag{4.4} $$

Δ denotes the longitudinal polarization of the parton. Since the hadron is assumed unpolarized, there is no splitting of longitudinally polarized PDFs into DTMDs. Contrary to the collinear case, there are also non-vanishing pseudoscalar distributions with one parton unpolarized and the other longitudinally polarized:

$$ {}^{11}T^{ll'}_{g\to \Delta q\bar{q}}(u) = -{}^{11}T^{ll'}_{g\to q\Delta\bar{q}}(u) = -iT_F(u-\bar{u})\varepsilon^{ll'} \,. \tag{4.5} $$

$\varepsilon^{ll'}$ is the transverse antisymmetric tensor. We take $\varepsilon^{12} = +1$, so that

$$ \mathbf{y}_+^i \mathbf{y}_-^j \varepsilon^{ij} = y_+ y_- \sin\angle(\mathbf{y}_+, \mathbf{y}_-) \,. \tag{4.6} $$

The color-octet part is obtained simply by multiplication by a color factor:

$$
\begin{aligned}
{}^{88}T^{ll'}_{g\to q\bar{q}}(u) &= -{}^{88}T^{ll'}_{g\to \Delta q\Delta\bar{q}}(u) = -\frac{1}{\sqrt{N^2-1}}\,{}^{11}T^{ll'}_{g\to q\bar{q}}(u),\\
{}^{88}T^{ll'}_{g\to \Delta q\bar{q}}(u) &= -{}^{88}T^{ll'}_{g\to q\Delta\bar{q}}(u) = -\frac{1}{\sqrt{N^2-1}}\,{}^{11}T^{ll'}_{g\to \Delta q\bar{q}}(u)\,.
\end{aligned}
\tag{4.7}
$$

To write the mass-dependent splitting formula, let us define

$$
\mathcal{K}_n(M,\mathbf{y}_+,\mathbf{y}_-) = \big(|\mathbf{y}_+|M\big)K_n\big(|\mathbf{y}_+|M\big)\times\big(|\mathbf{y}_-|M\big)K_n\big(|\mathbf{y}_-|M\big)\,,\qquad \text{for } n=0,1\,. \tag{4.8}
$$

K_n is the modified Bessel function of the second kind. With this notation, in the mass-dependent case we obtain

$$
\begin{aligned}
{}^{R_1R_2}F_{a_1a_2,\mathrm{spl}} = \frac{\alpha_S(\mu)}{2\pi^2}\,\frac{f_{a_0}(x_1+x_2;\mu)}{x_1+x_2}\,\frac{\mathbf{y}_+^l\mathbf{y}_-^{l'}}{\mathbf{y}_+^2\mathbf{y}_-^2}\\
\times\left[{}^{R_1R_2}T^{ll'}_{g\to a_1a_2}\Big(\frac{x_1}{x_1+x_2}\Big)\mathcal{K}_1(M,\mathbf{y}_+,\mathbf{y}_-)+\delta^{ll'}\,c(R_1R_2)\,\mathcal{K}_0(M,\mathbf{y}_+,\mathbf{y}_-)\right]
\end{aligned}
\tag{4.9}
$$

for scalar distributions (that is: $a_1a_2 = Q\bar{Q}$, $\Delta Q\Delta\bar{Q}$, where Q is the massive quark), with the color factors:

$$
c(11)=1\,,\qquad c(88)=-\frac{1}{\sqrt{N^2-1}}\,, \tag{4.10}
$$

and

$$
{}^{R_1R_2}F_{a_1a_2,\mathrm{spl}} = \frac{\alpha_S(\mu)}{2\pi^2}\,\frac{f_{a_0}(x_1+x_2;\mu)}{x_1+x_2}\,\frac{\mathbf{y}_+^l\mathbf{y}_-^{l'}}{\mathbf{y}_+^2\mathbf{y}_-^2}\,{}^{R_1R_2}T^{ll'}_{g\to a_1a_2}\Big(\frac{x_1}{x_1+x_2}\Big)\mathcal{K}_1(M,\mathbf{y}_+,\mathbf{y}_-) \tag{4.11}
$$

for pseudoscalars $Q\Delta\bar{Q}$, $\Delta Q\bar{Q}$ (in this case the splitting kernels are simply multiplied my a mass-dependent factor).

As will be apparent from the flavor structure of DPDs in the cross-section formula given in Section 5.1.2, at the lowest order in α_S the short-distance splitting part does not contribute to the production of like-sign W bosons. The relevant terms appear at order α_S^2, and are presented in Fig. 4.2. The argument for neglecting the twist-three part given in the case of collinear double parton distributions in Section 3.3 does not hold in the transverse momentum-dependent case, since orbital momentum can balance the parton helicities [69]. However, as seen from the graphs given in Fig. 4.3, and the flavor structure of the cross-section given in Section 5.1.2, in the considered order the

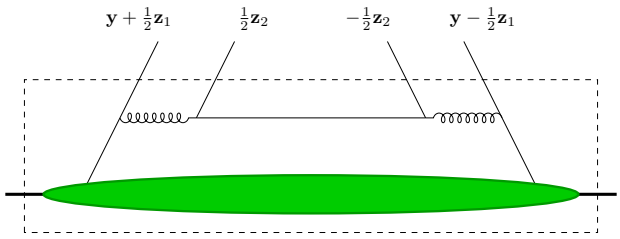

Figure 4.2: The lowest order (α_S^2) splitting contribution to DTMDs contributing to the production of a like-sign W pair.

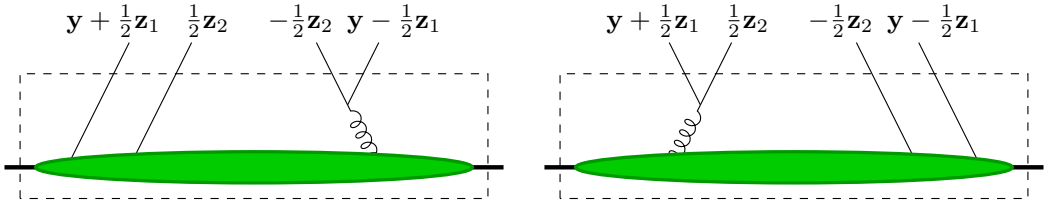

Figure 4.3: Contribution to DTMD from the perturbative splitting of twist-three TMDs.

twist-three part does not contribute to the production of like-sign W pair, just like the splitting part. It should be included in the full analysis of the opposite-sign W production, especially in the context of DPS/SPS subtraction, which is beyond the scope of this work. It will be only briefly introduced for completeness since it appears later in the context of subtractions between DPS and SPS. The relevant graphs are shown in Fig. 4.3. Based on the same reasoning as in the splitting part discussed before, at small transverse momenta the graphs in Fig. 4.3 are treated as contributions to double parton scattering, and are used in the subtraction formula presented in [69], and described briefly in Section 2.4. This is however beyond the scope of this work, and will not be considered in the presented analysis.

The last term, called the intrinsic part involves terms with no perturbative splitting and can be written

$$ {}^{R_1R_2}F_{a_1a_2,int.} = {}^{R_1R_2}G_{a_1a_2}(x_i;\mu_0) + \mathcal{O}(\alpha_S^1)\,, \tag{4.12}$$

where ${}^{R_1R_2}G_{a_1a_2}$ is a quasipartonic collinear twist-four distribution, and the higher-order corrections are given in terms of a convolution of G with perturbative splitting kernels, obtained from corrections presented in Fig. 4.4. These kernels are currently unknown, and in our analysis, we are limited to the leading-order approximation. At the leading order, the short-distance intrinsic part is obtained by taking the limit of vanishing transverse distances in the matrix element defining double parton distributions, cf. Section 2.3. The limit should be taken before renormalization, therefore at higher

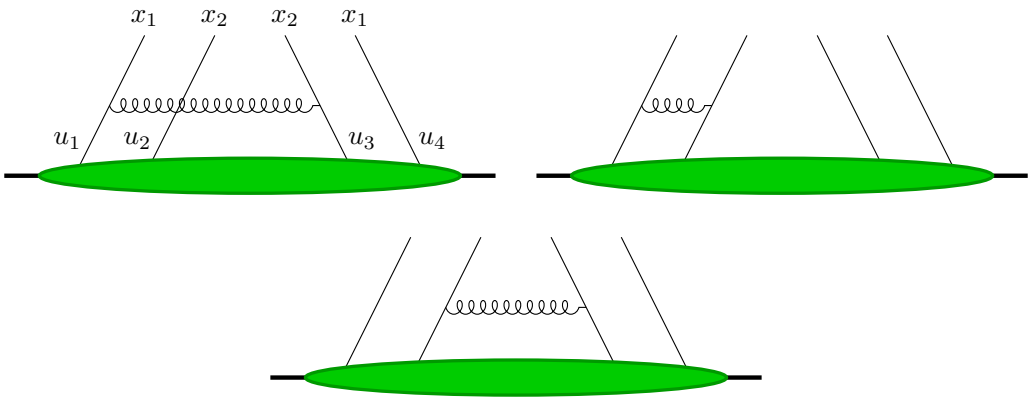

Figure 4.4: NLO corrections to twist-4 DTMDs. x_i and u_i denote the longitudinal momenta fractions.

pQCD orders the limit of vanishing distances of (4.12) is different than the $y \to 0$ limit of the collinear intrinsic part.

As in the previous part, we consider DTMDs with $n_f = 5$ active quarks, and we take the mass-dependent splitting formula for the bottom quark.

4.1.1 Choice of coordinates

The natural distances appearing in the splitting formulas in Section 4.1 are $\mathbf{y}_\pm$, so one may find it useful to perform the computation taking as the coordinates the lengths $\mathbf{y}_+, \mathbf{y}_+$, a sum $\mathbf{z}_+ = \frac{1}{2}(\mathbf{z}_1+\mathbf{z}_2)$, and the angles between these vectors. As will be discussed in App. F, this would introduce serious complications in the numerical computation of the differential cross section, due to appearance of a triple Hankel transform in the formula. DPS is most naturally described in terms of individual momenta $\mathbf{q}_i$ of the produced bosons, since both hard scattering processes are independent. The description in terms of momenta combinations $\mathbf{q}_\pm = \frac{1}{2}(\mathbf{q}_1 + \mathbf{q}_2)$ is explained in App. F. For this reason, we will use the distances $\mathbf{y}, \mathbf{z}_1, \mathbf{z}_2$ just like in the large-$\mathbf{y}$ part. It remains to fix the angular coordinates. The first will describe the angle between $\mathbf{z}_1$ and $\mathbf{z}_2$:

$$\varphi_z \equiv \angle(\mathbf{z}_1, \mathbf{z}_2) \implies \mathbf{z}_1 \cdot \mathbf{z}_2 = |\mathbf{z}_1|\,|\mathbf{z}_2|\,\cos\varphi_z\,. \tag{4.13}$$

It allows to compute the length of the relevant combinations of $\mathbf{z}_1, \mathbf{z}_2$:

$$\mathbf{z}_\pm = \frac{1}{2}\big(\mathbf{z}_1 \pm \mathbf{z}_2\big)\,, \tag{4.14}$$

$$\mathbf{z}_\pm^2 = \frac{1}{4}\Big(\mathbf{z}_1^2 + \mathbf{z}_2^2 \pm 2|\mathbf{z}_1|\,|\mathbf{z}_2|\,\cos\varphi_z\Big)\,. \tag{4.15}$$

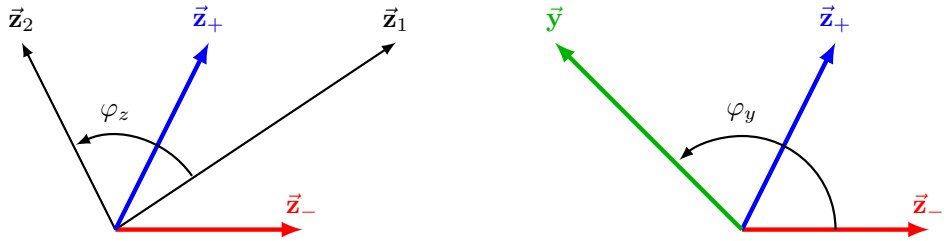

Figure 4.5: Transverse distances describing DTMDs and the corresponding angular coordinates.

Due to rotation invariance of the cross-section formula in Eq. (2.67), see also Eq. (5.90), there remains only one angle to be fixed. We found that the cut-off on distances $|\mathbf{y}_\pm|$ is conveniently enforced if one takes as the last coordinate the angle between $\mathbf{z}_-$ and $\mathbf{y}$:

$$\varphi_y \equiv \angle(\mathbf{z}_-, \mathbf{y}) \implies \mathbf{y}\cdot\mathbf{z}_- = |\mathbf{y}|\,|\mathbf{z}_-|\,\cos\varphi_y\,. \tag{4.16}$$

In the special case where $|\mathbf{z}_1 - \mathbf{z}_2| = 0$, we set the coordinate system in such a way that the angle between the vector $\hat{e}_x$ and the vectors $\mathbf{z}_1 = \mathbf{z}_2$ (identical in that case) equals π, and we define the angle φ_y with respect to $\hat{e}_x$ as

$$\varphi_y = \angle(\hat{e}_x, \mathbf{y}) \quad \text{if } \mathbf{z}_- = 0\,. \tag{4.17}$$

The total information about interpartonic distances is therefore encoded by 5 variables: $\big(|\mathbf{y}|, |\mathbf{z}_1|, |\mathbf{z}_2|, \varphi_z, \varphi_y\big)$. The use coordinates are described in Fig. 4.5. As discussed in Section 4.2, the short-distance Collins-Soper kernel depends also on the combinations of $\mathbf{y}$ and $\mathbf{z}_+$ given by

$$\mathbf{v}_\pm = \mathbf{y} \pm \mathbf{z}_+\,. \tag{4.18}$$

The length of $\mathbf{z}_\pm$ is easily obtained using the given coordinates. The angle between $\mathbf{z}_+$ and $\mathbf{y}$ is given by

$$\angle(\mathbf{z}_+, \mathbf{y}) = \begin{cases} \angle(\mathbf{z}_-, \mathbf{y}) - \arccos\frac{\mathbf{z}_1^2 - \mathbf{z}_2^2}{4|\mathbf{z}_+|\,|\mathbf{z}_-|} & \angle(\mathbf{z}_1, \mathbf{z}_2) \in [0, \pi] \\ \angle(\mathbf{z}_-, \mathbf{y}) + \arccos\frac{\mathbf{z}_1^2 - \mathbf{z}_2^2}{4|\mathbf{z}_+|\,|\mathbf{z}_-|} - 2\pi & \angle(\mathbf{z}_1, \mathbf{z}_2) \in (\pi, 2\pi) \end{cases}; \tag{4.19}$$

It can be obtained by computing $\angle(\mathbf{z}_-, \mathbf{z}_+) = \angle(\mathbf{z}_-, \mathbf{y}) - \angle(\mathbf{z}_+, \mathbf{y})$ using the relation

$$\mathbf{z}_+\cdot\mathbf{z}_- = |\mathbf{z}_+|\,|\mathbf{z}_-|\,\cos\angle(\mathbf{z}_+, \mathbf{z}_-) = \frac{1}{4}\big(\mathbf{z}_1^2 - \mathbf{z}_2^2\big)\,, \tag{4.20}$$

$$\angle(\mathbf{z}_-, \mathbf{z}_+) = \begin{cases} \arccos\frac{\mathbf{z}_1^2 - \mathbf{z}_2^2}{4|\mathbf{z}_+|\,|\mathbf{z}_-|} & \angle(\mathbf{z}_1, \mathbf{z}_2) \in [0, \pi] \\ 2\pi - \arccos\frac{\mathbf{z}_1^2 - \mathbf{z}_2^2}{4|\mathbf{z}_+|\,|\mathbf{z}_-|} & \angle(\mathbf{z}_1, \mathbf{z}_2) \in (\pi, 2\pi) \end{cases}. \tag{4.21}$$

4.1.2 Matching scales

The initial conditions for short-distance DTMDs are formulated at a single factorization scale μ_0, contrary to the large-$\mathbf{y}$ case, where we used different scales for each parton. The question of the natural choice of the scale in this case is more involved than in Chapter 3, since here one has three two-dimensional transverse vectors forming numerous distance combinations, which enter the perturbative corrections. Since the short-distance region is constructed for the case $|\mathbf{y}| \sim |\mathbf{z}_i|$, we will fix the initial scales depending only on the distances $\mathbf{z}_1, \mathbf{z}_2$. Our choice is

$$\mu_0 = \frac{b_0}{\frac{1}{2}\left(|\mathbf{z}_1^*| + |\mathbf{z}_2^*|\right)}\,, \qquad \xi_0 = \mu_0^2\,. \tag{4.22}$$

This choice guarantees that the matching scales are of order $|\mathbf{q}_T|$ in the most relevant regions, while also allowing for a smooth extrapolation to larger distances. Moreover, we found that it allows for better consistency between the two DTMD approximations in the region where the "large-$\mathbf{y}$" and "short-distance" approximations overlap. This will be discussed in more detail in Section 5.2.1.

The uncertainty due to the scale variation will be estimated by modifying the scale μ_0 with the parameter κ, analogously to Eq. (3.56):

$$\mu_{0,\kappa} = \kappa \frac{b_0}{\frac{1}{2}\left(|\mathbf{z}_1^*| + |\mathbf{z}_2^*|\right)} + (1-\kappa)\,\mu_{\min}\,. \tag{4.23}$$

4.2 Collins-Soper kernel at small transverse distances

As noted in Section 2.3.6, when all transverse distances are small, the Collins-Soper kernel of DTMDs can be computed using perturbation theory. Contrary to the collinear case, the soft factor defined in Section 2.3.2 is non-diagonal in color representations, and therefore the rapidity evolution kernels form a matrix in the color representation space.

In this work we focus on two quark DPDs. The short-distance Collins-Soper kernel for two gluon, and quark+gluon DPDs can be found in Section 7.2 in [56].
The two quark kernel represented as a matrix has entries corresponding to

$${}^{R_1R_2,R_3R_4}M \;=\; \begin{pmatrix} \left[R_1R_1 = R_3R_4 = 11\right] & \left[R_1R_2 = 11,\; R_3R_4 = 88\right] \\ \left[R_1R_2 = 88,\; R_3R_4 = 11\right] & \left[R_1R_1 = R_3R_4 = 88\right] \end{pmatrix}. \tag{4.24}$$

The short-distance Collins-Soper kernel for a two-quark[1] DTMD can be written as a sum of a color-diagonal term, which consists of standard TMD rapidity evolution kernels, and a non-diagonal part M_{qq}, which is scale-independent:

$$ {}^{R_1R_2,R_3R_4}K_{qq}\big(\mathbf{z}_i,\mathbf{y};\mu\big) = \big[{}^1K_q(\mathbf{z}_i;\mu) + {}^1K_q(\mathbf{z}_2;\mu)\big]\delta_{R_1R_2,R_3R_4} + {}^{R_1R_2,R_3R_4}M_{qq}(\mathbf{z}_i,\mathbf{y})\,, \tag{4.25} $$

where

$$ {}^{R_1R_2,R_3R_4}M_{qq}(\mathbf{z}_i,\mathbf{y}) = \begin{pmatrix} 0 & \frac{\sqrt{N^2-1}}{2N}K_d \\ \frac{\sqrt{N^2-1}}{2N}K_d & -\frac{N}{2}K_y - \frac{1}{N}K_d \end{pmatrix}\,. \tag{4.26} $$

We recall that $N = 3$ denotes the number of colors. The kernels K_y, K_d up to α_S^2 can be written with the help of quark TMD Collins-Soper kernels ${}^1K_q$. Define the 'color-stripped' kernels K_0 as

$$ {}^1K_q(\mathbf{b};\mu) \;=\; C_F \;\times\; K_0(\mathbf{b};\mu)\,, \tag{4.27} $$

where $C_F = \frac{N^2-1}{2N} = \frac{4}{3}$. Using K_0, we can write the discussed terms as

$$ K_d = K_0\big(\mathbf{v}_+;\mu\big) + K_0\big(\mathbf{v}_-;\mu\big) - K_0\big(\mathbf{y}_+;\mu\big) - K_0\big(\mathbf{y}_-;\mu\big), \tag{4.28} $$

$$ K_y = K_0(\mathbf{z}_1;\mu) + K_0(\mathbf{z}_2;\mu) - K_0\big(\mathbf{v}_+;\mu\big) - K_0\big(\mathbf{v}_-;\mu\big). \tag{4.29} $$

This relation between the single-parton TMD Collins-Soper kernel, and DTMD rapidity evolution kernel, holding up to α_S^2 [102], will be crucial in our construction of Collins-Soper kernels extrapolated to large distances, as described later in Section 5.2.2.
The exponentiated non-diagonal part is

$$ \exp\big[\mathcal{L}M_{qq}\big] = \frac{1}{d_+ - d_-}\begin{pmatrix} d_+e^{\mathcal{L}d_-} - d_-e^{\mathcal{L}d_+} & \frac{\sqrt{N^2-1}}{2N}K_d\big(e^{\mathcal{L}d_+} - e^{\mathcal{L}d_-}\big) \\ \frac{\sqrt{N^2-1}}{2N}K_d\big(e^{\mathcal{L}d_+} - e^{\mathcal{L}d_-}\big) & d_+e^{\mathcal{L}d_+} - d_-e^{\mathcal{L}d_-} \end{pmatrix}, \tag{4.30} $$

where

$$ d_\pm = \frac{1}{N}\left[-\frac{N^2}{2}K_y - K_d \pm \sqrt{\Big(\frac{N^2}{2}K_y + K_d\Big)^2 + \Big(N^2-1\Big)K_d^2}\right]. \tag{4.31} $$

The parameter $\mathcal{L}$ in the exponential corresponds to $\frac{1}{2}\log\frac{\zeta}{\zeta_0}$, so that, with our choice of the scales, it is always larger or equal to 0. Moreover, let us notice that d_+ is always positive, and d_- is negative, which is relevant in the discussion of the behavior of the exponentiated kernels at vanishing transverse distances.

[1] By 'two-quark' we mean all configurations of quarks and antiquarks.

Vanishing transverse distances

The fixed-order perturbative expression of the color-stripped Collins-Soper kernel defined in Eq. (4.27), reads

$$K_0(\mathbf{b};\mu) = \log \frac{\mathbf{b}^2\mu^2}{b_0^2} \,. \tag{4.32}$$

The constant b_0 is given in Eq. (3.13). When one of the transverse distance arguments $\mathbf{b}$ in Eqs. (4.28)-(4.29) vanishes, then the value of d_+ given in Eq. (4.31) diverges like a power of $\log|\mathbf{b}|^{-1}$, so that the exponential $e^{\mathcal{L}d_+}$ has a power-law divergence, possibly non-integrable, since the parameter

$$\mathcal{L} = \log \frac{Q_1 Q_2}{\zeta_0}$$

may become sufficiently large to make the integrals divergent[2]. It arises from the resummation of the perturbative corrections in the region of transverse distances corresponding to large momentum scales where the factorization formalism is no longer motivated, and therefore should not be considered a physical effect. The problem is partially cured by resumming each term $K_0(\mathbf{b};\mu)$ independently, according to

$$K_0(\mathbf{b};\mu) = K_0(\mathbf{b};\mu_{\mathbf{b}}) - \int_{\mu_{\mathbf{b}}}^{\mu} \frac{d\mu'}{\mu'} \gamma_{K,0}(\mu') \,. \tag{4.33}$$

The 'color-stripped' anomalous dimension is obtained from the $\gamma_{K,q}$ of the quark TMD kernel:

$$\gamma_{K,0} = \frac{1}{C_F}\gamma_{K,q} \,. \tag{4.34}$$

Computing the Collins-Soper kernels in Eq. (4.28)-(4.29) at scales associated with the distance $\mathbf{b}$, and then evolving it to some common scale μ using the RGE of the kernel one obtains

$$\begin{aligned} K_d^{\text{res.}} &= K_0^{pt}(\mathbf{v}_+;\mu_{\mathbf{v}_+}) + K_0^{pt}(\mathbf{v}_-;\mu_{\mathbf{v}_-}) - K_0^{pt}(\mathbf{y}_+;\mu_{\mathbf{y}_+}) - K_0^{pt}(\mathbf{y}_-;\mu_{\mathbf{y}_-}) \\ &\quad + \int_{\mu_{\mathbf{y}_+}}^{\mu_{\mathbf{v}_+}} \frac{d\mu'}{\mu'}\gamma_{K,0}(\mu') + \int_{\mu_{\mathbf{y}_-}}^{\mu_{\mathbf{v}_-}} \frac{d\mu'}{\mu'}\gamma_{K,0}(\mu') \,, \end{aligned} \tag{4.35}$$

$$\begin{aligned} K_y^{\text{res.}} &= K_0^{pt}(\mathbf{z}_1;\mu_{\mathbf{z}_1}) + K_0^{pt}(\mathbf{z}_2;\mu_{\mathbf{z}_2}) - K_0^{pt}(\mathbf{v}_+;\mu_{\mathbf{v}_+}) - K_0^{pt}(\mathbf{v}_-;\mu_{\mathbf{v}_-}) \\ &\quad + \int_{\mu_{\mathbf{v}_+}}^{\mu_{\mathbf{z}_1}} \frac{d\mu'}{\mu'}\gamma_{K,0}(\mu') + \int_{\mu_{\mathbf{v}_-}}^{\mu_{\mathbf{z}_2}} \frac{d\mu'}{\mu'}\gamma_{K,0}(\mu') \,. \end{aligned} \tag{4.36}$$

[2]Notice that the exponentials $e^{\mathcal{L}d_-}$ vanish in the considered limit.

The dependence on the auxiliary scale μ vanished, as it should. The index $'pt'$ denotes the kernel computed at fixed order in perturbation theory. Notice that at LO the Collins-Soper kernel vanishes at the canonical scale. If one of the transverse distances vanishes, then the resummed kernels in Eq. (4.33) diverge like a double logarithm – the result at LO reads

$$K_0^{pt}(\mathbf{b},\mu_0) = -\frac{4}{\beta_0}\log\frac{\alpha_S(\mu_{\mathbf{b}})}{\alpha_S(\mu_0)} \approx \frac{4}{\beta_0}\log\left(\frac{\beta_0}{4\pi}\log\frac{\mu^2}{\Lambda^2_{QCD}}\right), \tag{4.37}$$

where we used the LO running of the strong coupling constant,
and $\beta_0 = 11/3\, C_A - 2/3\, n_f$. Depending on which of the relevant distances vanish, the exponentiated kernel exhibits different behavior – let us take for example the singularity at $|\mathbf{v}_+| \to 0$. In that case, the term K_y is free of singularities, while K_d behaves like

$$K_d \sim \frac{4}{\beta_0}\log\left(\frac{\beta_0}{4\pi}\log\frac{b_0^2}{\mathbf{v}_+^2\Lambda^2_{QCD}}\right). \tag{4.38}$$

Since $d_\pm \to \pm\infty$, and $\mathcal{L} > 0$, the exponentials $e^{\mathcal{L}d_+}$ become the divergent terms, and the exponentiated kernel diverges like

$$\sim \left(\log\frac{b_0^2}{\Lambda^2_{QCD}\mathbf{v}_+^2}\right)^{\frac{4N}{\beta_0}\mathcal{L}}. \tag{4.39}$$

On a 2-dimensional $\mathbf{z}_i$ or $\mathbf{y}$ plane, the contribution to the integrals from the region where any of the considered transverse distances is of order Q^{-1} is formally suppressed by Q^{-2}, however, the enhancement from the logarithmic divergence may lead to the contribution being rather large. For the initial rapidity parameter $\xi_0 = (10\text{ GeV})^2$, hard scales equal to the W mass, and $n_f = 5$ active flavors, the exponent in Eq. (4.39) is about

$$\frac{4N}{\beta_0}\mathcal{L} \approx 6.5\,. \tag{4.40}$$

To estimate if the small measure of the discussed region is enough to suppress the logarithmic behavior, let us integrate

$$\begin{aligned}&\int_0^{Q^{-1}} d^2\mathbf{b}\left(\log\frac{1}{\mathbf{b}^2\Lambda^2}\right)^\delta \\ &= \frac{\pi}{\Lambda^2}\Gamma\left(\delta+1,\log\frac{Q^2}{\Lambda^2}\right) \approx \frac{\pi}{Q^2}\left(\log\frac{Q^2}{\Lambda^2}\right)^\delta.\end{aligned} \tag{4.41}$$

$\Gamma(\delta+1,z)$ is the upper incomplete gamma function. The integral can be simply computed by substitution $t = \log\left(1/(\Lambda^2\mathbf{b}^2)\right)$. For a high power of the logarithm, the considered contribution may be significant. However, as pointed out before, for

distances of sizes comparable with Q^{-1} the use of the Collins-Soper resummed formula, even with RGE-improved kernels, is not justified. Therefore, we are free to regularize the rapidity evolution kernels so that the discussed regions do not get strongly enhanced by rapidity evolution. To achieve it, for the distance arguments of the Collins-Soper kernels we shall take distances regularized from below:

$$\mathbf{b}^*_{\rm UV} = \mathbf{b}\Big(1 + \big(b_{\rm min}/|\mathbf{b}|\big)^4\Big)^{-1/4}\,, \tag{4.42}$$

which do not modify the value of the distances as $|\mathbf{b}| \gg Q^{-1}$, but guarantee that the lengths do not get smaller than $b_{\rm min}$, and allow to avoid the problematic behavior of the integrands in the later analysis.
Finally, the regularized kernels $K^{\rm reg.}$ present in Eq. (4.25) are computed as

$$K^{\rm reg.} = K^{\rm res.}\Big|_{b\to b^*_{\rm UV}}\,, \tag{4.43}$$

where b denotes all of the transverse lengths in the arguments, and the resummed form of $K^{\rm res.}$ is given in Eq. (4.33).

In Fig. 4.6 we present 3 different components of the exponentiated full Collins-Soper kernel (4.25):

$$\begin{aligned}{}^{R_1R_2,R_3R_4}\Big[\exp\Big(K_{qq}(\mathbf{z}_i,\mathbf{y})\mathcal{L}\Big)\Big] \;&=\; \exp\Big[\big({}^1K_q(\mathbf{z}_1;\mu) + {}^1K_q(\mathbf{z}_2;\mu)\big)\mathcal{L}\Big] \\ &\times\quad {}^{R_1R_2,R_3R_4}\Big[\exp\Big(M_{qq}(\mathbf{z}_i,\mathbf{y})\mathcal{L}\Big)\Big]\,.\end{aligned} \tag{4.44}$$

The indices correspond to $(R_1R_2, R_3R_4) \in \big\{(11,11),\,(88,88),\,(11,88)\big\}$, and the results are presented as functions of $y = |\mathbf{y}|$. The transverse positions are defined by:

$$\begin{aligned}&\angle(\mathbf{y},\mathbf{z}_-) = 0\,, \qquad \angle(\mathbf{z}_1,\mathbf{z}_2) \in \{0,\,0.5\pi,\,\pi\}\,,\\ &|\mathbf{z}_1| = \frac{1}{2}|\mathbf{z}_2| = 0.2\ \text{GeV}^{-1}, \quad |\mathbf{y}| \in [0.01\ \text{GeV}^{-1}, 0.2\ \text{GeV}^{-1}]\,.\end{aligned} \tag{4.45}$$

The two off-diagonal elements of the matrix are equal. The renormalization and rapidity scales μ_0, ξ_0 are taken according to Eq. (4.22). Presented are the results for 2 values of the UV cut-off:

$$b_{\rm min,1} = \frac{b_0}{M_W}, \qquad b_{\rm min,2} = \frac{b_0}{10\,M_W}, \tag{4.46}$$

so that we can illustrate the effects of short-distance regularization. The values of φ_y, φ_z are chosen such that on the plots there are visible both $|\mathbf{y}_-| = 0$ and $|\mathbf{v}_\pm| = 0$ singularities. Notice that for most of the angular configurations, all of the relevant transverse distances are far from zero, and the UV regularization has no effect.

For the considered value of the short-distance cut-off $b_{\rm min,1} = b_0/M_W$, let us focus on the variation of the values of exponentiated kernels near the singular points, say, the

region where the results for the 2 different regularizations visibly differ. We observe that it is comparable with the difference between the values of the exponentiated kernels for fixed $|\mathbf{y}|$ away from the singular point at different φ_z – for example compare how the results differ at $|\mathbf{y}| = 0$ (where all $\mathbf{y}_\pm, \mathbf{v}_\pm, \mathbf{z}_{1,2}$ are perturbative but much larger than Q^{-1}), depending on the value of the angle between $\mathbf{z}_1$ and $\mathbf{z}_2$. Therefore, we conclude that even at the relatively small cut-off value $b_{\min,1}$, the regularization removes the pathological short-distance behavior to a sufficient extent, and therefore this value will be adapted as the short-distance regulator.

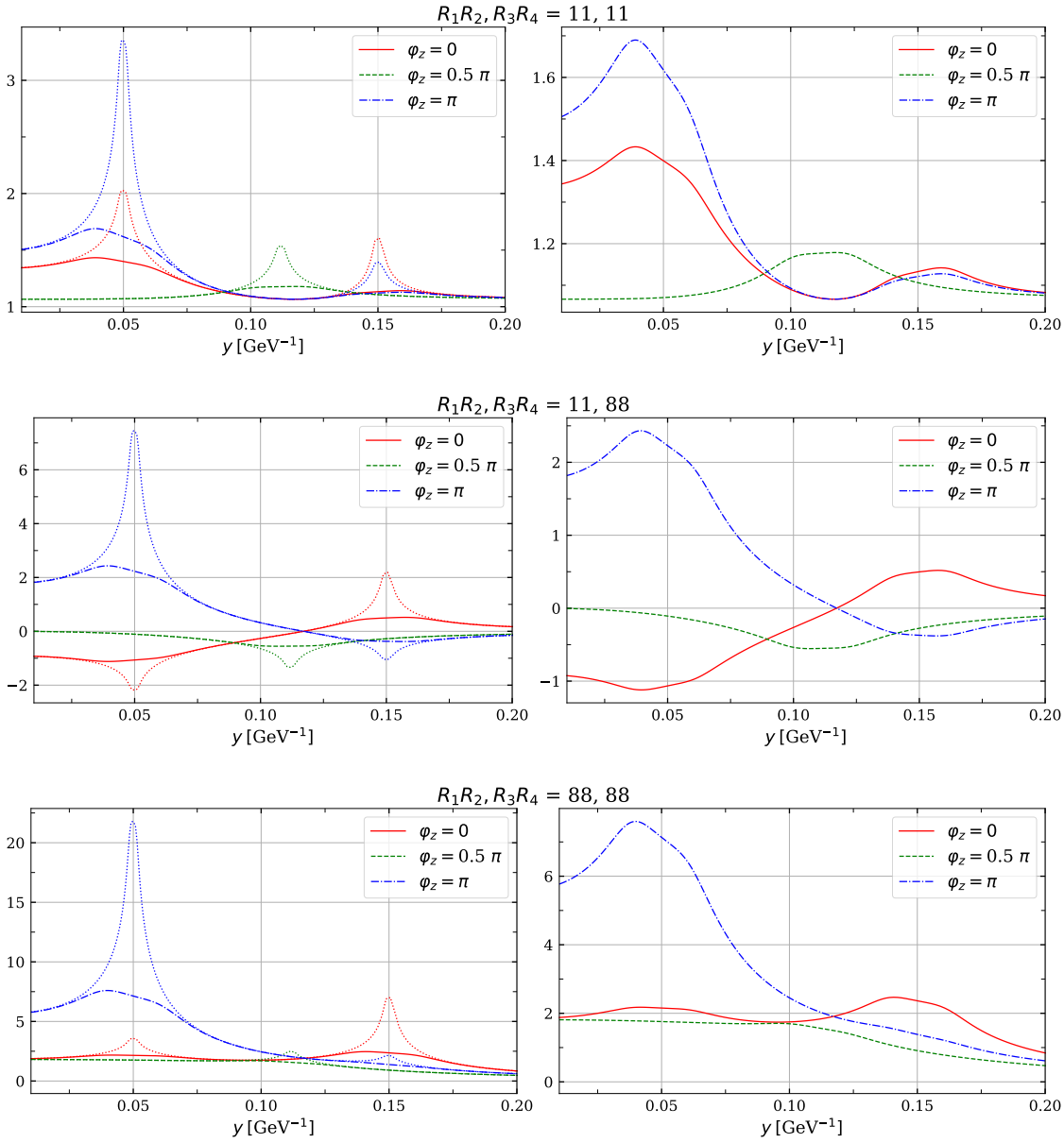

Figure 4.6: Three different components of $\exp\left[K\mathcal{L}\right]$ as functions of $y = |\mathbf{y}|$. In the plots on the right, shown are the exponentiated kernels for the standard choice of the parameter $b_{\min}$. In the plots on the left, solid lines correspond to the previous settings, while the dashed lines are the results for $b_{\min} = b_0/(10M_W)$, illustrating the effect of the short-distance regularization of the Collins-Soper kernels. Notice that for $\varphi_z = 0$ and π, where $\mathbf{y}, \mathbf{z}_+, \mathbf{z}_-$ are collinear for $\varphi_y = 0$, visible are peaks as $|\mathbf{y}| \to |\mathbf{z}_-|$ and $|\mathbf{y}| \to |\mathbf{z}_+|$, where either $|\mathbf{y}_-|$ or $|\mathbf{v}_\pm|$ approaches 0.

4.3 Numerical results

As discussed in Section 4.1, we limit our analysis to NLL accuracy, taking the kernels and anomalous dimensions orders according to Table 3.1. Plots of DTMDs in the short distance approximation as a function of $y = |\mathbf{y}|$ for different angular configurations, cf. Fig. 4.5, are presented in Figs. 4.7-4.14. We show the short-distance approximation of double parton distributions with their error estimation bands obtained via variation of the scales μ_0, ξ_0 according to Eq. (4.23). As previously, the considered values of the parameters defining the scale variation is $\kappa \in \{0.5, 0.75, 1, 1.5, 2\}$. It should be noted that the variation of the initial scales studied here is not equivalent to the variation of the matching scale analyzed in Chapter 3, despite the overall similarity. This issue will be discussed in more detail when combining both results in Section 5.6, in the context of estimation of the total uncertainty.

DTMDs in this part are presented for equal lengths of $\mathbf{z}_1$ and $\mathbf{z}_2$. To illustrate the change of sign of the splitting part due to the factor $T^{ll'}\mathbf{y}_+^j\mathbf{y}_-^{j'}$, in App. G.1 we provide complementary plots for $|\mathbf{z}_1| = 0.1\ \mathrm{GeV}^{-1}$, $|\mathbf{z}_2| = 0.5\,\mathrm{GeV}^{-1}$. The intrinsic part depends on the angular coordinates only via short-distance rapidity evolution kernel, as described in Section 4.2. As seen in the plots below, for a small value of φ_y ($= 0.1\pi$) the φ_z-dependence can be visible, however, away from φ_y close to 0 or π, the variation of the intrinsic part with the angle between $\mathbf{z}_1, \mathbf{z}_2$ becomes much weaker. On the other hand, since φ_z determines the value of $|\mathbf{z}_-|$, and hence the position of the $\mathbf{y}_\pm \to 0$ points, the dependence of the splitting part on this angle is much stronger, as seen in Figs. 4.7, 4.8, and in App. G.1 . As will be shown in Section 5.4, the dependence of the product of DTMDs on φ_z will introduce correlations between angles of the momenta $\mathbf{q}_1, \mathbf{q}_2$ in the cross-section. In Section 5.5.2 we show that the angular dependence turns out to be strong in channels involving DTMD splitting.

We observe in Figs. 4.7-4.8 and 4.11-4.13 that DTMDs in both approximations agree reasonably well at large y, where validity regions of both approximations overlap. The "large-y" DTMDs (at NLL, for the nominal matching scales) are shown using dashed black lines for $y > 0.25\ \mathrm{GeV}^{-1}$. Similarly to the previous Chapter, we see that in the case of the intrinsic part, longitudinally polarized DTMDs are much smaller than the unpolarized counterparts. At small y there is no suppression of the color-nonsinglet part, however, whereas the singlet part tends to vary less rapidly with growing y, the nonsinglet part becomes strongly suppressed in that region. The angular dependence is more pronounced in the case of the splitting contributions due to the $\mathbf{y}_\pm$-dependent prefactors in the splitting formula. For massless quarks one can observe the change of sign of the splitting part of scalar distributions as y crosses the value $|\mathbf{z}_-|$ due to the change sign of the scalar product $\mathbf{y}_+ \cdot \mathbf{y}_+$ – the example is given in Figs. G.6 and G.7 in Appendix G.1. In the case of massive quarks the position of zero crossing is changed due to the presence of mass-dependent terms – the corresponding plots are shown in Figs. G.2 and G.3 in the Appendix G. Moreover, for massive quark pair $b\bar{b}$ we observe

a rapid vanishing of the splitting contribution.

There is a strong suppression of the pseudoscalar part due to the prefactor in the splitting formula (4.5), which is antisymmetric with respect to interchange x_1 and x_2 – in the region of asymmetric x_i where that prefactor can be far from zero, the total longitudinal momenta of the parent gluons in DTMDs of both left- and righ-moving quarks become large, so that the splitting term is small. Moreover, at fixed $\mathbf{z}_1$, $\mathbf{z}_2$ the function vanishes more rapidly with larger y due to the prefactor $\mathbf{y}_+^j \mathbf{y}_-^{j'} \varepsilon^{jj'}$.

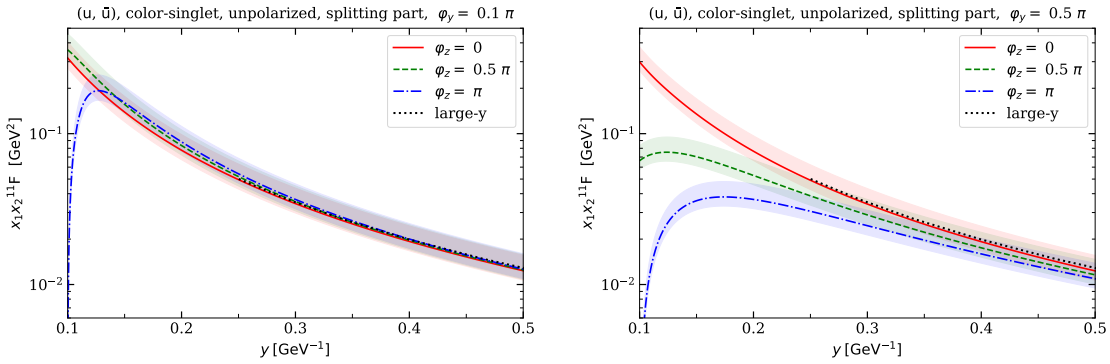

Figure 4.7: Unpolarized splitting part of the short-distance DTMDs at different ϕ_z (red, green, blue lines) versus their counterparts in the large-$\mathbf{y}$ form at NLL (dotted black line). On the left given is the result for $\phi_y = 0.1\pi$, and on the right: for $\phi_y = \frac{1}{2}\pi$. Presented are distributions in the color-singlet representation.

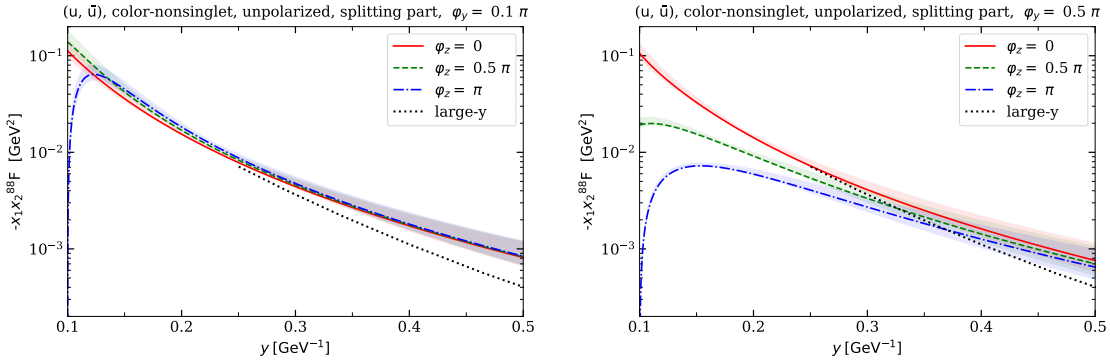

Figure 4.8: The same as in Fig. 4.7, but for color-nonsinglet representation.

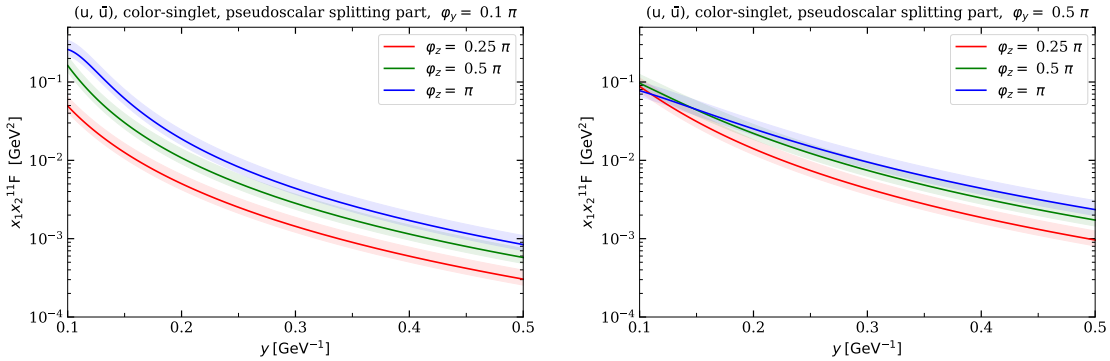

Figure 4.9: Imaginary part of the pseudoscalar DTMD $(u, \Delta u)$ computed using the splitting formula for $|\mathbf{z}_1| = |\mathbf{z}_2| = 0.1$ GeV, and asymmetric longitudinal momenta fractions $x_1 = \frac{M_W}{\sqrt{s}} e^{Y}$ and $x_2 = \frac{M_W}{\sqrt{s}} e^{-Y}$ with $Y = 1$. Presented are distributions in the color-singlet representation.

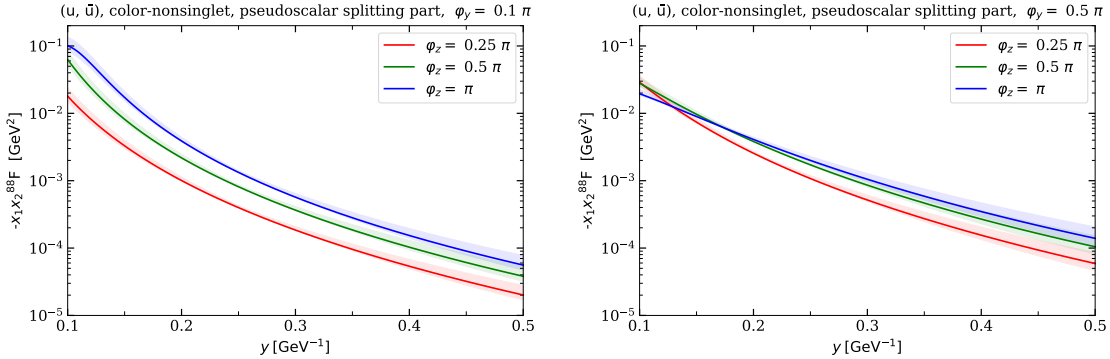

Figure 4.10: The same as in Fig. 4.9, but for color-nonsinglet representation.

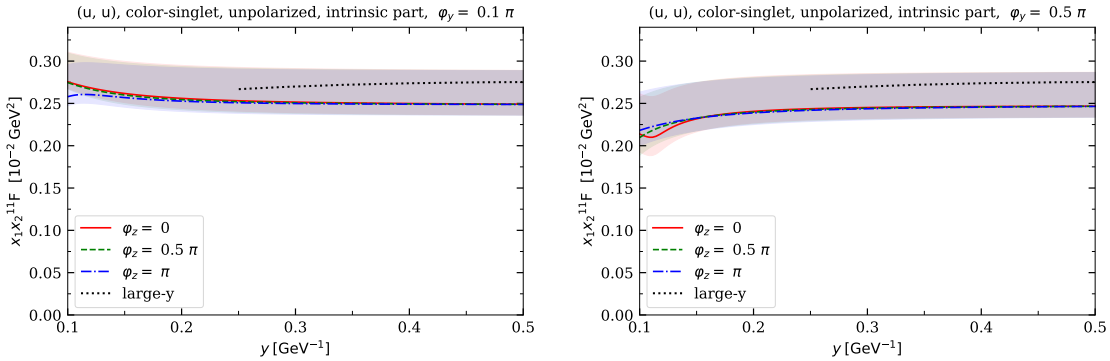

Figure 4.11: Unpolarized intrinsic part of the short-distance DTMDs at different ϕ_z (red, green, blue lines) versus their counterparts in the large-$\mathbf{y}$ form at NLL (dotted black line). Presented are distributions in the color-singlet representation. On the left given is the result for $\phi_y = 0.1$, and on the right: for $\phi_y = \frac{1}{2}\pi$.

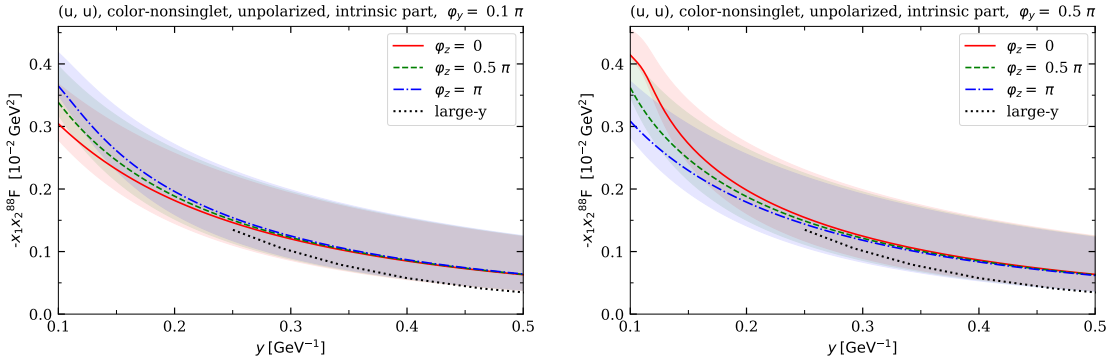

Figure 4.12: The same as in Fig. 4.11, but for color-nonsinglet representation.

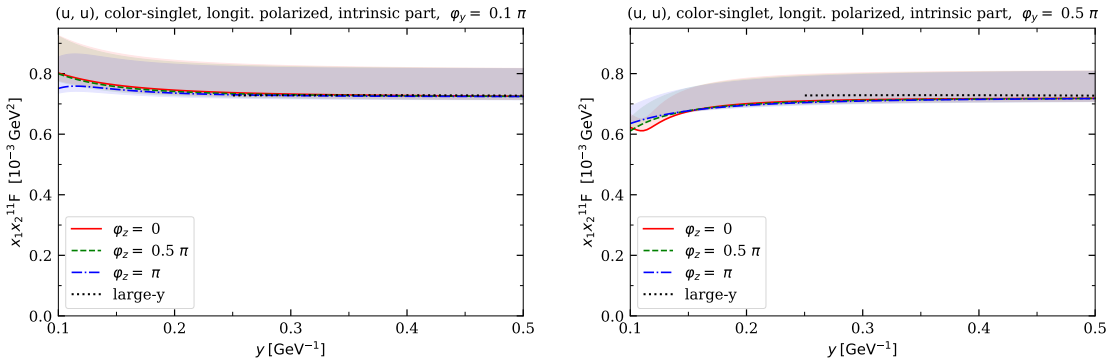

Figure 4.13: The same as in Fig. 4.11, but for both quarks longitudinally polarized.

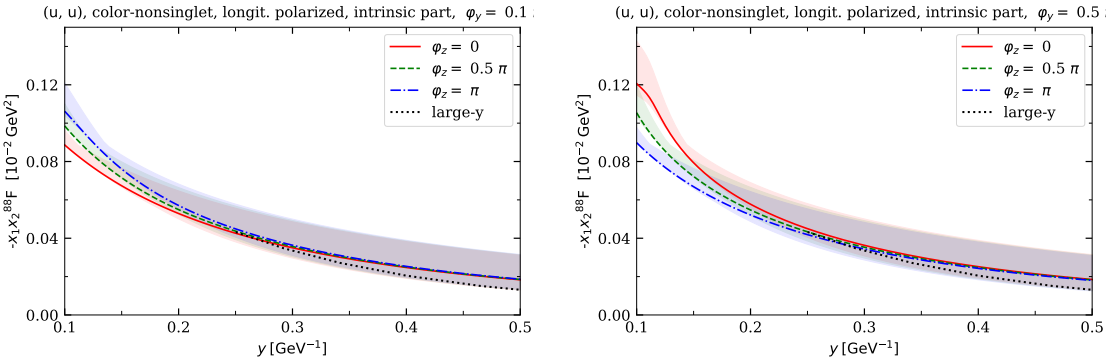

Figure 4.14: The same as in Fig. 4.13, but for color-nonsinglet representation.

4.3.1 Extrapolation to large z

Formulating the short-distance approximation we assume

$$Q^{-1} \ll |\mathbf{z}_i|, \qquad |\mathbf{y}| \sim |\mathbf{q}_T|^{-1} \ll \Lambda^{-1}, \tag{4.47}$$

however, the product of parton distributions needs to be extrapolated to

$$|\mathbf{z}_i| \in (0, \infty), \quad |\mathbf{y}| \in (0, y_{\max}]. \tag{4.48}$$

$y_{\max}$ is the maximal value of $|\mathbf{y}|$, for which one includes the short-distance part in the interpolation scheme, which will be described in Section 5.2.1. With our choice, it is given by

$$y_{\max} = \frac{3}{4} b_0 \,\mathrm{GeV}^{-1} \;\approx\; 0.84\,\mathrm{GeV}^{-1}. \tag{4.49}$$

For $|\mathbf{y}| > y_{\max}$ double parton distributions are described only in terms of the large-$\mathbf{y}$ approximation, independently on the values of $|\mathbf{z}_i|$.

The short-distance approximation needs to be extrapolated to the region of large $\mathbf{z}_i$, as we want to have continuous integrands in $\mathbf{z}_i$-space. The extrapolation scheme in which we would replace

$$\mathbf{y} \to \mathbf{y}^*, \quad \mathbf{z}_i \to \mathbf{z}_i^* \tag{4.50}$$

does not work here, since one can possibly encounter a situation where

$$\left|\mathbf{y}^* \pm \tfrac{1}{2}(\mathbf{z}_1^* \pm \mathbf{z}_2^*)\right| \approx 0 \qquad \text{for} \quad \tfrac{1}{2}|\mathbf{z}_1 \pm \mathbf{z}_2| \gg |\mathbf{y}|\,. \tag{4.51}$$

In such a situation one would encounter a spurious singularity $|\mathbf{y}_\pm|, |\mathbf{v}_\pm| \to 0$ in the Collins-Soper kernel, see the discussion in Section 4.2. For this reason, instead of the regularization like in Eq. (4.50), we replace all of the distances in the perturbative part of the rapidity evolution kernel by their *-regularized value:

$$\mathbf{b} \to \mathbf{b}^*\,, \qquad \mathbf{b} \in \{\mathbf{y}_\pm,\, \mathbf{v}_\pm,\, \mathbf{z}_{1,2}\}\,, \tag{4.52}$$

where $\mathbf{b}^*$ is given in Eq. (3.14). This is similar to what is done in the UV-regularization of the Collins-Soper kernels in Eq. (4.43), but it should be noted that there the short-distance regularization is applied to both the perturbative and nonperturbative parts of the kernel.

The extrapolated DTMDs will take the following form

$$\begin{aligned} &{}^{R_1R_2}F_{ab}\big(\mathbf{y}, \mathbf{z}_i, x_i; \mu_0(\{\mathbf{z}_i^*\}), \xi_0/(x_1x_2)\big) \\ &\quad = {}^{R_1R_2}F_{ab}^{\text{model}}\big(\mathbf{y}, \mathbf{z}_i, x_i; \mu_0(\{\mathbf{z}_i^*\}), \xi_0/(x_1x_2)\big) F_{\text{NP}}(x_i, \mathbf{z}_i, \mathbf{y}) \,, \end{aligned} \tag{4.53}$$

with the factor F_{NP} taken the same as in the large-$\mathbf{y}$ part, cf. Eq. (3.45). As described in Section 5.2.3, in the actual computation we take the function F_{NP} depending only on distances $\mathbf{z}_1, \mathbf{z}_2$, but not on the momenta fractions or $\mathbf{y}$. The absence of $\mathbf{y}$-dependence in the fall-off factor in Eq. (4.53) implies that DTMDs formulated in the short-distance part do not vanish at large $\mathbf{y}$ as quickly as those in the large-$\mathbf{y}$ model, where the large-distance behavior is also controlled at the level of DPDFs. However, as will be discussed in Section 5.2.1, Eq. (4.49), the short-distance part does not need to be regularized at large $\mathbf{y}$, as it is considered for $\mathbf{y}$ smaller than some upper bound y_{max} not too far from the perturbative region.

Chapter 5

Differential cross-section of W pair production

After the analysis of DTMDs in the large-$\mathbf{y}$ and short-distance approximations in Chapters 3 and 4, we are ready to present the results concerning a specific process, namely the production of two W bosons decaying into leptons in the double Drell-Yan (DDY) process, schematically:

$$p(p) + p(\bar{p}) \longrightarrow W^{\pm}(q_1)W^{\pm}(q_2) + X \longrightarrow l_1\nu_1 + l_2\nu_2 + X \,, \tag{5.1}$$

where l_i and ν_i are the lepton (antilepton) and the corresponding antineutrino (neutrino) into which a given boson W^- (W^+) decays. Momenta of the particles are indicated in parentheses. We will be particularly interested in the case of like-sign W pairs production, which was studied in several previous works [51–57], and is believed to be a promising channel for the study of double parton scattering.

The mass of W, its decay width Γ_W, weak mixing angle θ_W, and the CKM matrix elements are taken according to [103]:

$$M_W = 80.377\,\text{GeV}, \qquad \Gamma_W = 2.089\ \text{GeV}\,, \qquad \sin^2\theta_W = 0.23121\,. \tag{5.2}$$

The absolute values of the CKM matrix elements are taken as:

$$\begin{pmatrix} 0.97373 & 0.2243 & 0.00382 \\ 0.221 & 0.975 & 0.0408 \\ 0.0086 & 0.0415 & 1.014 \end{pmatrix} \tag{5.3}$$

We use only the leading-order expression in weak interactions, and the fine-structure constant at W mass scale is taken as:

$$\alpha(M_W) = \frac{1}{128}\,. \tag{5.4}$$

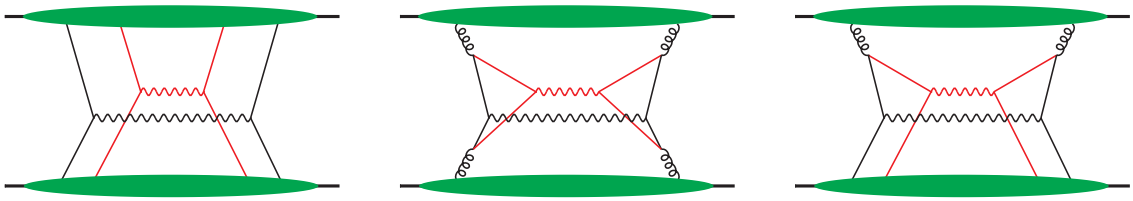

Figure 5.1: From the left: 2v2, 1v1 and 1v2 contributions to double parton scattering.

As described in the previous part, we decompose each DTMD into the intrinsic and splitting part, so in a product of two DTMDs one can distinguish 3 kinds of contributions, denoted 'nvm' (read "n versus m"):

- 2v2 – product of two intrinsic parts,
- 1v1 – product of two splitting parts,
- 2v1(+1v2) for the mixed terms.

The corresponding 'nvm' terms are presented schematically in Fig. 5.1.

5.1 Differential cross-section of the Double Drell-Yan process

In this section, we describe the formula for the differential cross section of W bosons pair production via double parton scattering. In Section 5.1.1 we introduce the reference frame in which the angular variables of the product, leptons are defined. In Section 5.1.2 we give the formula for the fully differential cross cross-section, and describe, how it is integrated with respect to different variables. Section 5.2 deals with the non-perturbative input in the discussed model.

After that, in Section 5.3 we present the quantitative analysis of the contribution of the large-$\mathbf{y}$ part, and in Section 5.4 – the short-distance region. In Section 5.6 we combine both contributions, and discuss the final results.

5.1.1 Reference frames

The reference frames are defined according to Section 2.2 of [53], which uses the Collins-Soper frame [11]. We start from the center-of-mass system of the colliding protons. Let Z be the axis pointing in the direction of the collision. The corresponding vector can be expressed as

$$Z^\mu = \frac{1}{\sqrt{2p\cdot\bar{p}}}\left(p-\bar{p}\right)^\mu . \tag{5.5}$$

The remaining axes X and Y can be chosen arbitrarily.

A significant simplification of the cross-section formula can be achieved if one expresses the hard part using momenta in the center-of-mass frames of the produced boson, which will be presented now. In the rest frame of the produced boson W_i, the vector Z_i is defined by

$$Z_i^\mu = \frac{1}{2}\sqrt{Q_i^2 + q_i^2}\left[\frac{p^\mu}{p\cdot q_i} - \frac{\bar{p}^\mu}{\bar{p}\cdot q_i}\right]^\mu , \tag{5.6}$$

and X_i is obtained by transforming the vector X according to

$$X_i^\mu = \frac{1}{\sqrt{1 + \left(X\cdot q_i\right)^2/Q_i^2}}\left[X^\mu - \frac{X\cdot q_i}{Q_i^2}q_i^\mu\right] . \tag{5.7}$$

Notice that replacing X_i with the vector X results in corrections of order $\mathbf{q}_i^2/Q_i^2$, which in the considered regime is a subleading term. Polar and azimuthal angles θ_i and ϕ_i of the momentum of lepton l_i in the rest frame of the decaying boson W_i are defined with respect to Z_i and X_i as shown in Fig. 5.2. For the antilepton, one defines those angles with respect to minus its momentum, as indicated by the dashed line in the figure.

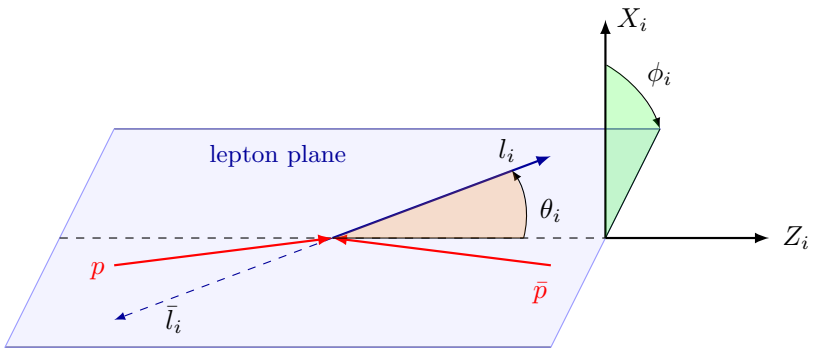

Figure 5.2: Definitions of the lepton's decay angles in the rest frame of the corresponding W boson. Red arrows represent the momenta of the incoming protons. The Z_i axis is the collision axis, and it bisects the angle between the spatial components of the protons' momenta p and $-\bar{p}$. The axis X_i is defined with respect to some fixed spatial direction, and in general, the protons' momenta are not contained in the X_iZ_i plane. The polar angle θ_i is defined with respect to the Z_i axis, and the azimuthal angle ϕ_i with respect to X_i. In the case of antilepton production, the angles are defined using minus its momentum, as represented in the picture.

5.1.2 Differential cross-section formula

The fully differential cross section of W pairs production via Drell-Yan depends on momenta fractions $x_{1,2}, \bar{x}_{1,2}$ of the active partons, transverse momenta of produced

bosons $\mathbf{q}_{1,2}$, and the decay angles of the leptons discussed in Section 5.1.1. The differential cross-section is written as

$$\frac{d\sigma^{\rm DPS}}{\prod_i dx_i d\bar{x}_i d\mathbf{q}_i d\Omega_i} = \frac{1}{C}\sum_{a_{1,\dots,4}}\sum_{R_1R_2=11,88}\frac{d\hat{\sigma}_{a_1a_3}}{d\Omega_1}\frac{d\hat{\sigma}_{a_2a_4}}{d\Omega_2} \int\frac{d^2\mathbf{z}_1}{(2\pi)^2}e^{-i\mathbf{z}_1\mathbf{q}_1}\int\frac{d^2\mathbf{z}_2}{(2\pi)^2}e^{-i\mathbf{z}_2\mathbf{q}_2}\int d^2\mathbf{y}\,{}^{R_1R_2}F_{a_1a_2}\,{}^{R_1R_2}\bar{F}_{a_3a_4}\,, \tag{5.8}$$

where $d\Omega_i = d(\cos\theta_i)\,d\phi_i$.
The partonic cross-section can be decomposed into 2 parts, as explained in Section 3.2 in [54]:

$$\frac{d\hat{\sigma}_{a_1a_2}}{d\Omega} = \big(1+\cos^2(\theta)\big)K_{a_1a_2}(Q) + 2\cos(\theta)K'_{a_1a_2}(Q)\,. \tag{5.9}$$

Using the relations between K and K' for all of the considered polarizations, as discussed in [53, 54], one obtains a significant simplification of Formula (5.8):

$$\begin{aligned}
&\frac{d\sigma^{\rm DPS}}{\prod_{i=1,2} dx_i d\bar{x}_i d^2\mathbf{q}_i d\Omega_i} \\
&= \frac{1}{C}\sum_{RR=11,88}\sum_{q_1,\dots,q_4}K_{q_1\bar{q}_3}(Q_1)K_{q_2\bar{q}_4}(Q_2)\int\frac{d^2\mathbf{z}_1}{(2\pi)^2}\int\frac{d^2\mathbf{z}_1}{(2\pi)^2}e^{-i\mathbf{z}_1\mathbf{q}_1-i\mathbf{z}_2\mathbf{q}_2}\int d^2\mathbf{y} \\
&\times\Big\{(1+\cos\theta_1)^2\,(1+\cos\theta_2)^2 \\
&\quad\times\big(F_{q_1q_2}+F_{\Delta q_1\Delta q_2}-F_{q_1\Delta q_2}-F_{\Delta q_1 q_2}\big)\big(\bar{F}_{\bar{q}_3\bar{q}_4}+\bar{F}_{\Delta\bar{q}_3\Delta\bar{q}_4}-\bar{F}_{\bar{q}_3\Delta\bar{q}_4}-\bar{F}_{\Delta\bar{q}_3\bar{q}_4}\big) \\
&+(1+\cos\theta_1)^2\,(1-\cos\theta_2)^2 \\
&\quad\times\big(F_{q_1\bar{q}_4}-F_{\Delta q_1\Delta\bar{q}_4}+F_{q_1\Delta\bar{q}_4}-F_{\Delta q_1\bar{q}_4}\big)\big(\bar{F}_{\bar{q}_3q_2}-\bar{F}_{\Delta\bar{q}_3\Delta q_2}+\bar{F}_{\bar{q}_3\Delta q_2}-\bar{F}_{\Delta\bar{q}_3 q_2}\big) \\
&+(1-\cos\theta_1)^2\,(1+\cos\theta_2)^2 \\
&\quad\times\big(F_{\bar{q}_3q_2}-F_{\Delta\bar{q}_3\Delta q_2}-F_{\bar{q}_3\Delta q_2}+F_{\Delta\bar{q}_3 q_2}\big)\big(\bar{F}_{q_1\bar{q}_4}-\bar{F}_{\Delta q_1\Delta\bar{q}_4}-\bar{F}_{q_1\Delta\bar{q}_4}+\bar{F}_{\Delta q_1\bar{q}_4}\big) \\
&+(1-\cos\theta_1)^2\,(1-\cos\theta_2)^2 \\
&\quad\times\big(F_{\bar{q}_3\bar{q}_4}+F_{\Delta\bar{q}_3\Delta\bar{q}_4}+F_{\bar{q}_3\Delta\bar{q}_4}+F_{\Delta\bar{q}_3\bar{q}_4}\big)\big(\bar{F}_{q_1q_2}+\bar{F}_{\Delta q_1\Delta q_2}+\bar{F}_{q_1\Delta q_2}+\bar{F}_{\Delta q_1 q_2}\big)\Big\}\,,
\end{aligned} \tag{5.10}$$

where we omit the color labels in DTMDs. $q_1,\dots,q_4$ are active quark flavors. The hard scattering factors $K_{a_1a_2}$ are given in App. E. Depending on the signs of $\cos\theta_{1,2}$, we

group the Eq. (5.90) into 4 parts:

$$\frac{d\sigma}{\prod_{i=1,2} dx_i d\bar{x}_i d^2\mathbf{q}_i d\Omega_i} = \int \frac{d^2\mathbf{z}_1}{(2\pi)^2} \int \frac{d^2\mathbf{z}_1}{(2\pi)^2} e^{-i\mathbf{z}_1\mathbf{q}_1 - i\mathbf{z}_2\mathbf{q}_2} \int d^2\mathbf{y} \sum_{\sigma_{1,2}=\pm 1} \big(1+\sigma_1\cos\theta_1\big)^2 \big(1+\sigma_2\cos\theta_2\big)^2 w_{\sigma_1\sigma_2}\big(\mathbf{z}_1,\mathbf{z}_2,\mathbf{y}\big) \,. \tag{5.11}$$

The functions $w_{\sigma_1\sigma_2}$ are defined as

$$w_{\sigma_1\sigma_2}\big(\mathbf{z}_1,\mathbf{z}_2,\mathbf{y}\big) = \frac{1}{C} \sum_{RR=11,88} \sum_{q_1,\ldots,q_4} K_{q_1\bar{q}_3}(Q_1) K_{q_2\bar{q}_4}(Q_2) \times \text{DTMD product} \,. \tag{5.12}$$

The DTMD product for a fixed $\sigma_1\sigma_2$ pair can be read off from Eq. (5.10). Dependence on arguments other than the distances $\mathbf{z}_i, \mathbf{y}$ in parenthesis is omitted. The integration over $d^2\mathbf{y}$ for the large-$\mathbf{y}$ part is straightforward. For the short-distance part more care is needed because of the short-distance cut-offs – it is discussed in more detail in Section 5.4.1.

In the following part we will denote the length of a given transverse vector $\mathbf{b}$ using b instead of $|\mathbf{b}|$. Let us define functions $W_{\sigma_1\sigma_2}$ as

- for large-y:

$$W_{\sigma_1\sigma_2}(\mathbf{z}_1,\mathbf{z}_2) = \frac{z_1 z_2}{(2\pi)^2} \int d^2\mathbf{y}\, w_{\sigma_1\sigma_2}\big(\mathbf{z}_1,\mathbf{z}_2,\mathbf{y}\big) \Phi^2(\mathbf{y})\, \Sigma_\delta\big(y, \max(z_1,z_2)\big) \,,$$

- for short-distance:

$$W_{\sigma_1\sigma_2}(\mathbf{z}_1,\mathbf{z}_2) = \frac{z_1 z_2}{(2\pi)^2} \int d^2\mathbf{y}\, w_{\sigma_1\sigma_2}\big(\mathbf{z}_1,\mathbf{z}_2,\mathbf{y}\big) \Phi(\mathbf{y}_+)\Phi(\mathbf{y}_-) \Big(1 - \Sigma_\delta\big(y, \max(z_1,z_2)\big)\Big) \,. \tag{5.13}$$

Σ_δ is used to interpolate between the two regimes. $\Phi(\mathbf{y}), \Phi(\mathbf{y}_\pm)$ are the short-distance cut-off functions used in the DGS subtraction scheme [69]. In this work, we take

$$\Phi(\mathbf{y}) = \theta\big(|\mathbf{y}| - y_{\text{cut}}\big) \,, \tag{5.14}$$

where $\theta(x)$ is a step function. The cut-off y_{cut} is taken equal to $b_{\min} = b_0/M_W$ in the large-y part. In the short-distance part it is varied, as will be described in Section 5.4.

The computation of oscillatory integrals over $d^2\mathbf{z}_i$ is performed by expressing them in terms of Hankel transforms. For the integrals in the large-$\mathbf{y}$ region there is no angular dependence in $W_{\sigma_1\sigma_2}$, and one can perform the angular integrals in $d^2\mathbf{z}_i$ analytically, and obtains

$$(5.11)\Big|_{\text{large-y}} = \int_0^\infty dz_1 \int_0^\infty dz_2\, J_0(q_1 z_1)\, J_0(q_2 z_2) \sum_{\sigma_{1,2}=\pm 1} \big(1+\sigma_1\cos\theta_1\big)^2 \big(1+\sigma_2\cos\theta_2\big)^2 W_{\sigma_1\sigma_2}(\mathbf{z}_1,\mathbf{z}_2) \,. \tag{5.15}$$

On the other hand, in the short-distance region, one finds a non-trivial angular dependence of the $W_{\sigma_1\sigma_2}$ term, as already was indicated by results for short-distance DTMD in Section 4.3.

Due to rotation invariance, $W_{\sigma_1\sigma_2}$ depend only on the angle between $\mathbf{z}_1$ and $\mathbf{z}_2$. Defining the polar angles ϕ_{z_i} of the vectors $\mathbf{z}_i$ on the transverse plane with respect to some fixed axis we can write

$$W_{\sigma_1\sigma_2}(\mathbf{z}_1, \mathbf{z}_2) \;=\; W_{\sigma_1\sigma_2}\big(|\mathbf{z}_1|, |\mathbf{z}_2|, \phi_{z_1} - \phi_{z_2} \equiv \varphi_z\big)\,. \tag{5.16}$$

As will be shown in Section 5.4.1, $W_{\pm\pm}$ is an even function of the angle φ_z, hence one can expand

$$W_{\sigma_1\sigma_2}\big(|\mathbf{z}_1|, |\mathbf{z}_2|, \varphi_z\big) \;=\; \sum_{n=0} \cos(n\varphi_z)\, W_{\sigma_1\sigma_2,n}(z_1, z_2)\,. \tag{5.17}$$

Using the relation

$$\int_0^{2\pi} d\varphi_z\, e^{-iqz\cos\varphi_z}\, \cos(n\varphi_z) \;=\; 2\pi(-i)^n\, J_n(qz)\,, \tag{5.18}$$

we obtain the expansion in the following form

$$\begin{aligned}(5.11)\Big|_{\text{short-dist.}} \;=\; &\sum_{n=0}^{\infty} \cos\big(n(\phi_{q_1} - \phi_{q_2})\big)(-1)^n \int_0^{\infty} dz_1 \int_0^{\infty} dz_2\, J_n(q_1 z_1)\, J_n(q_2 z_2) \\ &\times \sum_{\sigma_{1,2}=\pm 1} \big(1 + \sigma_1 \cos\theta_1\big)^2 \big(1 + \sigma_2 \cos\theta_2\big)^2\, W_{\sigma_1\sigma_2,n}(z_1, z_2)\,. \end{aligned} \tag{5.19}$$

As will be shown in Section 5.5.2, the expansion (5.19) converges slowly with higher Fourier modes, at least for opposite-sign W production. While the presented formula might not be the most efficient way of determining the total angular dependence of the cross-section, it allows us to compute the first Fourier modes with respect to the angle between $\mathbf{q}_1, \mathbf{q}_2$. In particular, the 0-th mode allows us to make a comparison in size with the large-$\mathbf{y}$ contribution, and analyze the effects of interpolation described in Section 5.2.1.

The double Bessel integrals (called also double Hankel transform) as presented in Eqs. (5.15) and (5.19) are computed using the modified Levin's method described in Section 2.5.2.

Switching variables from $(x, \bar{x})$ to (Y, Q).
While the cross-section is conveniently computed using partons' momenta fractions $x_i, \bar{x}_i$, the phenomenological analysis is easier performed in terms of the rapidity of a produced boson, denoted Y_i, and its momentum Q_i. These variables are related by

$$Q_i^2 \;=\; x_i \bar{x}_i s\,, \tag{5.20}$$

$$x_i \;=\; \frac{Q_i}{\sqrt{s}}\, e^{Y_i}\,, \quad \bar{x}_i \;=\; \frac{Q_i}{\sqrt{s}}\, e^{-Y_i}\,. \tag{5.21}$$

The Jacobian of the variable transformation is

$$\frac{\partial(x_i, \bar{x}_i)}{\partial(Q_i, Y_i)} = \frac{2x_i\bar{x}_i}{Q_i} \,, \tag{5.22}$$

so that

$$\frac{d\sigma}{\prod_{i=1,2} dQ_i dY_i} = \frac{4x_1\bar{x}_1x_2\bar{x}_2}{Q_1Q_2} \frac{d\sigma}{\prod_{i=1,2} dx_i d\bar{x}_i}\Big|_{x_i,\bar{x} \text{ given by (5.21)}} \,. \tag{5.23}$$

Integration over dQ_i

The hard scattering cross-section depends on Q_i via the propagator

$$\propto \frac{1}{\left(Q_i^2 - M_W^2\right)^2 + M_W^2\Gamma_W^2} \,. \tag{5.24}$$

Using the narrow-width approximation, one takes

$$\frac{1}{(Q^2 - M_W^2)^2 - \Gamma_W^2 M_W^2} \approx \frac{\pi}{2}\frac{1}{\Gamma_W M_W^2}\delta(Q - M_W) \,, \tag{5.25}$$

so that

$$\sigma \approx \left(\frac{\pi}{2}\Gamma_W\right)^2 \times \frac{d\sigma}{dQ_1 dQ_2}\Big|_{Q_1=Q_2=M_W} \,. \tag{5.26}$$

Integration over $d\Omega_i$

There is no dependence on the leptonic polar angle, so the integration simply produces a factor of 2π.

The integration over $d\cos\theta_i$ gives the same result for all combination of signs of $\cos\theta_i$ as given in Formula (5.10), since

$$\int_{-1}^{1} d\cos\theta \left(1 \pm \cos\theta\right)^2 = \frac{8}{3} \,. \tag{5.27}$$

Hence, the cross-section integrated over leptonic angles reads

$$\begin{aligned}\frac{d\sigma}{\prod_i dQ_i dY_i d^2\mathbf{q}_i} = &\left(\frac{16\pi}{3}\right)^2 \sum_{n=0}^{\infty} \cos\left(n(\phi_{q_1} - \phi_{q_2})\right)(-1)^n \\ &\times \int_0^\infty dz_1 \int_0^\infty dz_2 \, J_n(q_1 z_1) \, J_n(q_2 z_2) \sum_{\sigma_{1,2}=\pm 1} W_{\sigma_1\sigma_2,n}(z_1, z_2) \,.\end{aligned} \tag{5.28}$$

Integration over $d^2\mathbf{q}_i$
Since in the region of $|\mathbf{q}| \sim Q$ the TMD-factorization breaks, one cannot integrate to arbitrarily large transverse momenta. Instead, we will consider the cross section integrated up to some maximal value $q_{\max} \geq |\mathbf{q}_i|$. Integration over the angular coordinates of $\mathbf{q}_{1,2}$ leads to the vanishing of the higher Fourier modes $n \geq 1$ in Eq. (5.19), so we need to consider only the integrals involving Bessel functions J_0. Applying the relation

$$\int d^2q\, J_0(qz) \;=\; \frac{2\pi}{z} q\, J_1(qz)\,, \tag{5.29}$$

to either Eq. (5.15) or (5.19) we obtain

$$\begin{aligned}\frac{d\sigma}{dq_1 dY_1 dY_2}\Big|_{q_2\leq q_{max}} \;&=\; \frac{4x_1x_2\bar{x}_1\bar{x}_2}{Q_1Q_2}\Big(\frac{16\pi}{3}\Big)^2(2\pi)^2\,\Big(\frac{\pi}{2}\Gamma_W\Big)^2 \\ &\times\; q_{\max}\int dz_1\, J_0(q_1z_1)\int dz_2\, J_1(q_{\max}z_2)\sum_{\sigma_{1,2}=\pm1}\frac{1}{z_2}W_{\sigma_1\sigma_2,0}(z_1,z_2)\,,\end{aligned} \tag{5.30}$$

$$\begin{aligned}\frac{d\sigma}{dY_1 dY_2}\Big|_{q_1,q_2\leq q_{max}} \;&=\; \frac{4x_1x_2\bar{x}_1\bar{x}_2}{Q_1Q_2}\Big(\frac{16\pi}{3}\Big)^2(2\pi)^2\,\Big(\frac{\pi}{2}\Gamma_W\Big)^2 \\ &\times\; q_{\max}^2\int dz_1\, J_1(q_{\max}z_1)\int dz_2\, J_1(q_{\max}z_2)\sum_{\sigma_{1,2}=\pm1}\frac{1}{z_1z_2}W_{\sigma_1\sigma_2,0}(z_1,z_2)\,,\end{aligned} \tag{5.31}$$

where we recall that $q_i = |\mathbf{q}_i|$.

5.2 Non-perturbative input

Before proceeding, let us discuss the nonperturbative input that needs to be independently modeled. This will not include the parametrization of the collinear double parton distributions – we assume them to be *given* at the initial scales, and the uncertainties due to DPDF modeling, other than from the Collins-Soper kernel, are not included in this work.

5.2.1 Interpolating between two DTMD approximations

Approximations of DTMDs presented in Chapters 3 and 4 are valid in two regions:

- Perturbative DPDF-DTMD matching for $|\mathbf{y}| \gg |\mathbf{z}_i|, \quad |\mathbf{z}_i| \ll \Lambda^{-1}$,
- Short-distance expansion for $|\mathbf{y}| \sim |\mathbf{z}_i| \ll \Lambda^{-1}$.

There arise two natural questions:

1. There exists an overlap region, where all distances are perturbatively small, but $|\mathbf{y}|$ is still much larger than $|\mathbf{z}_i|$ – in this case, both approximations described in Chapters 3 and 4 are valid. How to interpolate in that case?

2. In both regions it is assumed that $\mathbf{z}_i$ is perturbatively small. How to extrapolate to larger distances, and in particular, how to combine the extrapolated large-$\mathbf{y}$ and short-distance terms?

Our interpolation scheme will be constructed using two variables: $y = |\mathbf{y}|$, and the largest value of the pair $|\mathbf{z}_1|, |\mathbf{z}_2|$, denoted as

$$z \;=\; \max\big(|\mathbf{z}_1|,\, |\mathbf{z}_2|\big)\,. \tag{5.32}$$

Let us describe the construction of the interpolation scheme on the $y \times z$ plane used in this work. This will be done in 3 steps – first, we will discuss the case when at least one of the discussed expressions for DTMD can be treated as not extrapolated. Then, we consider the case where z is still perturbative, but the assumptions necessary for both approximations break. Finally, we extend the interpolation scheme to the remainder of the phase space.

Non-extrapolated approximation
First, we will establish in which regions the considered approximations may be regarded as valid and not requiring extrapolation. The obvious bound for both large-$\mathbf{y}$ and short-distance approximations is

$$z \leq b_{\max}\,, \tag{5.33}$$

where

$$b_{\max} = \frac{1}{2} b_0 \,\mathrm{GeV}^{-1} \approx 0.56\,\mathrm{GeV}^{-1}\,. \tag{5.34}$$

Let us choose a parameter δ such that

$$0 \;<\; \delta \;<\; \frac{1}{2}\,. \tag{5.35}$$

We shall use the large-y approximation, whenever

$$\delta\, y \;\geq\; z\,, \tag{5.36}$$

even for nonperturbatively large z – in that case we extrapolate DTMDs according to Section 3.5.

In the computation of the short-distance term, one encounters distance combinations $\mathbf{y}_\pm, \mathbf{v}_\pm$ defined in Section 4.1.1, which should be no larger than $b_{\max}$ for the perturbative expansion to be valid. It is easy to check that if

$$y + \frac{1}{2} z > b_{\max} \qquad \Longrightarrow \qquad z > 2\big(b_{\max} - y\big)\,, \tag{5.37}$$

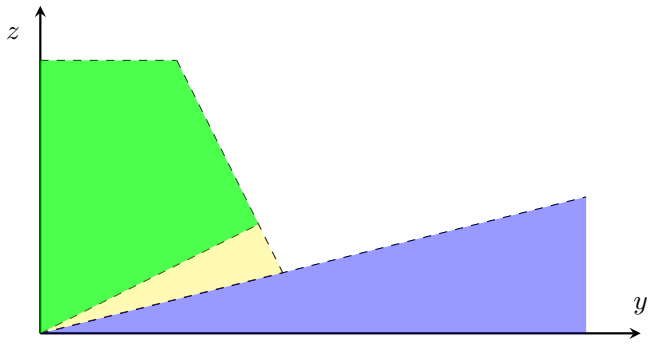

Figure 5.3: Partition of the $y \times z$ plane in the region – first step. Green color corresponds to the short-distance approximation, blue to the large-y, and in the yellow triangle one interpolates between the two formulas.

then for any value of the angle φ_z, defined in Eqs. (4.13), there exist such values of φ_y, see Eq. (4.16), that at least one of the distances $\mathbf{y}_\pm, \mathbf{v}_\pm$ becomes larger than $b_{\max}$. To see this, notice that if at least one of $\mathbf{z}_1, \mathbf{z}_2$ is larger than z, then the length of one of the combinations $\mathbf{z}_\pm$ must be at least as large as $z/2$, which follows from triangle inequality $|\mathbf{z}_+| + |\mathbf{z}_-| \geq |\mathbf{z}_{1,2}|$. Then, by taking $\mathbf{y}$ parallel to $\mathbf{z}_+$ or $\mathbf{z}_-$ one gets the required result. For this reason, the necessary condition for the short-distance expansion to be valid is

$$z \;\leq\; b_{\max} \quad \text{and} \quad z \leq 2\big(b_{\max} - y\big)\,. \tag{5.38}$$

Notice that this is a *necessary*, but not *sufficient* condition – even if Eq. (5.38) is fulfilled, there still may exist such angular configurations that some of the discussed distances become large. However, including such a situation in the interpolation scheme would require constructing an interpolating function depending on all components of $\mathbf{z}_1, \mathbf{z}_2, \mathbf{y}$, which would greatly complicate the computation.

Inside of the region of such (y, z) that fulfill Eq. (5.38), we will use only the short-distance approximation of DTMDs, if

$$z \;\leq\; \frac{1}{2} y\,. \tag{5.39}$$

For the intermediate y in this region, which is too small to use the large-y approximation only, that is

$$\delta y \;< z \;<\; \frac{1}{2} y\,, \tag{5.40}$$

we will interpolate between the two DTMD forms. In Fig. 5.3 we present the division of the $y \times z$ plane defined so far.

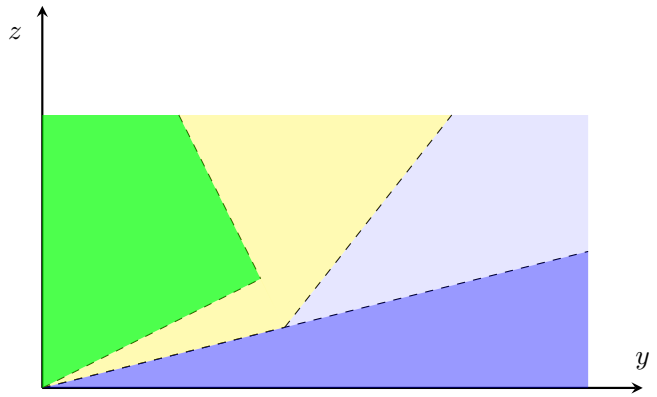

Figure 5.4: Partition of the $y \times z$ plane in the region – second step. The lighter blue color indicates that in the corresponding region one uses the large-y form of DTMD, despite the fact that $\delta\, y \leq z$, that is outside of the primary region of the validity of the approximation.

Perturbative z

In the next step, we consider the region of perturbative $z \leq b_{\max}$, where the assumptions of both of the described approximations of DTMD are not valid, so that neither Eq. (5.36) or (5.38) applies. We continue the construction of the interpolating function by defining the boundaries of the regions, where only one DTMD form is used – for reference see Fig. 5.4. It is straightforward for the short-distance region (in green), defined already in the previous step by Eq. (5.38). On the other hand, limiting the large-y region to $\delta y > z$ up to $z \leq b_{\max}$ would require using the extrapolated short-distance form for y as large as $\frac{1}{\delta} b_{\max} > 1\,\mathrm{GeV}^{-1}$. To avoid this, we will construct the interpolation region in such a way that for

$$y \geq \frac{3}{2} b_{\max} = \frac{3}{4} b_0 \approx 0.84\ \mathrm{GeV}^{-1} \tag{5.41}$$

we use only the large-**y** approximation, possibly extrapolated in $\mathbf{z}_i$. The "large-**y**" condition $\delta y > z$ in Eq. (5.36) was applied in the region defined by Eq. (5.38), where *also* the short-distance approximation is valid. For (z, y) outside of the perturbative region, we relax this condition by applying the "large-y" approximation for

$$\left(y - \frac{2b_{\max}}{2+\delta}\right)\left(1 - \frac{2b_{\max}\delta}{2+\delta}\right) \geq \left(z - \frac{2\delta b_{\max}}{2+\delta}\right)\left(\frac{3}{2} - \frac{2b_{\max}}{2+\delta}\right), \tag{5.42}$$

if Eq. (5.38) is not fulfilled and $z < b_{\max}$. It is chosen in such way, that for $z = b_{\max}$ one uses only the large-y form of DTMDs already at $y \geq \frac{3}{2} b_{\max}$. The resulting shape of the interpolation region constructed so far is presented in Fig. 5.4.

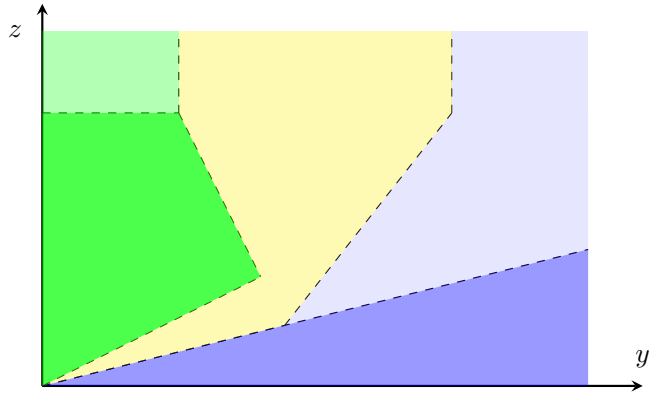

Figure 5.5: Interpolation between the short-distance and large-**y** approximations of DTMDs used in the computation of differential cross-section of W pairs production. Green (blue) colors correspond to the regions when we use exclusively the short-distance (large-**y**) form of DTMDs. Lighter colors are used to indicate that in some regions the approximations are no longer strictly valid, and one needs to extrapolate in $\mathbf{z}_i$. In the yellow region we interpolate between the two (possibly extrapolated) DTMD approximations.

The remaining part

Finally, to extend the discussed interpolation scheme to larger values of z, we take the following division of the phase space:

$$\text{if } \max(z_1, z_2) \geq b_{\max}: \quad \begin{cases} \text{large-}\mathbf{y} & \text{for} \quad y \geq \frac{3}{2} b_{\max} \\ \text{short-distance} & \text{for} \quad y \leq \frac{1}{2} b_{\max} \\ \text{interpolate} & \text{for} \quad \frac{1}{2} b_{\max} < y < \frac{3}{2} b_{\max} \end{cases} . \tag{5.43}$$

The resulting phase space is represented in Fig. 5.5.

Interpolating function

As seen in Fig. 5.5, for a fixed value of z there exist a pair of limiting values $y_L(z)$, $y_R(z)$ that on the right of y_R one uses only the large-y model, while for $y < y_L$ only the short-distance part. Let us define the interpolating function Σ_δ (depending on a parameter δ) according to

$$\Sigma_\delta(y, z) = \begin{cases} 1 & y \geq y_R(z)\,, \\ 0 & y \leq y_L(z)\,, \\ \rho\left(\frac{y - y_L}{y_R - y_L}\right) & y_L < y < y_R\,. \end{cases} \tag{5.44}$$

The profile function $\rho(x)$ should be such that $\rho(x) = 0$ for $x = 0$, and $\rho(x) = 1$ for $x = 1$. Additionally, we require that the first and second derivatives vanish at the

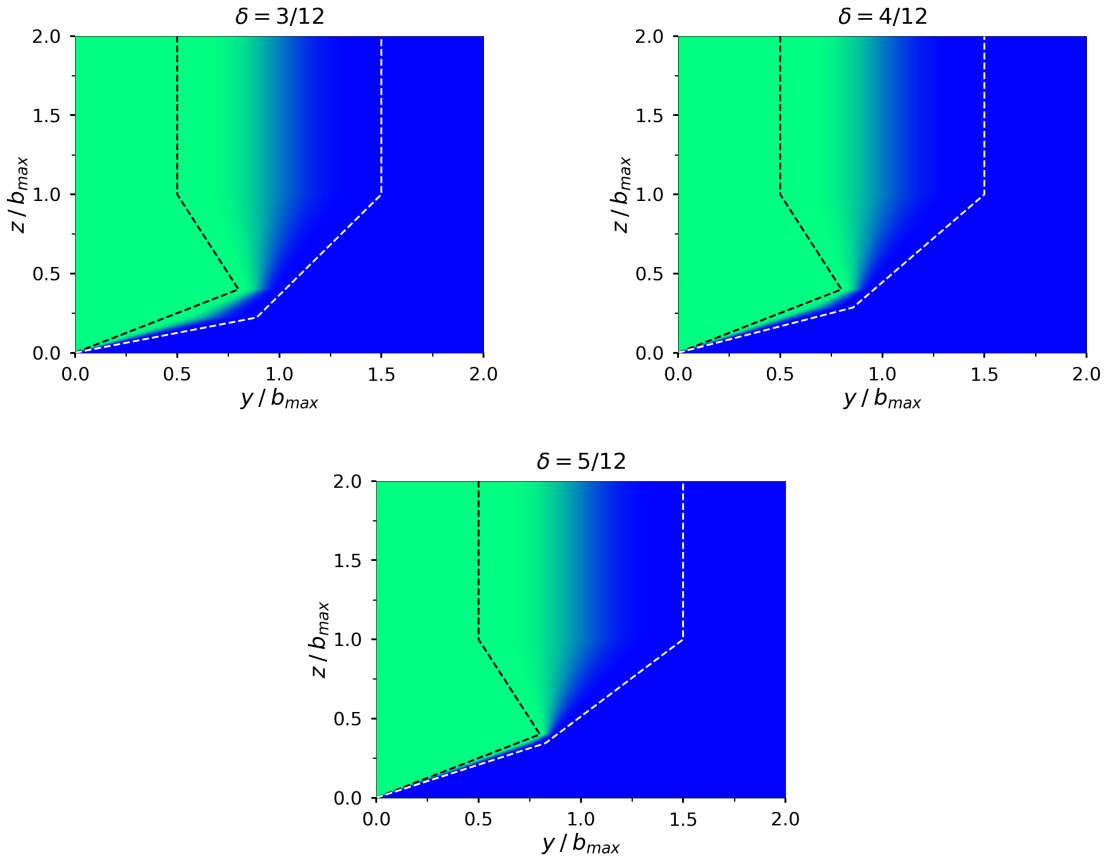

Figure 5.6: Function interpolating between the large-**y** and short-distance approximation of DTMD on the $y \times z$ plane for the parameter $\delta \in \left\{\frac{3}{12}, \frac{4}{12}, \frac{5}{12}\right\}$. In the region on the right of the white line (in blue), one uses only the large-y approximation, while on the left of the black line (green region) – only the short-distance DTMD form.

endpoints. Our choice is

$$\rho(u) \;=\; \sin^2\left(\frac{\pi}{2}\sin^2\left(\pi x/2\right)\right). \tag{5.45}$$

Let us notice that at fixed z the interpolating function is equal to $\frac{1}{2}$ at $y = \frac{1}{2}(y_L + y_R)$, that is for y exactly in the middle of y_L and y_R. The cut-off functions Σ_δ on the $y \times z$ plane for the values of δ considered in this analysis, which are

$$\delta \in \left\{\frac{3}{12}, \frac{4}{12}, \frac{5}{12}\right\}, \tag{5.46}$$

are shown in Fig. 5.6.

5.2.2 Collins-Soper kernel at large distances

In this work, we consider a collection of Collins-Soper kernels: ${}^{R}K_a$, ${}^{R}J$ for $|\mathbf{y}| \gg |\mathbf{z}_i|$, and ${}^{R_1R_2R_1'R_2'}K_q(\mathbf{z}_i, \mathbf{y})$ for short distances, which govern the rapidity evolution of both DTMDs and DPDFs, as described in Sections 2.3.4 and 2.3.5. The experimental data is available only for the singlet quark kernel ${}^{1}K_q$ [86–88, 104], and recently the extraction of the kernel from the lattice data also have been analyzed [105–107].

We build the Ansatz for all of the kernels based on two remarkable properties of perturbative QCD, which hold up to $\mathcal{O}(\alpha_S^2)$ [108, 109].

- The large-$\mathbf{y}$ kernels can be written using the 'color-stripped' kernel K_0, defined by the relation:

$$K_0^{pt}\big(\mathbf{b};\mu\big) = \frac{1}{C_F}\,{}^{1}K_q^{pt}\big(\mathbf{b};\mu\big)\,, \tag{5.47}$$

  as:

$$\begin{aligned}
&{}^{8}K_q^{pt}\big(\mathbf{b};\mu\big) = -\frac{1}{2N}K_0^{pt}\big(\mathbf{b};\mu\big)\,,\\
&{}^{R}K_g^{pt}\big(\mathbf{b};\mu\big) = c_g(R)\,K_0^{pt}\big(\mathbf{b};\mu\big)\,,\\
&\qquad c_g(A) = c_g(S) = \frac{N}{2}, \quad c_g(10) = 0, \quad c_g(27) = -1\,,\\
&{}^{8}J^{pt}\big(\mathbf{b};\mu_1,\mu_2\big) = \frac{N}{2}\Big(K_0^{pt}\big(\mathbf{b};\mu_1\big) + K_0^{pt}\big(\mathbf{b};\mu_2\big)\Big)\,,\\
&{}^{R}J^{pt}\big(\mathbf{b};\mu_1,\mu_2\big) = c_J(R)\,{}^{8}J^{pt}\big(\mathbf{b};\mu_1,\mu_2\big)\,,\\
&\qquad c_J(8) = \frac{N}{2}, \quad c_J(10) = 3, \quad c_J(27) = 4\,.
\end{aligned} \tag{5.48}$$

  This is often referred to as Casimir scaling [108, 109].

- The soft-factor, which has been computed perturbatively at small transverse distances up to NNLO, up to order α_S^2 depends solely on terms obtained from a gluon exchanged independently between pairs of Wilson lines [102], as in Fig. 5.7. Exchanges involving 3 Wilson lines cancel between graphs with different orientation of the Wilson lines, e.g. diagrams (a) and (b) in Fig. 5.7. At α_S^3 a new type of correction appears due to graphs connecting 4 Wilson lines (quadruple terms), see Fig. 5.7, graph (c).

  Hence, the short-distance DTMD Collins-Soper kernel can be written up to α_S^2 using the kernels $K_0(\mathbf{b};\mu)$ depending on a single interparton distance as in

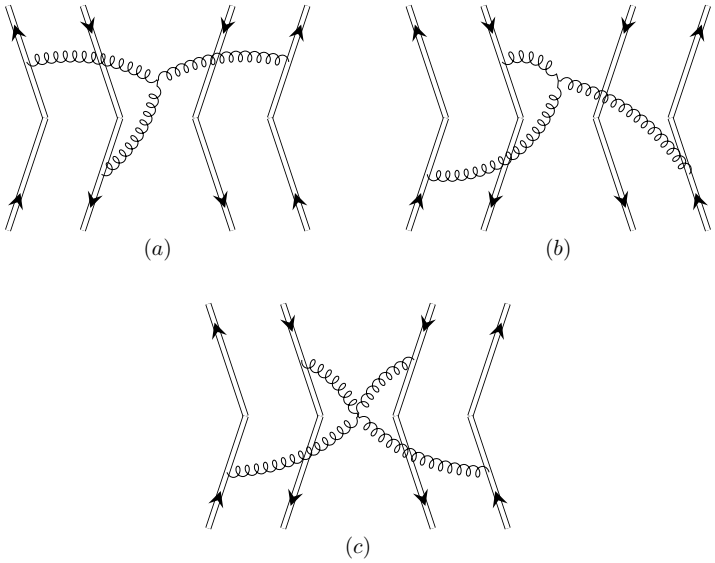

Figure 5.7: Feynman graphs relevant for the short-distance Collins-Soper kernel for DPDs. For simplicity, we do not draw the cut line in the middle. (a) and (b) cancel due to opposite signs. (c) is the example of a lowest-order contribution that cannot be described in terms of the kernels K_0 defined in (5.47).

Eqs. (5.49)-(5.50).

$$K_{qq}^{pt}(\mathbf{z}_i, \mathbf{y}; \mu) = C_F \left({}^1K^{pt}(\mathbf{z}_1; \mu) + {}^1K^{pt}(\mathbf{z}_2; \mu) \right) \begin{pmatrix} 1 & 0 \\ 0 & 1 \end{pmatrix} + \begin{pmatrix} 0 & \frac{\sqrt{N^2-1}}{2N} K_d \\ \frac{\sqrt{N^2-1}}{2N} K_d & -\frac{N}{2} K_y - \frac{1}{N} K_d \end{pmatrix} , \tag{5.49}$$

where we recall from Section 4.2 that

$$\begin{aligned} K_d^{pt} &= K_0^{pt}(\mathbf{v}_+; \mu) + K_0^{pt}(\mathbf{v}_-; \mu) - K_0^{pt}(\mathbf{y}_+; \mu) - K_0^{pt}(\mathbf{y}_-; \mu) , \\ K_y^{pt} &= K_0^{pt}(\mathbf{z}_1; \mu) + K_0^{pt}(\mathbf{z}_2; \mu) - K_0^{pt}(\mathbf{v}_+; \mu) - K_0^{pt}(\mathbf{v}_-; \mu) . \end{aligned} \tag{5.50}$$

Promoting the relations (5.48)-(5.49) to the full large-distance kernels (removing the index '*pt*'), one reduces the problem of extrapolating all of the kernels to just a single kernel.

The Ansatz for the singlet quark Collins-Soper kernel used to construct the remaining ones using the discussed relations is given by

$${}^1K_q(\mathbf{b}; \mu) = {}^1K_q^{pt}(\mathbf{b}^*; \mu) + g(\mathbf{b}) , \tag{5.51}$$

where $g(\mathbf{b})$ is the nonperturbative part. The perturbative part at regularized distance $\mathbf{b}^*$ and arbitrary scale μ is obtained by first computing the fixed-order perturbative expression at the $\mathbf{b}^*$-dependent scale $\mu_{\mathbf{b}^*}$, and then evolving to the scale μ using the RGE equation of the Collins-Soper kernel:

$$ {}^1K_q^{pt}(\mathbf{b}^*;\mu) = {}^1K_q^{pt}(\mathbf{b}^*;\mu_{\mathbf{b}^*}) - \int_{\mu_{\mathbf{b}^*}}^{\mu} \frac{d\mu'}{\mu'}\, {}^1\gamma_{K,q}(\mu') \,. \tag{5.52} $$

The Collins-Soper kernels and their anomalous dimensions are given in App. B.

The results of the fits of $g(\mathbf{b})$, together with the formulas for the *-prescription used in the cited works are summarized below:

$$ \begin{aligned} &\text{DPT24} \qquad g(\mathbf{b}) = -\frac{1.89}{2}\, f\!\left(\frac{0.094}{1.89}\ \text{GeV}^2\ \mathbf{b}^2 + \frac{0.007}{1.89}\ \text{GeV}^4\ \mathbf{b}^4\right) \\ &\qquad\qquad \mathbf{b}^*(\mathbf{b}) = b_0\, f\big(x + x^3/2 + 3x^5/8\big), \quad x = |\mathbf{b}|/b_0 \,, \\ &\qquad\qquad\quad \text{where } f(x) = x/\sqrt{1+x^2} \,. \end{aligned} \tag{5.53} $$

$$ \begin{aligned} &\text{ART23} \qquad g(\mathbf{b}) = -\left(0.074 + 0.116\ \log\frac{|\mathbf{b}^*|}{1.496\ \text{GeV}^{-1}}\right) \mathbf{b}\mathbf{b}^* \\ &\qquad\qquad \mathbf{b}^*(\mathbf{b}) = \frac{\mathbf{b}}{\sqrt{1 + \left(\mathbf{b}/1.496\ \text{GeV}^{-1}\right)^2}} \,, \end{aligned} \tag{5.54} $$

$$ \begin{aligned} &\text{MAP22} \qquad g(\mathbf{b}) = -0.031\, \mathbf{b}^2 \\ &\qquad\qquad \mathbf{b}^*(\mathbf{b}) = \frac{\mathbf{b}}{\sqrt{1 + \left(\mathbf{b}/1\ \text{GeV}^{-1}\right)^2}} \,, \end{aligned} \tag{5.55} $$

$$ \begin{aligned} &\text{SV19} \qquad g(\mathbf{b}) = -0.085\, \mathbf{b}\mathbf{b}^* \\ &\qquad\qquad \mathbf{b}^*(\mathbf{b}) = \frac{\mathbf{b}}{\sqrt{1 + \left(\mathbf{b}/1.93\ \text{GeV}^{-1}\right)^2}} \,, \end{aligned} \tag{5.56} $$

for reference see [86–89].

Let us recall that the $*$-prescription used in this work is given by

$$ \begin{aligned} \mathbf{b}^*(\mathbf{b}) \ &= \ \mathbf{b}\left(\frac{1 - \left(b_{\min}/|\mathbf{b}|\right)^4}{1 - \left(|\mathbf{b}|/b_{\max}\right)^4}\right)^{1/4} , \\ b_{\min} = \frac{b_0}{80.377\ \text{GeV}}, \quad & b_{\min} = \frac{1}{2} b_0\ \text{GeV}^{-1} \,. \end{aligned} \tag{5.57} $$

Therefore, to use the Ansatz for the Collins-Soper kernel consistent with the ones used in the cited works, we need to use function $g(\mathbf{b})$ modified to account for the different values of regularized distances computed using the *-prescription defined in the considered model $\mathbf{b}^*_{\text{model}}$, and the one used in this work, denoted as $\mathbf{b}^*$:

$$g(\mathbf{b}) \;=\; g_{\text{model}}(\mathbf{b}) \;+\; {}^1K^{pt}\big(\mathbf{b}^*_{\text{model}};\mu_{\mathbf{b}^*}\big) \;-\; {}^1K^{pt}\big(\mathbf{b}^*;\mu_{\mathbf{b}^*}\big)\,. \tag{5.58}$$

As discussed in Section 4.2, the perturbative part of the Collins-Soper kernel has a singularity at vanishing transverse distances. Since *-prescriptions used in the other works do not include the short-distance regularization, cf. Eqs. (5.53)-(5.56), using a *-prescription that is not regularized at small distances in Eq. (5.58) would introduce the logarithmic singularities in $g(\mathbf{b})$. To avoid it, for all distances $\mathbf{b}$ we replace the full Collins-Soper kernels $K(\mathbf{b})$ with the kernels computed at distances regularized at small values according to Eq. (4.42):

$$K\big(\mathbf{b}^*_{\text{UV}};\mu\big) = K^{pt}\big((\mathbf{b}^*_{\text{UV}})^*;\mu\big) + g(\mathbf{b}^*_{\text{UV}})\,. \tag{5.59}$$

We recall that $\mathbf{b}^*_{\text{UV}}(b)$ saturates at some minimal distance b_{min} as $|\mathbf{b}| \to 0$, and approaches $\mathbf{b}$ if the distance is large. Notice that the distance argument of K^{pt} is regularized twice – once only at short-distances using Eq. (4.42), and once using the *-prescription in Eq. (5.57).

Plots of kernels ${}^1K_q\big(\mathbf{b};\mu = 2\,\text{GeV}\big)$ for the considered models are shown in Fig. 5.8.

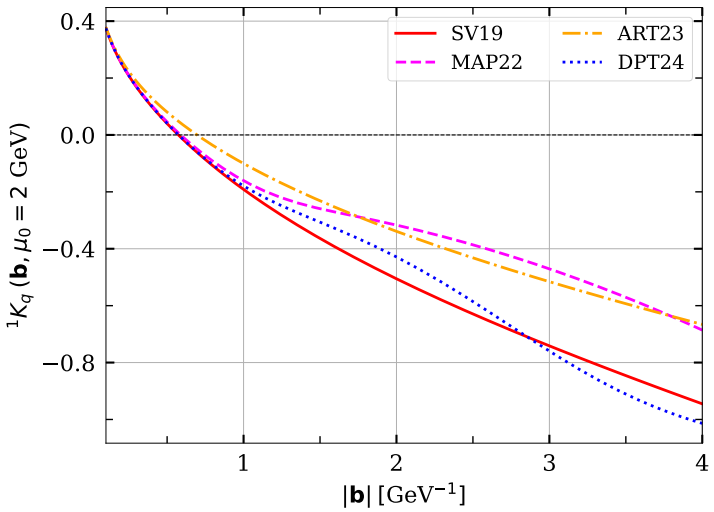

Figure 5.8: Collins-Soper kernel ${}^1K_q$ obtained using the considered models.

5.2.3 Extrapolation to large $\mathbf{z}_i$

In TMD literature, one extrapolates single parton densities according to

$$f_{\mathrm{TMD}}\big(x,\mathbf{z};\mu,\zeta\big) = \exp\left(K(\mathbf{z};\mu)\log\frac{\sqrt{\zeta}}{\sqrt{\zeta_0}}\right) f^{pt}_{\mathrm{TMD}}\big(x,\mathbf{z}^*;\mu,\zeta_0\big) \times f^{\mathrm{tmd}}_{\mathrm{NP}}(|\mathbf{z}|,x)\,. \tag{5.60}$$

f^{pt}_{TMD} denotes the TMD obtained by perturbative matching to a PDF. Assuming DTMDs as a product of ordinary TMDs multiplied by some $\mathbf{y}$-dependent function, in analogy to the DPDF product model, as described in Section 3.3, one would get the prefactor for double parton distributions F_{NP} in the form

$$F_{\mathrm{NP}}(\mathbf{z}_i,x_i) \;=\; f^{\mathrm{tmd}}_{\mathrm{NP}}(|\mathbf{z}_1|,x_1) \times f^{\mathrm{tmd}}_{\mathrm{NP}}(|\mathbf{z}_2|,x_2)\,. \tag{5.61}$$

In this analysis, we consider the simplest form of the nonperturbative prefactors that does not depend on the momenta fractions or the parton flavors:

$$F_{\mathrm{NP}}(\mathbf{z}_i;r) = \exp\left(-\frac{1}{2}(r\lambda)^2\big(\mathbf{z}_1^2+\mathbf{z}_2^2\big)\right), \tag{5.62}$$

with fixed value of λ, and parameter $r=\mathcal{O}(1)$ used to estimate how much the shape of the falloff actually affects the phenomenological predictions in the considered process. Therefore, the product of DTMDs appearing in the computation of the cross-section formula at large $\mathbf{z}_i$ will behave like

$$F\bar{F}\Big|_{\text{large }\mathbf{z}_i} \;\sim\; F_{\mathrm{NP}}(\mathbf{z}_i;r)^2 \;=\; \exp\Big(-(r\lambda)^2\times\big(\mathbf{z}_1^2+\mathbf{z}_2^2\big)\Big)\,. \tag{5.63}$$

To have some guidance from the results of TMD fits, we will compare the behavior of Eq. (5.63) with large-$\mathbf{z}$ asymptotics that one would get using the product Ansatz of Eq. (5.61), which is

$$F\bar{F}\Big|_{\text{large }\mathbf{z}_i,\,(5.61)} \;\sim\; \Big[f^{\mathrm{tmd}}_{\mathrm{NP}}(|\mathbf{z}_1|,x_1)f^{\mathrm{tmd}}_{\mathrm{NP}}(|\mathbf{z}_1|,\bar{x}_1)\Big]\times\Big[f^{\mathrm{tmd}}_{\mathrm{NP}}(|\mathbf{z}_2|,x_2)f^{\mathrm{tmd}}_{\mathrm{NP}}(|\mathbf{z}_2|,\bar{x}_2)\Big]\,. \tag{5.64}$$

Therefore, to make a connection between the simple Gaussian prefactor used in this analysis with the TMD product form, we need to compare

$$\exp\big(-(r\lambda)^2\,z^2\big) \quad \text{vs} \quad f^{\mathrm{tmd}}_{\mathrm{NP}}(z,x)f^{\mathrm{tmd}}_{\mathrm{NP}}(z,\bar{x})\,. \tag{5.65}$$

Let us take the rapidity-dependent momenta fractions corresponding to the production of W pairs at $\sqrt{s}=13$ TeV:

$$x=\frac{M_W}{13\text{ TeV}}e^{Y},\quad \bar{x}=\frac{M_W}{13\text{ TeV}}e^{-Y},\qquad \text{where}\quad \frac{M_W}{13\text{ TeV}}\approx 6.2\times10^{-3}\,. \tag{5.66}$$

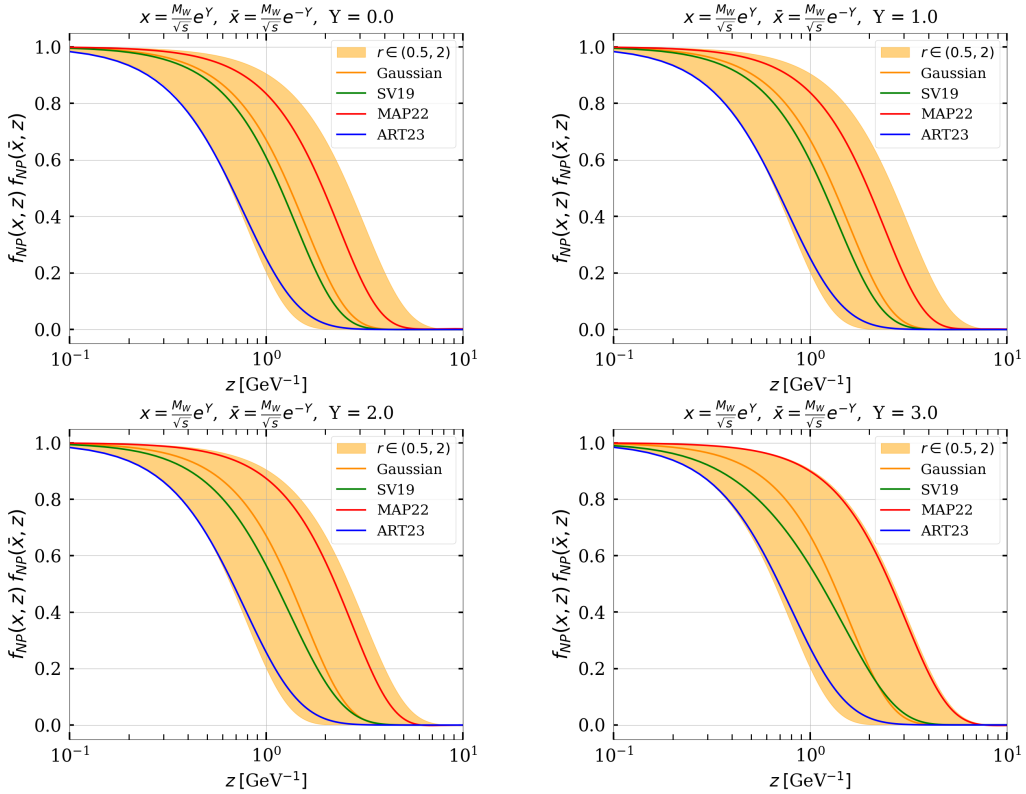

Figure 5.9: Comparison of falloff functions from different TMD models and the family of falloffs defined in Eq. (5.62).

Y is the value of the rapidity of the produced boson. In Fig. 5.9 there is shown a family of functions $\exp\big(-(r\lambda)^2\, z^2\big)$ for

$$\lambda^2 = 0.4\,, \quad r \in [0.5,\ 2]\,, \tag{5.67}$$

compared against a product of nonperturbative TMD factors $f_{\mathrm{NP}}^{\mathrm{tmd}}(z,x) f_{\mathrm{NP}}^{\mathrm{tmd}}(z,\bar{x})$ for different models [86–88] at different values of rapidity Y. Notice that taking Y with the opposite sign one obtains the same product of $f_{\mathrm{NP}}^{\mathrm{tmd}}(z,x) f_{\mathrm{NP}}^{\mathrm{tmd}}(z,\bar{x})$. In the case of ART23 model, $f_{\mathrm{NP}}^{\mathrm{tmd}}$ is presented for sea quarks. For up and down quark in this model, the falloff gets closer to the one of SV19.

Large-z behavior of octet quark DTMDs

Scaling of the color-octet quark Collins-Soper kernel in (5.48) together with the postulated large-distance behavior of the kernels derived from the results for the kernel ${}^1K_q(\mathbf{z})$ implies that at large $\mathbf{z}$ the kernel ${}^8K_q(\mathbf{z})$ becomes large and positive – in upper-left panel of Fig. 5.10 presented are the resulting values of the kernel for different models. This means that the rapidity evolution enhances the product of two octet double quark

distributions in the cross section by a factor of

$$\exp\left({}^{8}K_q(\mathbf{z},\mu_{01})\,\log\frac{Q_1Q_2}{\xi_0}\right). \tag{5.68}$$

This enhancement is visible even at perturbatively small $\mathbf{z}$. Since our model of extrapolation of the Collins-Soper kernel (based on Casimir scaling) is consistent with this behavior, we do not modify the function g in this channel, and allow for large values of the rapidity evolution factor (5.68), since the parton distributions eventually become suppressed by the non-perturbative factor $f_{\rm NP}$, so that the sign of rapidity evolution kernels does not make DPDs grow at very large distances. It is verified in Fig. (5.10), where the values of the z-dependent octet quark Collins-Soper kernel, as well as the products

$$\exp\left({}^{8}K_q(\mathbf{z};\mu_{\mathbf{z}^*})\log\frac{Q_1Q_2}{\xi_0}\right)\,\times\,\exp\big(-(r\lambda)^2\mathbf{z}^2\big)\,, \tag{5.69}$$

are presented for $Q_1=Q_2=M_W$, and $\xi_0=\mu^2_{\rm min.}=4\,{\rm GeV}^2$. The choice of a minimal value of ξ_0 corresponds to $y\to\infty$, and maximizes the effects of rapidity evolution.

5.3 Large-y region

Recalling the results of Section 5.1.2, we have

$$\begin{aligned}\frac{d\sigma^{\rm DPS}}{\prod_{i=1,2}dx_i d\bar{x}_i d^2\mathbf{q}_i d\Omega_i} \;=\; &\int_0^\infty\frac{z_1}{2\pi}dz_1\int_0^\infty\frac{z_2}{2\pi}dz_2\;J_0(q_1z_1)\;J_0(q_2z_2)\\ &\sum_{\sigma_{1,2}=\pm1}\big(1+\sigma_1\cos\theta_1\big)^2\big(1+\sigma_2\cos\theta_2\big)^2\,W_{\sigma_1\sigma_2}(\mathbf{z}_1,\mathbf{z}_2)\,,\end{aligned} \tag{5.70}$$

where $W_{\sigma_1\sigma_2}$ is given in Eq. (5.13). The evolution of quark DTMDs does not depend on polarizations. The product of two DTMDs in a definite color representation at the final scales is given by

$$\begin{aligned}&{}^{RR}F\big(x_i,\mathbf{z}_i,\mathbf{y};\mu_i,\zeta\big)\,{}^{RR}\bar{F}\big(\bar{x}_i,\mathbf{z}_i,\mathbf{y};\mu_i,\bar{\zeta}\big)\\ &=\exp\Big(S_q\big(\mu_{01},\mu_1,x_1\sqrt{\zeta}\big)+S_q\big(\mu_{01},\mu_1,\bar{x}_1\sqrt{\zeta}\big)\\ &\qquad+S_q\big(\mu_{02},\mu_2,x_2\sqrt{\zeta}\big)+S_q\big(\mu_{02},\mu_2,\bar{x}_2\sqrt{\zeta}\big)\Big)\\ &\quad\times\exp\left(\frac{1}{2}\Big({}^{R_1}J(\mathbf{y};\mu_{0i})+{}^{R_1}K_q(\mathbf{z}_1;\mu_{01})+{}^{R_2}K_q(\mathbf{z}_2;\mu_{02})\Big)\left(\log\frac{x_1x_2\zeta}{\xi_0}+\log\frac{\bar{x}_1\bar{x}_2\bar{\zeta}}{\xi_0}\right)\right)\\ &\quad\times{}^{RR}F^{pt}\big(x_i,\mathbf{z}_i^*,\mathbf{y};\mu_{0i},\xi_0/(x_1x_2)\big)\,{}^{RR}\bar{F}^{pt}\big(\bar{x}_i,\mathbf{z}_i^*,\mathbf{y};\mu_i,\bar{\zeta}/(\bar{x}_1\bar{x}_2)\big)\;F^2_{\rm NP}(\mathbf{z}_1,\mathbf{z}_2)\,.\end{aligned} \tag{5.71}$$

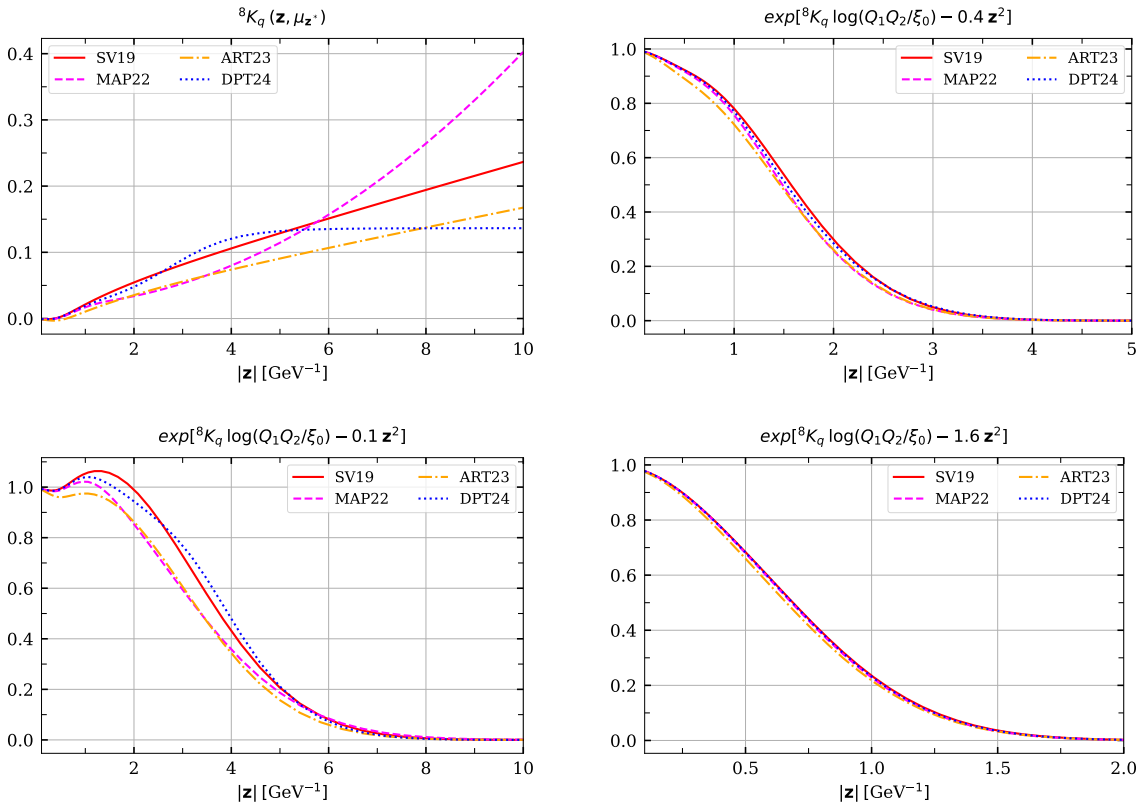

Figure 5.10: Upper-left: values of the kernel $^8K_q(\mathbf{z}; \mu_{\mathbf{z}^*})$ for the considered models of the Collins-Soper kernel. Upper-right: rapidity evolution exponential times the z-falloff for the default choice of the falloff parameter $r = 1$, see Eq. (5.62). Lower: the same product, but for minimal ($r = 0.5$) and maximal ($r = 2$) values of the falloff parameter.

The exponentials in the second and third line are the Sudakov factors obtained by RGE evolving the partons distributions from μ_{0i} to the final scales. The factors from left- and right- moving hadrons can be conveniently combined:

$$\begin{aligned}
&\exp\Big(S_q\big(\mu_{01},\mu_1,x_1\sqrt{\zeta}\big)\Big)\;\times\;\exp\Big(S_q\big(\mu_{01},\mu_1,\bar{x}_1\sqrt{\bar{\zeta}}\big)\Big)\\
&\quad=\exp\left(\int_{\mu_{01}}^{\mu_1}\frac{d\mu}{\mu}\Big(\gamma_q(\mu)-\gamma_{K,q}\log\frac{x_1\sqrt{\zeta}}{\mu}\Big)\;+\;\int_{\mu_{01}}^{\mu_1}\frac{d\mu}{\mu}\Big(\gamma_q(\mu)-\gamma_{K,q}\log\frac{\bar{x}_1\sqrt{\bar{\zeta}}}{\mu}\Big)\right)\\
&\quad=\exp\left(2\int_{\mu_{01}}^{\mu_1}\frac{d\mu}{\mu}\Big(\gamma_q(\mu)-\gamma_{K,q}\log\frac{Q_1}{\mu}\Big)\right)\\
&\quad=\exp\Big(2\,S_q\big(\mu_{01},\mu_1,Q_1\big)\Big)\,,
\end{aligned}\tag{5.72}$$

and analogously for the second scale. To get this result one uses

$$\sqrt{\zeta\bar{\zeta}}=s,\quad\text{and}\quad x_i\bar{x}_i s=Q_i^2\,.$$

The logarithms in the rapidity evolution part (3rd line in (5.71)) can be combined into

$$\frac{1}{2}\log\frac{x_1x_2\zeta}{\xi_0}+\frac{1}{2}\log\frac{\bar{x}_1\bar{x}_2\bar{\zeta}}{\xi_0}\;=\;\log\frac{Q_1Q_2}{\xi_0}\,.\tag{5.73}$$

Finally, one obtains the simplified form of a product of right- and left-moving hadron DTMDs:

$$\begin{aligned}
&{}^{RR}F\big(x_i,\mathbf{z}_i^*,\mathbf{y};\mu_{0i},\xi_0/(x_1x_2)\big)\;{}^{RR}F\big(\bar{x}_i,\mathbf{z}_i^*,\mathbf{y};\mu_{0i},\xi_0/(\bar{x}_1\bar{x}_2)\big)\\
&\quad=\;{}^{RR}F^{pt}\big(x_i,\mathbf{z}_i,\mathbf{y};\mu_{0i},\xi_0/(x_1x_2)\big)\;{}^{RR}F^{pt}\big(\bar{x}_i,\mathbf{z}_i,\mathbf{y};\mu_{0i},\xi_0/(\bar{x}_1\bar{x}_2)\big)\times F_{\rm NP}^2(\mathbf{z}_1,\mathbf{z}_2)\\
&\qquad\times\exp\Big(2S_{a_1}\big(\mu_{01},\mu_1,Q_1\big)\Big)\times\exp\Big(2S_{a_1}\big(\mu_{02},\mu_2,Q_2\big)\Big)\\
&\qquad\times\exp\left(\Big[{}^{R_1}K_{a_1}(\mathbf{z}_1;\mu_{01})+{}^{R_2}K_{a_2}(\mathbf{z}_2;\mu_{02})+{}^{R_1}J(\mathbf{y};\mu_{0i})\Big]\log\frac{Q_1Q_2}{\xi_0}\right)\,.
\end{aligned}\tag{5.74}$$

Integration grids for $|\mathbf{y}|$

In this part we describe grids in transverse position used in the integration. The settings are taken based on the previous studies of DPDFs using ChiliPDF [71].
The grid in $y=|\mathbf{y}|$ is split into 2 subgrids:

1. Lower grid with limits

$$\Big[\frac{b_0}{M_W},\;\frac{1}{2}b_0\;\mathrm{GeV}^{-1}=b_{\rm min}\Big]\,.\tag{5.75}$$

The variable transformation on this subgrid is

$$u(y) \;=\; -y^{-0.2}\,. \tag{5.76}$$

The number of grid points depends on the color representation. We take 16 points for color singlet, and 24 points for color non-singlet. The motivation for taking the larger number of gridpoints in the color non-singlet case is the fact, that due to rapidity evolution effects, the first subgrid yields the dominant contribution to the non-singlet sector of the final results, as can be already seen from DTMD y-dependence plots in Figs. 3.9-3.10.

2. The upper subgrid with the limits

$$\big[\frac{1}{2}b_0\ \mathrm{GeV}^{-1}, \infty\big]\,. \tag{5.77}$$

The variable transformation is

$$u \;=\; -\exp\Big(-\big(m^2\cdot y^2 + m\cdot y\big)/4\Big)\,, \quad m = \sqrt{\frac{1}{4h_{gg}}}\ \mathrm{GeV}\ = 0.232\ \mathrm{GeV}\ . \tag{5.78}$$

We take 16 points on this subgrid. The grid parameter is taken such that it assures high integration precision for functions with Gaussian falloff $\propto \exp\big(-y^2/(4h_{gg})\big)$, see Eq. (3.27). The same settings were used in already existing studies [67].

Integration grids for $|\mathbf{z}_1|, |\mathbf{z}_2|$

The grids in $z_{1,2} = |\mathbf{z}_{1,2}|$ are chosen such that one can precisely compute the Bessel transform for a wide range of transverse momenta q, at least $0 < q \leq 20\,\mathrm{GeV}$. Based on the analysis done in [1], for an integrand with the Gaussian large-z behavior:

$$W(z) \;\sim\; \exp\big(-(r\lambda)^2\, z^2\big)\,, \tag{5.79}$$

a relative accuracy better than 10^{-4} for q up to $100\,\mathrm{GeV}$ is expected if one takes a grid with variable transformation:

$$u = -\exp\big(-mz/4\big)\,, \tag{5.80}$$

with the grid parameter m such that

$$\frac{r\lambda}{m} \;\in\; [2, 8]\,. \tag{5.81}$$

Since we are going to consider a family of functions F_{NP}, for which the integrand (5.74) behaves like in (5.79) with

$$\lambda = \sqrt{0.4}\ \mathrm{GeV}\ \approx\ 0.634\ \mathrm{GeV}, \quad r \in [0.5, 2]\,, \tag{5.82}$$

we find that the grid transformation that leads to precise computation of the required Bessel transforms is given by

$$u = -\exp\left(-\sqrt{0.4}\ \text{GeV}\ \times z\right). \tag{5.83}$$

This choice ensures that the relation (5.81) is fulfilled for all of the considered choices of the function $F_{\rm NP}$. We recall that z is in units of GeV^{-1}.
Results of [1] show also that a better accuracy is obtained when splitting the integration grid into 2 subgrids – an appropriate choice was found to be

$$\left[0,\ 0.1\,\text{GeV}^{-1},\ \infty\right], \tag{5.84}$$

with 24 points on the first, and 32 points on the second subgrid.

Finally, we summarize the default settings for the non-perturbative input, and the procedure of estimation of the related model uncertainties.

- DPDF model – as described in Section 3.3. We treat the collinear double parton distributions as given, and do not modify them in a way other than by changing the non-perturbative part of the kernel ${}^{R}J$. In particular, this means that while we vary the function $F_{\rm NP}(\mathbf{z})$, the **y**-dependent prefactors given in Section 3.3 are fixed in the whole analysis.

- Switching between the large-**y** and short-distance forms of DTMDs in the $z_i \times y$ space is described in Section 5.2.1, with the interpolating function controlled by the parameter δ, see Eq. (5.6). Our default choice is $\delta = \frac{4}{12}$.

- Collins-Soper kernels – our default choice is DPT24, given in Eq. (5.53), cf. [89]. To estimate the uncertainties due to the non-perturbative part of the kernels, we repeat the computation for the remaining models given in (5.54)-(5.56).

- Matching kernels – to estimate the impact of higher-order QCD corrections to the matching kernels, we vary the matching scales $\mu_{0i}(z_i)$ according to Eq. (3.56). Contrary to the scale variation in the case of DTMD studies, we take only 3 values of κ:

  $$\kappa\ \in\ \{0.5,\ 1,\ 2\}, \tag{5.85}$$

  omitting the intermediate values $\kappa = 0.75,\ 1.5$. The central value $\kappa = 1$ is the default setting.

- Large-**z** behavior – we consider a family of the large-distance factors $F_{\rm NP}(\mathbf{z}_1, \mathbf{z}_2)$ as

  $$F_{\rm NP}(\mathbf{z}_1, \mathbf{z}_2) = \exp\left(-\frac{1}{2}\,(r\lambda)^2\,(\mathbf{z}_1^2 + \mathbf{z}_2^2)\right), \tag{5.86}$$

  with $\lambda = \sqrt{0.4}$ GeV, and $r \in [0.5,\ 2]$. The default choice is $r = 1$.

5.3.1 Differential cross section – perturbative uncertainty at different orders

First, let us compare the differential cross-sections at NLL and NNLL accuracies for default settings. The objective of this exercise is to investigate, how the higher-order corrections change the result, compare the variations with the uncertainty estimates obtained by the matching-scale variation, and verify if the error estimates become smaller at higher pQCD orders.
In Figs. 5.11 and 5.12 we present the partially integrated differential cross-section

$$\frac{d\sigma^{\mathrm{DPS}}}{dq_1 dY_1 dY_2}\Big|_{q_2 \leq 20\,\mathrm{GeV}} . \tag{5.87}$$

In this work, we performed a detailed study of the q-dependent differential cross-section for 5 pairs of W bosons rapidities:

$$(Y_1, Y_2) \in \big\{(0,0),\ (1.5,0),\ (0,3),\ (3,3),\ (3,-3)\big\} . \tag{5.88}$$

In Figs. 5.11 and 5.12 shown are results for $(Y_1, Y_2) = (0,0)$ and $(3,3)$. All of the results are collected in App. G.2. The qualitative behavior of those points is consistent with those presented in the main part of the work. The rapidity-dependence in a wider range will be studied in Section 5.6.4.

We limit our plots to $q_1 \in [5\ \mathrm{GeV},\ 20\,\mathrm{GeV}]$. For smaller transverse momenta the assumption of the small z_1 giving the dominant contribution to the differential cross section is no longer justified, while for larger q_1 we can no longer say that $q_1 \ll Q = M_W$. The result is integrated over the second transverse momentum up to 20 GeV, and includes the region of $q_1 \in [0,\ 5\ \mathrm{GeV})$, however, as seen from Eq. (5.30), the corresponding integral is also expressible as a Hankel transform dominated by short distances, and hence including the region of small momenta should not spoil the assumption of dominant small distances.

We observe that in most cases at NNLL we obtain results larger compared with NLL, the only exception being the opposite-sign W production at large rapidities. The relative difference between NLL and NNLL is large, typically from about 50% to over 100%. The virtual 1-loop QCD corrections to the hard-scattering factors K_{ab} are positive and of size about 10% of the LO expression, so the largest enhancement of the result is due to an increase of DTMDs at higher order. The uncertainty estimation is visibly reduced at higher order for larger transverse momenta. For momenta close to 5 GeV the absolute value of the error estimate is comparable at both orders, although the relative error is reduced due to the enhancement of the overall result. We observe that the NLL error bands in most cases do not overlap with the NNLL result – as discussed in the case of DTMDs, this is probably due to a local minimum of some double-parton distributions as functions of the matching scale μ_{0i}. A similar effect was reported in the study of W boson production in single-parton scattering [111].

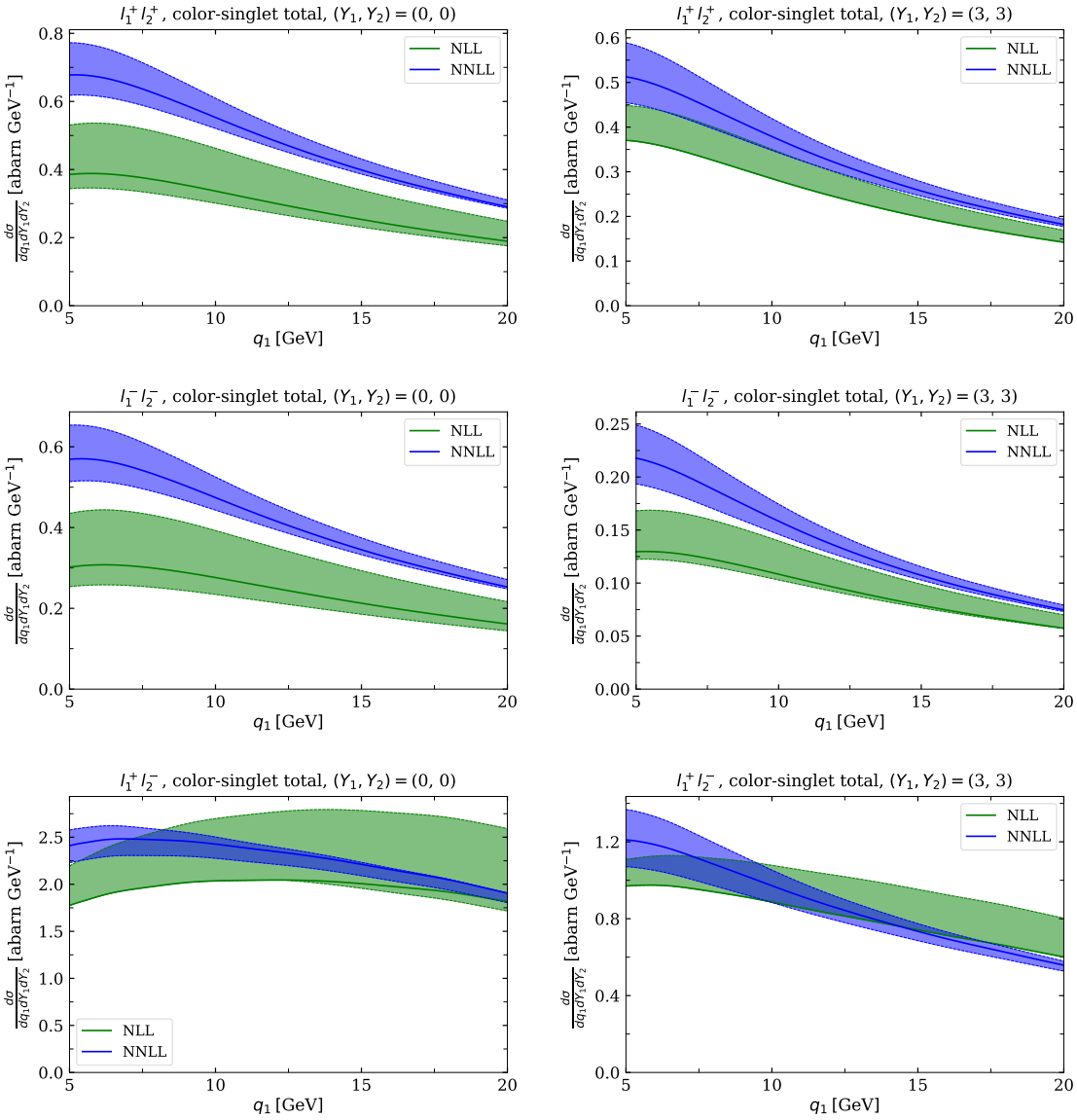

Figure 5.11: Large-**y** region, color-singlet sector contribution to the differential cross-section of production of two W bosons scattering into a pair of leptons l_1, l_2. The label 'total' refers to the sum over all "n vs m" terms. Considered are two values of rapidities of the bosons: $(Y_1, Y_2) = (0, 0)$ (left), and $(Y_1, Y_2) = (3, 3)$ (right). Presented are the results and the estimation of the error due to the perturbative matching at NLL (green) and NNLL (blue) accuracy.

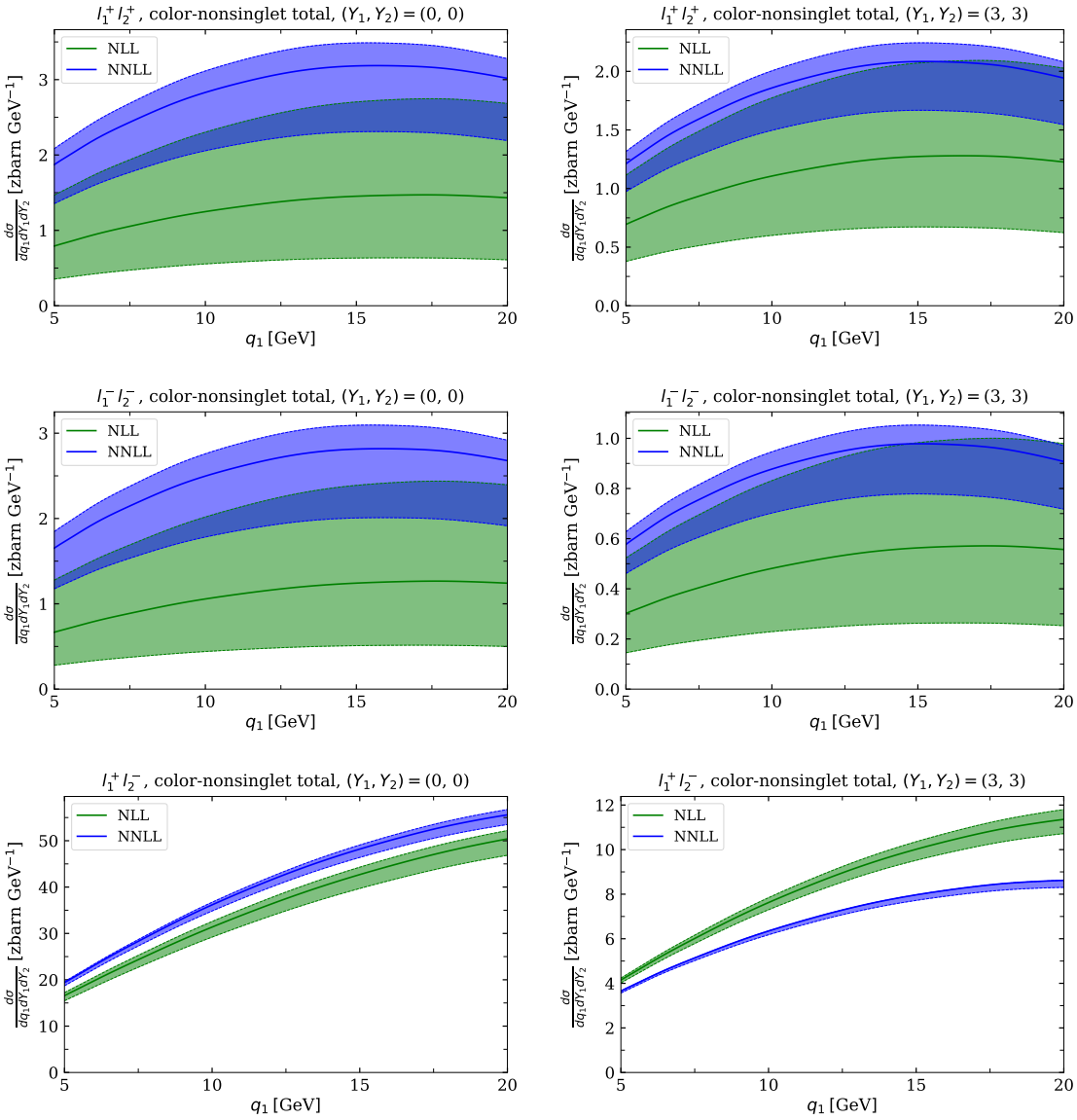

Figure 5.12: Large-**y** region, color-nonsinglet sector contribution to the differential cross-section of production of two W bosons scattering into a pair of leptons l_1, l_2. The label 'total' refers to the sum over all "n vs m" terms. We point out that the units here are zbarn ($= 10^{-3}$ abarn). Considered are two values of rapididies of the bosons: $(Y_1, Y_2) = (0, 0)$ (left), and $(Y_1, Y_2) = (3, 3)$ (right). Presented are the results and the estimation of the error due to the perturbative matching at NLL (green) and NNLL (blue) accuracy.

5.3.2 Combined uncertainties at NNLL

The results of Section 5.3.1 imply that the higher-order pQCD corrections yield a significant modification of the differential cross-section of the considered process, in some cases the corrections are as large as the NLL result. A variation of the matching scales μ_{0i} provides a working estimate of the higher-order corrections. As discussed in Section 5.2, the unknown pQCD terms are not the only source of the error, due to model input such as the non-perturbative part of the Collins-Soper kernels, large-**z** behavior of parton distributions, and the interpolation between the two considered approximations for transverse distance-dependent DPDs. In this part, we will assess the size of the corresponding uncertainties and their relative significance independently for each boson channel, and each 'n vs m' DPD combination. We recall that the uncertainty due to DPDF modeling, and as follows, the uncertainty due to the unknown behavior of double parton distributions at large **y** is not included in the estimates.

The procedure for the estimation of the uncertainties is as follows. We consider 4 independent parameters: the parameter κ in Eq. (3.56) which rescales the matching scales μ_{0i}, model of the Collins-Soper kernel in Section 5.2.2, parameter r in Eq. (5.86) which governs the large-**z** falloff of DTMDs, and the parameter δ in Eq. (5.44) defining the interpolation between the large-**y** and short-distance DTMD approximation.

The 'default' choice of these parameters is given by

$$\kappa = 1, \quad \text{DPT24}, \quad r = 1, \quad \delta = \frac{3}{12}\,. \tag{5.89}$$

All of the possible variations of these parameters are summarized in Section 5.2. At each step of the procedure, we allow for a variation of the first $n = 1, 2, 3, 4$ parameters, thus obtaining the combined uncertainties:

- $n = 1$, CS kernel, r, δ fixed – pQCD uncertainty, denoted 'μ_0'
- $n = 2$, r and δ fixed – (pQCD + CS kernel) uncertainty, denoted '$\delta K + \mu_0$'.
- $n = 3$, δ fixed – (pQCD + CS kernel + $F_{\rm NP}$) uncertainty, denoted '$r + \delta K + \mu_0$'.
- $n = 4$, vary all parameters – the total uncertainty, denoted '$\Sigma_{yz} + \delta K + \mu_0$'.

It is necessary to emphasize that the variation of δ gives the uncertainty due to the interpolation only when one combines the large-**y** and short-distance contributions. However, we keep this variation also in the analysis of this part, for two reasons:

- It allows to already estimate the size of the contribution of the interpolation region to the final result.
- Since at the currently accessible accuracy of the PDF→DTMD splitting formula, the parton distributions describing production of like-sign W bosons are zero,

the $2v1 + 1v2$ and $1v1$ contribution from the short-distance region of $W^{\pm}W^{\pm}$ production vanishes. Hence, the δ variation for this channel already provides the interpolation uncertainty at the considered pQCD accuracy.

Plots of the partially integrated differential cross section of W pair production are collected in Figs 5.13-5.14, cf. Eq. (5.87), defined as in Section 5.1.2. The black line represents the prediction obtained using the default settings and bands of different colors represent the accumulated uncertainties due to variation of the parameters.

For the opposite-sign W pair production, the maximum of the 1v1 color-singlet part is strongly shifted towards the larger momenta compared to the 2v2 and 2v1+1v2 channels, while the maximum of the 1v1 color-nonsinglet terms is not even reached at $q_2 \leq 20$ GeV. It should be noted, however, that in the discussed plots shown is not the *total* contribution to the given 'n vs m' channels, but only the large-$\mathbf{y}$ part, which excludes $\mathbf{z}_i$ of similar size of $\mathbf{y}$. As seen in the plots of $\mathbf{y}$-dependent DTMDs in Section 3.7, the splitting part of DPDs contributing to the 1v1 channel gets the largest contribution at $|\mathbf{y}| < \frac{1}{2}b_0$ GeV^{-1}. It implies that for smaller momenta, where larger values $\mathbf{z}_i$ are more relevant to the cross-section, the most important region of the phase space corresponds to the short-distance rather than large-$\mathbf{y}$ region, and thus does not contribute to the presented part of the total result. As already seen in the previous part, there is little difference between the differential cross-section of production of likesign pairs W^+W^+ and W^-W^-, also at the level of individual DPD channels, so in this part we present the combined cross-section of production of like-sign leptons either with positive or negative sign.

After discussing the general properties of the presented results, let us describe the sources of uncertainties and their relative importance.

In the color-singlet channel, the most significant source of uncertainty remains the one due to higher-order corrections. For the 2v1 and 1v1 channels the variation of the result due to a change of the interpolation becomes important, and is the strongest pronounced for opposite-sign W production via the 1v1 channel.

In the color-nonsinglet case, the variation due to the μ_0 choice turns out to be smaller than due to variation of δ and the Collins-Soper kernel. It is remarkable that in the color-nonsinglet 1v1 channel of opposite-sign W production, the variation due to the variation of the interpolation function is of order of 100% of the result, which implies that the short-distance contribution in the corresponding channel is significant.

It is clearly seen that the uncertainty due to Collins-Soper kernel is strongly asymmetric – the lower estimate due to the model is almost not visible on the plots, unlike the upper estimate. We checked that this upper boundary corresponds to the ART23 model, which is a kind of an outlier within the considered models, as gives a visibly larger kernel even at relatively small distances, see Fig. 5.8.

Another important feature is the weak dependence of the result on the value of the parameter r in $F_{\rm NP}$ defined in Eq. (5.62) (green band). This implies that for any

considered model of large-**z** behavior of DTMDs discussed in Section 5.2.3 and shown in Fig. 5.9, one obtains consistent results.

For color non-singlet distributions the corresponding error bands are not even visible on the plots, which can be explained by the shape of the interpolating function. Observe that at large values of **z**, which are affected by the change of r, one integrates over dy from a rather large lower limit $= \frac{1}{4}b_0\,\mathrm{GeV}^{-1}$, see the interpolation functions in Section 5.2.1. Since DTMDs at large **y** in the color-octet case are suppressed due to rapidity evolution effects, as discussed in Section 3.7, the large-**y** octet part is also more strongly suppressed at large **z**.

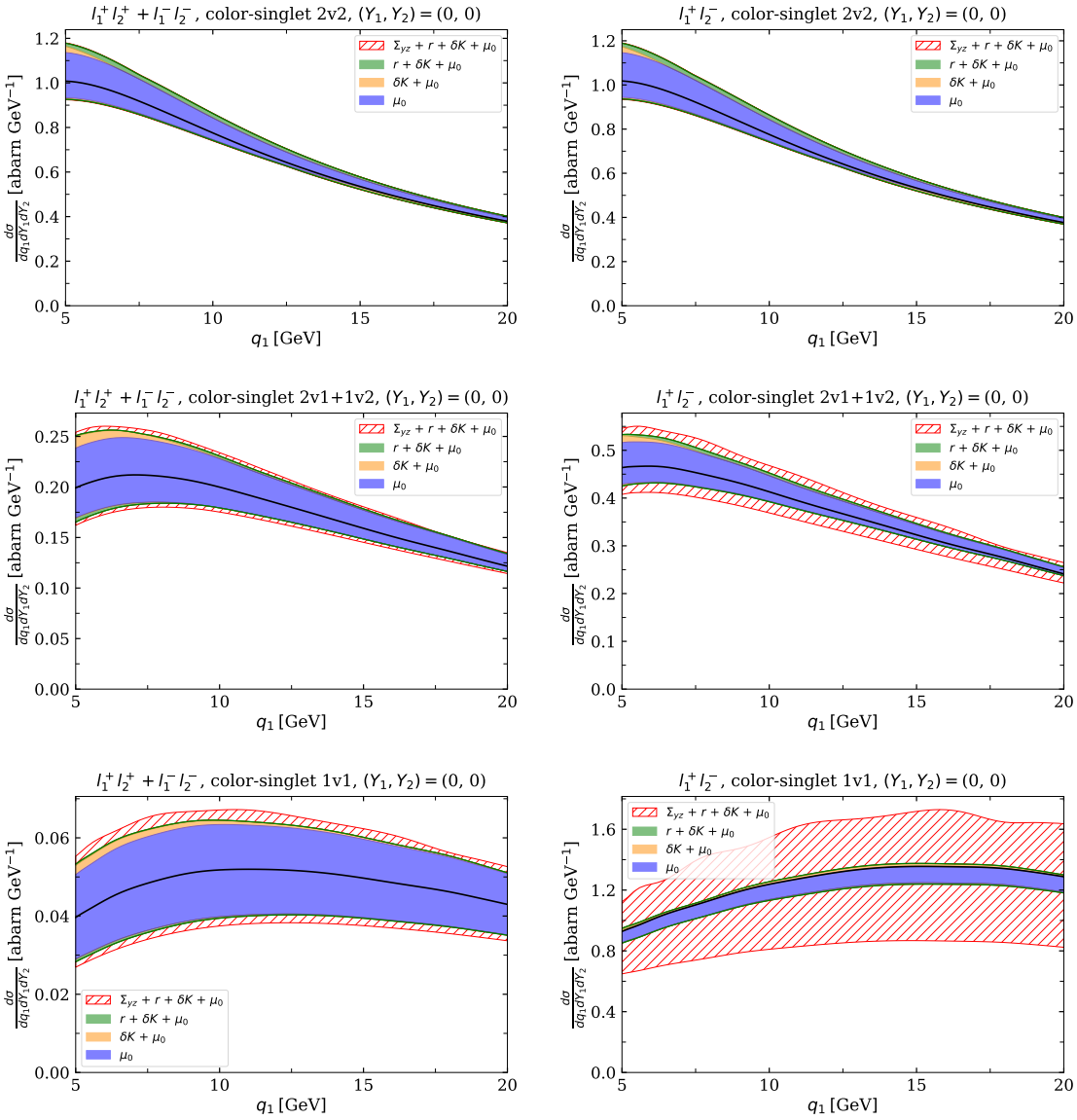

Figure 5.13: Large-**y** region, singlet sector contribution to the differential cross-section of production of two W bosons of rapidities $(Y_1, Y_2) = (0, 0)$, scattering into a pair of leptons.

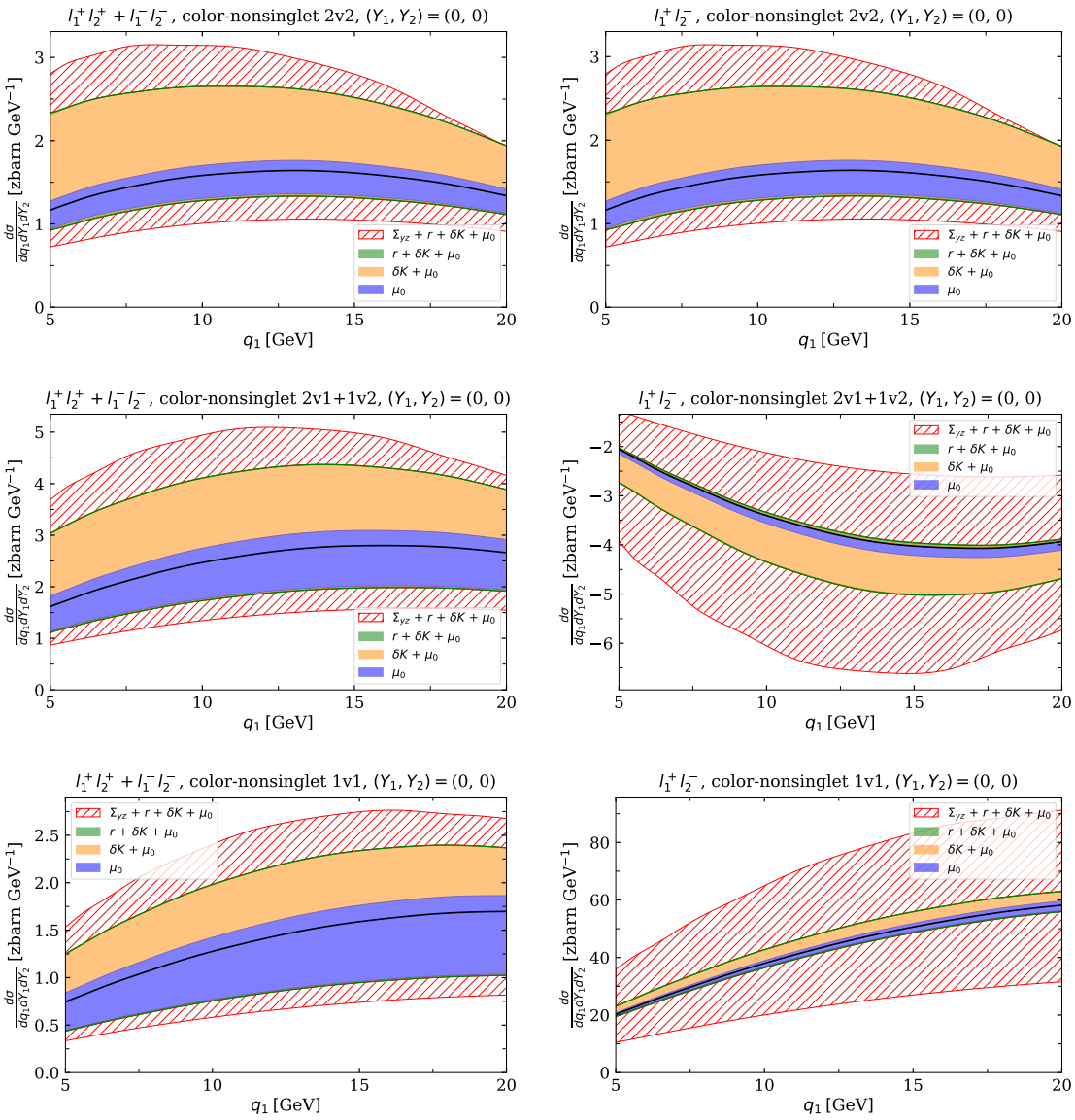

Figure 5.14: Large-**y** region, nonsinglet sector contribution to the differential cross-section of production of two W bosons of rapidities $(Y_1, Y_2) = (0, 0)$, scattering into a pair of leptons.

5.4 Short-distance region

Results for short-distance DTMDs presented in Section 4.3 clearly show that the function $w_{\sigma_1\sigma_2}$, defined in Eq. (5.11), which is the basic building block of the cross-section given in Eq. (5.19), exhibits a non-trivial dependence on the angular variables

φ_y, φ_z defined in Section 4.1.1. Recalling the results of Section 5.1.2, we obtained the short-distance contribution in the following form:

$$\frac{d\sigma}{\prod_{i=1,2} dx_i d\bar{x}_i d^2\mathbf{q}_i d\Omega_i} = \int \frac{d^2\mathbf{z}_1}{(2\pi)^2} \int \frac{d^2\mathbf{z}_1}{(2\pi)^2} e^{-i\mathbf{z}_1\mathbf{q}_1 - i\mathbf{z}_2\mathbf{q}_2} \int d^2\mathbf{y} \sum_{\sigma_{1,2}=\pm 1} (1+\sigma_1\cos\theta_1)^2 (1+\sigma_2\cos\theta_2)^2 \, w_{\sigma_1\sigma_2} \,, \tag{5.90}$$

where $w_{\sigma_1\sigma_2}$ is a product of DTMDs weighted by hard cross-sections:

$$w_{\sigma_1\sigma_2} = \frac{1}{C} \sum_{RR=11,88} \sum_{q_1,\ldots,q_4} K_{q_1\bar{q}_3}(Q_1) K_{q_2\bar{q}_4}(Q_2) (F\bar{F})_{q_1,\ldots,\bar{q}_4,\sigma_1\sigma_2} \times \Big(1 - \Sigma_\delta\big(y, \max(z_1,z_2)\big)\Big) \theta(y_+ - y_{\rm cut}) \theta(y_+ - y_{\rm cut}) \,. \tag{5.91}$$

$1 - \Sigma_\delta\big(y, \max(z_1,z_2)\big)$ is the function used to interpolate between short-distance and large-$\mathbf{y}$ approximations, as described in Section 5.2.1. Notice that Σ approaches 1 as y becomes sufficiently larger than $\max(z_1,z_2)$ or $y > y_{\max}$, hence the short-distance part is multiplied by the combination $(1-\Sigma)$. The step function $\theta(y_\pm - y_{\rm cut})$ is the short-distance cut-off – because of the $1/\mathbf{y}_\pm^2$ singularity in the $1v1$ contribution, the integral over all transverse distances is infinite. In theory, if one includes all of the double-counting subtraction terms, as described in Section 2.4, the dependence of the total result on the value of parameter $y_{\rm cut}$ should be a subleading effect as long as it is taken of order Q^{-1} – this analysis is at this moment beyond the scope of this thesis. According to the discussion in Section 4.1, including the subtraction terms requires modeling and study of evolution equations of twist-3 DPDs, as well as the inclusion of the DPS/SPS interference [69].

The term $(F\bar{F})$ denotes the product of double parton distributions correponding to a given combination of signs of $\cos\theta_i$ in Eq. (5.90). Contrary to the previous study in the large-y regime, the pseudoscalar DTMDs enter the cross-section in the splitting part, see Eq. (4.5). As we will argue in Section 5.4.1, due to the angular dependence of the corresponding terms, the cross-terms $F_{q\bar{q}} \times F_{q\bar{q}}$ vanish, and only the product of two pseudoscalar distributions survives after the integration over angular variables $d\varphi_z, d\varphi_y$. Therefore, the splitting pseudoscalar DTMDs enter the differential cross-section only in the $1v1$ term, and effectively the products of DTMD in Eq. (5.91) can be replaced by

$$\begin{aligned} &\big(F_{q_1q_2}F_{\Delta q_1\Delta q_2} - F_{q_1\Delta q_2} - F_{\Delta q_1 q_2}\big) \times \big(\bar{F}_{\bar{q}_3\bar{q}_4} + \bar{F}_{\Delta\bar{q}_3\Delta\bar{q}_4} - \bar{F}_{\bar{q}_3\Delta\bar{q}_4} - \bar{F}_{\Delta\bar{q}_3\bar{q}_4}\big) \\ \to\quad &\big(F_{q_1q_2} + F_{\Delta q_1\Delta q_2}\big)\big(\bar{F}_{\bar{q}_3\bar{q}_4} + \bar{F}_{\Delta\bar{q}_3\Delta\bar{q}_4}\big) + \big(F_{q_1\Delta q_2} + F_{\Delta q_1 q_2}\big)\big(\bar{F}_{\bar{q}_3\Delta\bar{q}_4} + \bar{F}_{\Delta\bar{q}_3\bar{q}_4}\big) \,, \end{aligned} \tag{5.92}$$

in the $(F\bar{F})_{q_1,\ldots,\bar{q}_4,++}$ term, and analogously in the remaining ones. The color representation indices have been suppressed for simplicity.

Let us show, how the product of DTMDs entering the cross-section formula is factorized into the model-dependent and perturbative parts. Using the solutions of the short-distance Collins-Soper equation, and the RGEs we get

$$\begin{aligned}
&{}^{R_1R_2}F_{a_1a_2}\big(x_i,\mathbf{z}_i,\mathbf{y};\mu_i,\zeta\big)\\
&= \exp\Big(S_q\big(\mu_0,\mu_1,x_1\sqrt{\zeta}\big)+S_q\big(\mu_0,\mu_2,x_2\sqrt{\zeta}\big)\Big)\\
&\quad\times\exp\Big(\frac{1}{2}\big({}^1K_q(\mathbf{z}_1;\mu_0)\;+\;{}^1K_q(\mathbf{z}_2;\mu_0)\big)\log\frac{\zeta}{\zeta_0}\Big)\\
&\quad\times\sum_{R_1'R_2'}{}^{R_1R_2,\bar{R}_1'\bar{R}_2'}\Big[\exp\Big(\frac{1}{2}\big(M_{qq}(\mathbf{z}_i,\mathbf{y};\mu_i)\log\frac{\zeta}{\zeta_0}\Big)\Big]\;{}^{R_1'R_2'}F^{\text{model}}_{a_1a_2}\big(x_i,\mathbf{z}_i,\mathbf{y};\mu_0,\zeta_0\big)\,.
\end{aligned}\tag{5.93}$$

Finally, combining the evolution exponents from both right- and left-moving hadrons we arrive at the final form of the product:

$$\begin{aligned}
&\sum_{R_1R_2}{}^{R_1R_2}F\;{}^{R_1R_2}\bar{F}=\\
&\quad=\sum_{R_1R_2,\bar{R}_3\bar{R}_4}{}^{R_1R_2,R_3R_4}\Big[\exp\Big(\big(M_{qq}(\mathbf{z}_i,\mathbf{y};\mu_i)\log\frac{Q_1Q_2}{\xi_0}\Big)\Big]\\
&\qquad{}^{R_1R_2}F^{\text{model}}\big(x_i,\mathbf{z}_i,\mathbf{y};\mu_{0i},\xi_0/(x_1x_2)\big)\;{}^{R_3R_4}F^{\text{model}}\big(\bar{x}_i,\mathbf{z}_i,\mathbf{y};\mu_{0i},\xi_0/(\bar{x}_1\bar{x}_2)\big)\\
&\qquad\times\exp\Big(2S_q\big(\mu_0,\mu_1,Q_1\big)\Big)\times\exp\Big(2S_q\big(\mu_0,\mu_2,Q_2\big)\Big)\\
&\qquad\times\exp\Big(\big({}^1K_q(\mathbf{z}_1;\mu_0)+{}^1K_q(\mathbf{z}_2;\mu_0)\big)\log\frac{Q_1Q_2}{\xi_0}\Big)\,.
\end{aligned}\tag{5.94}$$

The RGE exponentials, and the diagonal part of the exponentiated Collins-Soper kernel have been organized just like in the analogous case of large-$\mathbf{y}$ given in Eq. (5.74). The new feature in this case is the mixing between different color representations $R_1R_2 = 11, 88$ of DTMDs formulated at the initial scales due to the representations mixing under rapidity evolution. As clearly visible in Fig. 4.6, the non-diagonal tem of the evolution matrix for two-quark distributions is non-negligible. This obstructs the splitting of the differential cross-section into the color-singlet and color-nonsinglet

contributions, as this was done previously. For this reason, when combining the contributions to the cross-section we shall not make the distinction between different color channels, and simply consider the version summed over singlets and octets. On the other hand, to assess the importance of the color-nonsinglet channels, in Section 5.5.4 we will compare two cross-sections – one computed using the settings outlined here, and another for pure color-singlet initial conditions, that is ${}^{88}F\big|_{\xi_0/(x_1x_2)} = 0$.

5.4.1 Numerical integration

We find that the computation of integrals defining the Double Drell Yan (DDY) cross-section is much more involved than in the case of the large-$\mathbf{y}$ approximation, due to two additional angular integrals, and problems related to the short-distance splitting singularities.

In this part, we describe the numerical procedure which we developed in order to compute the DDY observables, outline the settings in the numerical integration, and discuss the overall precision. The order of integration is the following:

1. Compute the integral over $d\varphi_y$. If the difference $|\mathbf{y}|-|\mathbf{z}_-|$ is smaller than the small distance cutoff $y_{\rm cut}$, then for some values of the angle φ_y one has $y_\pm = |\mathbf{y}_\pm| < y_{\rm cut}$, so that appropriate integration limits must be applied. They will be defined in Eq. (5.102).

2. Compute the integral over dy. Since the condition $y_\pm \geq y_{\rm cut}$ is enforced in the previous integral, no new cut-offs are needed in this case. However, we find that the first derivative of the integrand is discontinuous at

$$y = |\mathbf{z}_-| \pm y_{\rm cut} \,, \tag{5.95}$$

   and the overall integrand becomes steep near these points, hence splitting into subgrids is used.

3. Compute the Fourier modes in φ_z of the result obtained according to Eq. (5.17).

4. Compute the double Bessel integral with J_n for the n-th Fourier mode from point 3.

All of these steps will now be discussed in detail in the subsequent parts.

φ_y integration

We have developed the described integration method specifically for the integrands with singularities $y_\pm^{-2}$, and such behavior will be of the main interest in the following analysis. However, we found the also the integrals with a $y_\pm^{-1}$ singularity (present in the 2v1+1v2

terms), as well as the 2v2 contribution can be precisely studied with the described grid transformation, albeit with fewer grid points and some grid transformation parameters modified.

Recall that φ_y is defined as the angle between $\mathbf{z}_-$ and $\mathbf{y}$, as presented in Fig. 5.15. A special case when $|\mathbf{z}_-| = 0$ is treated differently, by defining φ_y with respect to x-axis.

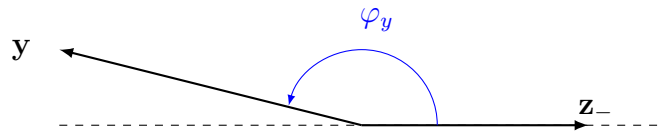

Figure 5.15: A sketch of the considered coordinates

Some simplifications may be obtained by considering the symmetries of the product of DTMDs, regardless of whether it is the intrinsic/splitting part. Consider:

$$\mathbf{y} \longrightarrow -\mathbf{y} \,. \tag{5.96}$$

As seen from the definitions of the distances, this transformation is equivalent to the following substitutions in DTMDs and the evolution kernels:

$$\mathbf{y}_\pm \to -\mathbf{y}_\mp \,, \qquad \mathbf{v}_\pm \to -\mathbf{v}_\mp \,. \tag{5.97}$$

The Collins-Soper kernel depends only on the absolute sizes of these distances, and is symmetric with respect to interchanging

$$\mathbf{y}_+ \longleftrightarrow \mathbf{y}_- \quad \text{and} \quad \mathbf{v}_+ \longleftrightarrow \mathbf{v}_- \,.$$

The scale choice and the intrinsic part are not affected at all by this change. Finally, the prefactor in the splitting part of scalar DTMDs remains the same, while the prefactor in the pseudoscalar splitting part changes the sign

$$\mathbf{y}_+^l \mathbf{y}_-^{l'} \epsilon^{ll'} \;\to\; (-\mathbf{y}_-)^l (-\mathbf{y}_+)^{l'} \epsilon^{ll'} \;=\; -\mathbf{y}_+^l \mathbf{y}_-^{l'} \epsilon^{ll'} \,. \tag{5.98}$$

This has two important implications:

- Since for $\varphi_y \to \varphi_y + \pi$ the pseudoscalar splitting part changes sign, and all of the other terms remain unchanged, then the cross products of the pseudoscalar and scalar parton distributions vanish in the cross-section.

- The discussed symmetry allows to integrate only on the upper halfplane, that is

$$\varphi_y \in [0, \pi] \,. \tag{5.99}$$

Now we describe, how the cut-off condition

$$|\mathbf{y} \pm \mathbf{z}_-| \geq y_{\rm cut} \tag{5.100}$$

is implemented at the level of angular integration. Let us fix the vector $\mathbf{z}_-$. On the $\mathbf{y}$-plane, the regions affected by the cut-off are two circles, possibly overlapping, as shown in Figs. 5.16 and 5.17.

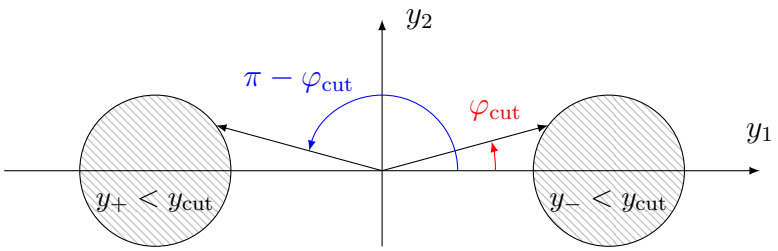

Figure 5.16: Cut-off regions (shaded circles) in the $\mathbf{y}$-plane for fixed $\mathbf{z}_-$. Shown are the angles corresponding to the cut-off in the upper half-plane. Axis 'y_1' is parallel to $\mathbf{z}_-$. The distance between the centers of the shaded circles is equal to $2|\mathbf{z}_-|$.

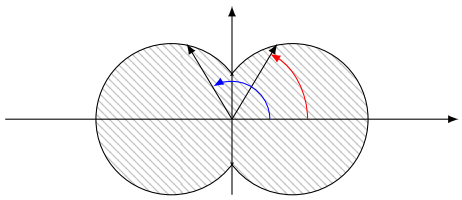

Figure 5.17: The cut-off region in the special case $|\mathbf{z}_-| < y_{\rm cut}$, in which two circles overlap. The formula for $\varphi_{\rm cut}$ remains the same, but there exists a minimal length $y_{\rm min}$, for which the integrand does not vanish for all φ_y. This case will be studied in more detail when discussing integration over dy.

It is obvious that the length of $\mathbf{y}_+$ or $\mathbf{y}_-$ can get smaller than $y_{\rm cut}$ only if

$$\big|\, |\mathbf{y}| - |\mathbf{z}_-| \,\big| < y_{\rm cut}\ , \tag{5.101}$$

which we shall assume now. Using the cosine theorem we obtain that for $\varphi_y \in [0, \pi]$:

$$\begin{aligned} |\mathbf{y}_-| < y_{\rm cut} \quad &\Longleftrightarrow \quad \varphi_y \in [0, \varphi_{\rm cut})\ , \\ |\mathbf{y}_+| < y_{\rm cut} \quad &\Longleftrightarrow \quad \varphi_y \in (\pi - \varphi_{\rm cut}, \pi]\ , \end{aligned}$$

$$\text{where } \varphi_{\rm cut} = \operatorname{acos}\!\left(\frac{y^2 + z_-^2 - y_{\rm cut}^2}{2yz_-}\right). \tag{5.102}$$

We observe that for $\varphi_{\rm cut} \geq \pi/2$ the angular cut-off excludes all of the values of φ_y, thus making the integral vanish. This special case is treated in the context of y-integration, see the case (d) in Fig. 5.18. In the following considerations in this part, we will assume $\varphi_{\rm cut} < \pi/2$.

Let us investigate, how the integrand changes at fixed $y = |\mathbf{y}|$ – to that end, focus only on the most important term, namely the splitting prefactor $1/(\mathbf{y}_-^2 \mathbf{y}_+^2)$. As $\varphi_y = \pi/2$ it has its minimum, which is equal to

$$\frac{1}{\mathbf{y}_+^2}\frac{1}{\mathbf{y}_-^2}\Big|_{\varphi_y=\pi/2} \approx \frac{1}{4y^4}\,, \tag{5.103}$$

where we use $y - |\mathbf{z}_-| \sim y_{\rm cut}$ and neglect the terms of order $y_{\rm cut}$. Now, as φ_y approaches one of the cut-off values, one has

$$\frac{1}{\mathbf{y}_+^2}\frac{1}{\mathbf{y}_-^2}\Big|_{\varphi_y=\pi/2} \approx \frac{1}{4y^2}\frac{1}{y_{\rm cut}^2}\,. \tag{5.104}$$

It is clearly seen that the ratio between the largest and smallest value of the φ_y-integrand is of order $(y/y_{\rm cut})^2$. For typical sizes of z_1, z_2 – and from what it follows – the typical size of $|\mathbf{y}|$ in the region of $|\mathbf{y}| \approx |\mathbf{z}_i|$, the ratio is $\gtrsim 50$, while for the maximal considered values of $|\mathbf{y}|$ the ratio approaches 10^3.

In order to obtain good numerical accuracy, we apply the variable transformation, which will minimize the variation of the integrand on the considered domain. Since initialization of a new grid for each set of the interval limits $[\varphi_{\rm cut}, \pi - \varphi_{\rm cut}]$ would be extremely time-consuming, especially when applied to the first of 5 integrals, we first use the linear transformation

$$[\varphi_{\rm cut},\ \pi - \varphi_{\rm cut}] \ni \varphi_y \ \mapsto\ t = \frac{\varphi_y - \pi/2}{\pi/2 - \varphi_{\rm cut}} \in [-1, 1]\,, \tag{5.105}$$

so that each angular integral is performed on $[-1, 1]$ interval. Then, we apply a variable transformation $u(t)$ such that the corresponding Jacobian turns the integrand into a function that can be well-approximated with polynomials. We take:

$$u(t) = \log\frac{t + t_0}{t_0 - t}, \quad t_0 = 1 + \epsilon_\varphi. \tag{5.106}$$

The Jacobian is

$$\frac{\partial t}{\partial u} = \frac{(t + t_0)(t_0 - t)}{2t_0}, \qquad \lim_{t\to\pm 1}\frac{\partial t}{\partial u} = \epsilon_\varphi \frac{2 + \epsilon_\varphi/2}{1 + \epsilon_\varphi}. \tag{5.107}$$

With the appropriately chosen value of ϵ_φ we obtain a well-behaved integrand, which after the transformations reads:

$$\begin{aligned}&\int_{\varphi_{\rm cut}}^{\pi-\varphi_{\rm cut}} d\varphi_y\, w(\varphi_y)\\ &= \big(\pi/2 - \varphi_{\rm cut}\big) \int_{u(-1)}^{u(1)} du \frac{(t + t_0)(t_0 - t)}{2t_0}\, w\big(\varphi_y(u)\big)\,.\end{aligned} \tag{5.108}$$

To conclude this part, we shall present the grid settings used in this work. To avoid under probing the intermediate angles, we split the grid in t into 2 subintervals: $[-1,0]$ and $[0,1]$ with equal number of the gridpoints on each subgrid. Depending on the DPD channel 'n versus m', we take different numbers of gridpoints, and the transformation parameter:

$$\begin{aligned} &[-1,0,1]_{(24,24)}\,, \quad \epsilon_\varphi = 10^{-2} \qquad \text{for } 1v1\,, \\ &[-1,0,1]_{(16,16)}\,, \quad \epsilon_\varphi = 0.05 \qquad \text{for } 2v1+1v2\,, \\ &[-1,0,1]_{(12,12)}\,, \quad \epsilon_\varphi = 1 \qquad \text{for } 2v2\,. \end{aligned} \tag{5.109}$$

$[a,b,c]_{(n_1,n_2)}$ means that on the subgrid $[a,b]$ there are n_1 points, and n_2 points on $[b,c]$.

For the final remarks, let us comment on the possibility of using different grids depending on y – as seen in Eqs. (5.103)-(5.104), the variation of the integrand depends strongly on the absolute length of $\mathbf{y}$, so that using the variable transformation in Eq. (5.106) we will not get a well-behaved integrand for arbitrarily large distances. Fortunately, we consider only $y < y_{\max}$, but even on this limited range it is tempting to use a couple of parameters ϵ_φ (and, as it follows, a couple of new grids in $t(\varphi_y)$), each for a given range of y – hopefully this would lead to improvement of the integration accuracy. However, we found using only a single grid to provide satisfactory integration precision with the current settings.

$|\mathbf{y}|$ integration

Due to the short-distance cut-off being employed for $y = |\mathbf{y}| \in \big(|\mathbf{z}_-| - y_{\text{cut}}\,,\, |\mathbf{z}_-| + y_{\text{cut}}\big)$, one observes a discontinuity in the first derivative of the y-integrand at those two points. This motivates us to split the integration domain into 3 subintervals:

$$[0, |\mathbf{z}_-| - y_{\text{cut}}] \,\cup\, (|\mathbf{z}_-| - y_{\text{cut}},\, |\mathbf{z}_-| + y_{\text{cut}}] \,\cup\, (|\mathbf{z}_-| + y_{\text{cut}}, y_{\max}]\,. \tag{5.110}$$

A special care is required where $|\mathbf{z}_-| < y_{\text{cut}}$. As already indicated in Fig. 5.17, in such case there exists a minimal length y_0, for which the integral over φ_y does not vanish due to the cut-off:

$$y_0 = \sqrt{y_{\text{cut}}^2 - \mathbf{z}_-^2}\,. \tag{5.111}$$

In that case, the subinterval limits are taken as

$$(y_0,\, |\mathbf{z}_-| + y_{\text{cut}}] \,\cup\, (|\mathbf{z}_-| + y_{\text{cut}}, y_{\max}]\,. \tag{5.112}$$

If one of the upper subinterval limits in Eq. (5.110) becomes larger than $y_{\max}$, then we simply replace it with the upper y limit, and drop the next subintervals[1].

In the following, to have a systematic description of the subgrid structure, we will take the naming convention:

[1] To avoid uncontrolled behavior, our implementation includes also the situation, when $|\mathbf{z}_-| + y_{\text{cut}} > y_{\max}$ in the case of Eq. (5.112). However, such configuration cannot happen unless $y_{\text{cut}} > \frac{1}{2} y_{\max}$.

- The first grid:

$$y \in \left[0,\ \min(|\mathbf{z}_-| - y_{\rm cut}, y_{\rm max})\right] \qquad \text{for } |\mathbf{z}_-| > y_{\rm cut}\ . \tag{5.113}$$

  If $|\mathbf{z}_-|$ is smaller than the cut-off, then the first subgrid is not used. If the upper interval limit turns to be equal $y_{\rm max}$, then the second and third intervals are reduced to zero and not used.

- The second subgrid:

$$\begin{aligned} &y \in \left[|\mathbf{z}_-| - y_{\rm cut},\ \min(|\mathbf{z}_-| + y_{\rm cut}, y_{\rm max})\right] && \text{for } |\mathbf{z}_-| > y_{\rm cut}\ , \\ &y \in \left[y_0,\ |\mathbf{z}_-| + y_{\rm cut}\right] && \text{for } |\mathbf{z}_-| < y_{\rm cut}\ . \end{aligned} \tag{5.114}$$

  As in the previous case, if the upper limit reaches $y_{\rm max}$, the third subinterval is not needed.

- The third grid:

$$y \in \left[|\mathbf{z}_-| + y_{\rm cut},\ y_{\rm max})\right] \qquad \text{for } |\mathbf{z}_-| + y_{\rm cut} < y_{\rm max}\ . \tag{5.115}$$

The possible subgrid structures are sketched in Fig. 5.18. Notice that in the 1v1 term there is a strong minimum at $y = |\mathbf{z}_-|$ – this is because the prefactor in the scalar splitting part $\mathbf{y}_+ \cdot \mathbf{y}_- = \mathbf{y}^2 - \mathbf{z}_-^2$ becomes zero for equal lenghts.

On the edges of the considered subintervals one may again expect a strong variation of the integrand. Once again, in order to avoid constructing a new grid for any new values of the interval limits, we use a linear transformation

$$[y_1,\ y_2] \ni y\ \mapsto\ t = \frac{2t - (y_1 + y_2)}{y_2 - y_1} \in [-1, 1]\ . \tag{5.116}$$

We found that also in this case the variable transformation given in Eq. (5.106) leads to good integration precision, if the transformation parameters are correctly adjusted.

Each transformed subgrid in $t(y)$ has the limits $[-1, 1]$ with n_i points $n = 1, 2, 3$. For all subgrids we use the same form of the variable transformation $u_i(t)$, but with a different parameter t_{0i}:

$$u_i(t) = \log \frac{t + t_{0i}}{t_{0i} - t}, \quad t_{0i} = 1 + \epsilon_i\ , \quad i = 1, 2, 3\ . \tag{5.117}$$

The settings depending on the DPD channel are summarized in Table 5.1.

DPD channel	n_1	ϵ_1	n_2	ϵ_2	n_3	ϵ_3
1v1	24	0.1	12	0.1	24	0.2
2v1+1v2	16	0.1	12	0.1	16	0.8
2v2	16	1.0	12	1.0	16	1.0

Table 5.1: Settings for three subsequent subgrids in variable $t(y)$ defined in Eq. (5.116) for each DPD channel.

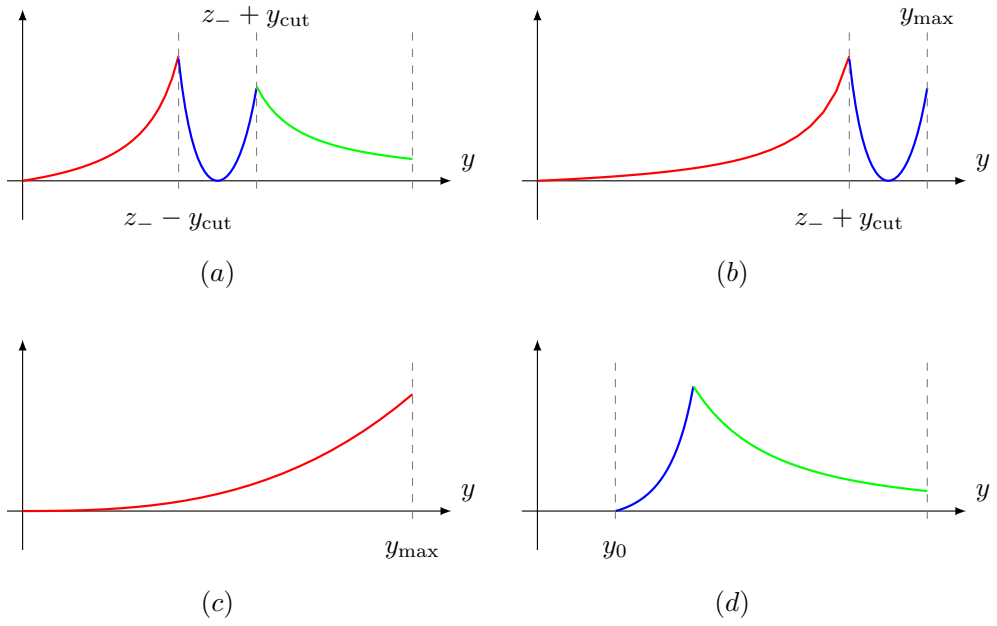

Figure 5.18: Sketch of the configurations of the interval limits of y-integrals, before multiplication by the interpolating factor $1 - \Sigma$. The figure does not indicate the relative sizes of the integrand in different cases, and should be taken only for qualitative discussion. The red, blue, and green colors correspond to the first, second, and third grid in Eqs. (5.113)-(5.115) respectively. The case (a) is the most most relevant one, cases (b) and (c) occur for larger values of $|\mathbf{z}_-|$, where the $|\mathbf{z}_-| \pm y_{\rm cut} > y_{\rm max}$. Finally, (d) occurs if $z_- < y_{\rm cut}$, see Fig. 5.17.

φ_z integration

The variable φ_z enters the Fourier exponential in the cross-section formula (5.11). A numerical integration of a total φ_z-dependent product of $w_{\sigma_1\sigma_2}$ and $e^{i\mathbf{q}_i\mathbf{z}_i}$ would lead to integrals over the distances dz_i involving a highly oscillatory function, whose analytic form we do not know, greatly complicating the numerical analysis.

Instead, we choose to expand the intermediate integral $W_{\sigma_1\sigma_2}(\mathbf{z}_1, \mathbf{z}_2)$ defined in Eq. (5.13) in its Fourier modes using the angle φ_z. Recall from Section 4.1.1 that φ_z is defined as the angle between the vectors $\mathbf{z}_1$ and $\mathbf{z}_2$. It can be shown that the considered function is symmetric with respect to the change of sign of φ_z. To see this let us consider, how the product of DTMDs integrated over the angular variable of $\mathbf{y}$ changes under $\varphi_z \to -\varphi_z$. Instead of integrating over $d\varphi_y$ (angle between $\mathbf{z}_-$ and $\mathbf{y}$), one can use $\phi'_y = \angle(\mathbf{z}_1, \mathbf{y})$, which is simply a shift of the integration variable. Without loss of generality let $\mathbf{z}_1$ be along the first axis, $\mathbf{z}_1 = (|\mathbf{z}_1|, 0)$. Changing the angles $\varphi_z \to -\varphi_z$ and $\phi'_y \to -\phi'_y$, changes the sign of the second coordinate of the remaning

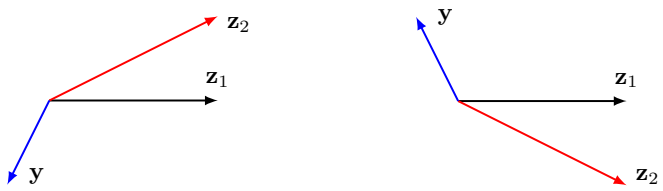

Figure 5.19: On the left: vectors $\mathbf{z}_1, \mathbf{z}_2, \mathbf{y}$ before (left) and after (right) changing the sign of the angles φ_z and ϕ'_y.

vectors and all of their combinations, see Fig. 5.19, which does not modify the scalar product, but changes the sign of $\varepsilon^{ij}\mathbf{a}_i\mathbf{b}_j = a_1 b_2 - a_2 b_1$, which appears in the splitting formula in Eq. (4.5). Therefore, one obtains the same scalar DTMDs, and pseudoscalar DTMDs with changed sign. The change of sign of ϕ'_y does not change the result of the full integral over the angle. Since it was shown that mixed products of scalar and pseudoscalar DPDs vanish after integration, the non-vanishing part of the integral is the same after the transformation, and $W_{\sigma_1\sigma_2}(\mathbf{z}_1, \mathbf{z}_2)$ is symmetric under the change of sign of φ_z.
Hence, the expansion takes a simple form

$$W_{\sigma_1\sigma_2}(\mathbf{z}_1, \mathbf{z}_2) = \sum_{n=0}^{\infty} \cos(n\varphi_z)\, W_{\sigma_1\sigma_2,n}(z_1, z_2)\,, \tag{5.118}$$

where $z_i = |\mathbf{z}_i|$. Recalling Eq. (5.19), we write:

$$\begin{aligned}
&\frac{d\sigma^{\mathrm{DPS}}}{\prod_{i=1,2} dx_i d\bar{x}_i d^2\mathbf{q}_i d\Omega_i}\Big|_{\text{short dist.}} \\
&\quad = \sum_{n=0}^{\infty} \cos\big(n(\phi_{q_1} - \phi_{q_2})\big)(-1)^n \int_0^{\infty} dz_1 \int_0^{\infty} dz_2 \\
&\quad\quad \times\; J_n(q_1 z_1)\, J_n(q_2 z_2) \sum_{\sigma_{1,2}=\pm 1} \big(1 + \sigma_1 \cos\theta_1\big)^2 \big(1 + \sigma_2 \cos\theta_2\big)^2\, W_{\sigma_1\sigma_2,n}(z_1, z_2)\,.
\end{aligned} \tag{5.119}$$

At each pair of z_1, z_2 the Fourier coefficients are computed numerically according to

$$W_n = \begin{cases} \frac{1}{\pi}\int_0^{\pi} d\varphi_z\, W(z_1, z_2, \varphi_z), & n = 0 \\ \frac{2}{\pi}\int_0^{\pi} d\varphi_z\, W(z_1, z_2, \varphi_z)\, \cos(n\varphi_z), & n \geq 1 \end{cases}. \tag{5.120}$$

The $'\sigma_1\sigma'_2$ indices have been suppressed for simplicity. We found that in the 1v1 part the dependence of the integrand on the angle φ_z becomes steep at $\varphi_z \to 0$, especially for

$|\mathbf{z}_1| \approx |\mathbf{z}_2|$. This is because for vanishing φ_z the length of $\mathbf{z}_-$ is minimized so that also the distance between the points $|\mathbf{y}_\pm| \to 0$ on the $\mathbf{y}$-plane gets smaller, cf. Fig. 5.16. This results in the corresponding singularities getting enhanced, see Fig. 5.16. To improve the precision of the integration over $d\varphi_z$, we apply the variable transformation

$$u \mapsto \log\left(\varphi_z + \epsilon_{\varphi_z}\right) . \tag{5.121}$$

Since the integration limits are fixed, as opposed to the previous integrals, no scaling is applied beforehand. The settings of the integration grids for each DPD channel are:

$$\begin{aligned} &[0, 2\pi]_{(24)} , \quad \epsilon_{\varphi_z} = 0.05 \qquad \text{for } 1v1 , \\ &[0, 2\pi]_{(16)} , \quad \epsilon_{\varphi_z} = 0.05 \qquad \text{for } 2v1 + 1v2 , \\ &[0, 2\pi]_{(12)} , \quad \epsilon_{\varphi_z} = 1.0 \qquad \text{for } 2v2 . \end{aligned} \tag{5.122}$$

In our analysis, we focus mostly on the lowest term $n = 0$, however, in Section 5.5.2 we study the higher modes.

Integration over z_1, z_2

Using the results of the previous part, we expressed the n-th Fourier mode in the angle between $\mathbf{q}_1$ and $\mathbf{q}_2$ as a double integral weighted by Bessel functions $J_n(\mathbf{q}_i\mathbf{z}_i)$. For any $n \geq 0$ we compute these integrals using the optimized Levin's method [1]. In that work we found that dividing the integration grid into 2 subgrids leads to a good integration accuracy, while improving the computation time, therefore for the Bessel integrals in the short-distance region for the 2v1+1v2 and 2v2 channels we use the subinterval structure

$$\left[0,\ 0.1\ \text{GeV}^{-1},\ \infty\right]_{(16,24)} . \tag{5.123}$$

The subinterval limits are the same as for the integrals in the large-$\mathbf{y}$ part described in Section 5.3, but here we take fewer points due to the larger computational cost of each (z_1, z_2) point. The resulting integration precision for the 2v1+1v2 channel is presented in Fig. 5.30. Since the 2v2 contribution is over 2 orders of magnitude smaller than the latter, and the corresponding integrands are better behaved, we do not perform the precision study in that case.

It turns out, however, that the integrals for the 1v1 channel are much more challenging, and the described z_i-grids give the relative error estimate of order $\sim 10\%$ – to have better control over the numerics, in that specific channel we use denser grids with 4 subgrids:

$$\left[0,\ 0.1\ \text{GeV}^{-1},\ 0.5\ \text{GeV}^{-1},\ 1\ \text{GeV}^{-1},\ \infty\right]_{(24,24,24,12)} . \tag{5.124}$$

For all grids the variable transformation is identical with the one in Eq. (5.80).

5.5 Short-distance contribution to the cross-section

After describing the model for short-distance DTMDs, and the numerical methods, we present the contribution of the relevant region to the differential cross section of W pair production. Due to the lack of NLO kernels for the short-distance DTMD model, see Section 4.1, the results presented here are computed at NLL. For the corresponding perturbative orders of various perturbative ingredients, see Table 3.1.

Contrary to the large-$\mathbf{y}$ part, there is no clear distinction between the color-singlet and color-nonsinglet contributions, hence in most cases, only the combined contribution will be presented.

The cut-off dependence is discussed for the 1v1 and 2v1+1v2 channels. We show that the unsubtracted 1v1 term dominates the opposite-sign W production, and exhibits a large cut-off dependence, so that the subtraction of DPS/SPS double counting is necessary to make the predictions for this channel. In the case of the 2v1+1v2 contribution, the integrands in the transverse position space diverge like $y_{\pm}^{-1}$, which is however an integrable singularity in a 2-dimensional space. Because of that, the 2v1+1v2 part exhibits a much weaker cut-off dependence than the 1v1 channel, however, the corresponding variation with the value of y_{cut} is still relevant for quantitative studies. The central choice of the cut-off y_{cut} for channels involving the splitting part will be

$$y_{\text{cut}} = \frac{2b_0}{M_W} \qquad \text{for 1v1 or 2v1+1v2 .} \tag{5.125}$$

For these 'n vs m' contributions we consider also $y_{\text{cut}} = b_0/M_W$, and $y_{\text{cut}} = 4b_0/M_W$.

The 2v2 contribution has no singularities at $y_{\pm} = 0$, but since in that case the region of $y_{\pm} \lesssim M_W^{-1}$ gives a suppressed contribution, in that term, we use the smallest value of the cut-off $y_{\text{cut}} = b_0/M_W$, so that the same integration routines can be used.

As in Section 5.3, we will present the differential cross-section partially integrated over the second transverse momentum $\mathbf{q}_2$ up to 20 GeV. In Section 5.5.1 we present q_1-dependence as it was done for the large-$\mathbf{y}$ part in Section 5.3. In Section 5.5.2 we discuss the dependence of the result on the angle between the momenta $\mathbf{q}_1, \mathbf{q}_2$, emerging from the correlations between $\mathbf{z}_1$ and $\mathbf{z}_2$ at DTMD level. We show that the angular dependence in the 1v1 and 2v1+1v2 channels is strong, and the expansion of Eq. (5.28) converges rather slowly. However, one still can extract the corresponding Fourier modes. The estimation of the integration precision of the most challenging terms, 1v1 and 2v1+1v2 is presented in Section 5.5.3. In Section 5.5.4 we compare the relative sizes of the color-singlet and nonsinglet parts in the 2v2 and 2v1+1v2 channels, for a specific rapidity scale, at which one separates the color channels (cf. the discussion in Section 4.2). The individual contribution of different color representations in the 1v1 channel is not studied, because of the large cut-off dependence of this contribution without the subtraction term.

5.5.1 q_1-dependence

We present the same error analysis as described in Section 5.2, with the only difference that for the short-distance part we keep a fixed model of the Collins-Soper kernel, as in Eq. (5.53). The short-distance 2v2 contribution to the differential cross section of like-sign lepton pair production is presented in Fig. 5.20. At the considered order in perturbation theory is the only short-distance contribution to this channel. We present the results for two values of rapidities: the central one $(0, 0)$, and large symmetric values $(3, 3)$. We find that for other considered rapidities, as well as in the case of opposite-sign lepton production the results look similar, and bring no new insight.

In Fig. 5.21 given is the 2v1+1v2 contribution for opposite-sign leptons for the same rapidites as in the previous case. We observe that also in this case the shapes of the differential cross sections do not differ much between different rapidities, but there is much stronger suppression at larger values of (Y_1, Y_2). At large and asymmetric rapidites $(3, -3)$ the result is about 300 times smaller than for the $(Y_1, Y_2) = (0, 0)$. The same observations apply to the case of the smaller cut-off $y_{\rm cut} = b_0/M_W$. The comparison between the results at different cut-offs for a larger number of rapidity pairs is shown in App. G.4.

In Figs. 5.22-5.23 we show the contribution for the opposite-sign lepton pair production from the 1v1 channel. We take 3 values of the cut-off:

$$y_{\rm cut} = \frac{b_0}{M_W}, \frac{2b_0}{M_W}, \frac{4b_0}{M_W} \,. \tag{5.126}$$

By comparing the results for subsequent values of the cut-off we can estimate how large is the value of the DPS/SPS subtraction term. Since this channel turns out to be more important, and the rapidity-dependence is more pronounced than in the remaining channels, we show the results for

$$(Y_1, Y_2) = (0, 0),\ (1.5, 0),\ (3, 0), (3, 3).$$

The result for strongly asymmetric rapidities $(3, -3)$ is not shown, since is turns out to be of order 10^{-2} zbarn/ GeV $= 10^{-5}$ abarn/ GeV.

We notice that for large Y the 1v1 part of the differential cross section for symmetric rapidities (Y, Y) is larger than for asymmetric ones $(Y, -Y)$, since it is proportional to a product of two gluon PDFs at momenta fractions $(x_1 + x_2)$ (righ-moving hadron) and $(\bar{x_1} + \bar{x}_2)$ (left-moving):

$$\begin{aligned} &x_1 + x_2 = 2x_0 e^{Y}, && \text{and} \quad \bar{x_1} + \bar{x}_2 = 2x_0 e^{-Y} && \text{for } (Y, Y)\,, \\ &x_1 + x_2 = x_0(e^{Y} + e^{-Y}), && \text{and} \quad \bar{x_1} + \bar{x}_2 = x_0(e^{Y} + e^{-Y}) && \text{for } (Y, -Y)\,. \end{aligned} \tag{5.127}$$

In the first case, the parent gluon with small longitudinal momentum gets the enhancement at small x. On the other hand, in the second case, the momentum

fractions of both gluons are relatively large, and the corresponding PDF product is suppressed. For $Y = 3$, there is one gluon with $x \approx 0.25$, and other with $\bar{x} \approx 6.2 \times 10^{-4}$ for symmetric rapidities, and two gluons with $x = \bar{x} \approx 0.12$ for asymmetric rapidities.

We observe that in some 1v1 plots, e.g. $(Y_1, Y_2) = (1.5, 0)$ and $(3, 0)$ for the smallest cut-off, visible are some oscillations of the results in the q_1-space. As indicated by the precision study in Section 5.5.3, this is most likely due to numerical errors of the integrations. Notice that oscillations vanish at larger y_{cut}, where the integration precision is better.

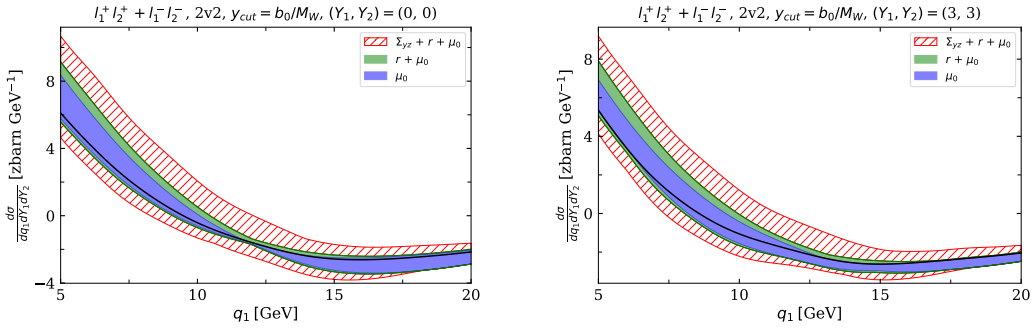

Figure 5.20: Like-sign leptons production, short-distance 2v2 contribution. On the left: central rapidities $(0, 0)$, on the right: large rapidities $(3, 3)$. Notice that the result is given in the units of zbarn/GeV.

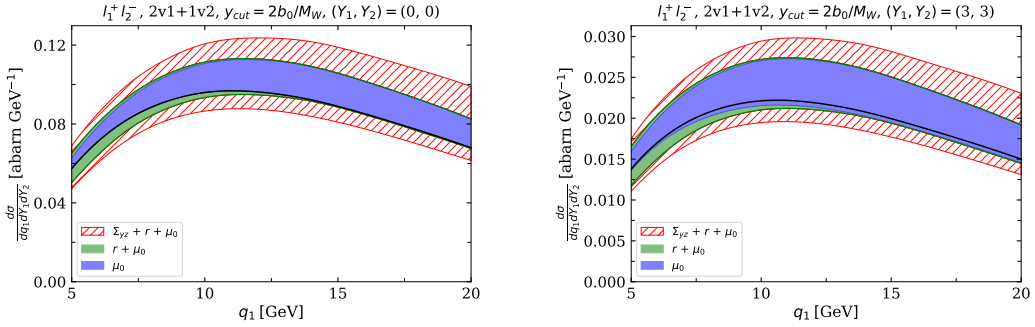

Figure 5.21: Opposite-sign leptons production, short-distance 2v1 contribution. On the left: central rapidities $(0, 0)$, on the right: large rapidities $(3, 3)$. The result is presented in the units of abarn/GeV.

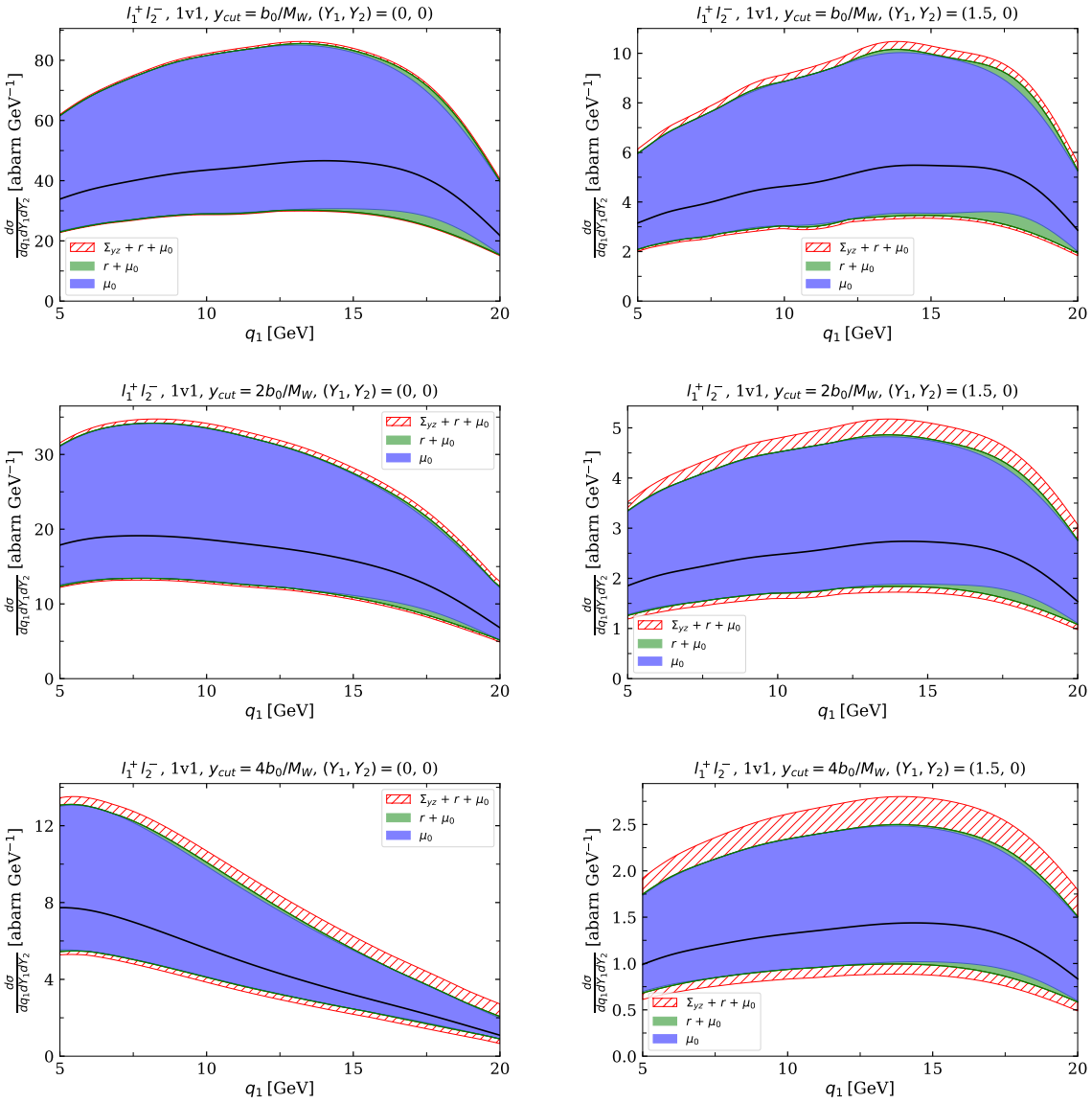

Figure 5.22: Upper part: $y_{\text{cut}} = b_0/M_W$, middle: $y_{\text{cut}} = 2b_0/M_W$, lower part: $y_{\text{cut}} = 4b_0/M_W$.

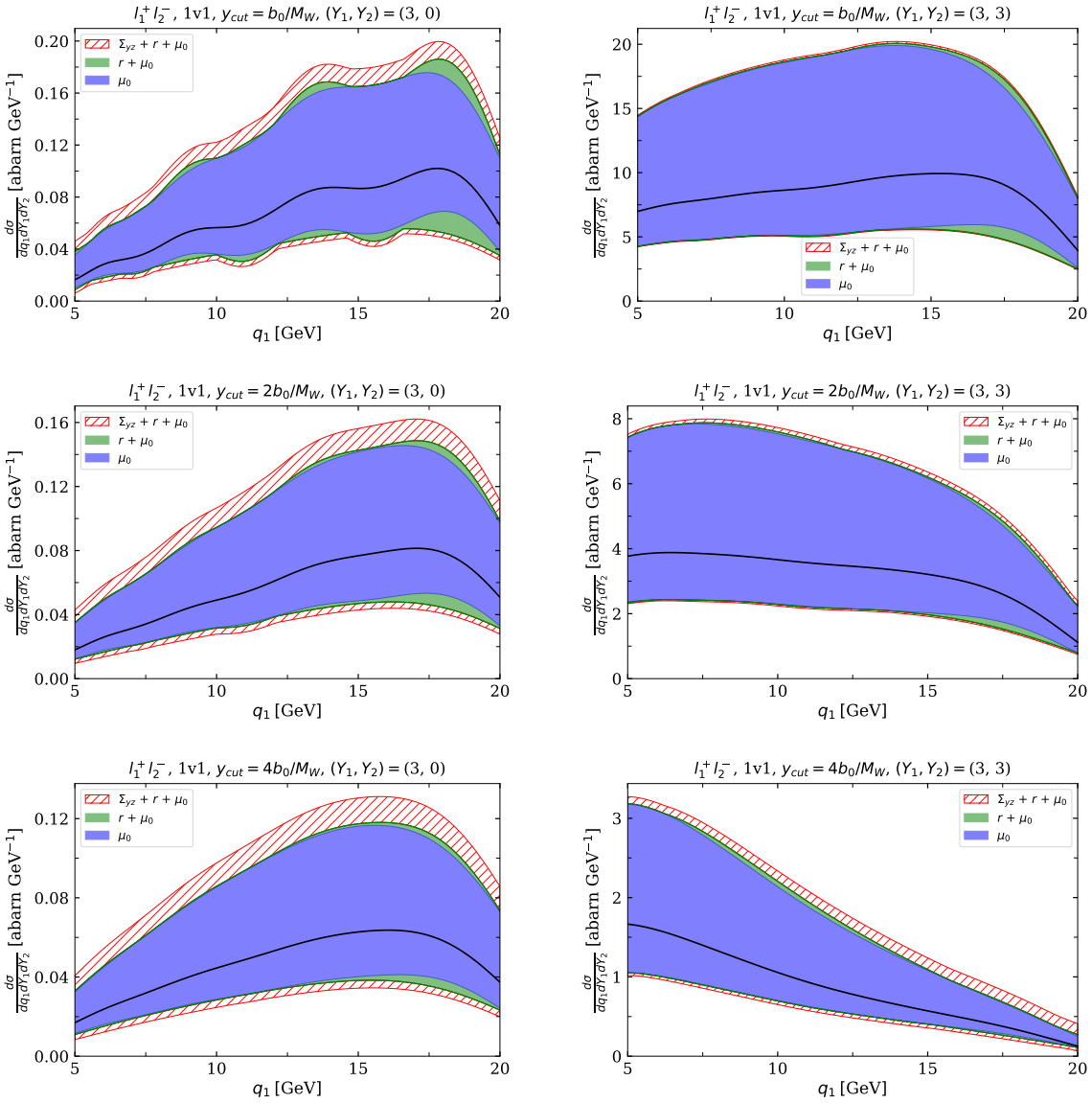

Figure 5.23: Upper part: $y_{\text{cut}} = b_0/M_W$, middle: $y_{\text{cut}} = 2b_0/M_W$, lower part: $y_{\text{cut}} = 4b_0/M_W$.

5.5.2 Dependence on the angle $\angle(\mathbf{q}_1, \mathbf{q}_2)$

As discussed in Chapter 4, the angular correlations between the distances $\mathbf{z}_1$ and $\mathbf{z}_2$ at the level of DTMDs lead to nontrivial angular dependence of the differential cross-section on the angle ϕ_q between the transverse momenta $\mathbf{q}_{1,2}$ of the produced W bosons. As described in Section 5.1, Eq. (5.19), the short-distance part of the differential cross-section can be expanded as a series in $\cos(n\phi_q)$ for integer $n \geq 0$, where ϕ_q is the angle

between the momenta of W bosons:

$$\phi_q = \angle(\mathbf{q}_1, \mathbf{q}_2) \,. \tag{5.128}$$

The differential cross-section can be expanded as:

$$\frac{d\sigma}{d\phi_q \prod_{i=1,2} dq_i dY_i} = \sum_{n_q=0}^{\infty} \frac{d\sigma(n_q)}{\prod_{i=1,2} dq_i dY_i} (-1)^{n_q} \cos\left(n_q \phi_q\right) \,. \tag{5.129}$$

As it turns out, for the 1v1 and 2v1+1v2 channel without subtractions, the expansion converges slowly so that the full description of the angular dependence is a difficult task. A better choice of integration variables would be $\mathbf{y}, \mathbf{z}_+, \mathbf{z}_-$, since the enhancement of the integrand occurs at small $\mathbf{z}_-$. However, this would lead to expressing the differential cross-section in terms of combinations of the transverse momenta:

$$\mathbf{q}_\pm = \frac{1}{2}\left(\mathbf{q}_1 \pm \mathbf{q}_2\right) \,, \tag{5.130}$$

see App. F. Such form would make the comparison with the large-$\mathbf{y}$ part more difficult, therefore we do not change the integration variables in this work. However, we want to note that the integration algorithm presented in Section 5.4.1 can be straightforwardly adapted to integrate over $(\varphi_y, |\mathbf{y}|, |\mathbf{z}_+|, |\mathbf{z}_-|)$, and the angle between $\mathbf{z}_+, \mathbf{z}_-$. In Figs. 5.24 and 5.25 we show the first 6 Fourier modes defined in Eq. (5.129) for the 1v1 and 2v1+1v2 channels, obtained using the central value of the cut-off $y_{\text{cut}} = 2b_0/M_W$. We see that the convergence with higher modes n_q is slow, making it difficult to provide the angular dependence in terms of momenta $\mathbf{q}_1, \mathbf{q}_2$.

$$(Y_1, Y_2) = (0, 0), \quad q_1 \in [5 \text{ GeV}, 20\,\text{GeV}] \,, \quad q_2 = 10 \text{ GeV}, 15 \text{ GeV} \,. \tag{5.131}$$

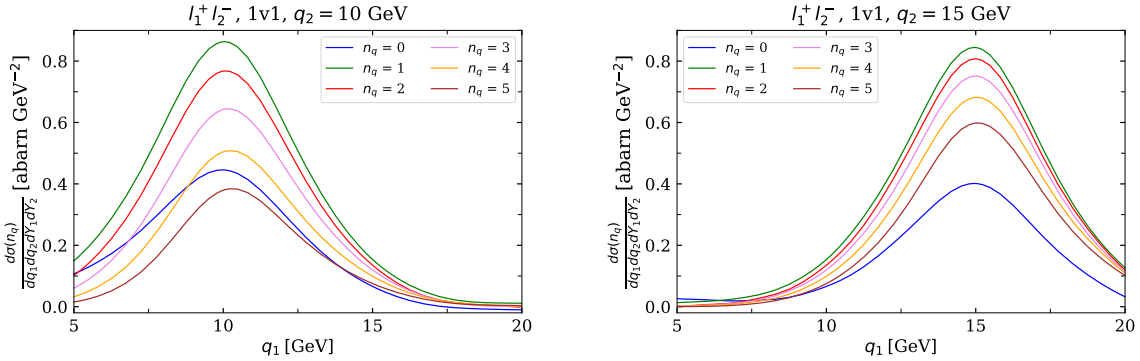

Figure 5.24: First 6 Fourier modes of the 1v1 part of the differential cross section of production of opposite-sign W pair decaying into $l_1^+ l_2^-$ leptons, see Eq. (5.129).

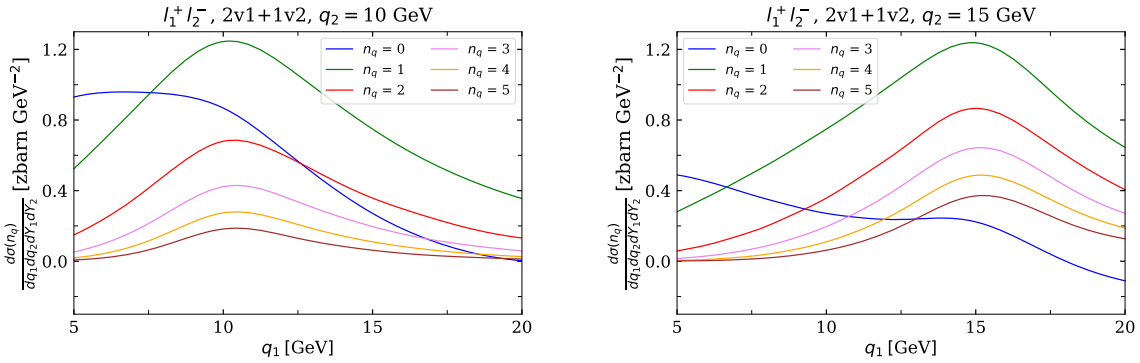

Figure 5.25: First 6 Fourier modes of the 2v1+1v2 part of the differential cross section of production of opposite-sign W pair decaying into $l_1^+ l_2^-$ leptons, see Eq. (5.129).

Because of a large number of the Fourier modes, plots in Figs. 5.24-5.25 were obtained using grids with a doubled number of points in φ_z integrals, see Eq. (5.109), and z_i-grids with the same limits as in Eqs. (5.124)-(5.123), but with $(24, 24, 24, 24)$ points for 1v1, and $(24, 32)$ points for 2v1+1v2.

To obtain the estimation of the model uncertainties in this channel, we perform the analogous analysis as for the angle-integrated case. For $n_q = 1, 2$ we compute the corresponding Fourier modes, and integrate the result in momentum q_2 up to 20 GeV:

$$\int_0^{20\ \mathrm{GeV}} q_2\, dq_2 \int_0^{2\pi} \cos\left(n_q \phi_q\right) \frac{d\sigma}{d\phi_q \prod_{i=1,2} dq_i dY_i} \,. \tag{5.132}$$

We apply the same uncertainty analysis as in Section 5.5.1. This provides a straightforward comparison of the impact of different model uncertainties at the considered Fourier modes.

In Fig. 5.26 we show the Fourier modes of 1v1 term for 3 considered values of the short-distance cut-off at central rapidity. As in the previous case, we observe a strong cut-off dependence of the result, cf. Figs. 5.22-5.23. In Fig. 5.27 we compare the same Fourier modes in the case of 2v1+1v2 channel for $y_{\rm cut} = b_0/M_W$ and $y_{\rm cut} = 2b_0/M_W$. Contrary to the 1v1 case, the cut-off dependence in this channel is much weaker but still visible. In both cases, the dominant contribution to the uncertainty estimate is due to the matching scale variation. However, the interpolation dependence seems weaker than in the angle-integrated cases, which should not be surprising, as in the limit $y \gg z_i$ the dependence of DTMDs on the angle φ_z vanishes. The presented behavior holds also for other studied pairs of rapidities (Y_1, Y_2).

Let us notice that in the 2v2 channel we find the considered Fourier modes to be of order 10^{-1} zbarn/ GeV, which is completely negligible compared to the total large-$\mathbf{y}$ + short-distance contribution. We observe strong oscillations due to the Bessel transform, therefore our only claim in that channel is that the angular dependence in the discussed

channel, and – what follows – the angular dependence at NNLL like-sign W pairs production is a suppressed effect. This might be modified after including higher-order PDF-DTMD splitting.

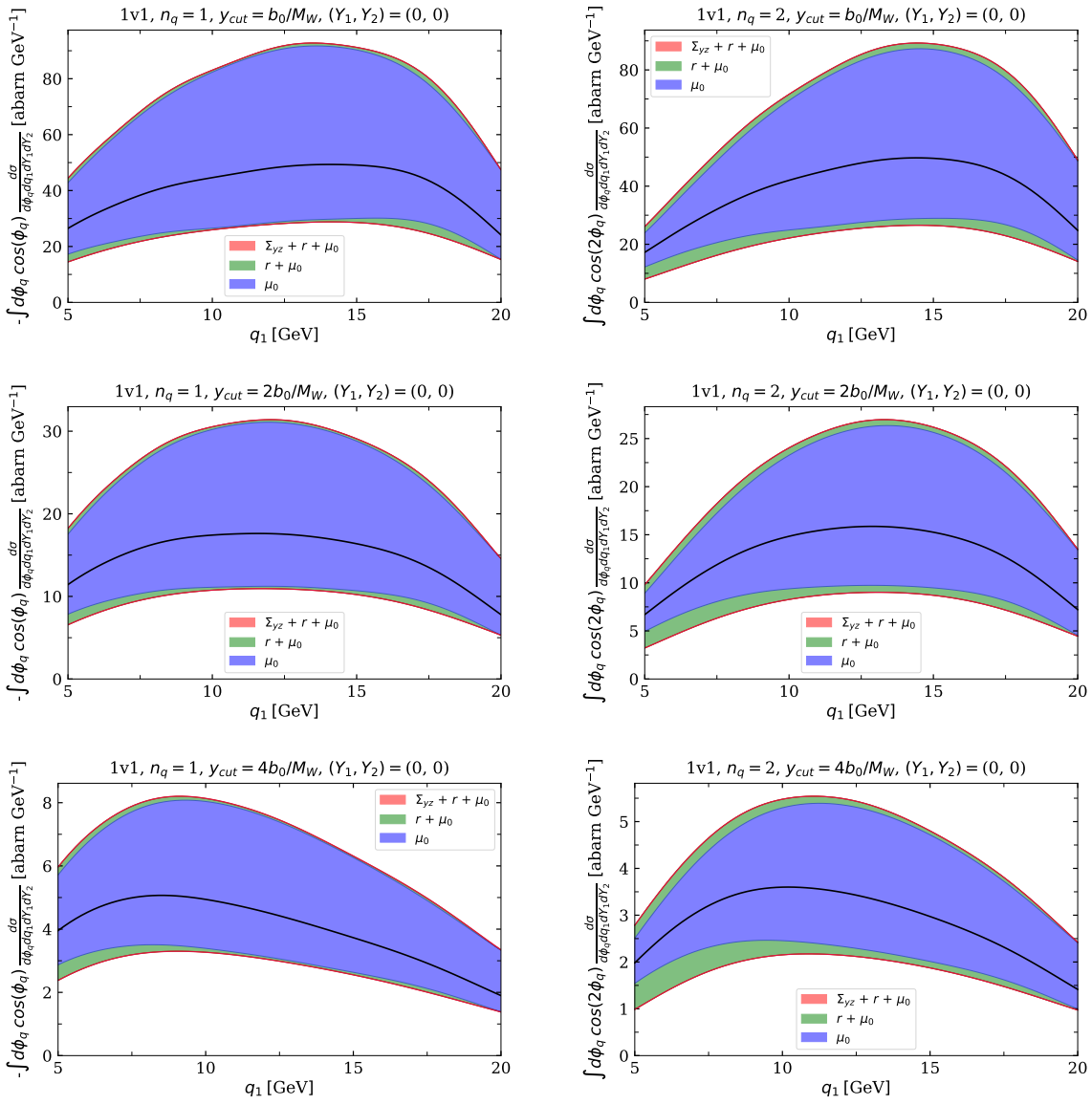

Figure 5.26: First (left) and second (right) Fourier mode of 1v1 contribution to the differential cross section. Presented are the results for 3 different cut-off values: $y_{\rm cut} = b_0/M_W$ (top), $y_{\rm cut} = 2b_0/M_W$ (middle), and $y_{\rm cut} = 4b_0/M_W$ (bottom).

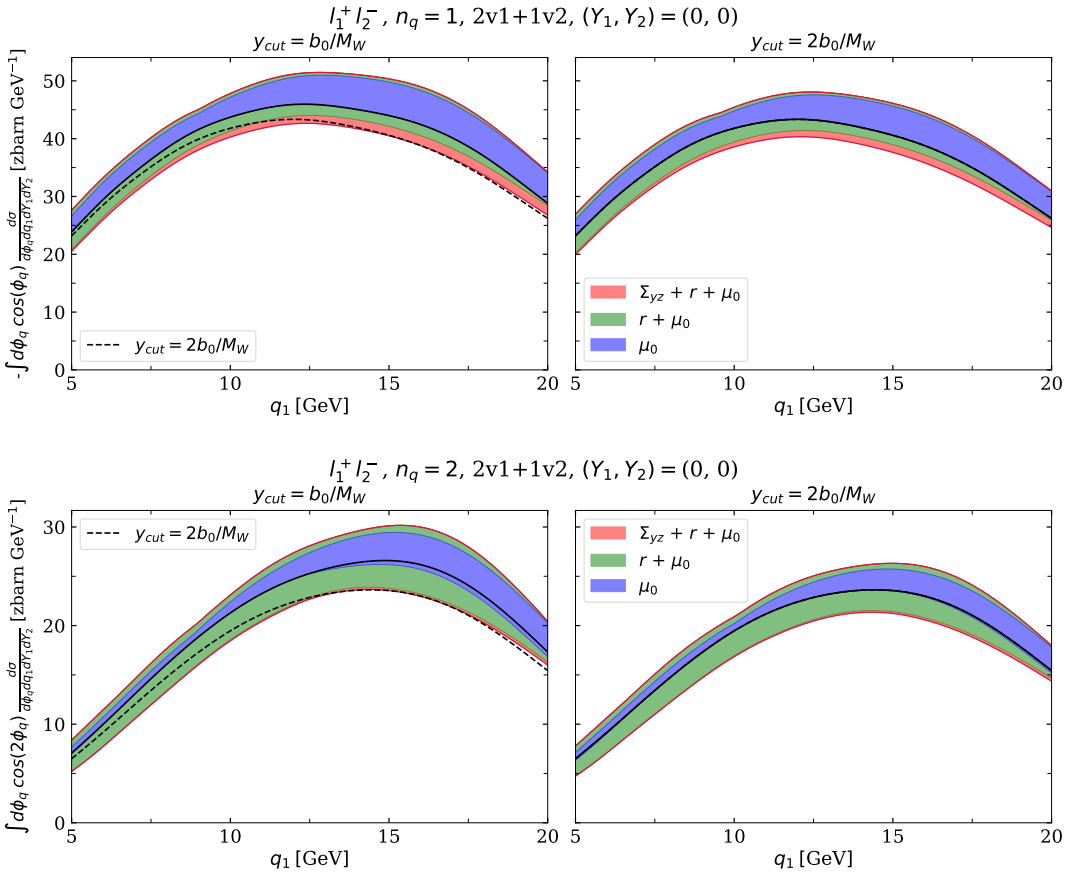

Figure 5.27: First (top) and second (bottom) Fourier mode of 2v1+1v2 contribution to the differential cross-section. Left: the result at the cut-off value $y_{\text{cut}} = b_0/M_W$, and on the right: for $y_{\text{cut}} = 2b_0/M_W$. Solid black lines indicate the result for the default settings at a fixed cut-off. The dashed black line on the left (equal to the solid line on the right) is the result for a larger cut-off, added to show more clearly the difference between the results at different cut-offs.

5.5.3 Precision estimation for numerical integration

In this part, we discuss the integration precision of the results presented in the previous section. We show that the integration errors of 1v1 and 2v1+1v2 contributions, which tend to be especially difficult in numerical integration due to the $1/y_{\pm}$-singularities, the numerical errors are sufficiently small, and should not affect the results concerning the sizes of the results at different cut-offs, or the relative sizes of our estimates for the model uncertainties.

First, we estimate the integration error by doubling the number of gridpoints in the integrals over $d^2\mathbf{y}$ and $d\varphi_z$ and computing the relative difference between such a result

and the one obtained using the nominal grids described in Section 5.5.3: Eq. (5.109), Table 5.1, and Eq. (5.122).

Since the computation of the 1v1 term is already quite expensive due to many points in the z_i-grids, for this test, we compute the 1v1 terms (both with standard and enhanced precision in $d^2\mathbf{y}d\varphi_z$) using smaller grids in z_i, namely:

$$\left[0,\ 0.1\ \text{GeV}^{-1},\ \infty\right]_{(32,24)} \quad \text{for } z_1, \qquad \left[0,\ 0.1\ \text{GeV}^{-1},\ \infty\right]_{(32,26)} \quad \text{for } z_2\ . \tag{5.133}$$

The z_i-grids used to test the precision of the 2v1+1v2 term are identical to the nominal ones in Eq. (5.123).

To estimate the precision of the Hankel transforms, we use denser grids in z_1, z_2:

$$\begin{aligned} &\{32, 32, 32, 16\} \text{ points} && \text{for } 1v1\ , \\ &\{24, 32\} \text{ points} && \text{for } 2v1 + 1v2\ , \end{aligned} \tag{5.134}$$

and compare with results obtained with the grid settings in Eqs. (5.123)-(5.124). As shown in Section 5 of [1], the precision of the Bessel integrals computed using the method described therein grows rapidly with the number of gridpoints, and based on that we expect the described upgrade of the grids to give a sufficiently good estimate.

In Fig. 5.28 we show the error estimates for the results for the 1v1 channel presented in Section 5.5.1 for 3 different values of the cut-off parameter y_{cut}. The precision for the first two Fourier moments of the 1v1 term, defined in Eq. (5.132) and shown in Section 5.5.2, is shown in Fig. 5.29, in this case only for $y_{\text{cut}} = 2b_0/M_W$.

We find that the error estimates for $d^2\mathbf{y}d\varphi_z$ integrals are indeed small – in most cases about 10^{-3}, with a single exception at the smallest cut-off value, on the upper-left plot in Fig. 5.28, and lower-right plot of Fig. 5.29. A comment should be made on the peak of the error estimate for $n_F = 2$ at $(Y_1, Y_2) = (3, 0)$ – we found that for the z_i grid settings given in Eq. (5.133) there is a zero-crossing in the result, which leads to large relative errors.

The precision of the Bessel integrals is worse by about one order of magnitude and goes up to around 10% for the most problematic rapidity pair, see the $(Y_1, Y_2) = (3, 0)$ results. At larger cut-off values the precision improves, and the error estimate drops below 1%.

Finally, in Fig. 5.30 we present the precision estimates for the 2v1+1v2 part, for a single value of the cut-off $y_{\text{cut}} = b_0/M_W$, which is the most challenging cut-off value in this channel. For the angle-integrated cross-section the precision deteriorates at larger values of q_1, but for $q_1 \lesssim 12$ GeV remains at around 1% level. For the Fourier modes $n_q = 1, 2$ the precision estimate is at the level of a few %. Based on our experience with the 1v1 part, modification of grids in z_i, as well as optimization of the variable transformation parameters of Section 5.4.1 would improve the errors, however, given a rather small contribution of this term, we decided that the current precision is satisfactory.

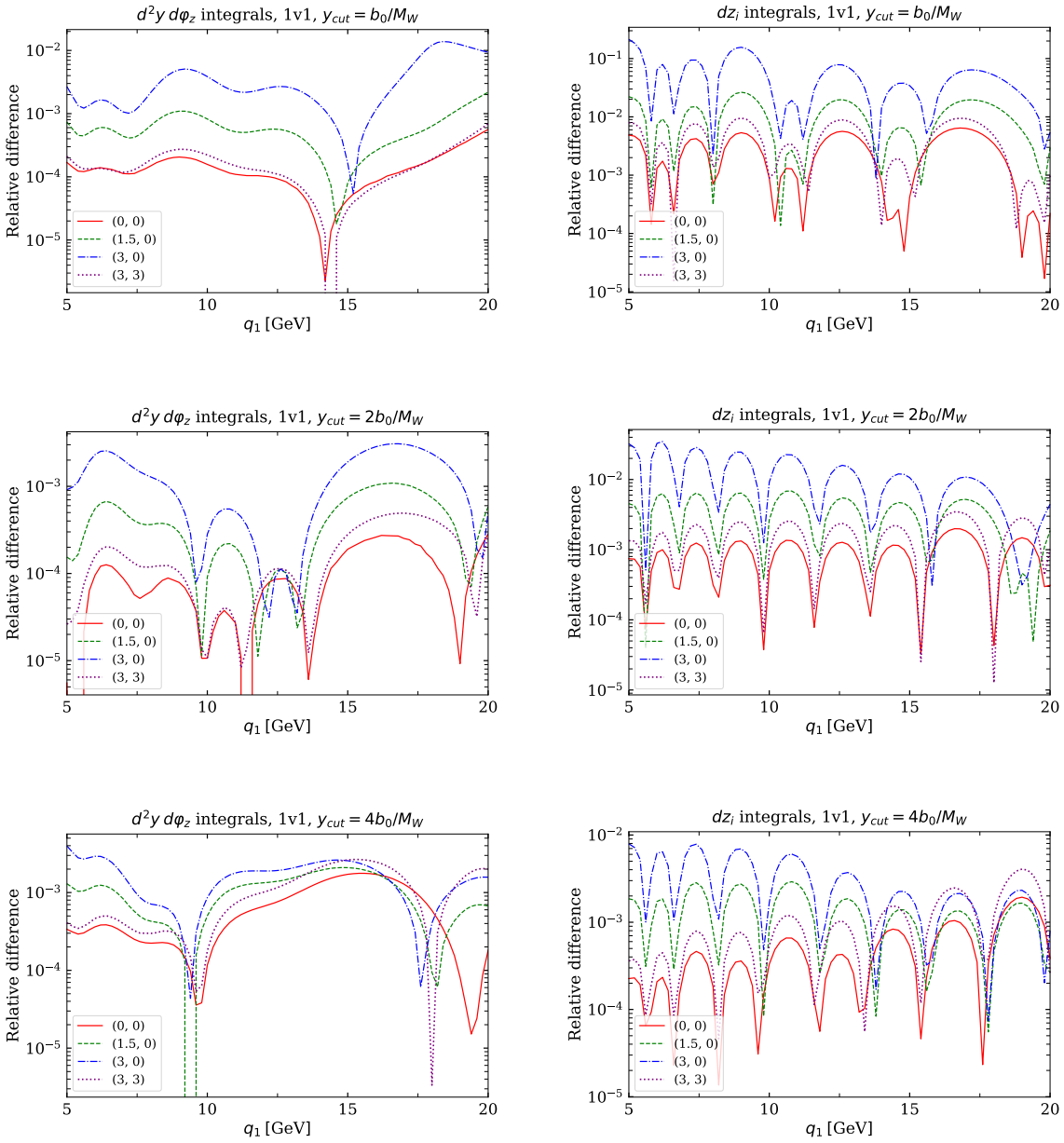

Figure 5.28: Integration precision, cross section integrated over the angular part of $\mathbf{q}_{1,2}$.

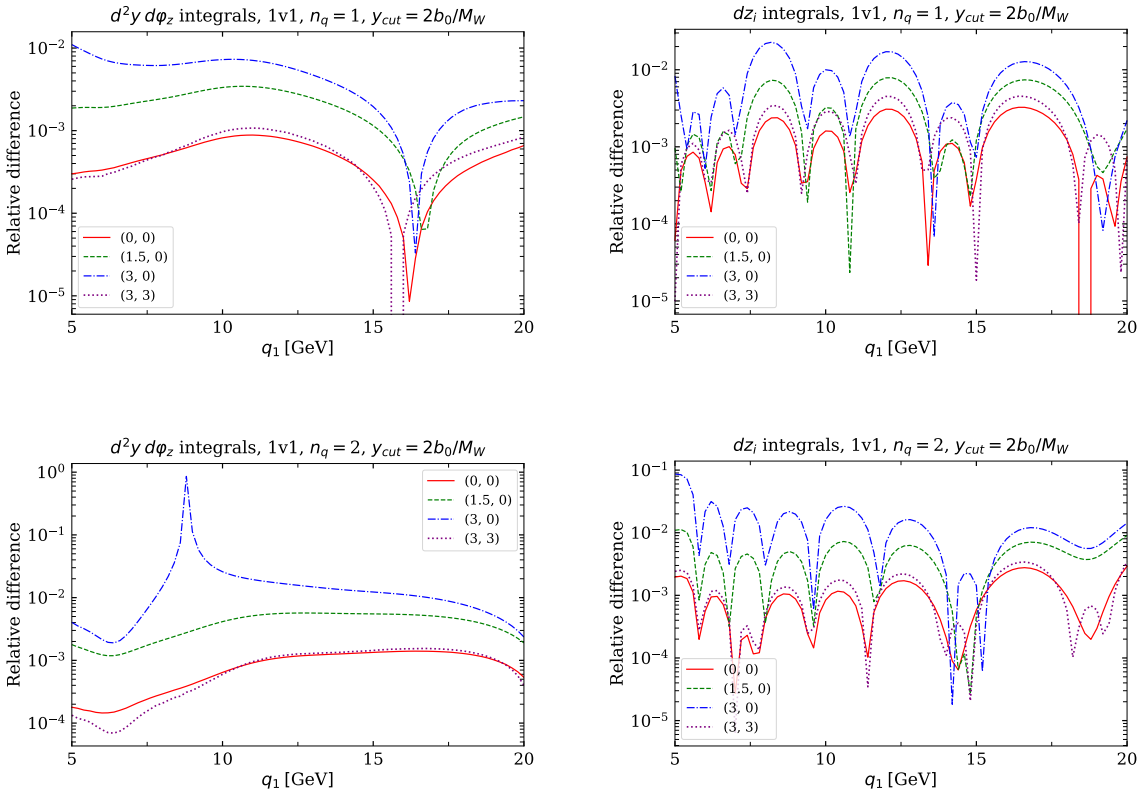

Figure 5.29: Integration precision of the 1v1 part, first and second moment of ϕ_q.

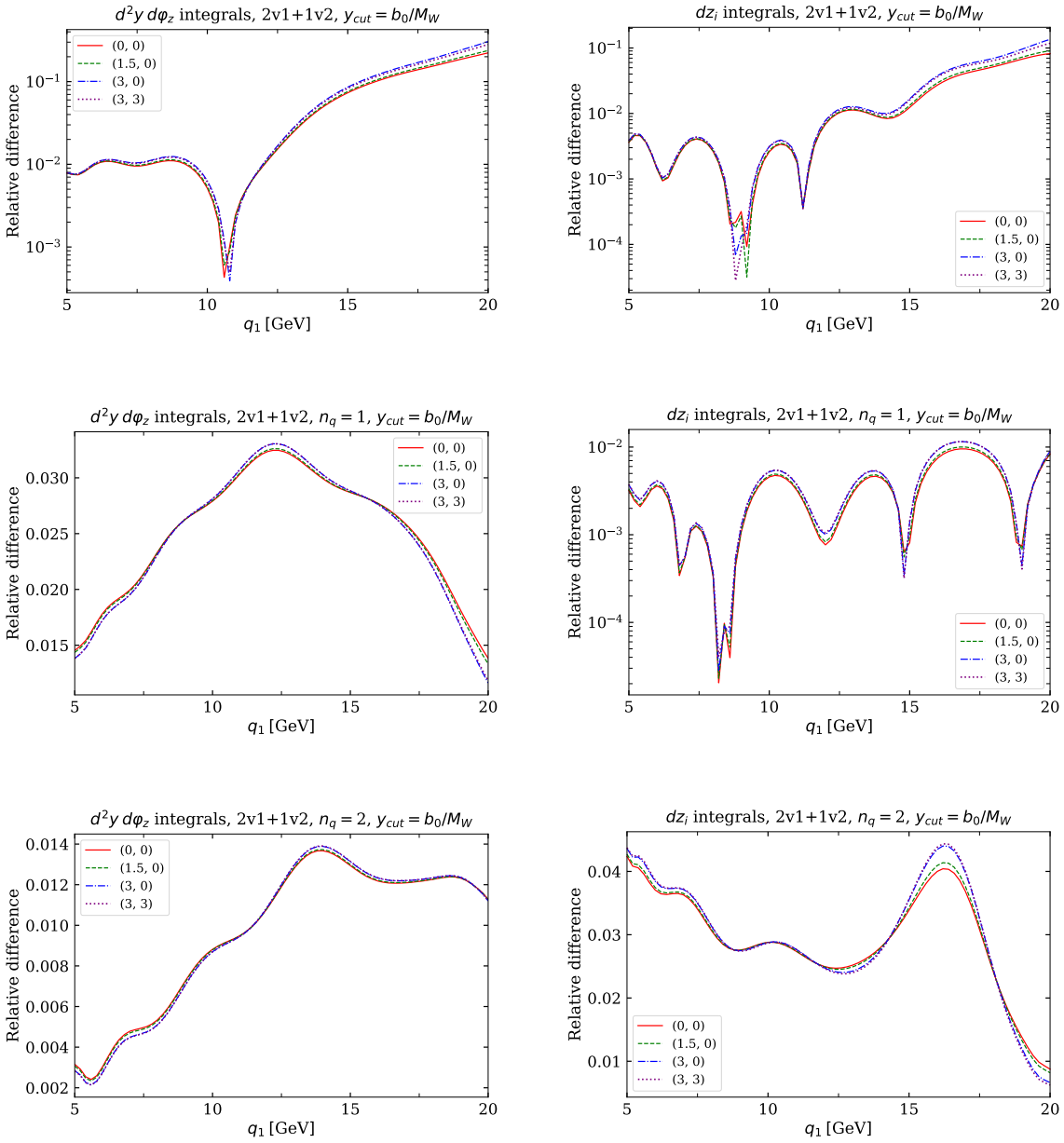

Figure 5.30: Integration precision of the 2v1+1v2 term. Top: angle-integrated results. Middle and bottom: first and second moment in ϕ_q.

5.5.4 Color-singlet vs color-nonsinglet part

The distinction between different color channels in the short-distance region is not clear due to color-representation mixing under the rapidity evolution, see Section 4.2. Trying to define a contribution from a given color representation, as it was done in the large-$\mathbf{y}$

case, one runs into a problem of the mixing between singlet and octet terms in the product of evolved DTMDs.

However, to gain some insight into the dependence of the total result on the color-nonsinglet part, we will make the distinction at the initial scales, where one formulates the Ansatz for DTMDs – in this way, we will assess the model dependence of our nonperturbative model for parton distributions in the color-nonsinglet channels. As seen from Eq. (5.4), the product of DTMDs in the cross-section contains 4 combinations of parton distributions at initial scales: ${}^{11}F\,{}^{11}\bar{F}$, ${}^{11}F{}^{88}\bar{F}$, ${}^{88}F{}^{11}\bar{F}$, ${}^{88}F{}^{88}\bar{F}$. For simplicity, we compute only the $11,11$ part and the total result, and compare their relative sizes. The individual contributions for the 2v2 term are given in Fig. 5.31, and for 2v1+1v2 in Fig. 5.32. The qualitative behavior for all combinations of leptons l_1, l_2 charges is the same, hence we present only the result for the production of like-sign lepton pairs.

It is clearly seen that the color-singlet part dominates over the remainder term. The error bands correspond to the combined uncertainties due to the initial scale variation, $F_{\rm NP}$ parametrization, and the interpolation function.

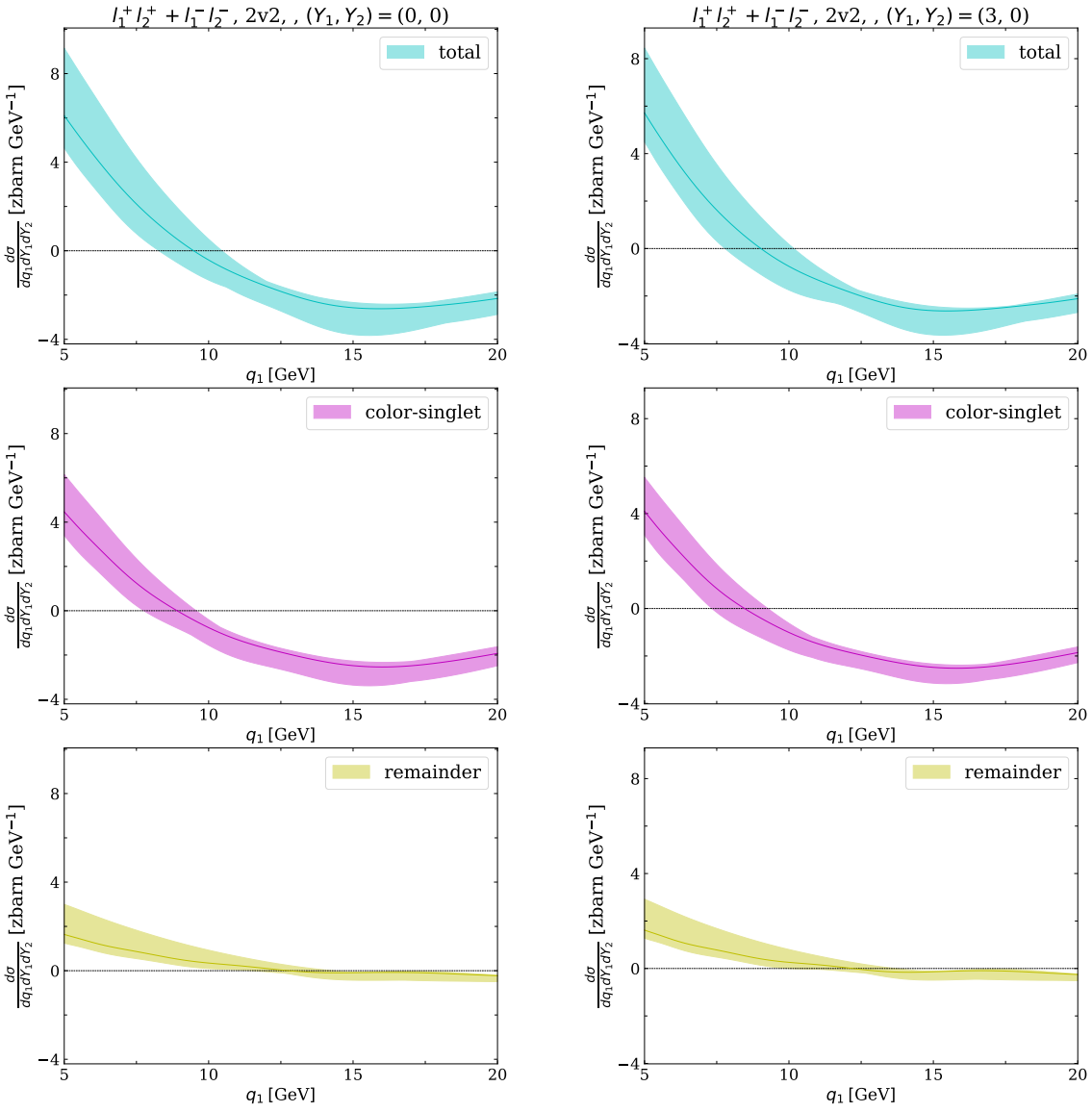

Figure 5.31: Comparison of the contribution of different color channels to the short-distance 2v2 part for the production of like-sign lepton pair. Left: central rapidities, right: $(Y_1, Y_2) = (3, 0)$. The 'remainder' is the difference between the total result and the singlet part. On all of the plots, the value of 0 is indicated with a black line.

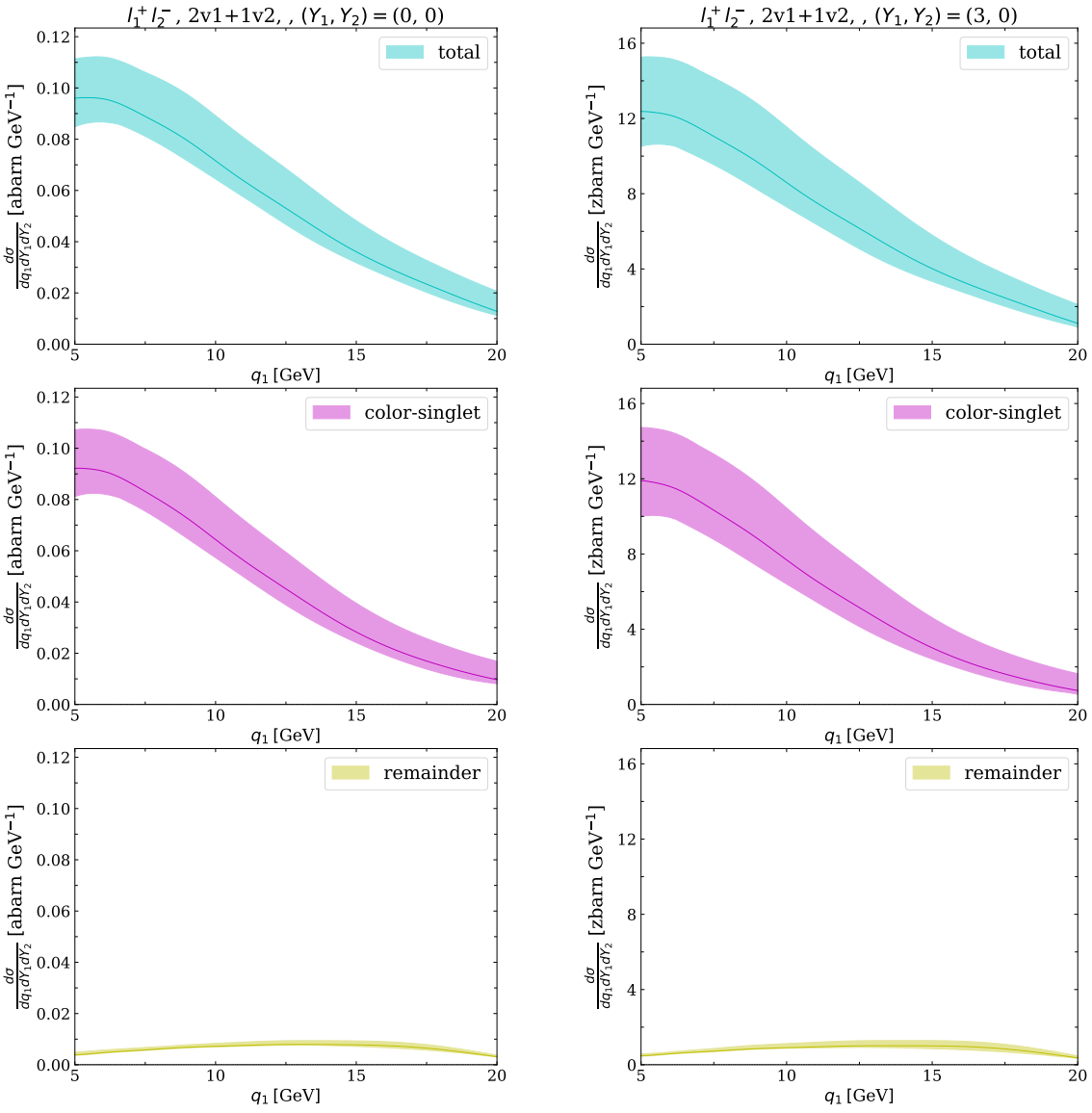

Figure 5.32: Comparison of the contribution of different color channels to the short-distance 2v1+2v1 part for production of opposite-sign lepton pair. Left: central rapidities, right: $(Y_1, Y_2) = (3, 0)$.

5.6 Total cross-section

In Sections 5.3 and 5.4 we have studied the individual contributions to the differential cross-section of W boson pair production via double-parton scattering in both "large-$\mathbf{y}$" and "short-distance" regions. We discussed the theoretical aspects of the computation,

such as the choice of the intermediate scales, the rapidity evolution, in particular, the treatment of the corresponding short-distance singularities, as well as the numerical part of the computation. We compared the relative sizes of contributions from all DPD channels 'n vs m', for partons in the color-singlet and color-nonsinglet representations.

In this Section we combine the previously obtained results, allowing us to present a discussion of the size of the predictions and the error estimation for the considered process. It should be noted that the large-$\mathbf{y}$ part is computed at NNLL, and the short-distance part at NLL accuracy, see Table 3.1.

5.6.1 Combining the short-distance and large-y terms

Both large-$\mathbf{y}$ and short-distance terms require the non-perturbative input. In the previous part, we estimated the uncertainty of individual terms by varying these parameters and finding the resulting minimal and maximal value at each point. A similar approach will be applied to the sum of both contributions, but two points should be addressed beforehand. First, as stated in Section 5.4, in the short-distance part, we consider only a single parametrization of the Collins-Soper kernel given in Eq. (5.53). However, we combine it with the large-$\mathbf{y}$ term with different choices of δK, since that contribution, by construction, is more sensitive to the rapidity evolution kernel.

Secondly, care is needed for the choice of the matching scales. Although the choice of the DTMD-DPDF matching scales (μ_{01}, μ_{02}), and the short-distance matching scale μ_0 look very similar, they should not be regarded as equivalent, hence we combine the large-$\mathbf{y}$ and short-distance scales using the 7-point variation for the matching scales in both terms. Recall from Eq. (3.56) and (4.23) that the choice of the matching scales is parametrized by a single parameter denoted as κ, meaning that for a perturbatively small distance $\mathbf{b}$ the corresponding scale is

$$\mu_0\big(\mathbf{b}, \kappa\big) \approx \kappa \times \frac{b_0}{|\mathbf{b}^*|}\,, \tag{5.135}$$

the "$\approx$" is used since we omit the constant term that ensures that at large distances the matching scale approaches the same value independently on κ. For each term we consider $\kappa \in \{1, 2, \frac{1}{2}\}$ – using the 7-point rule means that while we consider combinations of the large-y and short-distance terms with different respective values of κ, we disregard the combinations with extreme values on the parameter.

To formalize, for possible choices of the matching scales parametrized by κ_1, κ_2, the nonperturbative part of the Collins-Soper kernel δK, see Eqs. (5.56)-(5.53), the parameter r describing the large-z behavior of DTMDs, and the interpolating function Σ_{yz}, we consider the combinations:

$$\begin{aligned} &\sigma^{\text{large-y}}\big(\kappa_1, \delta K, r, \Sigma_{yz}\big) \;+\; \sigma^{\text{short-dist}}\big(\kappa_2, \text{DPT24}, r, \Sigma_{yz}\big)\,, \\ &\text{such that } (\kappa_1, \kappa_2) \neq \big(2, \tfrac{1}{2}\big) \text{ or } \big(\tfrac{1}{2}, 2\big)\,. \end{aligned} \tag{5.136}$$

The combined results in the 2v1+1v2 channel for opposite-sign W production are presented in Fig. 5.33. Recall that the corresponding contribution to opposite-sign W production only has the large-$\mathbf{y}$ part at the considered accuracy. In Fig. 5.34 we show the combined 1v1 large-$\mathbf{y}$ term plus the short-distance one with the largest considered cut-off $y_{\rm cut} = 4b_0/M_W$. In this channel, we see significant cancellations of the interpolation uncertainties at smaller rapidities – for large and asymmetric values of (Y_1, Y_2) the splitting short-distance part is strongly suppressed compared with the large-$\mathbf{y}$ part. We see that also for smaller values of the cut-off, however, in that case the short-distance splitting part completely dominates the result, and hence one cannot see the cancellations on a plot. In Fig. 5.35 we provide the comparison of the interpolation uncertainties for two extreme values of the cut-off, and show that in both cases they are almost identical (as it should be, since the cut-off does not affect the interpolation region), and the cancellation works independently of the cut-off value.

Since for the 2v2 channel, the large-$\mathbf{y}$ part is 2 orders of magnitude larger than the short-distance part for all boson channels, we do not show the individual and combined plots with the error band for that part.

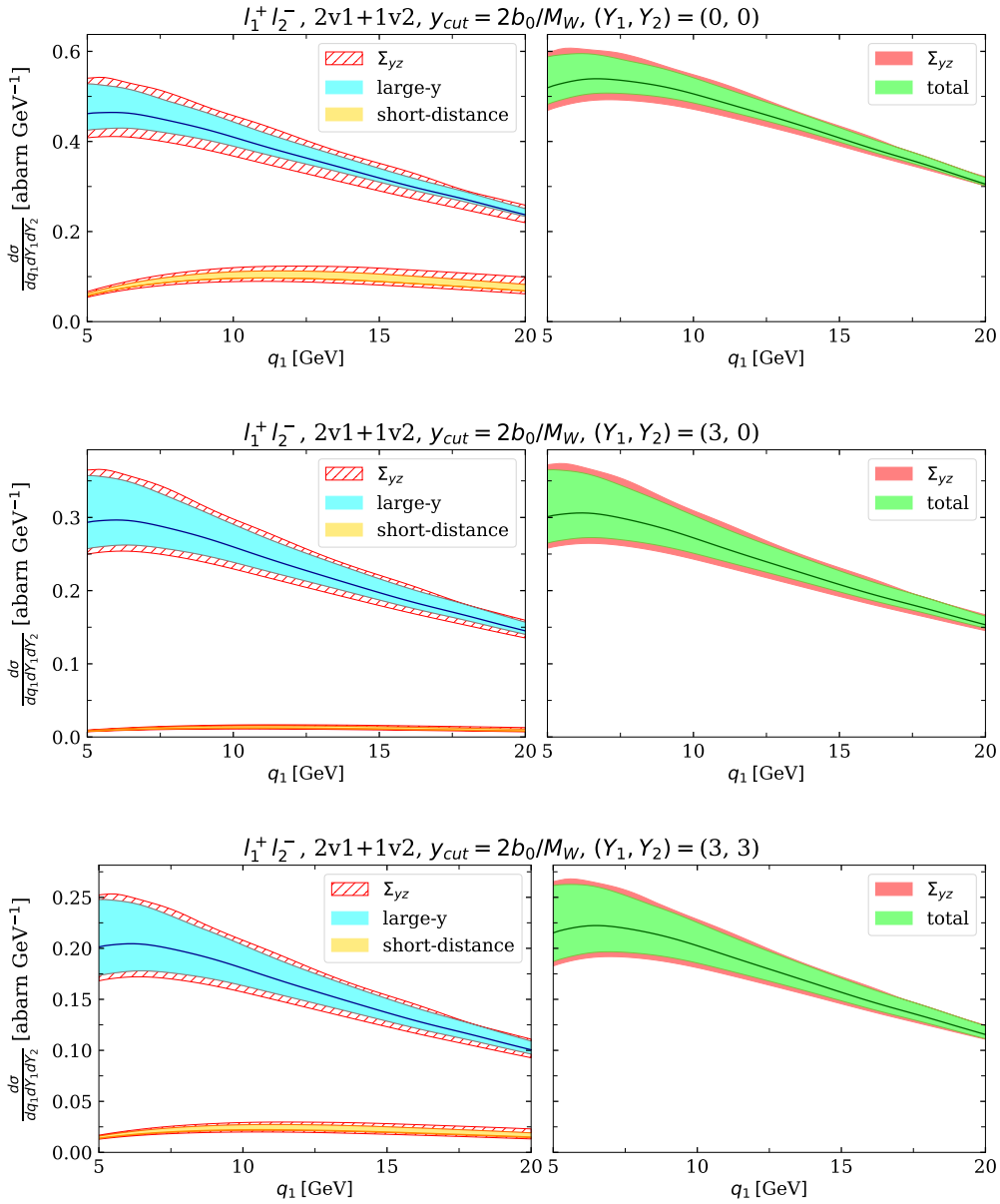

Figure 5.33: Combined large-**y** and short-distance contributions to the 2v1+1v2 channel at different rapidities.

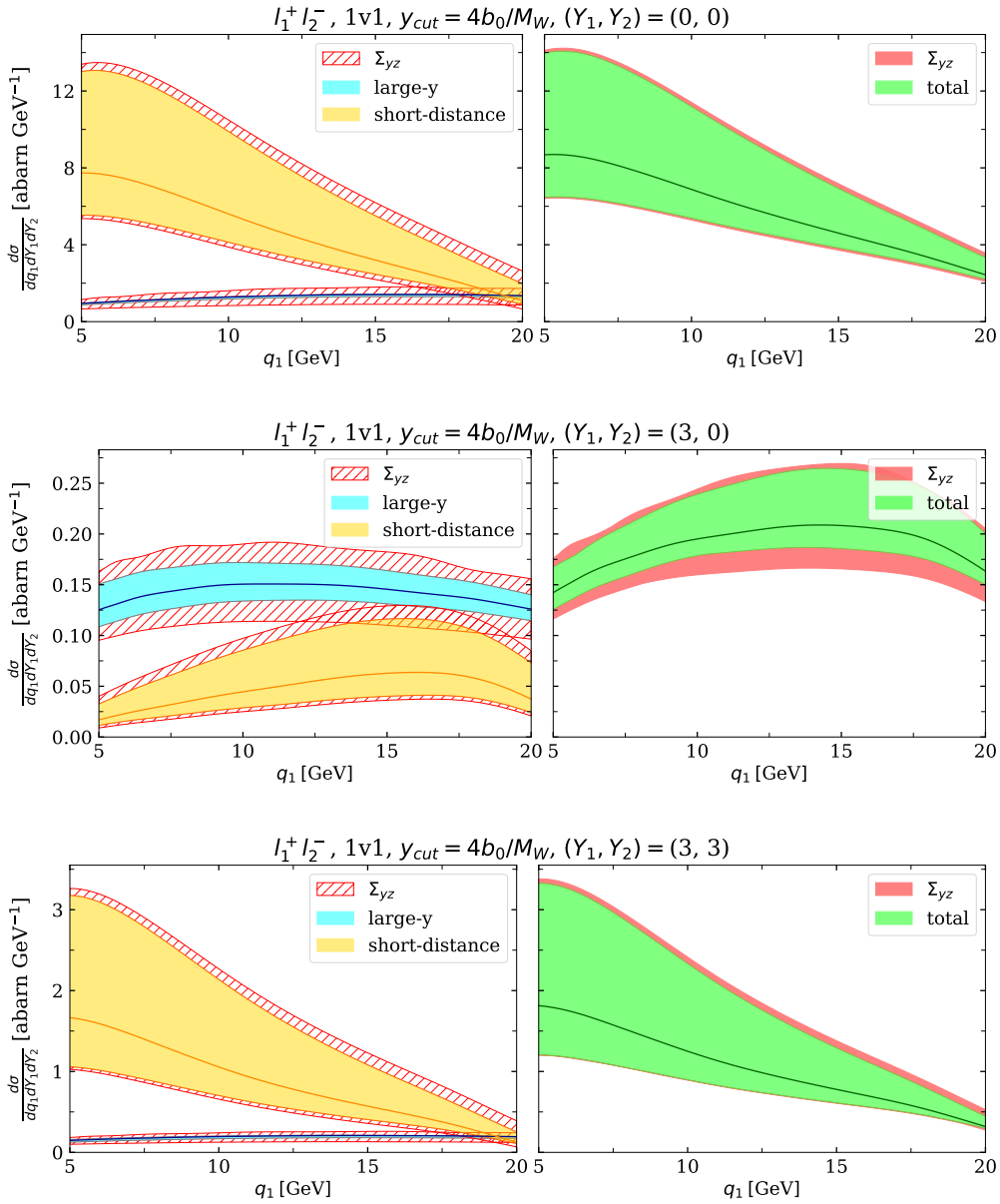

Figure 5.34: Combined large-**y** and short-distance contributions to the 1v1 channel at different rapidities for the largest value of the cut-off $y_{\text{cut}} = 4b_0/M_W$.

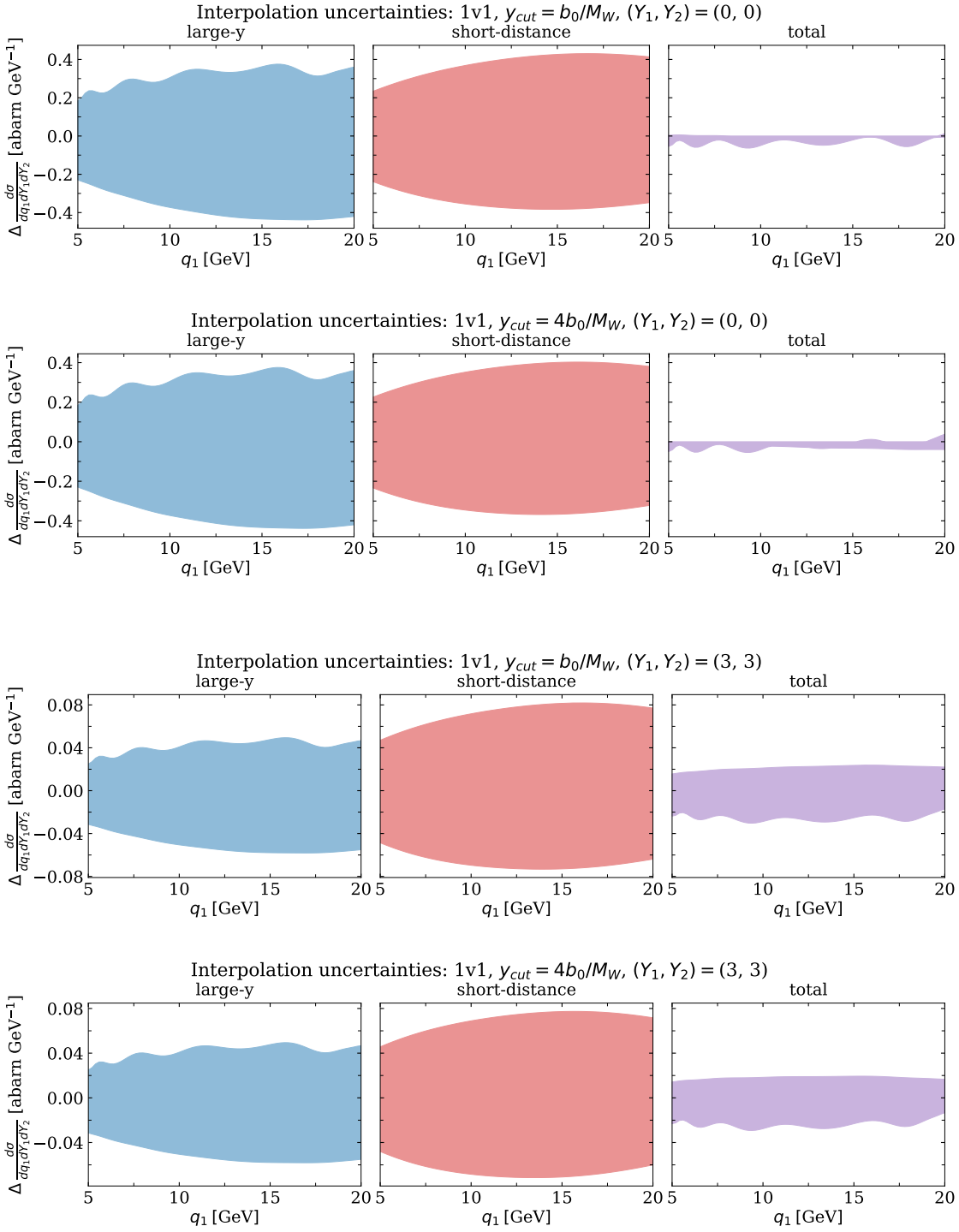

Figure 5.35: Interpolation uncertainty bands at remaining nonperturbative settings fixed ($\kappa = 1$, DPT24, $r = 1$) for individual and combined contributions in 1v1 channel.

5.6.2 Opposite-sign W production – summary

Let us summarize our results concerning the production of opposite-sign W boson pair in double-parton scattering. Due to the lack of subtraction terms, we cannot present the full result, but the analysis performed in this work allows us to describe which DPD channels and regions of the phase space should give the most significant contributions.

In the large-**y** region, all 3 kinds of 'nvm' terms give contributions of comparable size. We see that the color-singlet contribution strongly dominates over the color-nonsinglet part in the large-**y** part. In the color-nonsinglet sector, the 1v1 term visibly dominates over the remaining channels.

In the short-distance region, we observe a large cut-off dependence of the unsubtracted 1v1 term. As noted in the summary Section of [69], the variation of this term with the cut-off value y_{cut} can be used to estimate the size of higher-order corrections to the corresponding SPS process. In Figs. 5.36-5.37 we present the comparison of the 1v1 short-distance contribution at 3 different values of y_{cut} versus the sum of the large-**y** + short-distance contributions at the largest considered values of the cut-off (that is: $4b_0/M_W$ for 1v1, and $2b_0/M_W$ for 2v1+1v2). This allows us to compare the sizes of the DPS terms with the perturbative corrections to SPS. We observe that for central $(0, 0)$, and large but symmetric $(3, 3)$ rapidities the difference between 1v1 contributions at different cut-offs dominates over the estimate for the DPS contribution, so that in that region the perturbative corrections to the SPS should be more important than the contribution of double-parton scattering. For $(Y_1, Y_2) = (1.5, 0)$ we observe that both values become comparable in size, while for $(Y_1, Y_2) = (3, 0)$ the 1v1 short-distance terms are smaller than the large-**y** contribution, signaling that for the corresponding kinematics the DPS corrections may become more important than the higher-order SPS corrections. For large and asymmetric rapidities $(Y_1, Y_2) = (3, -3)$ the large-**y** part is 10^4 larger than the short-distance 1v1, see the bottom plot in Fig. 5.36.

To better understand the rapidity dependence, recall the discussion from Section 5.5.1. The momenta fractions $x_{L/R}$ of parent gluons of left/right hadron in the 1v1 channel are

$$x_L = x_0\big(e^{Y_1} + e^{Y_2}\big)\,, \qquad x_R = x_0\big(e^{-Y_1} + e^{-Y_2}\big)\,. \tag{5.137}$$

For large absolute values of Y_1, Y_2, the size of $x_{L/R}$ is determined by the largest exponents. Without loss of generality assume $Y_1 > 0$. If the rapidities are such that $Y_1 \approx Y_2$, the momentum fraction x_L is enhanced by a factor of $\sim e^{Y_1}$, and x_R is reduced by $\sim e^{-Y_1}$. The corresponding decrease of the gluon density $f_g(x_L)$ is then compensated by the enhancement of $\bar{f}_g(x_R)$, as long as x_R and x_L are in the region where f_g has an approximate power-law behavior. If $Y_1 \gg Y_2 > 0$, then x_R is reduced only by $\sim e^{-Y_2}$, and the compensation in the product of two gluon PDFs is incomplete, resulting in an overall smaller result. For negative Y_2, both PDFs are strongly suppressed, hence the strong diminishing at $(Y_1, Y_2) = (3, -3)$.

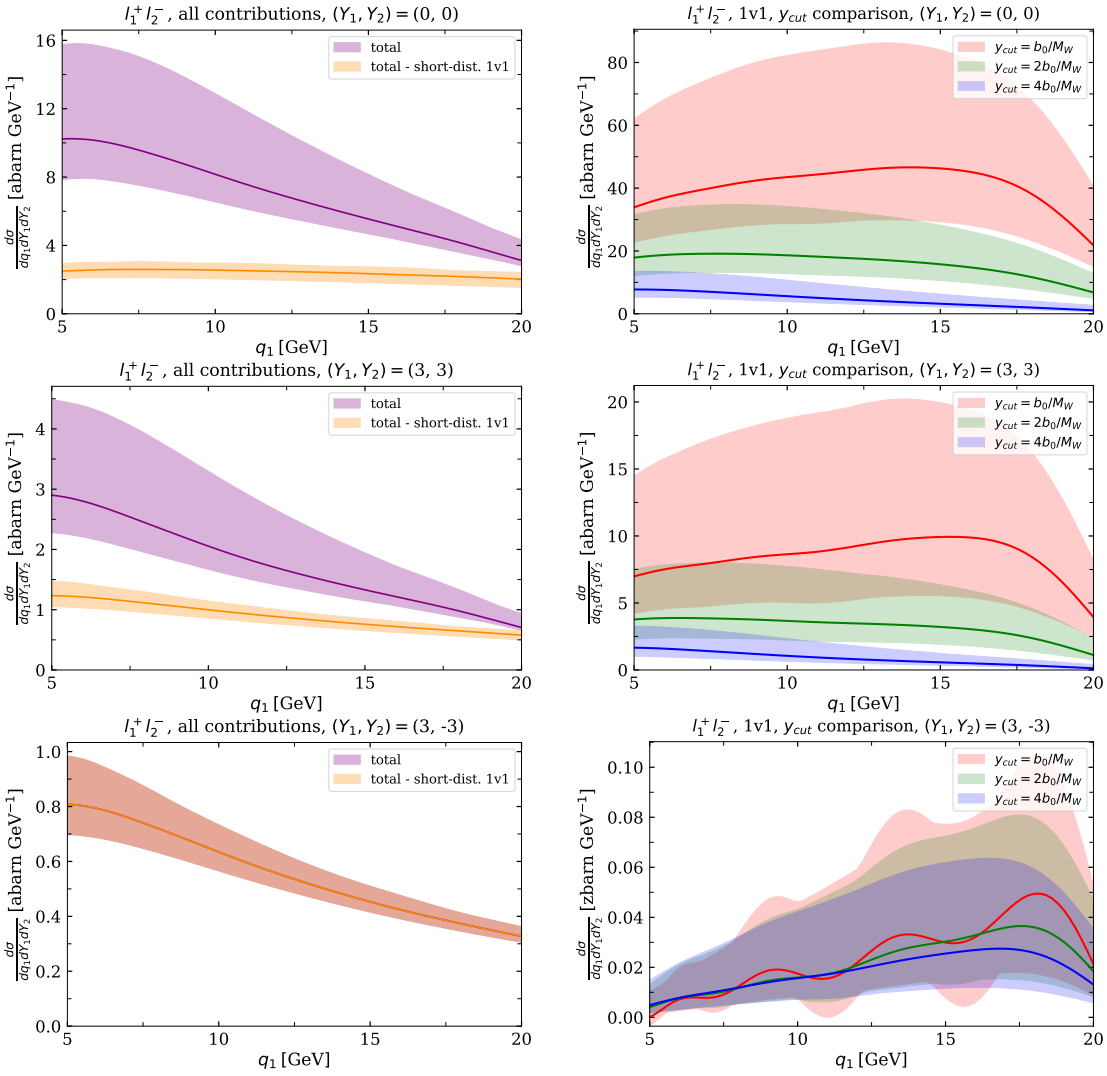

Figure 5.36: On the left: total (large-$\mathbf{y}$ + short-distance) contribution to DPS (in purple), and the (total - 1v1 at short-distance) part (orange). Right: the 1v1 short-distance term at 3 different values of the cut-off. Bands on all plots represent the total uncertainties of the corresponding terms. Presented rapidities: $(Y_1, Y_2) = (0, 0)$, $(3, 3)$, $(3, -3)$. Notice that the 1v1 short-distance term for $(3, -3)$ is in units of zbarn/GeV, and is $\mathcal{O}(10^{-4})$ times smaller than the corresponding large-$\mathbf{y}$ contribution.

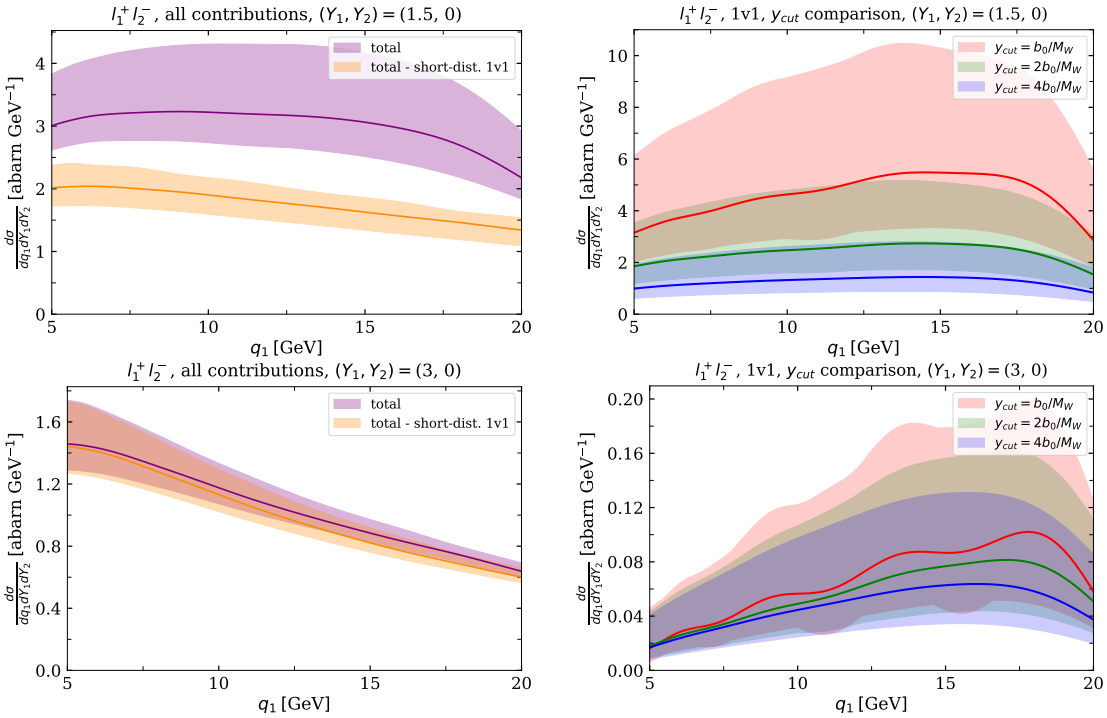

Figure 5.37: The same as in Fig. 5.36, but for rapidities $(Y_1, Y_2) = (1.5, 0)$ and $(3, 0)$.

5.6.3 Total transverse momentum-dependent cross-section of like-sign W production

In the remaining part of this work we focus on the production of like-sign W boson pairs. Results presented in the previous Sections show that the large-**y** color-singlet contribution completely dominates the cross-section of this process. That part is dominated by the 2v2 contribution, however, the 2v1+1v2 and 1v1 terms contribute about 20% of the total result. We found that the remaining terms (large-y color-octet and short-distance part) contribute at the level $\lesssim$1% of the total. In Fig. 5.38 we present the differential cross-section integrated over the transverse momentum q_2 up to 20 GeV for different values of the rapidities. We find that the general properties of the (q_1, Y_1, Y_2)-dependent cross-section, such as its shape in q_1 or the relative sizes of uncertainties remain the same for both W^+W^+ and W^-W^- channels, as well for all considered rapidity values. However, we see that the differential cross section of production of negative-sign W pair production diminishes faster at larger rapidities than in the positive-sign W case. To understand this, we note that at larger rapidities one combines partons with small and (relatively) large longitudinal momenta – for two protons colliding, only the sea quarks, suppressed at large x_i, can produce W^-W^- pairs. On the other hand, in the process of W^+W^+, one can have active valence up

quarks, whose densities decrease less fast at larger momenta fractions.

Combining the short-distance and large-$\mathbf{y}$ allows us to provide a full discussion of the estimation of uncertainties, as now we have a complete interpolation error. It needs to be emphasized, however, that this is still not the total uncertainty of the prediction, and in this work, we are focused solely on the description of the transverse momentum dependence. Owing to the approximations presented in Chapters 3 and 4, we can separate it from the modeling of the collinear DPDs, which we consider to be given. Owing to the implementation of DTMDs in ChiliPDF, one can reproduce the predictions for other models of the collinear DPDs, allowing to include the corresponding error estimates in the studies.

The largest contribution to the uncertainty is due to the matching uncertainty, estimated by the variation of the matching scale. The uncertainty due to the Collins-Soper kernel (in orange) is visible only at small momenta, corresponding to larger transverse distances. It is strongly asymmetric, since the largest outlier within the considered kernels, ART23 [88], see Eq. (5.54), is visibly larger than the remaining fit results, see Fig. 5.8. The error estimation due to the unknown large-distance falloff, estimated as described in Section 5.2.3, extends to larger momenta, but also diminishes at larger values.

5.6.4 Rapidity dependence of cross sections partially integrated over transverse momenta

Finally, we discuss the rapidity dependence of the differential cross-section partially integrated over the transverse momenta:

$$\frac{d\sigma^{\mathrm{DPS}}}{dY_1}\Big|_{|\mathbf{q}_1|,|\mathbf{q}_2|\leq q_{\max}}, \qquad q_{\max} \in \left\{10\ \mathrm{GeV},\ 15\ \mathrm{GeV},\ 20\ \mathrm{GeV}\right\}. \tag{5.138}$$

Since it was shown that the short-distance and color-nonsinglet contributions are much smaller than the total result, to obtain these results we use only the color-singlet large-$\mathbf{y}$ contribution. We compare them with the collinear limit obtained by replacing the DTMDs in Eq. (5.90) by collinear DPDFs, and removing the $\int d^2\mathbf{z}_i/(2\pi)^2$ and the associated Fourier exponentials. We emphasize that such a formula does not give the total collinear double Drell-Yan cross-section at NLO (which in this work has been implemented only at LO [2]), since the NLO corrections to the hard cross-sections in the collinear limit differ from those used in transverse-momentum dependent cross-sections – compare Appendix E here and Section 9 in [110]. This exercise is used to assess how fast the Fourier transforms in Eq. (5.90) integrated over the momenta approach the $\mathbf{z}_i \to 0$ of the integrand, rather than to provide a full comparison with the full NLO collinear cross-section.

[2]To compute the required Mellin convolutions of the hard scattering kernels with collinear parton distributions would require significant additional numerical work.

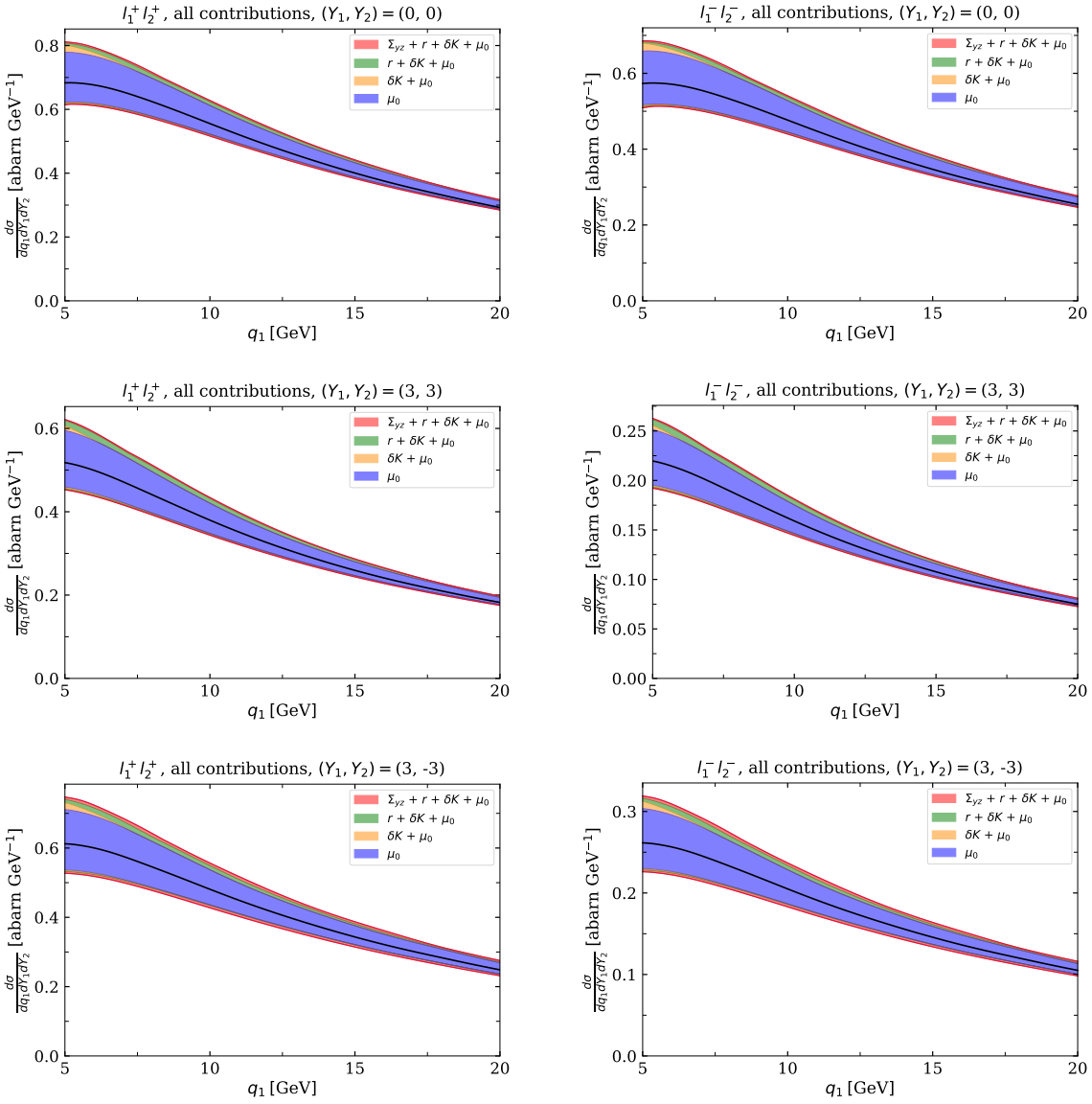

Figure 5.38: Total (large-$\mathbf{y}$ color singlet + color octet + short-distance) cross-section differential over transverse momentum q_1.

The ratio between the partially integrated cross-section and the collinear limit remains approximately constant for $|Y_1| \leq 4$, however, a small enhancement of the partially integrated ones at larger Y is visible. The differential cross-section integrated up to 10 GeV constitutes roughly 15% of the collinear limit value; up to 15 GeV about 30%, and around 45% for $q_{\max} = 20$ GeV. In order to assess how realistic the model of collinear double parton distributions used in this work is, we also present a fully integrated collinear cross-section computed using LO hard scattering cross-section, and DPDFs modeled with NLO PDFs. The cross-sections integrated over $Y_{1,2} \in [-5, 5]$ and over $|\mathbf{q}_{1,2}| < q_{\max}$ for all DPD channels are given in Tables 5.2 and 5.3. It is clearly seen that the splitting part contributes more at large transverse momenta, what one can attribute to the short-distance enhancement of that part.

We conclude that the phase-space region that can be described using the presented formalism, that is transverse momenta perturbatively large, but still much smaller than the hard scale M_W, has a significant size. The plots of the described ratios are given in App. G.5. The region of transverse momenta $|\mathbf{q}_i| \sim Q$ cannot be treated within the transverse momentum-dependent factorization – it requires a computation in a fixed-order perturbative expansion, which is not analyzed in this work.

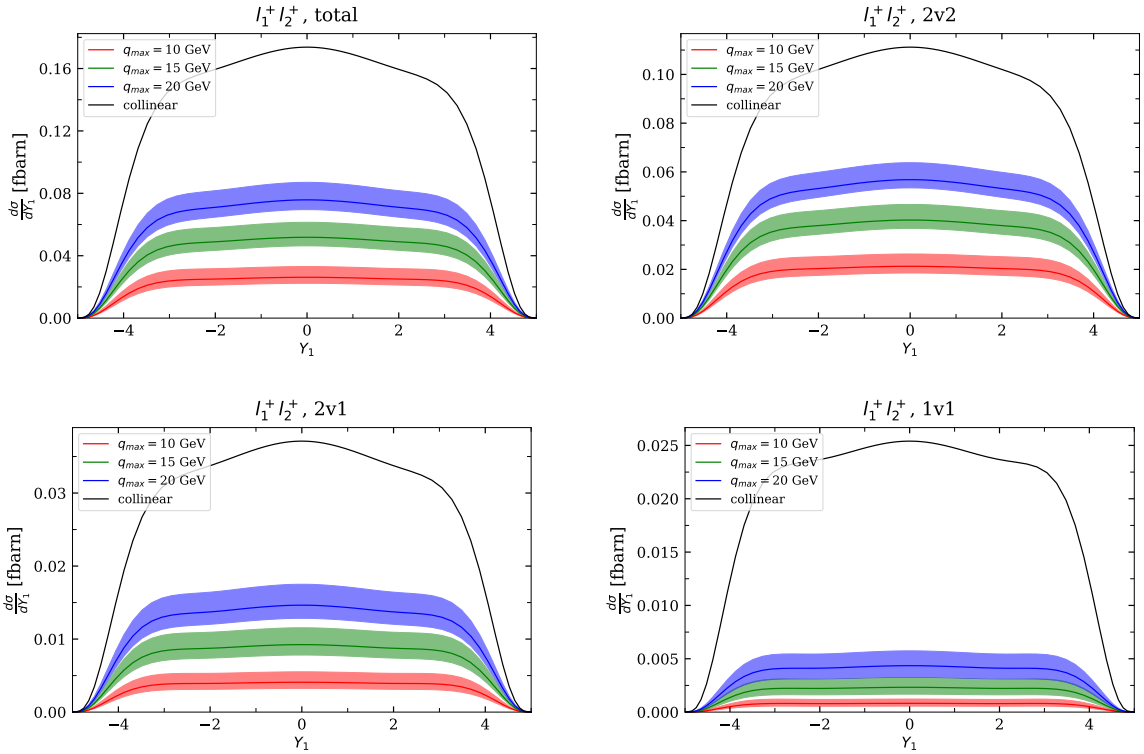

Figure 5.39: Differential cross section partially integrated over the transverse momenta vs the collinear limit for $l_1^+ l_2^+$.

$q_{T,\max}$	2v2	2v1+1v2	1v1	total
10 GeV	$0.164^{+0.039}_{-0.023}$ fb	$0.032^{+0.012}_{-0.007}$ fb	$0.0066^{+0.0034}_{-0.0020}$ fb	$0.203^{+0.055}_{-0.032}$ fb
15 GeV	$0.305^{+0.055}_{-0.029}$ fb	$0.071^{+0.018}_{-0.011}$ fb	$0.018^{+0.007}_{-0.005}$ fb	$0.394^{+0.080}_{-0.045}$ fb
20 GeV	$0.426^{+0.054}_{-0.029}$ fb	$0.112^{+0.021}_{-0.014}$ fb	$0.034^{+0.011}_{-0.008}$ fb	$0.572^{+0.086}_{-0.051}$ fb

Table 5.2: Partially integrated cross sections of W^+W^+ production for different DPD channels.

The total differential cross section (with LO hard scattering part) obtained using the considered DPDF model presented in Section 3.3 is

$$\sigma_{DPS}^{l^+l^+,coll.} \approx 1.08\,\text{fb}\,. \tag{5.139}$$

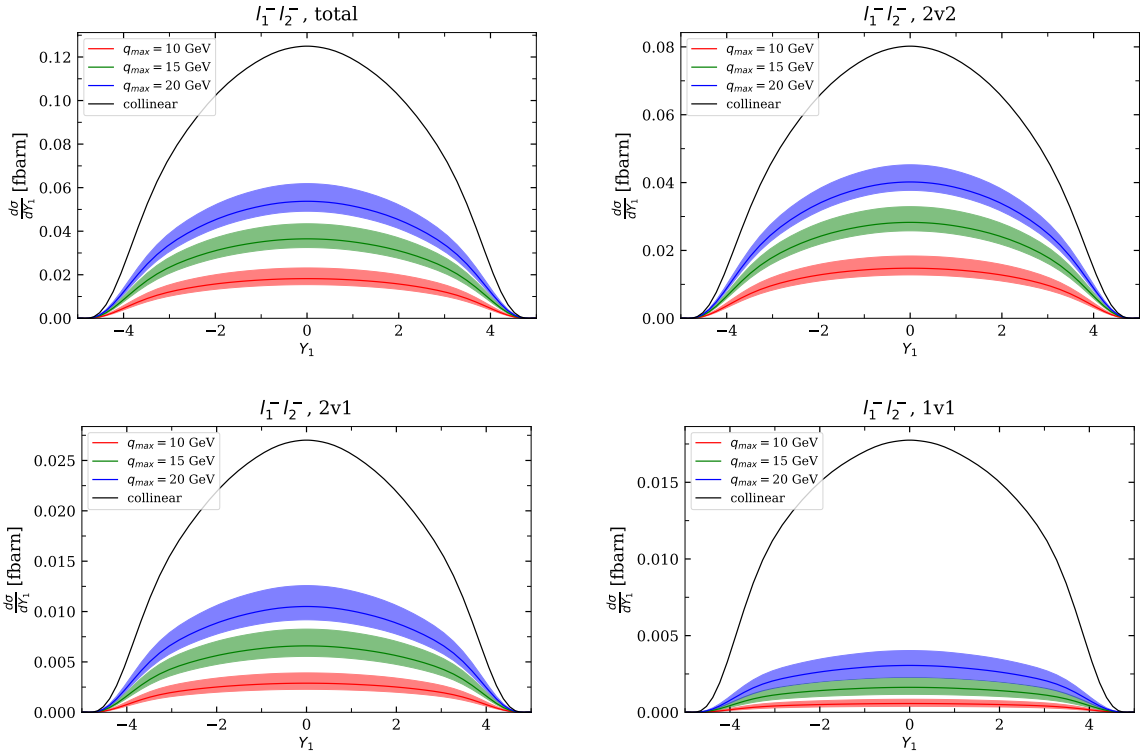

Figure 5.40: Differential cross section partially integrated over the transverse momenta vs the collinear limit for $l_1^- l_2^-$.

$q_{T,\max}$	2v2	2v1+1v2	1v1	total
10 GeV	$0.095^{+0.024}_{-0.013}$ fb	$0.019^{+0.007}_{-0.004}$ fb	$0.0038^{+0.0019}_{-0.0012}$ fb	$0.117^{+0.033}_{-0.018}$ fb
15 GeV	$0.179^{+0.030}_{-0.017}$ fb	$0.042^{+0.011}_{-0.006}$ fb	$0.011^{+0.004}_{-0.003}$ fb	$0.232^{+0.045}_{-0.026}$ fb
20 GeV	$0.252^{+0.032}_{-0.017}$ fb	$0.067^{+0.013}_{-0.009}$ fb	$0.020^{+0.006}_{-0.005}$ fb	$0.339^{+0.051}_{-0.031}$ fb

Table 5.3: Partially integrated cross sections of W^-W^- production for different DPD channels.

The total cross-section (with LO hard scattering part) for production of a fixed l^-l^- pair:

$$\sigma_{DPS}^{l^-l^-,coll.} \approx 0.64 \text{ fb} . \tag{5.140}$$

Adding the total cross sections for both $l_1^+ l_2^+$ and $l_1^- l_2^-$, and including all combinations of the produced leptons: e, μ, τ (treating all generation the same), we get the cross-section

of production of two like-sign W bosons decaying into a lepton pair equal to

$$\sigma^{\text{total}}\big(W^{\pm}W^{\pm} \to \text{ leptons}\big) \approx 10.3\,\text{fb}\,. \tag{5.141}$$

Comparing this with the CMS results [48], which give $\sigma^{\text{total}} = 80.7 \pm 11.2$ fb, we see that the predictions obtained using the considered DPDF model are about a factor of 8 smaller. They were obtained using NLO PDFs in the DPDFs model, and LO hard scattering cross-section. The NLO corrections to the hard part in the collinear cross-section are not likely to account for this discrepancy, as suggested by the size of the relevant corrections in a single Drell-Yan process [111]. According to results presented in Section 6 in [111], see Figs. 10 and 13, the NLO corrections are of the size of 45% of the LO result at central rapidity and about 25% at larger rapidities. In the case of the double Drell-Yan, this would correspond to about 50-90% enhancement at higher order (since the hard factor is squared there). A more recent work [112] predicts an even smaller difference between LO and NLO, see Section 3 there. We were not able to pinpoint the source of the difference in results between the two works. We note that our predictions are also smaller than the ones of the previous works on DPS [50, 52].

To discuss this difference, let us recall that in the simplest model of double-parton scattering, the product of two DPDFs integrated over the transverse plane is approximated by a product of the corresponding PDF divided by a constant σ_{eff}, called the effective cross-section:

$$\int d^2\mathbf{y}\, F_{a_1a_2}(x_i,\mathbf{y})\bar{F}_{b_1b_2}(\bar{x}_i;\mathbf{0}) \;=\; \frac{1}{\sigma_{\text{eff}}}\left(f_{a_1}(x_1)f_{a_2}(x_2)f_{b_1}(\bar{x}_1)f_{b_2}(\bar{x}_2)\right). \tag{5.142}$$

The DPDF model considered in this work takes a more complicated $\mathbf{y}$-dependence of DPDs, and one cannot assign to them a scale- and process-independent σ_{eff}. However, if the DPDF model was initialized at the hard scales of the process so that there was no DGLAP evolution of DPDs, it would be possible to assign the effective cross-section parameter to the 2v2 intrinsic color-singlet part. According to the definition in Eqs. (3.27) and (3.33), the corresponding effective cross-section would be

$$\sigma_{\text{eff}} = 8\pi h_{qq} \approx 68.5\,\text{mb}\,, \tag{5.143}$$

while the studies, e.g. [50, 52], assumed $\sigma_{\text{eff}} = 14.5$ mb, and the value extracted by the CMS experiment is $\sigma_{\text{eff}} = 12.2^{+2.9}_{-2.2}$ mb.

We notice that the model of DPDFs in this thesis was not motivated by the results concerning generalized parton distributions, see Section 4.1 in [113], rather than the double-parton scattering measurement. As the results show, the parameters in the model should be adjusted. The code implemented in ChiliPDF is independent of the model of the collinear parton distributions, which are provided as an input argument – for this reason the study of transverse momentum-dependent double-parton scattering for different DPDF models will be a straightforward task, which we leave for future work.

Chapter 6

Conclusions

In this work we presented a detailed study of transverse momentum-dependent double-parton distributions (DTMDs), and the corresponding differential cross sections of W boson pair decaying into lepton pairs.

We distinguished two regions of the phase space, where DTMDs can be described using approximate methods. The first one, called the "large-$\mathbf{y}$" region, corresponds to the distance between parton pairs much larger than the difference of the parton transverse positions on both sides of the cut. In that case one can apply the operator product expansion to operators defining DTMDs, obtaining the matching relation between the collinear parton distribution and the transverse position-dependent DPDs. In the "short-distance" region, where all distances are perturbatively small, we combine the intrinsic part of DTMDs with the part obtained from perturbative splitting of a single parton into two (PDF-DTMD splitting). In both cases we studied, how to extrapolate perturbatively obtained DPDs to large distances.

We studied DPDs obtained using both approximations, and used them to obtain the differential cross section of the process of W pair production. We developed an interpolation method allowing to combine both DTMD approximations in a consistent way. We identified the necessary nonperturbative input, and the corresponding sources of theoretical uncertainties.

After that preparation, we computed the differential cross section of the $p\bar{p} \to W^{\pm}(\to l_1^{\pm}\nu_1)W^{\pm}(\to l_2^{\pm}\nu_2)+X$ process. Since the considered double parton distributions are decomposed into 2 terms, intrinsic and splitting part, and there are different color representations involved, we studied each resulting contribution independently. We identified the terms that give the most important contributions, and analyzed the size of the corresponding model uncertainties. We found that it is the error due to perturbative matching that contributes the most to the overal error estimate.

Because of the absence of components necessary to remove double counting between double- and single parton scattering in the splitting part at small distances, we are not able to provide the total result for the differential cross section of opposite-sign W

bosons production. The obtained results show that if rapidities Y_1, Y_2 of the produced boson have similar values $Y_1 \approx Y_2$, the splitting short-distance part should dominate the result. If the rapidities are larger and not symmetric, the large-$\mathbf{y}$ part gives a larger contribution than the short-distance terms. The variation of the '1v1' short-distance contribution with the short distance cut-off imposed in the integration allows to estimate the size of higher order pQCD corrections to the corresponding SPS process – our results suggest that for large and asymmetric rapidities the DPS contribution should be of similar size, or even dominate over higher order corrections to the SPS.

In the case of like-sign W pair, we are able to provide a full description of DPS at NNLL accuracy. The SPS process is initiated by Feynman graphs suppressed by the second power in coupling compared with the DPS, and does not contribute at the considered order. We found that the result is completely dominated by the large-$\mathbf{y}$ color-singlet part. Integrating the cross section differential with respect to transverse momenta of the produced W bosons we find that the momenta, which are large enough to be considered perturbative, but also much smaller than the hard scale, contribute to about 40% of the total cross section. The comparison with the experimental results concerning like-sign W boson pair production [48] shows that the considered DPDF model leads to underestimated cross sections, which suggests that the parameters of the model need to be adjusted. Further studies of transverse momentum dependence in the considered class of processes utilizing a larger variety of DPDF models will be a subject of future research.

Appendix A

Color algebra

A.1 Projecting on definite color representations

Useful definitions can be found in
A. J. Macfarlane, A. Sudbery, P. H. Weisz, *On Gell-Mann's λ-Matrices, d- and f - Tensors, Octets, and Parametrizations of SU(3)*, Commun. Math. Phys. 11 (1968) 77.

Recall that DPDs in definite color representations are obtained using projection matrices $P_{R_1R_2}$:

$$ {}^{R_1R_2}F_{a_1a_2} = \varepsilon_{a_1}(R_1)\varepsilon_{a_2}(R_2)\frac{1}{\mathcal{N}_{a_1}\mathcal{N}_{a_2}}\frac{1}{\sqrt{m(R_1)}}P^{\underline{s}_1\underline{s}_2}_{R_1R_2}F^{\underline{s}_1\underline{s}_2}_{a_1a_2}\,, \tag{A.1} $$

where $\underline{s}_i$ are the color indices. In general, any color matrix can be decomposed according to

$$ M^{\underline{s}_1\underline{s}_2} = \sum_{R_1R_2}\frac{1}{m(R_1)}P^{\underline{s}_1\underline{s}_2}_{R_1R_2}\left(P^{\underline{r}_1\underline{r}_2}_{R_1R_2}M^{\underline{r}_1\underline{r}_2}\right). \tag{A.2} $$

Let us use indices i for fundamental representations, and a, b, c in the adjoint representation. Depending on the parton type, we have the following projection matrices:

• quark-quark – fundamental representation of SU(3):

$$ P_{11}^{i_1i'_1,i_2i'_2} = \frac{1}{N}\delta_{i_1i'_1}\delta_{i_2i'_2}\,, \tag{A.3} $$

$$ P_{88}^{i_1i'_1,i_2i'_2} = \frac{1}{N}t^a_{i_1i'_1}t^a_{i_2i'_2}\,, \tag{A.4} $$

• gluon-gluon – adjoint representation:

$$P_{11}^{a_1a_1',a_2a_2'} = \frac{1}{N^2-1}\delta_{a_1a_1'}\delta_{a_2a_2'}\,, \tag{A.5}$$

$$P_{AA}^{a_1a_1',a_2a_2'} = \frac{1}{N}f^{a_1a_1'b_1}f^{a_2a_2'b_1}\,, \tag{A.6}$$

$$P_{SS}^{a_1a_1',a_2a_2'} = \frac{N}{N^2-4}d^{a_1a_1'b_1}d^{a_2a_2'b_1}\,, \tag{A.7}$$

$$P_{AS}^{a_1a_1',a_2a_2'} = \frac{1}{\sqrt{N^2-4}}f^{a_1a_1'b_1}d^{a_2a_2'b_1}\,, \tag{A.8}$$

$$P_{SA}^{a_1a_1',a_2a_2'} = \frac{1}{\sqrt{N^2-4}}d^{a_1a_1'b_1}f^{a_2a_2'b_1}\,, \tag{A.9}$$

$$P_{10\,\bar{10}}^{a_1a_1',a_2a_2'} = \frac{1}{4}\Big(\delta_{a_1a_2}\delta_{a_1'a_2'}-\delta_{a_1a_2'}\delta_{a_1'a_2}\Big)-\frac{1}{2}P_{AA}^{a_1a_1',a_2a_2'}-\frac{i}{4}\Big(d^{a_1a_2b_1}f^{a_1'a_2'b_1}+f^{a_1a_2b_1}d^{a_1'a_2'b_1}\Big)\,, \tag{A.10}$$

$$P_{10\,\bar{10}}^{a_1a_1',a_2a_2'} = \frac{1}{4}\Big(\delta_{a_1a_2}\delta_{a_1'a_2'}-\delta_{a_1a_2'}\delta_{a_1'a_2}\Big)-\frac{1}{2}P_{AA}^{a_1a_1',a_2a_2'}+\frac{i}{4}\Big(d^{a_1a_2b_1}f^{a_1'a_2'b_1}+f^{a_1a_2b_1}d^{a_1'a_2'b_1}\Big)\,, \tag{A.11}$$

$$P_{27\,27}^{a_1a_1',a_2a_2'} = \frac{1}{2}\Big(\delta_{a_1a_2}\delta_{a_1'a_2'}-\delta_{a_1a_2'}\delta_{a_1'a_2}\Big)-P_{SS}^{a_1a_1',a_2a_2'}-P_{11}^{a_1a_1',a_2a_2'}\,. \tag{A.12}$$

• quark-gluon and gluon-quark – mixed fundamental and adjoint representations:

$$P_{11}^{ii',aa'} = P_{11}^{aa',ii'} = \frac{1}{\sqrt{N(N^2-1)}}\delta_{ii'}\delta_{aa'}\,, \tag{A.13}$$

$$P_{8A}^{ii',aa'} = P_{A8}^{aa',ii'} = \sqrt{\frac{2}{N}}t_{ii'}^{b}f^{aa'b}\,, \tag{A.14}$$

$$P_{8S}^{ii',aa'} = P_{S8}^{aa',ii'} = \sqrt{\frac{2}{N}}t_{ii'}^{b}d^{aa'b}\,. \tag{A.15}$$

A.2 Color representations in t-channel and s-channel

Due to simpler evolution, in this work we were using the color representations in the t-channel. As described in [58], before renormalization the DPDFs in the s-channel admits an interpretation as probability densities, and can be used to obtain positivity bounds in color space. Let us denote DPDFs in color representation $\tilde{R}_1\tilde{R}_2$ in s-channel as:

$$F_{a_1a_2}^{\tilde{R}_1\tilde{R}_2}\,, \tag{A.16}$$

For $q\bar{q}$ the definite color representations in the s-channel are $(\tilde{R}_1,\tilde{R}_2)\in\big\{(1,1)\,,\,(8,8)\big\}$, for qq distributions: $(\tilde{R}_1,\tilde{R}_2)\in\big\{(\bar{3},\bar{3}),(6,6)\big\}$, and for qg: $\tilde{R}_1\tilde{R}_2\in\big\{(3,3),(6,6),(15,15)\big\}$.

Definite representations for gg distributions are in the s-channel the same as in the t-channel.

There is a linear relation between DPDs in t-channel and s-channel:

$$ {}^{R_1R_2}F_{a_1a_2} = K_{ts}^{a_1a_2}\, F_{a_1a_2}^{\tilde{R}_1\tilde{R}_2} \tag{A.17} $$

The matrices $K_{ts}^{a_1a_2}$ read:

$$ K_{ts}^{qq} = K_{ts}^{\bar{q}\bar{q}} = 3\begin{pmatrix} 1 & 2 \\ -\sqrt{2} & \sqrt{2} \end{pmatrix}, \tag{A.18} $$

$$ K_{ts}^{q\bar{q}} = K_{ts}^{\bar{q}q} = \begin{pmatrix} 1 & 8 \\ 2\sqrt{2} & -2\sqrt{2} \end{pmatrix}, \tag{A.19} $$

$$ K_{ts}^{qg} = K_{ts}^{gq} = 3\begin{pmatrix} 1 & 2 & 5 \\ \sqrt{\frac{5}{2}} & -\sqrt{10} & \sqrt{\frac{5}{2}} \\ -3/\sqrt{2} & -\sqrt{2} & 5/\sqrt{2} \end{pmatrix}, \tag{A.20} $$

$$ K_{ts}^{\bar{q}g} = K_{ts}^{g\bar{q}} = 3\begin{pmatrix} 1 & 2 & 5 \\ \sqrt{\frac{5}{2}} & -\sqrt{10} & \sqrt{\frac{5}{2}} \\ 3/\sqrt{2} & \sqrt{2} & -5/\sqrt{2} \end{pmatrix}, \tag{A.21} $$

$$ K_{ts}^{gg} = \begin{pmatrix} 1 & 8 & 8 & 10 & 10 & 27 & 0 & 0 \\ 2\sqrt{2} & -\frac{24\sqrt{2}}{5} & 8\sqrt{2} & -8\sqrt{2} & \frac{54\sqrt{2}}{5} & 0 & 0 & \\ -2\sqrt{2} & -8\sqrt{2} & -8\sqrt{2} & 0 & 0 & 18\sqrt{2} & 0 & 0 \\ 0 & 0 & 0 & 4\sqrt{10} & -4\sqrt{10} & 0 & 0 & 16\sqrt{2} \\ 0 & 0 & 0 & 4\sqrt{10} & -4\sqrt{10} & 0 & 0 & -16\sqrt{2} \\ \sqrt{10} & -16\sqrt{\frac{2}{5}} & 0 & 2\sqrt{10} & 2\sqrt{10} & -9\sqrt{\frac{2}{5}} & 0 & 0 \\ 0 & 0 & 0 & 0 & 0 & 0 & 16\sqrt{2} & 0 \\ 3\sqrt{3} & \frac{24\sqrt{3}}{5} & -8\sqrt{3} & -2\sqrt{3} & -2\sqrt{3} & \frac{21\sqrt{3}}{5} & 0 & 0 \end{pmatrix} \tag{A.22} $$

A.3 Color nonsinglet intrinsic DPDFs

According to the model of intrinsic DPDFs in Eq. (3.33), the relation between color-singlet and color-nonsinglet collinear DPDs is:

$$ {}^{R_1R_2}F_{a_1a_2} \;=\; r_{a_1a_2}(R_1R_2)\,{}^{11}F_{a_1a_2}\,. \tag{A.23} $$

Factors $r(R_1R_2)$ are obtained by saturating the positivity bounds for DPDFs in definite color representation in the s-channel, that is: assuming that for each flavor pair a_1, a_2, only one $F_{a_1a_2}^{\tilde{R}_1\tilde{R}_2}$ is non-zero, see Eq. (A.16).

In the considered model the non-vanishing color representations in the s-channel are taken as:

- $(q\bar{q})$, $(\bar{q}q)$: $(8,8)$,
- $(qq), (\bar{q}g)$: $(\bar{3},3)$,
- $(\bar{q}\bar{q}), (qg)$: $(3,\bar{3})$,
- (g,g) (A,A) .

The resulting color factors are:

$$r_{qq}(88) = r_{\bar{q}\bar{q}}(88) = -\sqrt{2}\,, \tag{A.24}$$

$$r_{q\bar{q}}(88) = r_{\bar{q}q}(88) = -\frac{1}{2\sqrt{2}}\,, \tag{A.25}$$

$$r_{qg}(8S) = r_{\bar{q}g}(8S) = r_{gq}(S8) = r_{g\bar{q}}(8S) = \sqrt{5/2}\,, \tag{A.26}$$

$$r_{qg}(8A) = r_{\bar{q}g}(8A) = r_{gq}(A8) = r_{g\bar{q}}(8A) = -3/\sqrt{2}\,, \tag{A.27}$$

$$r_{gg}(SS) = \sqrt{2}\,, \qquad r_{gg}(AA) = -\sqrt{2}\ :, \tag{A.28}$$

$$r_{gg}(SA) = r_{gg}(AS) = r_{gg}(10\ \bar{10}) = r_{gg}(\bar{10}\ 10) = 0\,, \tag{A.29}$$

$$r_{gg}(27\ 27) = -\sqrt{3}\,. \tag{A.30}$$

For reference see Section 3.2 in [67].

Appendix B

Two-loop Collins-Soper kernels and anomalous dimensions

Collins-Soper kernels relevant in the evolution of DPDFs and DTMDs in the large-$\mathbf{y}$ approximation up to α_S^2 can be written using a single kernel:

$$K_0\big(\mathbf{b};\mu\big) = \frac{1}{C_F}\,{}^1K_q\big(\mathbf{b};\mu\big)\,, \tag{B.1}$$

so that

$$\begin{aligned}
&{}^8K_q\big(\mathbf{b};\mu\big) = -\frac{1}{2N}K_0\big(\mathbf{b};\mu\big)\,,\\[2ex]
&{}^RK_g\big(\mathbf{b};\mu\big) = c_g(R)\,K_0\big(\mathbf{b};\mu\big)\,,\\
&\qquad c_g(A) = c_g(S) = \frac{N}{2},\quad c_g(10) = 0,\quad c_g(27) = -1\,,\\[2ex]
&{}^8J\big(\mathbf{b};\mu_1,\mu_2\big) = \frac{N}{2}\Big(K_0\big(\mathbf{b};\mu_1\big) + K_0\big(\mathbf{b};\mu_2\big)\Big)\,,\\
&{}^RJ\big(\mathbf{b};\mu_1,\mu_2\big) = c_J(R)\,{}^8J\big(\mathbf{b};\mu_1,\mu_2\big)\,,\\
&\qquad c_J(8) = \frac{N}{2},\quad c_J(10) = 3,\quad c_J(27) = 4\,.
\end{aligned} \tag{B.2}$$

Defining

$$a_S = \frac{\alpha_S}{4\pi}\,,\qquad L(\mathbf{b},\mu) = \log\frac{\mathbf{b}^2\mu^2}{b_0}\,, \tag{B.3}$$

and using Eqs. (4.10)-(4.11) in [102], we can write

$$\begin{aligned}
K_0\big(\mathbf{b};\mu\big) \;=\; &-4a_SL(\mathbf{b},\mu)\\
&-2a_S^2\Big(\beta_0L^2(\mathbf{b},\mu) + 2\Gamma_2L(\mathbf{b},\mu) + C_A\Big(\frac{404}{27} - 14\zeta_3\Big) - \frac{56}{27}n_f\Big)\,,
\end{aligned} \tag{B.4}$$

where $\Gamma_2 = C_A\Big(\frac{67}{9} - \frac{\pi^2}{3}\Big) - \frac{10}{9}n_f$, $\beta_0 = \frac{11}{3}C_A - \frac{2}{3}n_f$, and ζ_3 is the value of the Riemann zeta function at 3, not to be confused with the rapidity parameter ζ.

Kernel ${}^1K_q$ is equal to the TMD quark Collins-Soper kernel. Its RGE reads:

$$\frac{d}{d\log\mu}{}^1K_q(\mathbf{b};\mu) = -\gamma_{K,q}(\mu)\,. \tag{B.5}$$

We have

$$\gamma_{K,q} \;= 8C_F\,a_S \;+\; a_s^2\,8C_F\Gamma_2\,. \tag{B.6}$$

The anomalous dimension of the gluon kernel $\gamma_{K,g}$ is obtained from the linear relation between ${}^1K_q$ and ${}^8K_g$.

The RGE of transverse position-dependent DPDs reads:

$$\frac{d}{d\log\mu_1}{}^{R_1R_2}F_{a_1a_2}\big(x_i,\mathbf{z}_i,\mathbf{y};\mu_i,\zeta\big) \;=\; \gamma_{F,a_1}(\mu,x_1^2\zeta)\,F_{a_1a_2}\big(x_i,\mathbf{z}_i,\mathbf{y};\mu_i,\zeta\big)\,, \tag{B.7}$$

where

$$\gamma_{F,a_1}(\mu,x_1^2\zeta) = \gamma_{a_1}(\mu) - \gamma K, a_1\log\frac{x_1\sqrt{\zeta}}{\mu}\,, \tag{B.8}$$

analogously for the scale μ_2. The kernels $\gamma_{K,a}$ are defined above, and the non-cusp anomalous dimensions are:

$$\begin{aligned}\gamma_q &= 6C_F\,a_s \\ &\quad + 4a_s^2\,\Big[C_F^2\Big(\frac{3}{4} - \pi^2 + 12\zeta_3\Big) + C_FC_A\Big(\frac{961}{108} + \frac{11}{12}\pi^2 - 13\zeta_3\Big) - C_Fn_f\Big(\frac{65}{54} + \frac{1}{6}\pi^2\Big)\Big]\,,\end{aligned} \tag{B.9}$$

$$\begin{aligned}\gamma_g &= 2\beta_0\,a_s \\ &\quad + 4a_s^2\,\Big[C_A^2\Big(\frac{346}{27} - \frac{11}{36}\pi^2 - \zeta_3\Big) + C_An_f\Big(-\frac{64}{27} + \frac{1}{18}\pi^2\Big) - C_Fn_f\Big]\,.\end{aligned} \tag{B.10}$$

Appendix C

Matching kernels

Taken from [56], Sections 7.3.4 - 7.3.5.

At the rapidity scale $x^2\zeta = \mu^2$, the color-singlet matching kernels in the parton basis are given by

$$C_{qq} = C_{\Delta q\Delta q} = \delta(1-y) + a_S\, C_F \left[2y + 2S_L\delta(y) - L\Big(\frac{4}{y_+} + 2(y-2)\Big)\right], \tag{C.1}$$

$$C_{qg} = a_S\, T_F \left[4y(1-y) - L \times 2\big((1-y)^2 + y^2\big)\right], \tag{C.2}$$

$$C_{\Delta q\Delta g} = a_S\, T_F \left[4y - L \times 2\big((1-y)^2 - y^2\big)\right], \tag{C.3}$$

$$C_{gq} = a_S\, C_F \left[2(1-y) - L \times 2\frac{1+y^2}{1-y}\right], \tag{C.4}$$

$$C_{\Delta g\Delta q} = a_S\, C_F \left[-4y - L \times 2\frac{1-y^2}{1-y}\right], \tag{C.5}$$

$$C_{gg} = \delta(1-y) + a_S\, C_A \left[2S_L\delta(y) - L \times 4\Big(\frac{1}{y_+} - 1 + \frac{y\big(1+(1-y)^2\big)}{1-y}\Big)\right], \tag{C.6}$$

$$C_{\Delta g\Delta g} = \delta(1-y) + a_S\, C_A \left[2S_L\delta(y) - 8y - L \times 4\Big(\frac{1}{y_+} - 1 + 2y\Big)\right], \tag{C.7}$$

where $y = 1 - x'$, and L, S_L are defined as

$$L = \log\frac{\mu^2\mathbf{z}^2}{b_0^2}\,, \qquad S_L = -\frac{1}{2}L^2 - \frac{\pi^2}{12}\,. \tag{C.8}$$

$\frac{1}{y_+} = \frac{1}{(1-x')_+}$ denotes the plus-distribution.
A plus-distribution of a function $f(x')$ is defined by:

$$\int_x^1 dx' \left[f(x')\right]_+ g(x') \;=\; \int_x^1 dx' f(x') \big(g(x') - g(1)\big) - g(1) \int_0^x dx'\, f(x')\,, \tag{C.9}$$

for any smooth test function $g(x)$, $x \in [0,1]$.

There is a simple scaling for different color representations:

$$^{R_1 R_2}C_{ab} = \delta_{ab}\delta(1-y) + c_{ab}(R_1 R_2) C_{ab}, \tag{C.10}$$

where the representation-dependent factors are:

$$\begin{aligned}
&c_{qq}(11) = 1, \qquad c_{qq}(88) = -\frac{1}{N^2-1},\\
&c_{qg}(8A) = c_{gq}(8A) = \sqrt{\frac{N^2}{2(N^2-1)}}, \qquad c_{qg}(8S) = c_{gq}(8S) = -\sqrt{\frac{N^2-4}{2(N^2-1)}},\\
&c_{\bar{q}\bar{q}} = c_{qq}, \quad c_{\bar{q}g}(8S) = c_{qg}(8S), \quad c_{\bar{q}g}(8A) = -c_{qg}(8A)\,.
\end{aligned} \tag{C.11}$$

At the order α_S^1, each kernel can be expressed using terms proportional to at most 3 different kinematics-dependent factors:

$$C_{ab} = a_S \Big[C^1_{ab} + L \times C^L_{ab} + S_L \times C^{S_L}_{ab}\Big]\,. \tag{C.12}$$

C.1 Massive quarks

As discussed in Section 3.2, we consider matching of collinear DPDFs with $n_f = 4$ active flavors onto DTMDs with $n_f = 5$. Therefore, one needs to account for the effects of the bottom quark mass in the relevant matching kernels. They can be obtained using the results for single parton TMDs [96].

Using terms C^1, C^L, C^S defined in decomposition (C.12), we write the matching kernel for a massive quark Q:

$$^{11}C_{Qg} = c^1_Q\, C^1_{qg} + c^L_Q\, C^L_{qg}\,, \tag{C.13}$$

$$^{11}C_{\Delta Q \Delta g} = c^1_Q\, C^1_{\Delta qg} + c^L_Q\, C^L_{\Delta qg}\,. \tag{C.14}$$

At the considered perturbative order, the massive quarks mix only with gluons. The coefficients c_{Qg} are

$$c^1_Q = (|\mathbf{z}|m_Q) K_1(|\mathbf{z}|m_Q), \qquad c^L_Q = 2K_0(|\mathbf{z}|m_Q)\,, \tag{C.15}$$

where m_Q is the quark mass, and K_i are modified Bessel functions of the second kind.

Appendix D

DPD splitting kernels

Presented formulas are taken from [56].

DTMD-PDF matching formula reads:

$$ {}^{R_1R_2}F_{a_1a_2,spl.}(x_i,\mathbf{z}_i,\mathbf{y};\mu) \;=\; \frac{\mathbf{y}_+^l\mathbf{y}_-^{l'}}{\mathbf{y}_+^2\mathbf{y}_-^2}\frac{\alpha_S(\mu)}{2\pi^2}\,{}^{R_1R_2}T_{a_0\to a_1a_2}\Big(\frac{x_1}{x_1+x_2}\Big)\frac{f_{a_0}(x_1+x_2;\mu)}{x_1+x_2}\,, \tag{D.1}$$

where $\mathbf{y}_\pm = \mathbf{y} + \frac{1}{2}(\mathbf{z}_1 - \mathbf{z}_2)$. Let us denote $u = x_1/(x_1+x_2)$ and $\bar{u} = 1-u$. The leading-order splitting kernels used in this work are:

$$ {}^{11}T^{ll'}_{g\to q\bar{q}} = -{}^{11}T^{ll'}_{g\to \Delta q\Delta\bar{q}} = T_F\big(u^2+\bar{u}^2\big)\delta^{ll'}\,, \tag{D.2}$$

$$ {}^{11}T^{ll'}_{g\to \Delta q\bar{q}} = -{}^{11}T^{ll'}_{g\to q\Delta\bar{q}} = -iT_F\big(u-\bar{u}\big)\epsilon^{ll'}\,, \tag{D.3}$$

$$ {}^{11}T^{ll'}_{q\to gq} = C_F\frac{1+\bar{u}^2}{u}\delta^{ll'}\,, \tag{D.4}$$

$$ {}^{11}T^{ll'}_{q\to \Delta g\Delta q} = C_F\big(1+\bar{u}\big)\delta^{ll'}\,, \tag{D.5}$$

$$ {}^{11}T^{ll'}_{g\to gg} = 2C_A\Big(\frac{u}{\bar{u}}+\frac{\bar{u}}{u}+u\bar{u}\Big)\,, \tag{D.6}$$

$$ {}^{11}T^{ll'}_{g\to gg} = 2C_A\Big(\frac{u}{\bar{u}}+\frac{\bar{u}}{u}+u\bar{u}\Big)\,, \tag{D.7}$$

$$ {}^{11}T^{ll'}_{g\to \Delta g\Delta g} = 2C_A\big(2-u\bar{u}\big)\delta^{ll'}\,. \tag{D.8}$$

The result for color-nonsinglet channels is obtained by multiplication by color factor:

$$ {}^{R_1R_2}T_{a_0\to a_1a_2} = c_{a_0\to a_1a_2}(R_1R_2)\;\;{}^{11}T_{a_0\to a_1a_2}\,. \tag{D.9}$$

We have:

$$ c_{g\to q\bar{q}}(88) = -\frac{1}{\sqrt{N^2-1}}\,, \tag{D.10}$$

$$c_{q\to gq}(A8) = -c_{q\to g\bar{q}}(A8) = -\frac{N}{\sqrt{2}}\,, \qquad c_{q\to gq}(S8) = c_{q\to g\bar{q}}(S8) = \sqrt{\frac{N^2-4}{2}}\,, \tag{D.11}$$

$$c_{g\to gg}(SS) = -c_{g\to gg}(AA) = \frac{\sqrt{N^2-1}}{2}\,, \qquad c_{g\to gg}(AS) = c_{g\to gg}(SA) = 0\,, \tag{D.12}$$

$$c_{g\to gg}(27\,27) = -\sqrt{3}\,, \qquad c_{g\to gg}(10\,\bar{10}) = c_{g\to gg}(\bar{10}\,10) = 0\,. \tag{D.13}$$

At LO the matching between DPDFs and PDFs is obtained by taking $\mathbf{z}_i = 0$, which effectively means replacing $\mathbf{y}_\pm \to \mathbf{y}$ in Eq. (D.1).

Appendix E

Hard scattering factors

For reference see Section 7.1 in [56], and Appendix A.1 in [53].

The factor $K_{q_1\bar{q}_2}$ used in Section 5.1, including 1-loop QCD corrections reads

$$K_{q_1\bar{q}_2}(Q) = \left(1 + \frac{\alpha_S}{2\pi} C_F \Big[-\log^2 \frac{Q^2}{\mu^2} + 3 \log \frac{Q^2}{\mu^2} - 8 + \frac{7\pi^2}{6} \Big] \right) \times K^{(0)}_{q_1\bar{q}_2}(Q) \,, \tag{E.1}$$

where the LO part is:

$$K^{(0)}_{q_1\bar{q}_2}(Q) = \frac{\alpha}{4N} \frac{|V_{q_1q_2}|^2}{\left(2\sin\theta_W\right)^4} \frac{Q^2}{\left(Q^2 - M_W^2\right)^2 + M_W^2\Gamma_W^2} \,,$$
$$q_1 \text{ up-type}, \qquad q_2 \text{ down-type} \,. \tag{E.2}$$

α is the fine structure constant, $N = 3$ is the number of colors, $V_{q_1q_2}$ denotes the CKM matrix element, θ_W is the weak mixing angle.
One has the analogous $K_{a_1a_2}$ factor in the case of W^- production, only with q_1 of down-type and q_1 up-type.

Appendix F

Alternative integration variables in the short-distance part

The integrals defining the transverse-position dependent differential cross-section have the form:

$$\int d^2\mathbf{y} \int d^2\mathbf{z}_1 \int d^2\mathbf{z}_2 \, e^{-i(\mathbf{q}_1\mathbf{z}_1+\mathbf{q}_2\mathbf{z}_2)} \, w(\mathbf{z}_1,\mathbf{z}_2,\mathbf{y}) \, . \tag{F.1}$$

One can instead use the variables

$$\mathbf{z}_\pm = \frac{1}{2}\big(\mathbf{z}_1 \pm \mathbf{z}_2\big) \, , \qquad \mathbf{q}_1\mathbf{z}_1 + \mathbf{q}_2\mathbf{z}_2 = \mathbf{z}_+(\mathbf{q}_1+\mathbf{q}_2) + \mathbf{z}_-(\mathbf{q}_1-\mathbf{q}_2) \, , \tag{F.2}$$

so that the integrand is

$$e^{-i(\mathbf{z}_+\mathbf{q}_+ + \mathbf{z}_-\mathbf{q}_-)} \, w(\mathbf{z}_1,\mathbf{z}_2,\mathbf{y}) \, , \qquad \mathbf{q}_\pm = \mathbf{q}_1 \pm \mathbf{q}_2 \, . \tag{F.3}$$

Recall from Section 5.4.1 that the short-distance splitting part integrated over $d^2\mathbf{y}$ is enhanced at small values of $|\mathbf{z}_-|$, due to small separation between the singularities at $|\mathbf{y}\pm\mathbf{z}_-| \to 0$ on the $\mathbf{y}$-plane. In $(\mathbf{z}_1,\mathbf{z}_2)$ variables it corresponds to specific configurations of these two vectors, while in variables $(\mathbf{z}_-,\mathbf{z}_+)$ it is simply controlled by a single variable $z_- = |\mathbf{z}_-|$. However, to make a close comparison with the large-y part, we continued to use $(\mathbf{y},\mathbf{z}_1,\mathbf{z}_2)$ also in the short-distance region.

It is tempting to further simplify the problem of singularities at $\mathbf{y}_\pm \to 0$, by using the variables $\mathbf{y}_+,\mathbf{y}_-,\mathbf{z}_+$ in the integration. Using $\mathbf{y}_+ - \mathbf{y}_- = 2\mathbf{z}_-$, we would get a Fourier factor involving all 3 vectors:

$$e^{i(\mathbf{q}_1\mathbf{z}_1+\mathbf{q}_2\mathbf{z}_2)} = e^{i\left(\mathbf{z}_+\mathbf{q}_+ + \frac{1}{2}\mathbf{y}_+\mathbf{q}_- - \frac{1}{2}\mathbf{y}_-\mathbf{q}_-\right)} \, . \tag{F.4}$$

Expressing the resulting integral in terms of Bessel integrals would require expanding the integral in terms of discrete double Fourier transform with respect to 2 angles, and the obtained double series involves a triple Hankel transform, which makes this form rather difficult for numerical computation.

Appendix G

Complementary plots

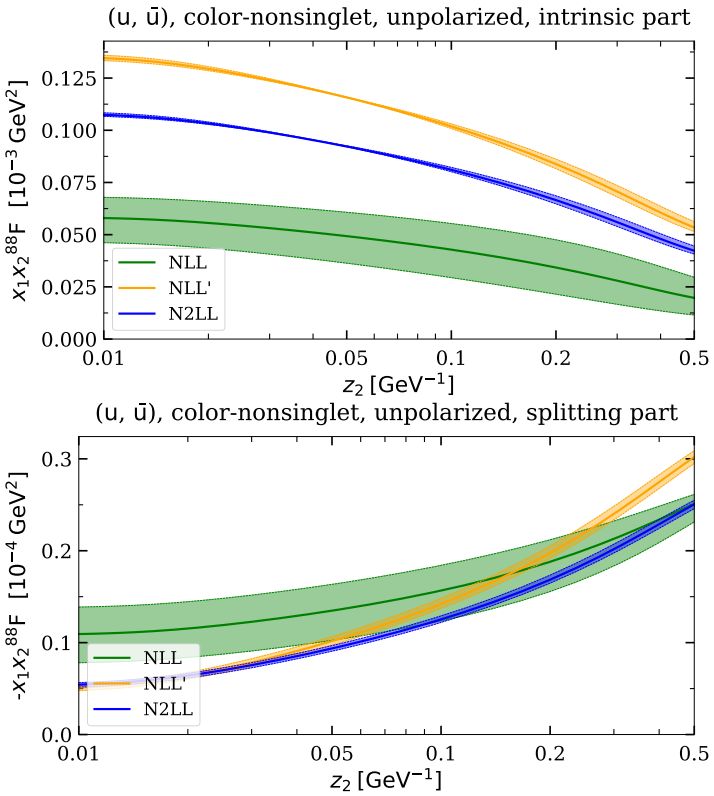

Figure G.1: Example of color-nonsinglet DTMD, for which the initial conditions (intrinsic vs splitting DPDF form) change the qualitative behavior at large $z_2 = |\mathbf{z}_2|$.

G.1 DTMDs in short-ditance approximation

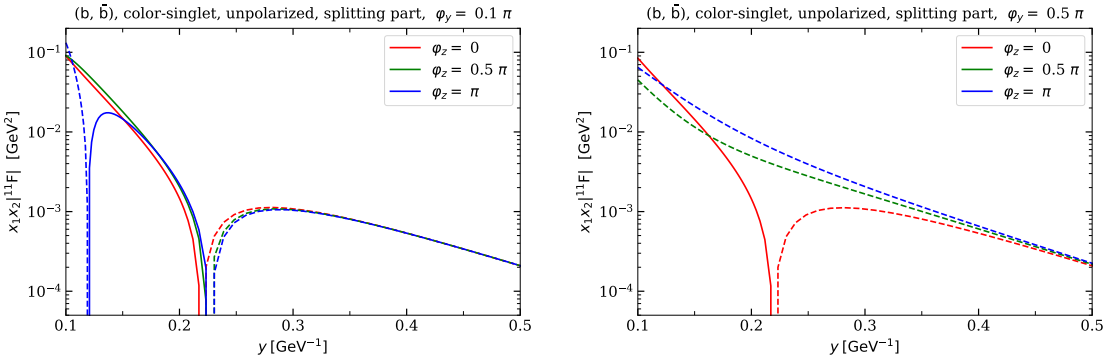

Figure G.2: Absolute value of the unpolarized splitting part of $b\bar{b}$ distribution at $|\mathbf{z}_1| = |\mathbf{z}_2| = 0.1$ GeV^{-1}. Solid lines correspond to the region where the distribution is positive, and dashed lines indicate negative value. Compated to the results for a pair $u\bar{u}$ presented in Fig. 4.7 one observes much faster vanishing of the splitting part of a massive quark pair compared to the massless case.

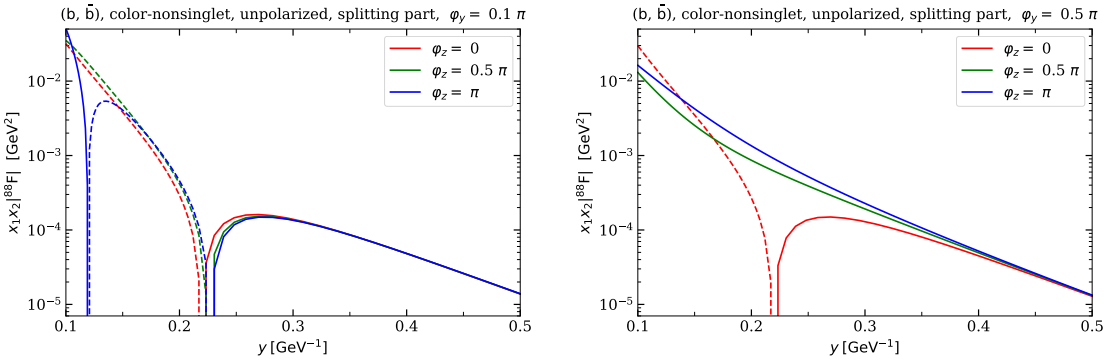

Figure G.3: The same as in Fig. G.2, but for color-nonsinglet representation.

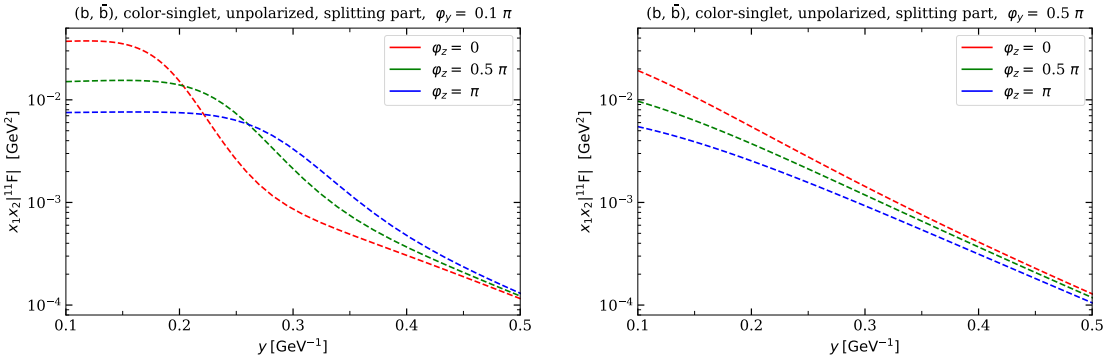

Figure G.4: The same as in Fig. G.2, but for non-symmetric values of $|\mathbf{z}_i|$: $|\mathbf{z}_1| = 0.1$ GeV^{-1}, $|\mathbf{z}_2| = 0.5$ GeV^{-1}.

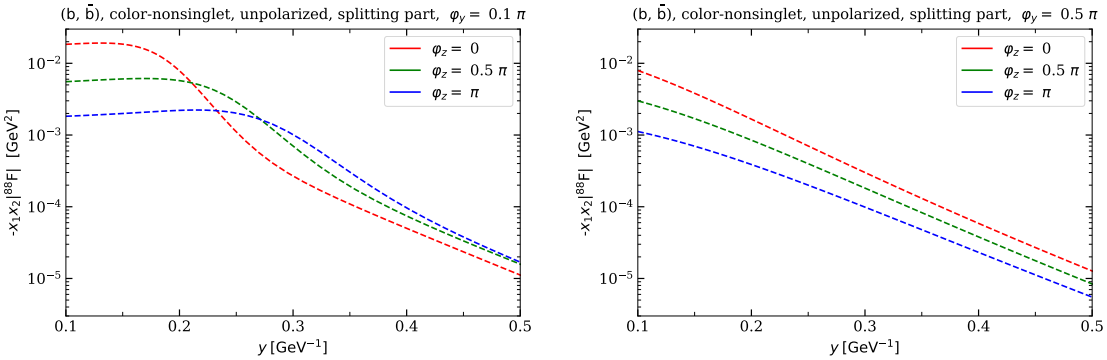

Figure G.5: The same as in Fig. G.4, but for color-nonsinglet representation.

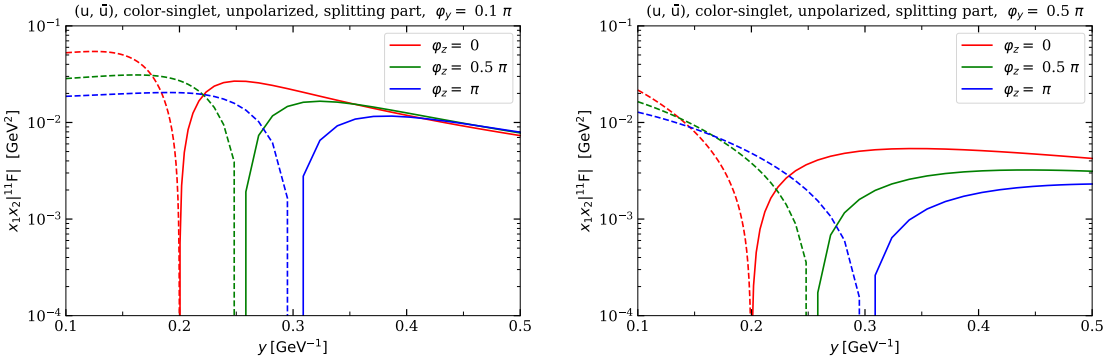

Figure G.6: The same as in Fig. 4.7, but for non-symmetric values of $|\mathbf{z}_i|$: $|\mathbf{z}_1| = 0.1$ GeV^{-1}, $|\mathbf{z}_2| = 0.5$ GeV^{-1}.

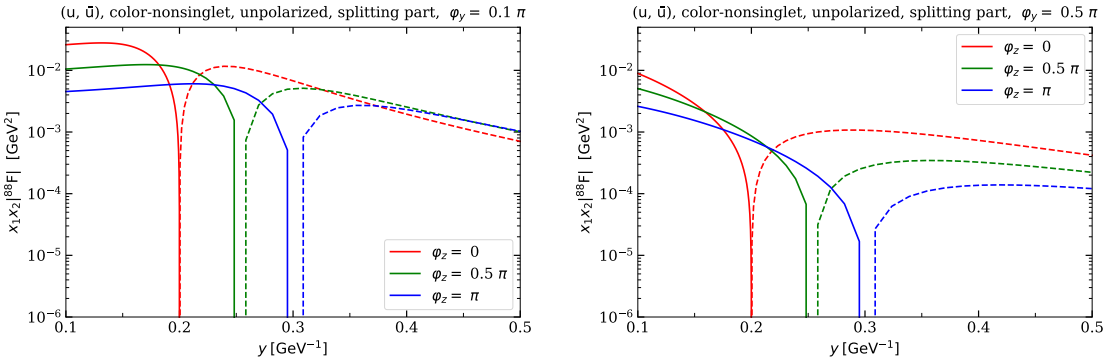

Figure G.7: The same as in Fig. G.6, but for color-nonsinglet representation.

G.2 NLL vs NNLL results the large-y part

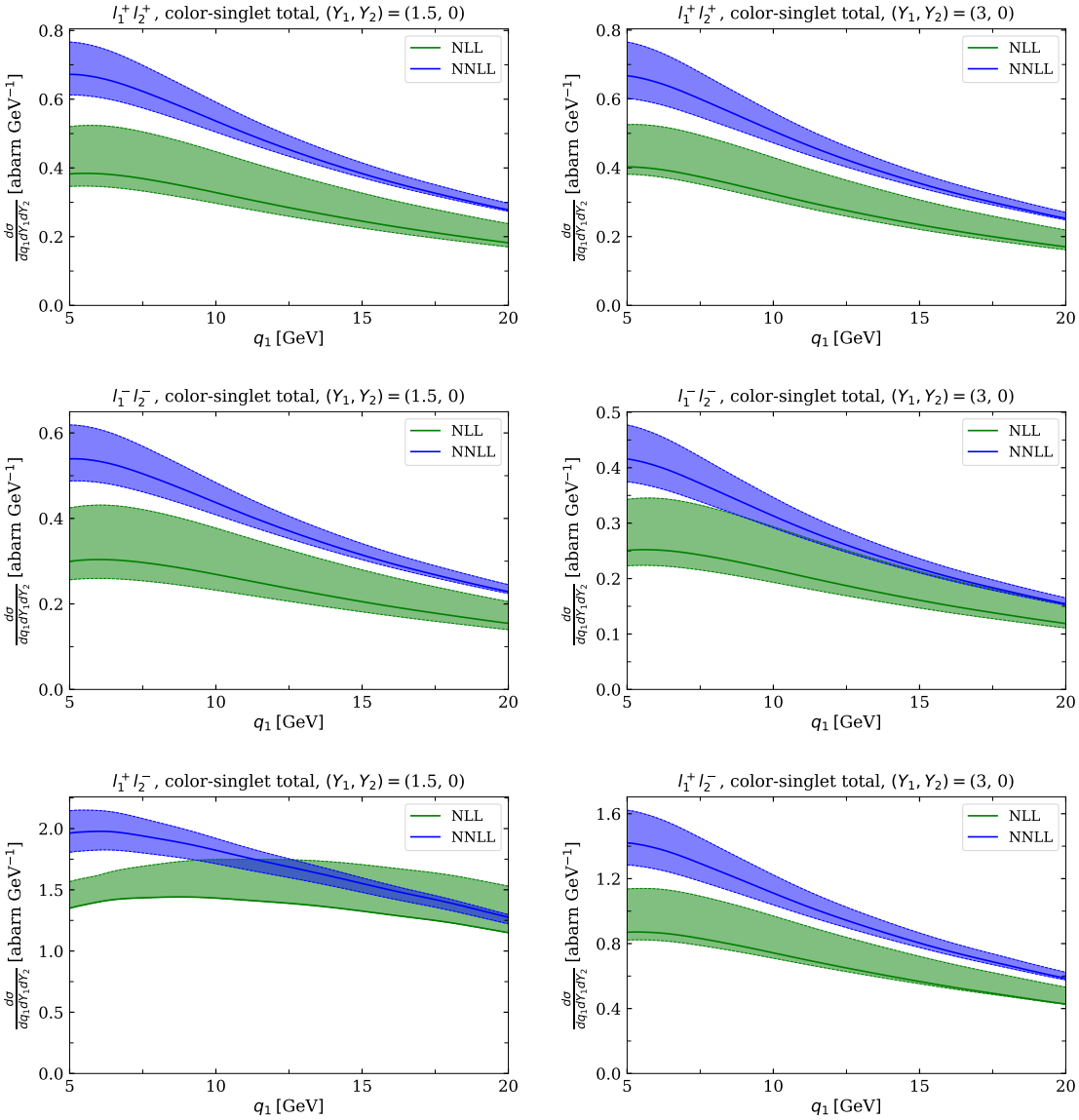

Figure G.8: Large-**y** region, singlet sector contribution to the differential cross-section of production of two W bosons scattering into a pair of leptons. Considered are two values of rapididies of the bosons: $(Y_1, Y_2) = (1.5, 0)$ (left), and $(Y_1, Y_2) = (3, 0)$ (right). Presented are the results and the estimation of the error due to the perturbative matching at NLL (green) and NNLL (blue) accuracy.

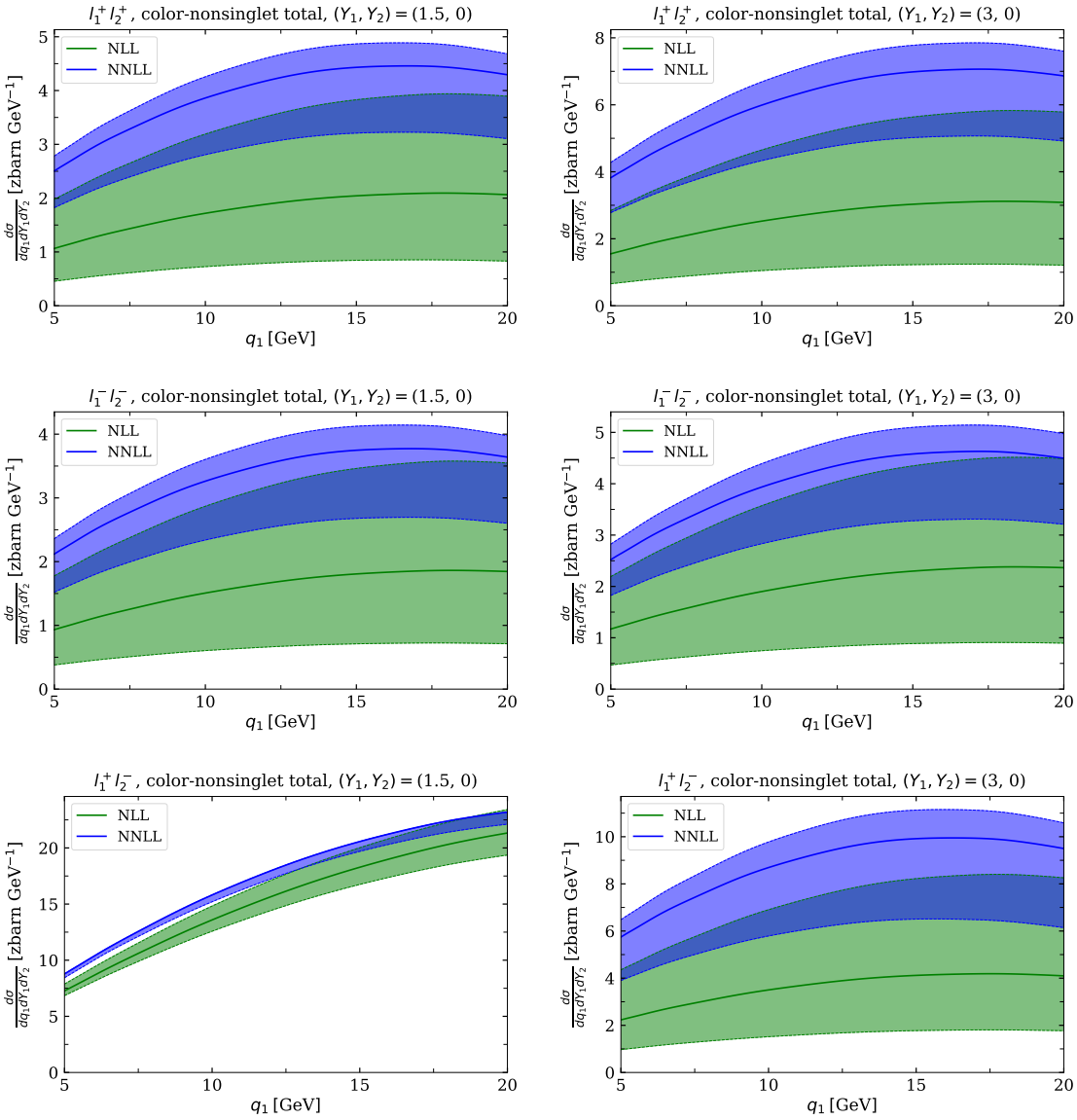

Figure G.9: Large-**y** region, nonsinglet sector contribution to the differential cross-section of production of two W bosons scattering into a pair of leptons. Considered are two values of rapidities of the bosons: $(Y_1, Y_2) = (1.5, 0)$ (left), and $(Y_1, Y_2) = (3, 0)$ (right). Presented are the results and the estimation of the error due to the perturbative matching at NLL (green) and NNLL (blue) accuracy.

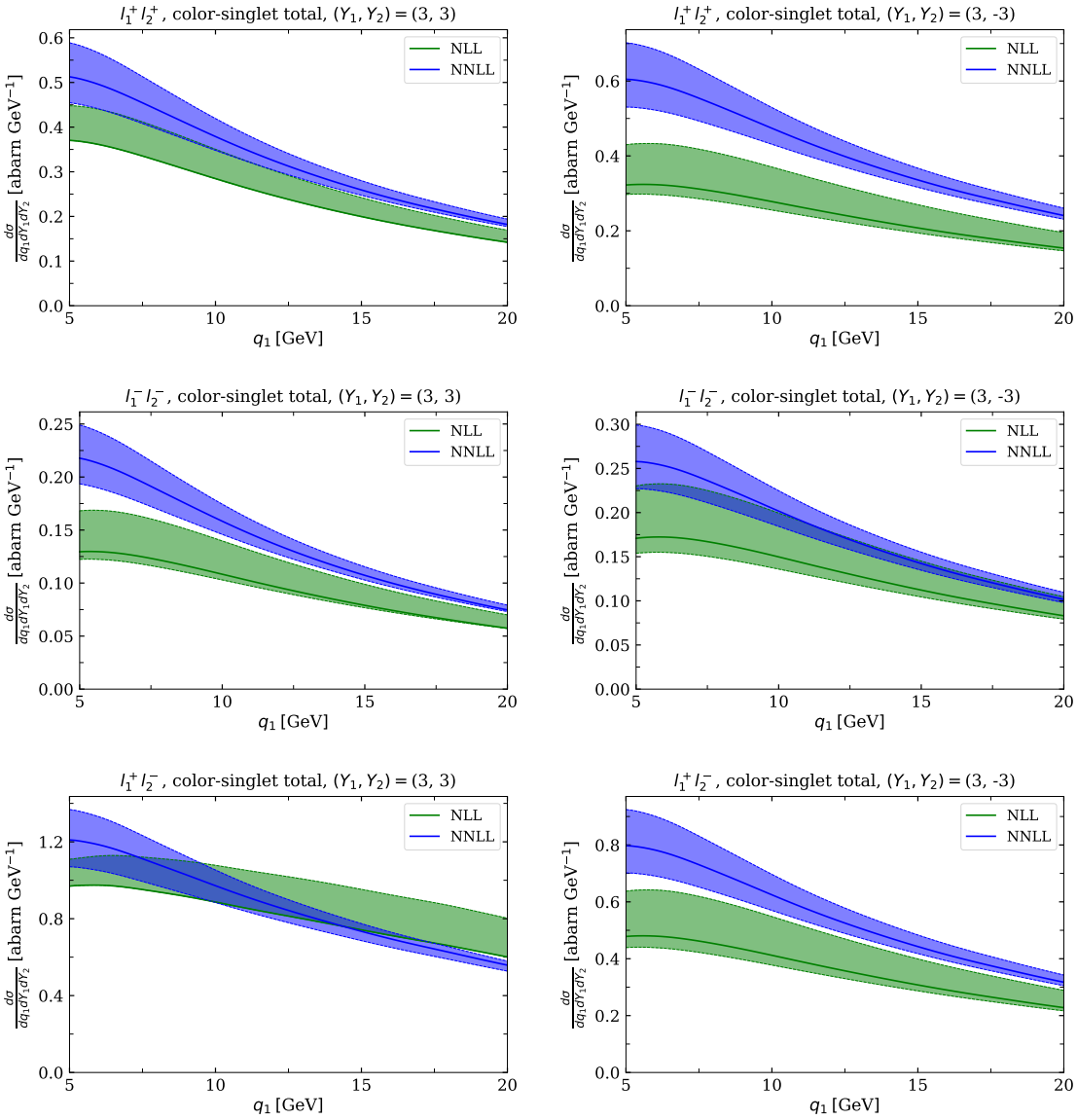

Figure G.10: Large-**y** region, singlet sector contribution to the differential cross-section of production of two W bosons scattering into a pair of leptons. Considered are two values of rapididies of the bosons: $(Y_1, Y_2) = (3, 3)$ (left), and $(Y_1, Y_2) = (3, -3)$ (right). Presented are the results and the estimation of the error due to the perturbative matching at NLL (green) and NNLL (blue) accuracy.

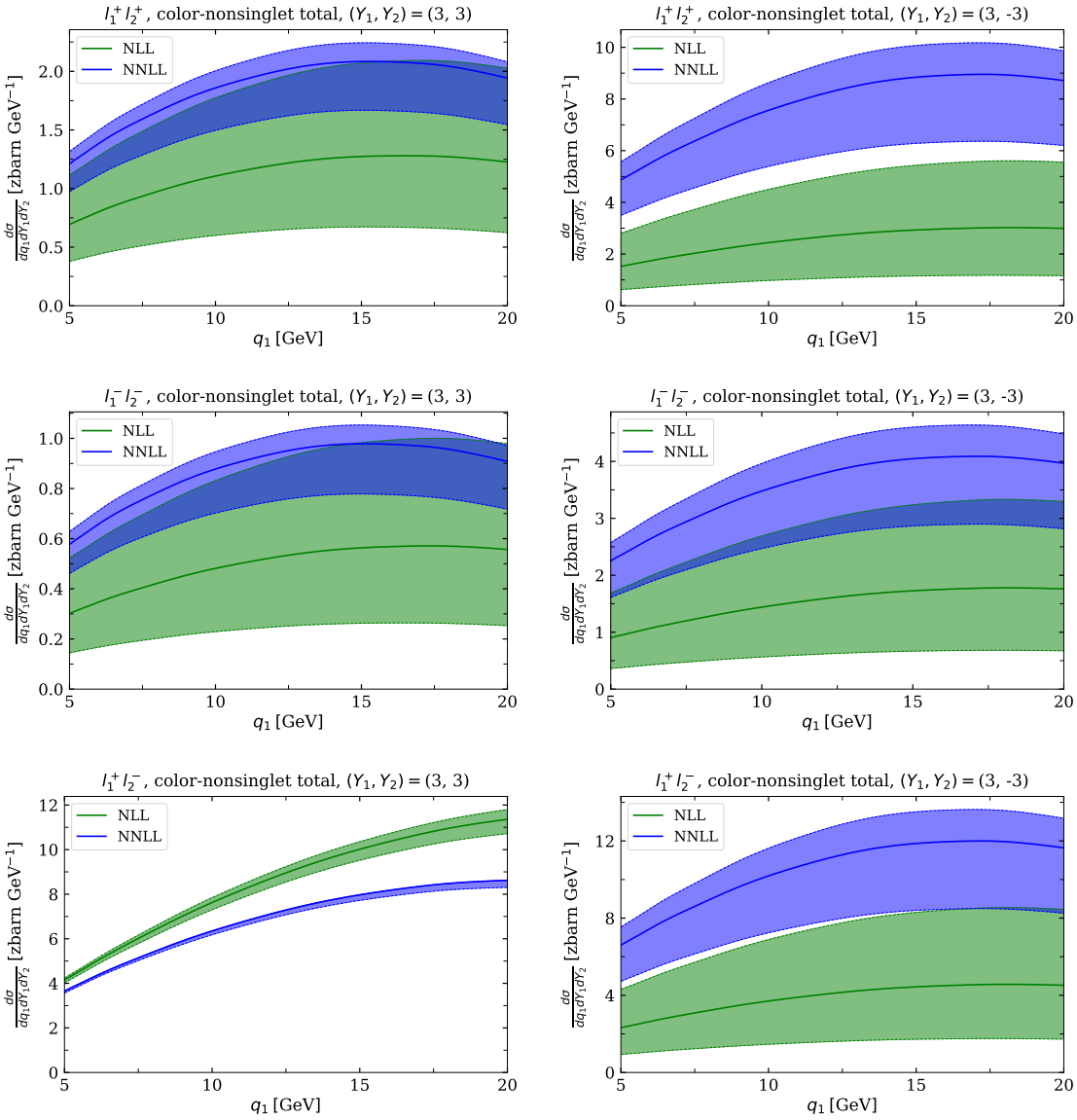

Figure G.11: Large-**y** region, nonsinglet sector contribution to the differential cross-section of production of two W bosons scattering into a pair of leptons. Considered are two values of rapidities of the bosons: $(Y_1, Y_2) = (3, 3)$ (left), and $(Y_1, Y_2) = (3, -3)$ (right). Presented are the results and the estimation of the error due to the perturbative matching at NLL (green) and NNLL (blue) accuracy.

G.3 Combined uncertainties at large-y

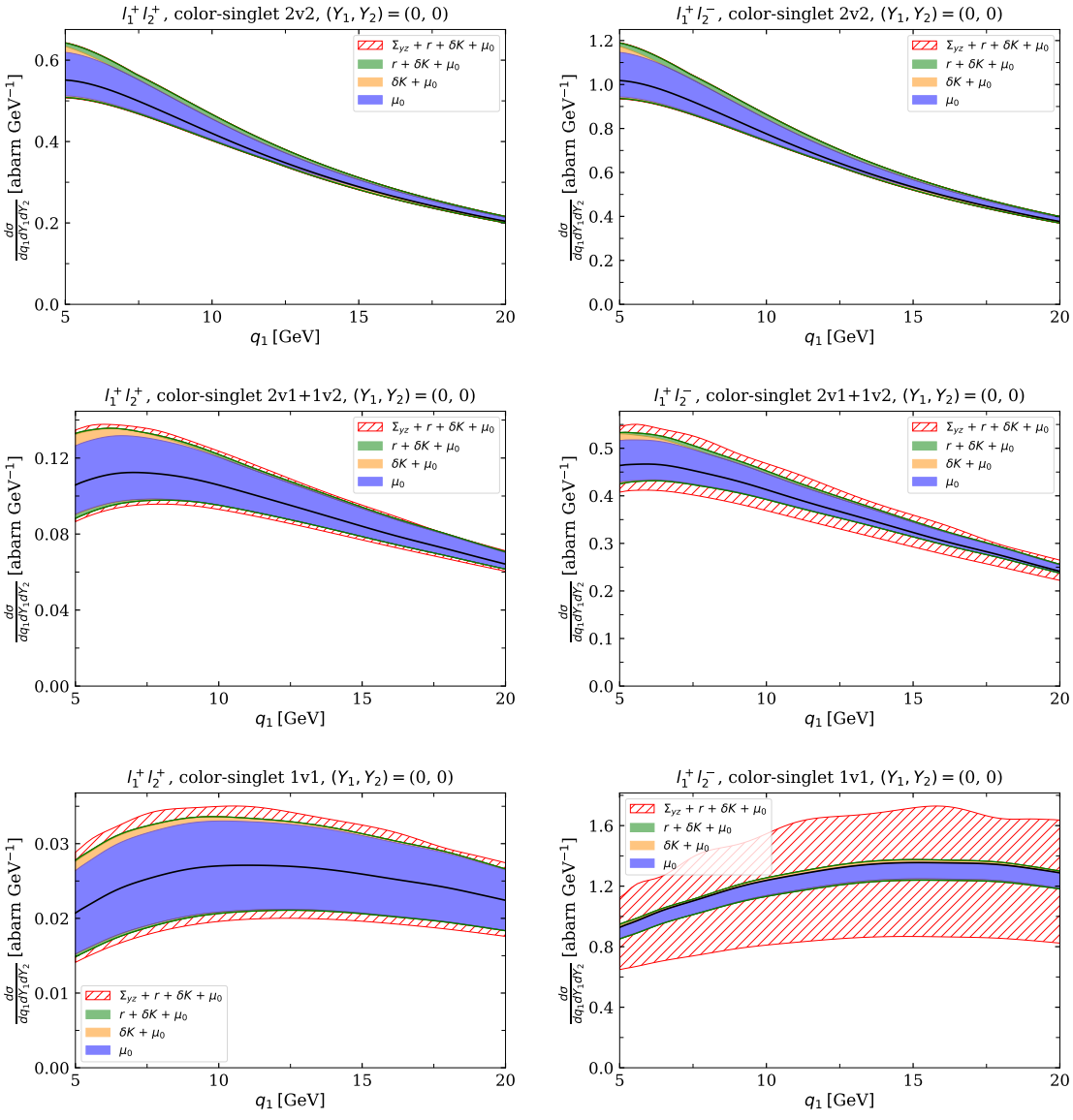

Figure G.12: Large-**y** region, singlet sector contribution to the differential cross-section of production of two W bosons of rapidities $(Y_1, Y_2) = (0, 0)$, scattering into a pair of leptons.

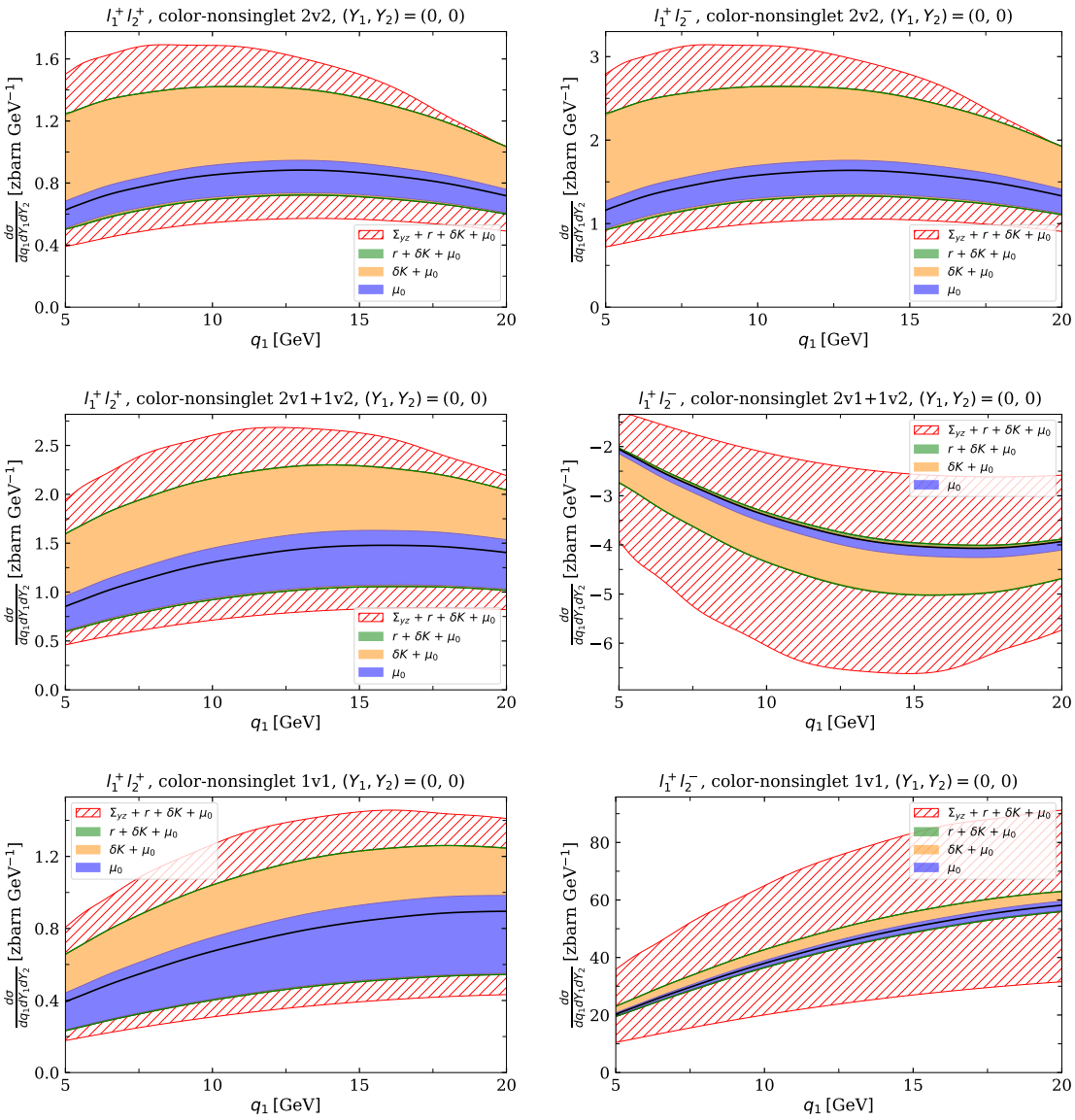

Figure G.13: Large-**y** region, nonsinglet sector contribution to the differential cross-section of production of two W bosons of rapididies $(Y_1, Y_2) = (0, 0)$, scattering into a pair of leptons.

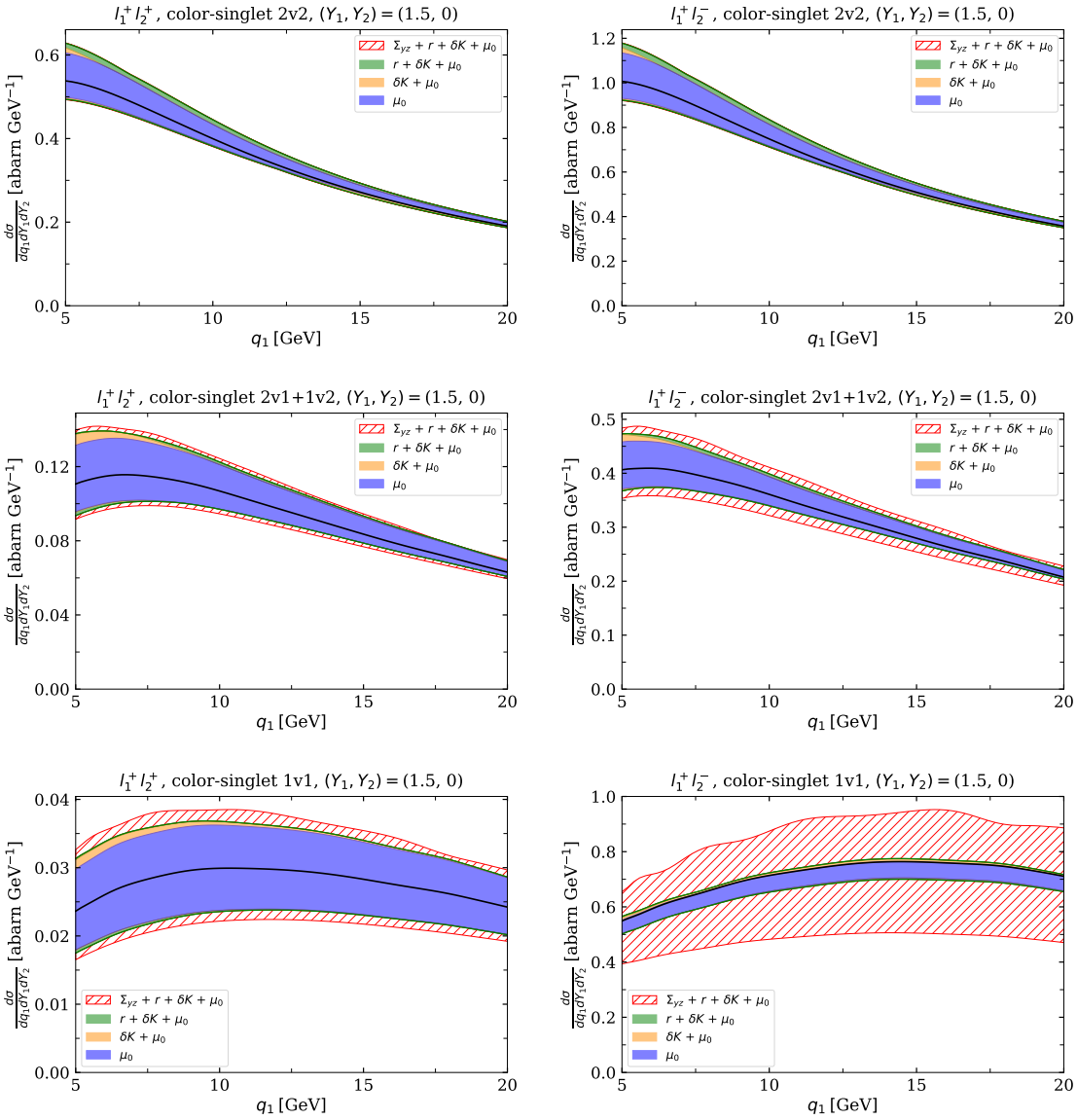

Figure G.14: Large-**y** region, singlet sector contribution to the differential cross-section of production of two W bosons of rapididies $(Y_1, Y_2) = (1.5, 0)$, scattering into a pair of leptons.

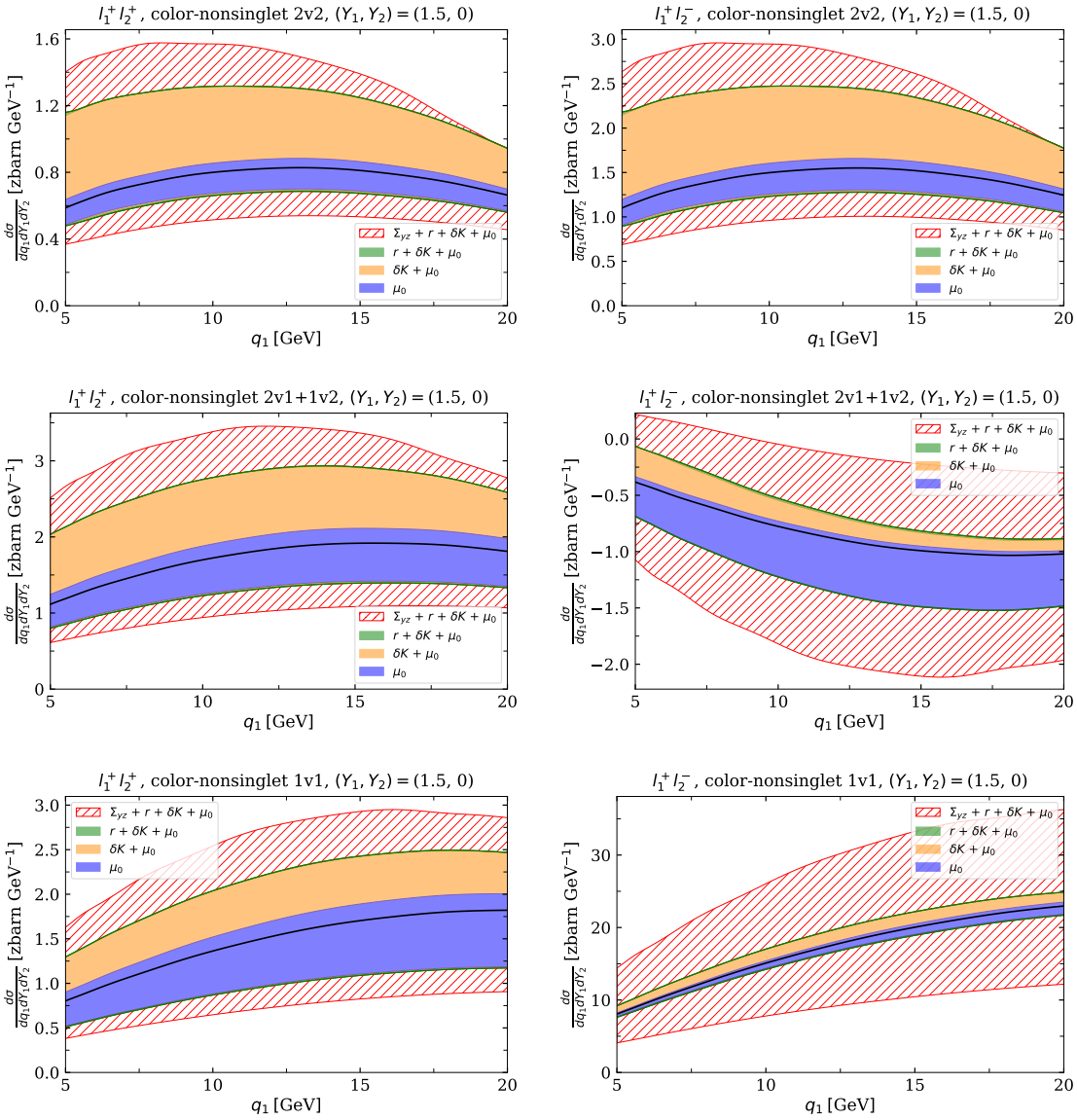

Figure G.15: Large-**y** region, nonsinglet sector contribution to the differential cross-section of production of two W bosons of rapidities $(Y_1, Y_2) = (1.5, 0)$, scattering into a pair of leptons.

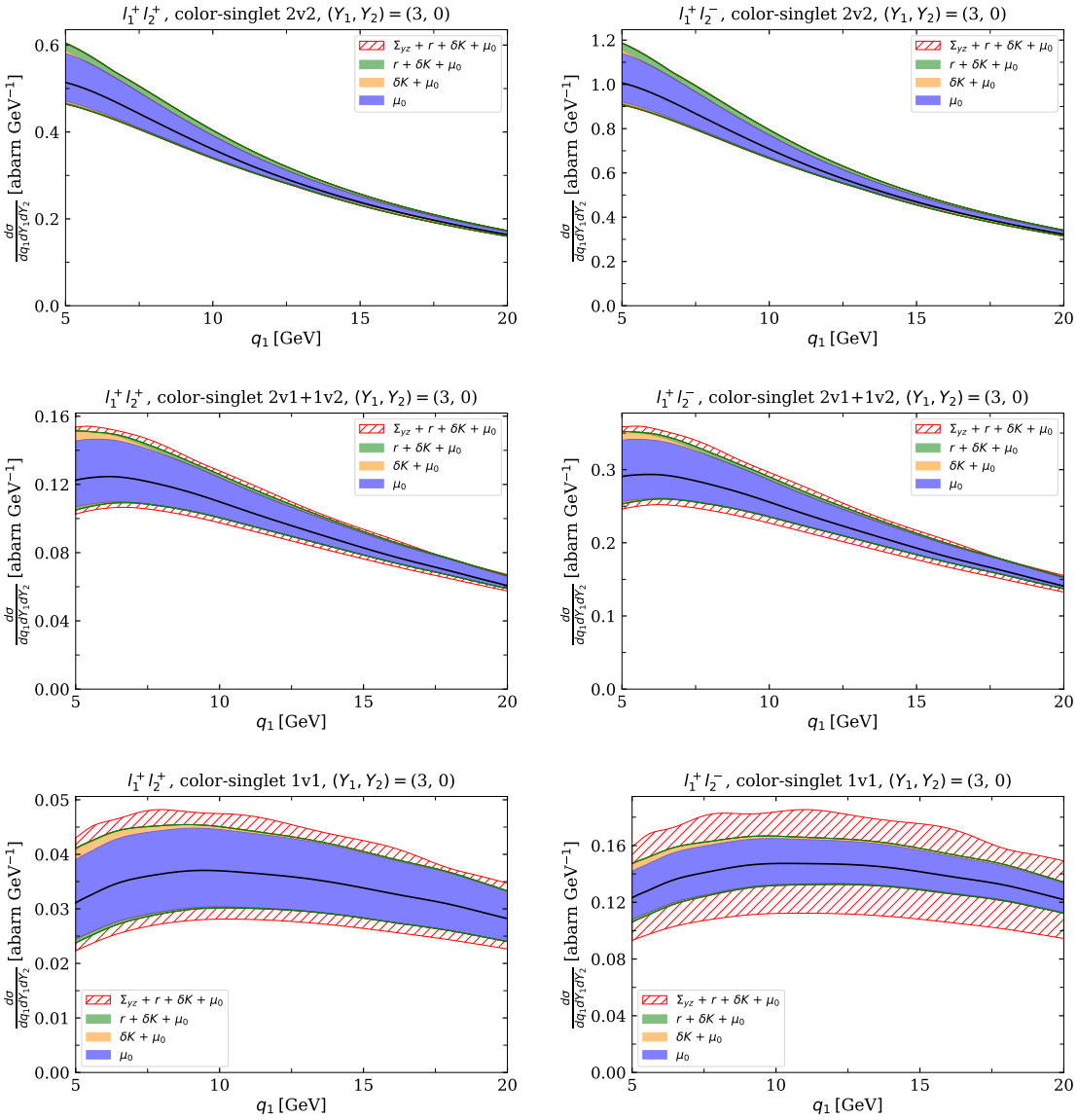

Figure G.16: Large-**y** region, singlet sector contribution to the differential cross-section of production of two W bosons of rapidities $(Y_1, Y_2) = (3, 0)$, scattering into a pair of leptons.

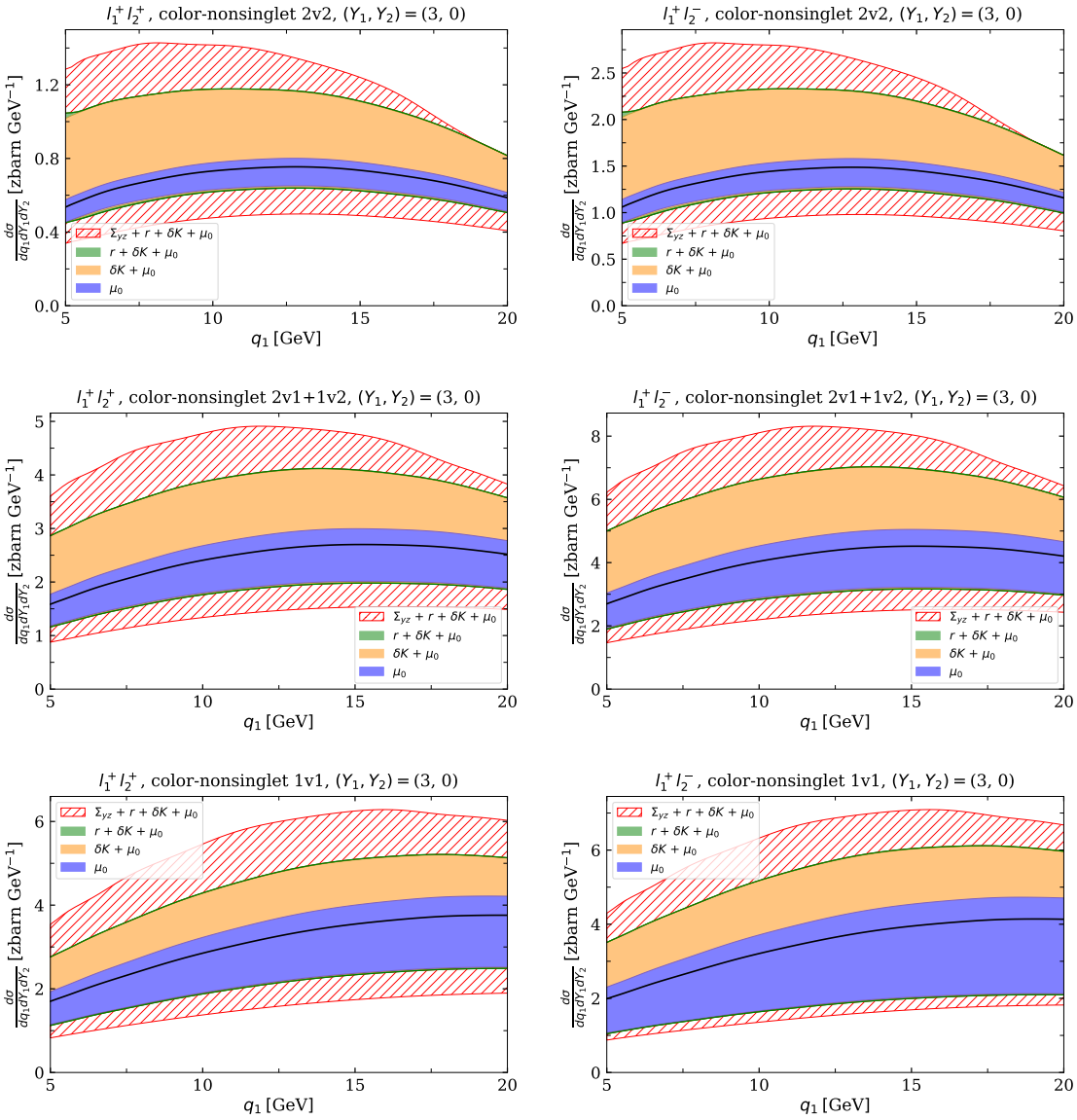

Figure G.17: Large-**y** region, nonsinglet sector contribution to the differential cross-section of production of two W bosons of rapididies $(Y_1, Y_2) = (3, 0)$, scattering into a pair of leptons.

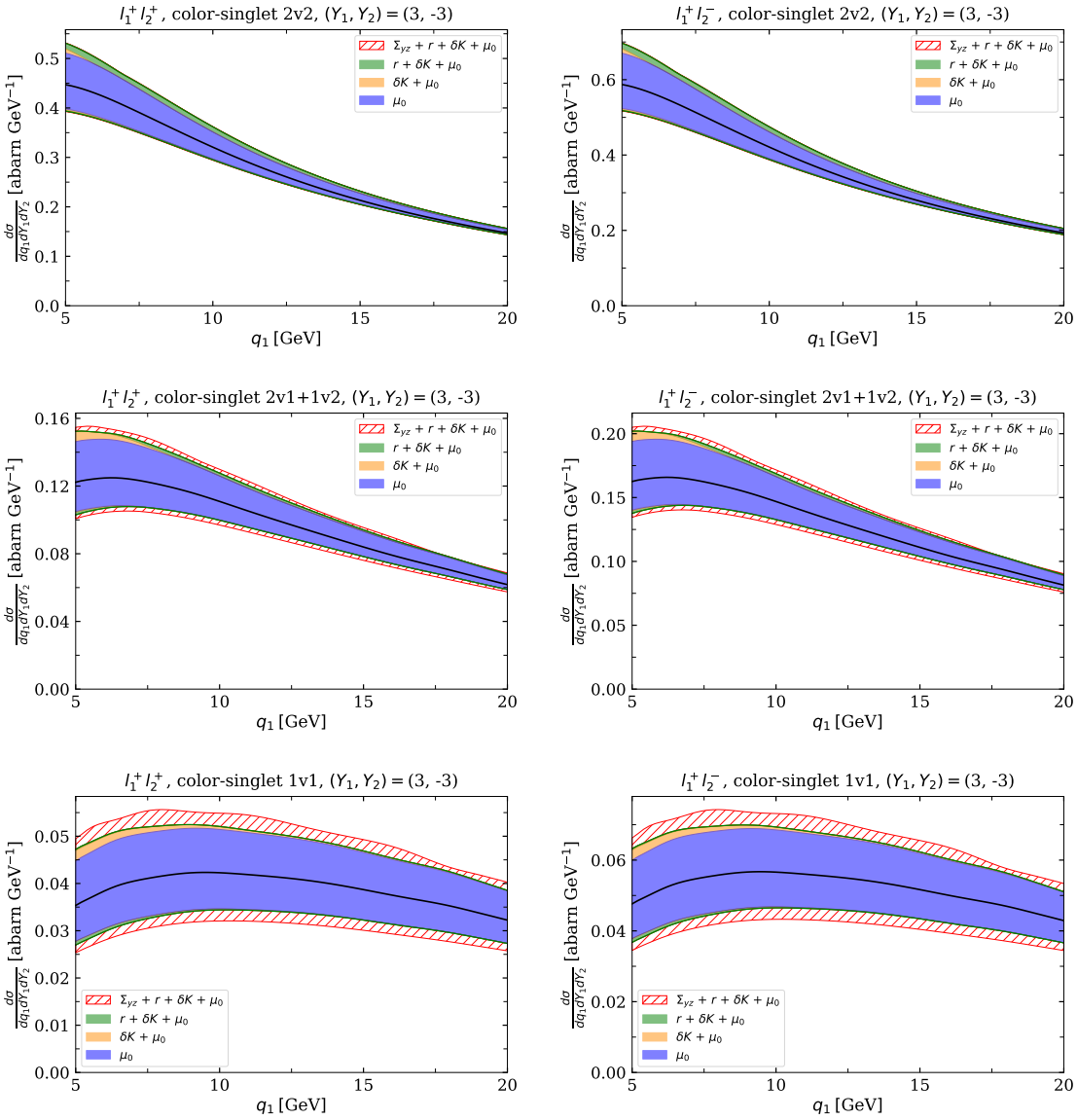

Figure G.18: Large-**y** region, singlet sector contribution to the differential cross-section of production of two W bosons of rapidities $(Y_1, Y_2) = (3, -3)$, scattering into a pair of leptons.

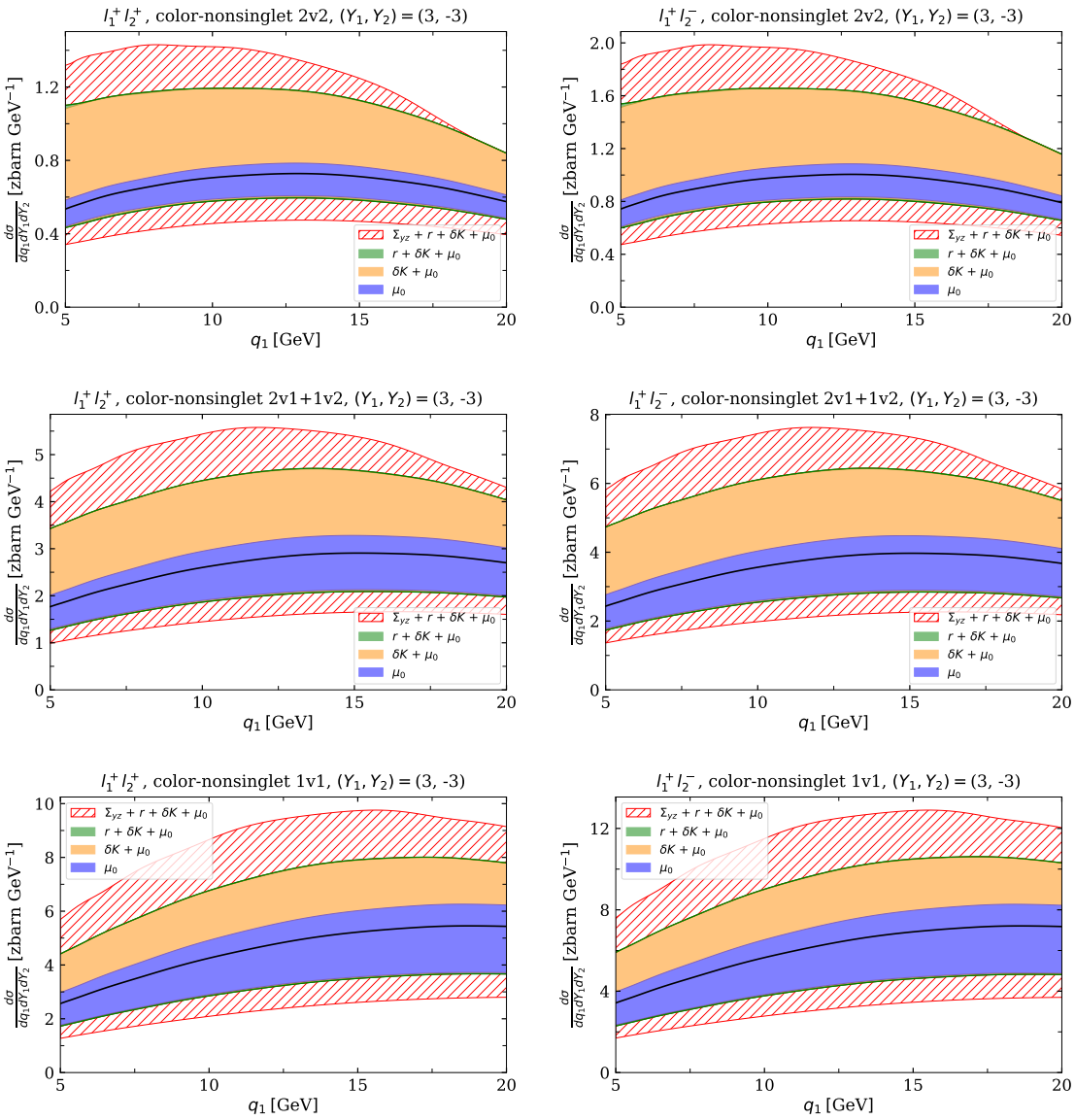

Figure G.19: Large-**y** region, nonsinglet sector contribution to the differential cross-section of production of two W bosons of rapidities $(Y_1, Y_2) = (3, -3)$, scattering into a pair of leptons.

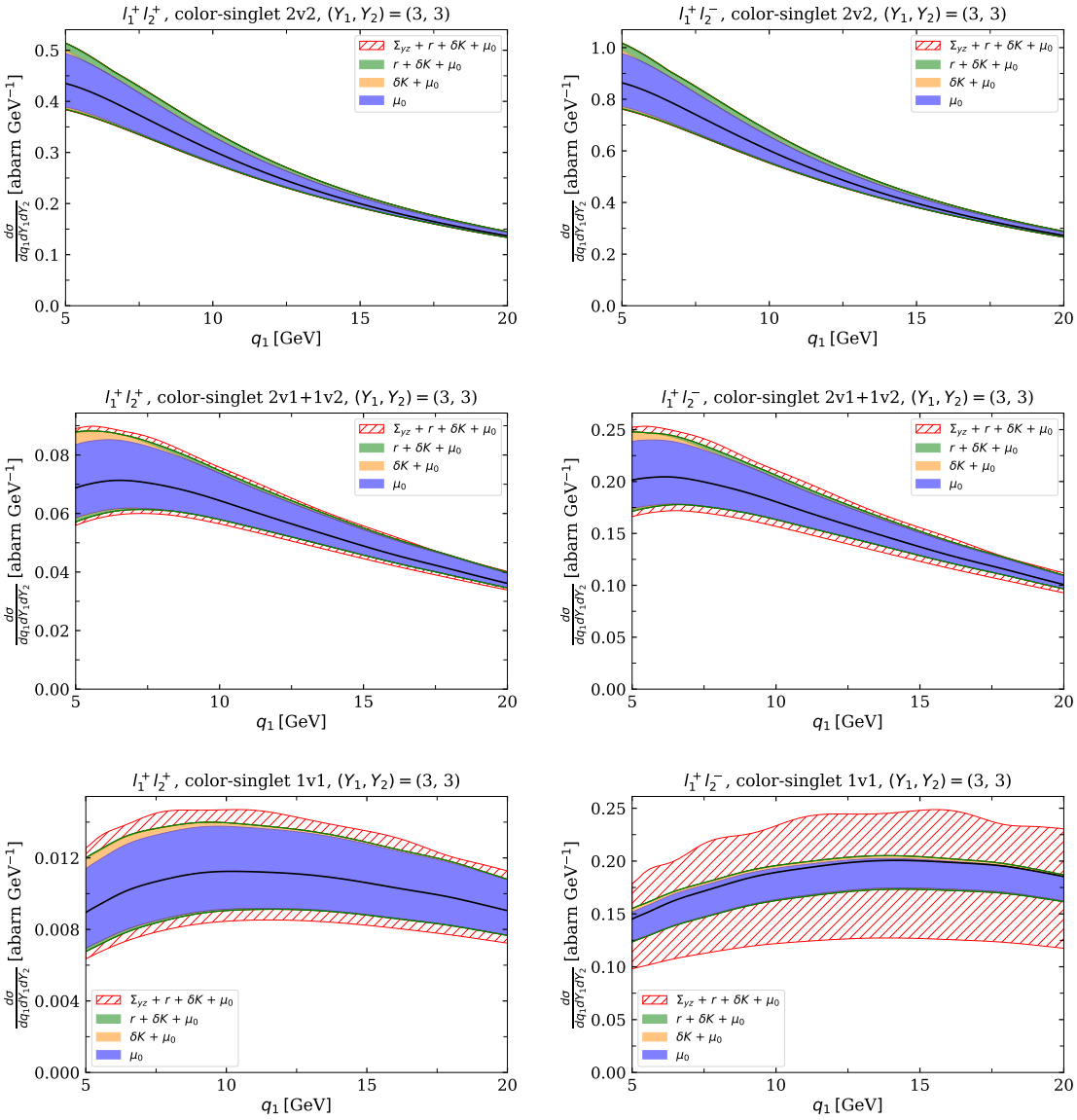

Figure G.20: Large-**y** region, singlet sector contribution to the differential cross-section of production of two W bosons of rapidities $(Y_1, Y_2) = (3, 3)$, scattering into a pair of leptons.

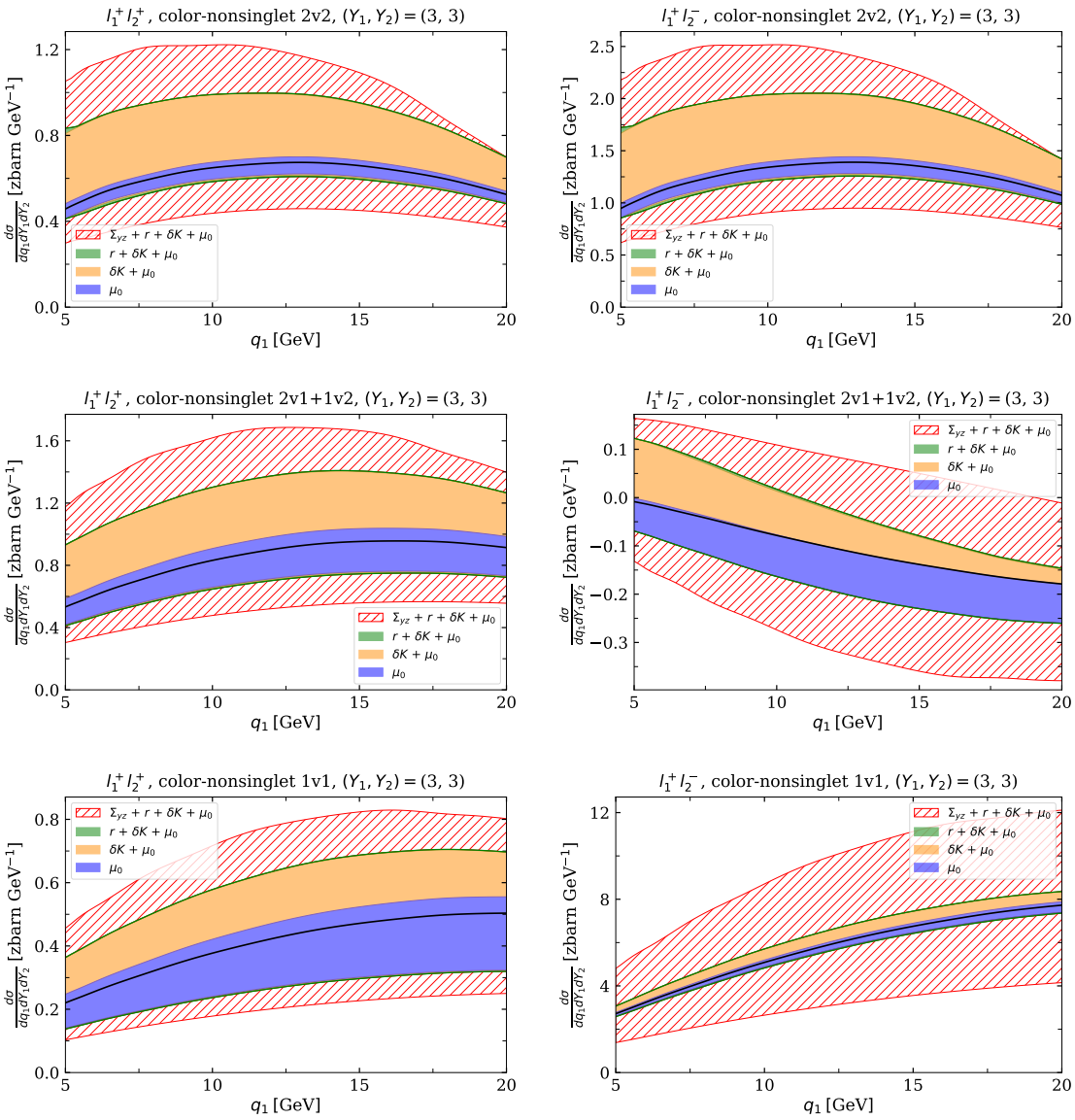

Figure G.21: Large-**y** region, nonsinglet sector contribution to the differential cross-section of production of two W bosons of rapididies $(Y_1, Y_2) = (3, 3)$, scattering into a pair of leptons.

G.4 2v1+1v2 short-distance result at different cut-offs

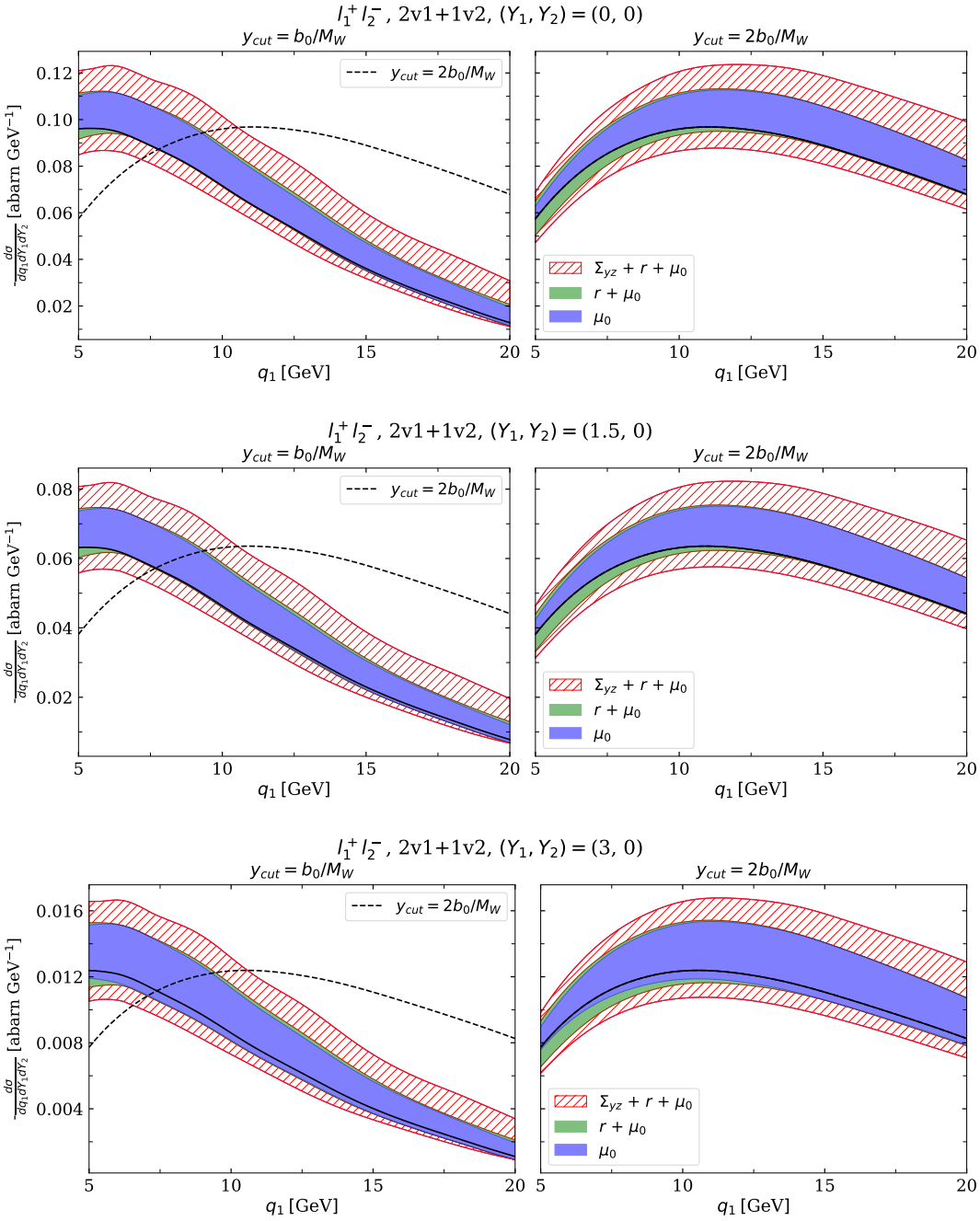

Figure G.22: Comparison of 2v1+1v2 short-distance contributions at cut-offs b_0/M_W and $2b_0/M_W$ for rapidities $(Y_1, Y_2) = (0, 0),\ (1.5, 0),\ (3, 0)$.

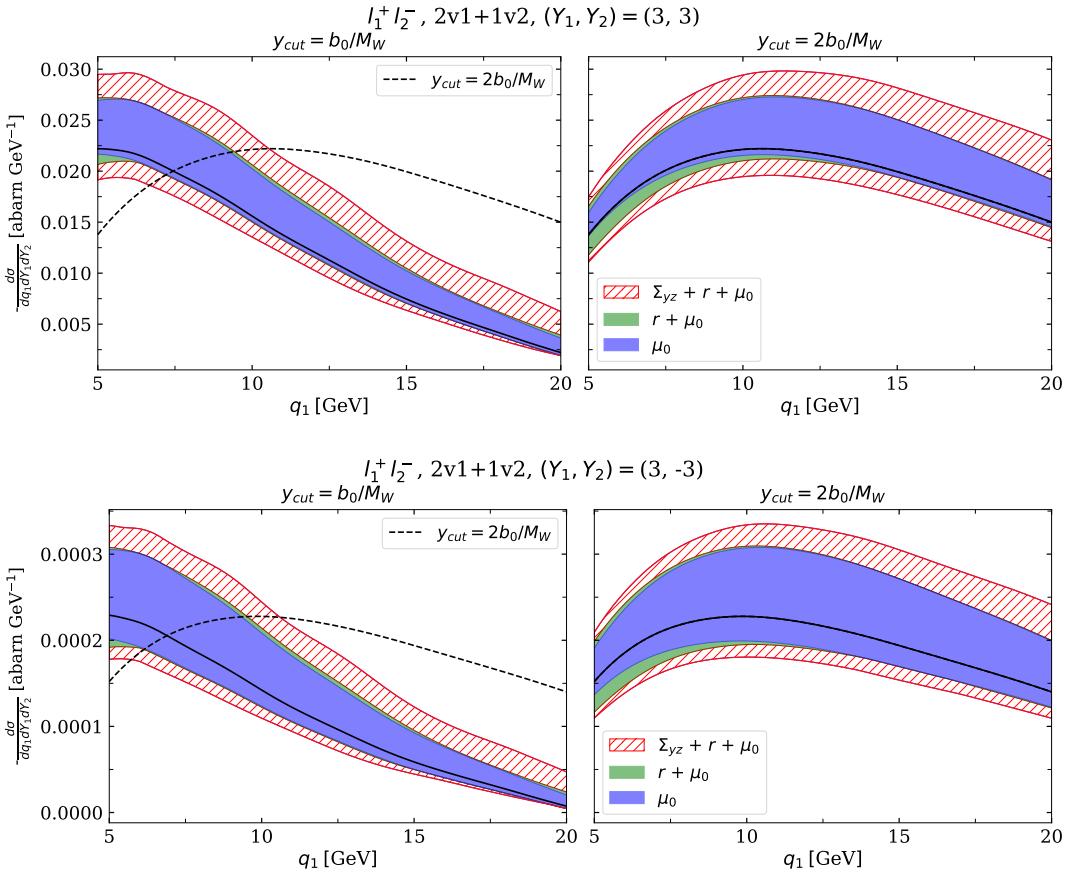

Figure G.23: Comparison of 2v1+1v2 short-distance contributions at cut-offs b_0/M_W and $2b_0/M_W$ for rapidities $(Y_1, Y_2) = (3, 3),\ (3, -3)$.

G.5 Ratios for partially integrated cross-sections

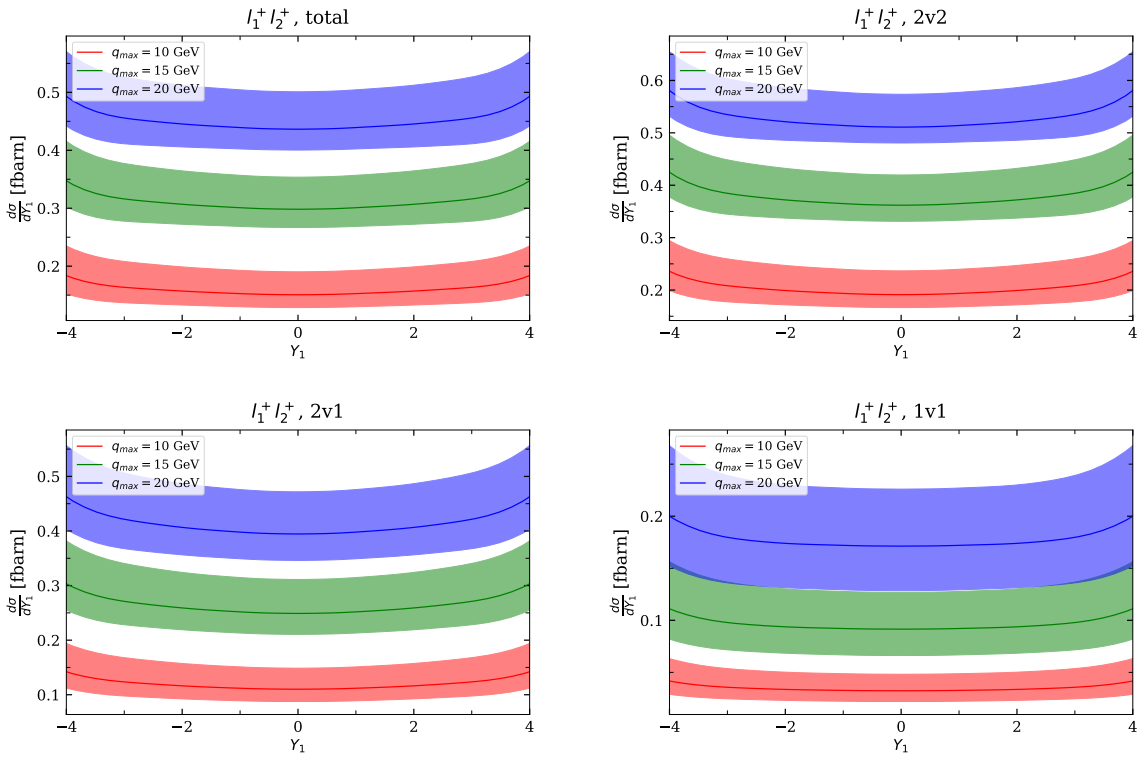

Figure G.24: Ratio of the differential cross section partially integrated over tranvserse momenta of the produced W up to $|\mathbf{q}_i| \leq q_{\max}$ to the result in the collinear limit. Result for a pair of $W_1^+ W_2^+$ decaying into $l_1^+ l_2^+$.

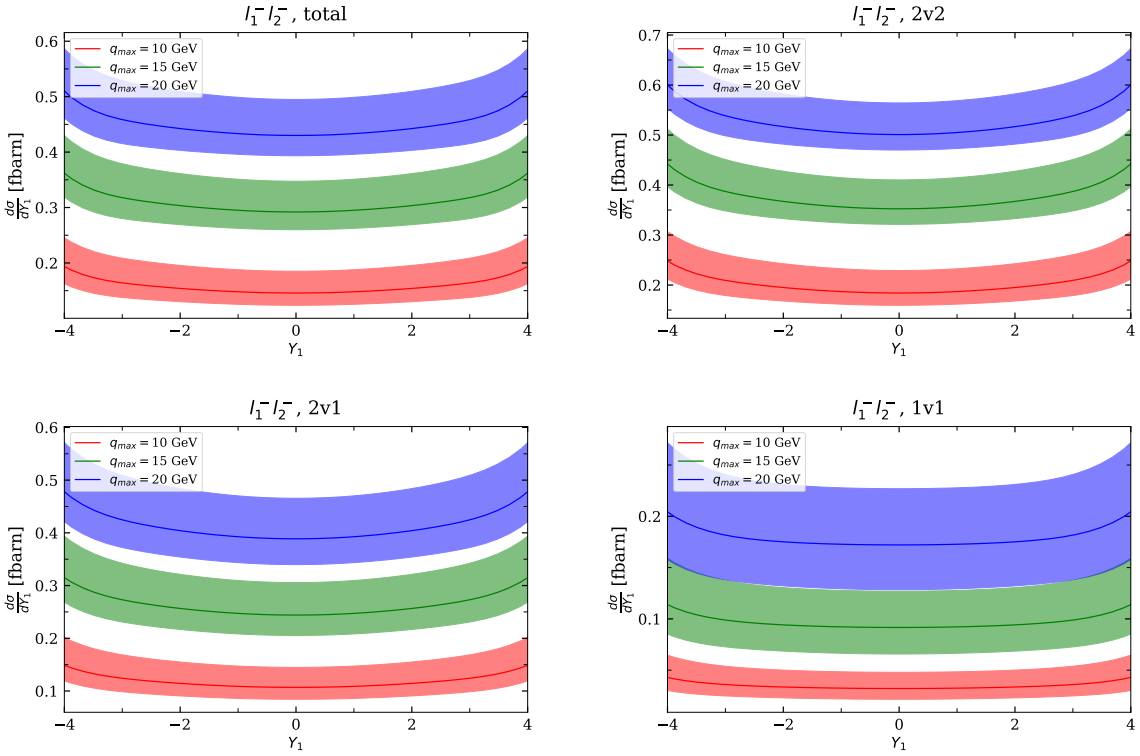

Figure G.25: Ratio of the differential cross section partially integrated over tranvserse momenta of the produced W up to $|\mathbf{q}_i| \leq q_{\max}$ to the result in the collinear limit. Result for a pair of $W_1^- W_2^-$ decaying into $l_1^- l_2^-$.

Bibliography

[1] M. Diehl, O. Grocholski, *Efficient computation of Fourier-Bessel transforms for transverse-momentum dependent parton distributions and other functions*, Eur. Phys. J. C 84 (2024) [2405.08616].

[2] M. Breidenbach et al. *Observed Behavior of Highly Inelastic Electron-Proton Scattering*, Phys. Rev. Lett. 23, 935 (1969) doi:10.1103/PhysRevLett.23.935.

[3] R.P. Feynman *Photon-Hadron Interactions*, W.A. Benjamin Inc., Reading Massachussets, (1972) doi:10.1201/9780429493331.

[4] G. Altarelli, G. Parisi, *Asymptotic Freedom in Parton Language*, Nuclear Physics B1 26, 298-318 (1977) doi:10.1016/0550-3213(77)90384-4.

[5] A.V. Efremov, A.V. Radyushkin, *Hard Processes, Parton Model and QCD.*, Riv. Nuovo Cim. 3, 1 (1980) doi:10.1007/BF02724326.

[6] J.C. Collins, D.E. Soper, G. Sterman, *Factorization of Hard Processes in QCD*, Adv.Ser.Direct.High Energy Phys.5:1-91 (1988) doi:10.1142/9789814503266_0001.

[7] I.I. Balitsky, V.M. Braun, *Evolution equations for QCD string operators*, Nuclear Physics B311 (1988/89) 541-584 doi:10.1016/0550-3213(89)90168-5.

[8] J.C. Collins, A. Freund, *Proof of factorization for deeply virtual Compton scattering in QCD*, Phys. Rev. D 59, 074009 (1999) [9801262].

[9] M. Diehl, *Generalized Parton Distributions*, Phys.Rept.388:41-277, 2003 [0307382].

[10] J.C. Collins, *Foundations of Perturbative QCD*, Cambridge University Press, Cambridge, 2011 doi:10.1017/CBO9780511975592.

[11] J.C. Collins, D.E. Soper, *Angular distribution of dileptons in high-energy hadron collisions*, Phys. Rev. D16 (1977) 10.1103/PhysRevD.16.2219.

[12] H. David Politzer, *Power corrections at short distances*, Nuclear Physics B 172 (1980) 349 doi:10.1016/0550-3213(80)90172-8.

[13] N. Paver and D. Treleani, *Multiquark scattering and large-pT jet production in hadronic collisions*, Il Nuovo Cimento A (1965-1970) 70 (1982) 215 doi:10.1007/BF02814035.

[14] V. P. Shelest, A. M. Snigirev and G. M. Zinovjev, *Gazing into the multiparton distribution equations in QCD*, Phys. Lett. B113 (1982) 325 doi:10.1016/0370-2693(82)90049-1.

[15] M. Mekhfi, *Correlations in Color and Spin in Multiparton Processes*, Phys. Rev. D 32 (1985) 2380 doi:10.1103/PhysRevD.32.2380.

[16] B. Humpert and R. Odorico, *Multiparton Scattering and QCD Radiation as Sources of Four Jet Events*, Phys. Lett. B, 154:211, 1985, doi:10.1016/0370-2693(85)90587-8.

[17] M. Mekhfi, *Multiparton processes: An application to the double Drell-Yan mechanism*, Phys. Rev. D 32 (1985) 2371 doi:10.1103/PhysRevD.32.2371.

[18] T. Sjöstrand and M. Van Zijl, *Multiple parton-parton interactions in an impact parameter picture*, Physics Letters B 188 (1987) 149, doi:10.1016/0370-2693(87)90722-2.

[19] M. Diehl and A. Schäfer, *Theoretical considerations on multiparton interactions in QCD*, Phys.Lett. B698 (2011) 389–402 [1102.3081].

[20] B. Blok, Y. Dokshitser, L. Frankfurt, M. Strikman, *pQCD physics of multiparton interactions*, The Eur. Phys. J. C, vol. 72, 1963 (2012) [1106.5533].

[21] A.V. Manohar, W.J. Waalewijn, *What is double parton scattering?*, Physics Letters B, Vol.713, 196-201 (2012) [1202.5034].

[22] M. Diehl, D. Ostermeier, A. Schäfer, *Elements of a theory for multiparton interactions in QCD*, J. of High Energy Physics, Vol. 2012, 89 (2012) [1111.0910].

[23] M. Diehl, J.R. Gaunt, D. Ostermeier, P. Plößl, A. Schäfer, *Cancellation of Glauber gluon exchange in the double Drell-Yan process*, Journal of High Energy Physics, Vol. 2016, 76 (2016) [1510.08696].

[24] M. Diehl, J.R Gaunt, *Double parton scattering theory overview*, Adv.Ser.Direct.High Energy Phys. 29 (2018) doi:10.1142/9789813227767_0002.

[25] M. Diehl and R. Nagar, *Factorisation of soft gluons in multiparton scattering*, JHEP 04 (2019) 124 [1812.09509].

[26] Axial Field Spectrometer collaboration, *Double Parton Scattering in pp Collisions at* $\sqrt{s}$ *= 63 GeV*, Z. Phys. C 34 (1987) 163, doi:10.1007/BF01566757.

[27] J. Alitti et al., *A study of multi-jet events at the CERN $p\bar{p}$ collider and a search for double parton scattering*, Phys. Lett. B 268, 145 (1991), doi:10.1016/0370-2693(91)90937-L.

[28] CDF collaboration, *Study of four jet events and evidence for double parton interactions in $p\bar{p}$ collisions at $\sqrt{s}$ = 1.8 TeV*, Phys. Rev. D 47 (1993) 4857, doi:10.1103/PhysRevD.56.3811.

[29] CMS collaboration, *Study of Z boson plus jets events using variables sensitive to double-parton scattering in pp collisions at 13 TeV*, JHEP 10 (2021) 176, [2105.14511].

[30] CMS collaboration, *Measurement of double-parton scattering in inclusive production of four jets with low transverse momentum in proton-proton collisions at $\sqrt{s}$ = 13 TeV*, JHEP 01 (2022) 177, [2109.13822].

[31] ATLAS collaboration, *Measurement of hard double-parton interactions in $W(\rightarrow l\nu)$ + 2 jet events at $\sqrt{s}$ = 7 TeV with the ATLAS detector*, New J. Phys. 15 (2013) 033038 [1301.6872].

[32] CMS collaboration, *Study of Double Parton Scattering Using W + 2-Jet Events in Proton-Proton Collisions at $\sqrt{s}$ = 7 TeV*, JHEP 03 (2014) 032 [1312.5729].

[33] D0 collaboration, *Study of double parton interactions in diphoton + dijet events in pp collisions at $\sqrt{s}$ = 1.96 TeV*, Phys. Rev. D 93 (2016) 052008 doi:10.1103/PhysRevD.93.052008

[34] D0 collaboration, *Observation and Studies of Double J/ψ Production at the Tevatron*, Phys. Rev. D 90 (2014) 111101 [1406.2380].

[35] ATLAS collaboration, *Observation and measurements of the production of prompt and non-prompt J/ψ mesons in association with a Z boson in pp collisions at $\sqrt{s}$ = 8 TeV with the ATLAS detector*, Eur. Phys. J. C 75 (2015) 229 [1412.6428].

[36] D0 collaboration, *Evidence for simultaneous production of J/ψ and Υ mesons*, Phys. Rev. Lett. 116 (2016) 082002 [1511.02428].

[37] LHCb collaboration, *Measurement of the J/ψ pair production cross-section in pp collisions at $\sqrt{s}$ = 13 TeV*, JHEP 06 (2017) 047 [1612.07451].

[38] CMS collaboration, *Observation of triple J/ψ meson production in proton-proton collisions*, Nature Phys. 19 (2023) 338 [2111.05370].

[39] M. W. Krasny and W. Placzek, *The LHC excess of four-lepton events interpreted as Higgs-boson signal: Background from Double Drell-Yan process?*, Acta Phys. Polon. B 45 (2014) 71 [1305.1769].

[40] ATLAS collaboration, M. Aaboud et al., *Study of the hard double-parton scattering contribution to inclusive four-lepton production in pp collisions at* $\sqrt{s}$ *= 8 TeV with the ATLAS detector*, Phys. Lett. B790 (2019) 595 [1811.11094].

[41] H. Baer, V. Barger, P. Huang, D. Mickelson, A. Mustafayev, et al., *Same sign diboson signature from supersymmetry models with light higgsinos at the LHC*, [1302.5816].

[42] CMS collaboration, V. Khachatryan et al., *Search for new physics in same-sign dilepton events in proton–proton collisions at* $\sqrt{s} = 13$ *TeV*, Eur. Phys. J. C76(8), 439 (2016) [1605.03171].

[43] A. M. Sirunyan et al., *Search for top quark partners with charge 5/3 in the same-sign dilepton and single-lepton final states in proton-proton collisions at* $\sqrt{s} = 13$ *TeV*, JHEP 03, 082 (2019) [1810.03188].

[44] CMS collaboration, *Search for physics beyond the standard model in events with jets and two same-sign or at least three charged leptons in proton-proton collisions at* $\sqrt{s}$ *= 13 TeV*, Eur. Phys. J. C 80 (2020) 752 [2001.10086].

[45] CMS Collaboration, *Double Parton Scattering cross section limit from same-sign W bosons pair production in di-muon final state at LHC*, CMS-PAS-FSQ-13-001 (2015).

[46] CMS Collaboration, *Measurement of double parton scattering in same-sign WW produc- tion in p-p collisions at* $\sqrt{s} = 13$ *TeV with the CMS experiment*, CMS-PAS-FSQ-16-009 (2017).

[47] CMS collaboration, *Constraints on the double-parton scattering cross section from same-sign W boson pair production in proton-proton collisions at* $\sqrt{s} = 8$ *TeV*, JHEP 02 (2018) 032 [1712.02280].

[48] CMS Collaboration, *Observation of same-sign WW production from double parton scattering in proton-proton collisions at* $\sqrt{s} = 13$ *TeV*, CMS-SMP-21-013, CERN-EP-2022-092 [2206.02681].

[49] M. Drees, T. Han, *Signals for Double Parton Scattering at the Fermilab Tevatron*, Phys.Rev.Lett. 77 (1996), [9605430].

[50] G. Calucci, D. Treleani, *Double parton scatterings in high energy hadronic collisions*, Nucl.Phys.Proc.Suppl. 71 (1999) [9711225].

[51] A. Kulesza, W.J. Stirling, *Like-sign W boson production at the LHC as a probe of double parton scattering*, Phys. Lett. B475 (2000) 168 [9912232].

[52] J.R. Gaunt, C.-H. Kom, A. Kulesza, W.J. Stirling, *Same-sign W pair production as a probe of double parton scattering at the LHC*, Eur. Phys. J. C69 (2010) 53 [1003.3953].

[53] T. Kasemets, M. Diehl, *Angular correlations in the double Drell-Yan process*, JHEP 1301 (2013) 121 [1210.5434].

[54] T. Kasemets, *Double parton scattering - a tale of two partons*, DESY-THESIS-2013-035, Hamburg University, Diss., 2013.

[55] F.A. Ceccopieri, M. Rinaldi, S. Scopetta, *Parton correlations in same-sign W pair production via double parton scattering at the LHC*, Phys. Rev. D95 (2017) 114030 [1702.05363].

[56] M.G.A. Buffing, M. Diehl, T. Kasemets, *Transverse momentum in double parton scattering: factorisation, evolution and matching*, J. of High Energy Physics, Vol. 2018, 44 (2018) [1708.03528].

[57] S. Cotogno, T. Kasemets and M. Myska, *A spin on same-sign W-boson pair production*, Phys. Rev. D 100 (2019) 011503 [1809.09024].

[58] T. Kasemets, P. J. Mulders, *Constraining double parton correlations and interferences*, Phys. Rev. D 91, 014015, [1411.0726].

[59] A. Vogt, S. Moch, J.A.M. Vermaseren, *The Three-loop splitting functions in QCD: The Singlet case*, Nucl. Phys. B 691 (2004) 129 [0404111].

[60] S. Moch, J.A.M. Vermaseren, A. Vogt, *The Three loop splitting functions in QCD: The Nonsinglet case*, Nucl. Phys. B 688 (2004) 101 [0403192]

[61] S. Moch, J.A.M. Vermaseren, A. Vogt, *The Three-Loop Splitting Functions in QCD: The Helicity-Dependent Case*, Nucl. Phys. B 889 (2014) 351 [1409.5131].

[62] J. Blümlein, P. Marquard, C. Schneider, K. Schönwald, *The three-loop unpolarized and polarized non-singlet anomalous dimensions from off shell operator matrix elements*, Nucl. Phys. B 971 (2021) 115542 [2107.06267].

[63] J. Blümlein, P. Marquard, C. Schneider, K. Schönwald, *The three-loop anomalous dimensions from off-shell operator matrix elements*, PoS LL2022 (2022) 048 [2207.07943].

[64] G. Falcioni, F. Herzog, S. Moch, A. Vogt, *Four-loop splitting functions in QCD – The quark-quark case*, Phys. Lett. B 842 (2023) 137944 [2302.07593].

[65] B. Blok, R. Segev, M. Strikman, *Hot spot model of nucleon and double parton scattering*, Eur. Phys. J. C 83 (2023) 415 [2212.08848].

[66] M. Diehl, F. Fabry, A. Vladimirov, *Two-loop evolution kernels for colour dependent double parton distributions*, JHEP 67 (2023) [2212.11843].

[67] M. Diehl, F. Fabry, P. Plößl, *Evolution of colour correlated double parton distributions: a quantitative study*, [2310.16432].

[68] J.C. Collins, D.E. Soper, G.E. Sterman, *Transverse Momentum Distribution in Drell-Yan Pair and W and Z Boson Production*, Nucl.Phys.B 250 (1985) 10.1016/0550-3213(85)90479-1.

[69] M. Diehl, J.R. Gaunt, K. Schönwald, *Double hard scattering without double counting*, JHEP 06 (2017) 083 [1702.06486].

[70] [76] M. Diehl, R. Nagar, F.J. Tackmann, *ChiliPDF: Chebyshev interpolation for parton distributions*, Eur. Phys. J. C 82 (2022) 257 [2112.09703].

[71] M. Diehl, R. Nagar, P. Plößl, F.J. Tackmann, *Evolution and interpolation of double parton distributions using Chebyshev grids*, Eur. Phys. J. C 83(6) (2023) [2305.04845]

[72] L.N. Trefethen, *Approximation Theory and Approximation Practice, Society for Industrial and Applied Mathematics* (2012).

[73] A. Buckley, J. Ferrando, S. Lloyd, K. Nordström, B. Page, M. Rüfenacht et al., *LHAPDF6: parton density access in the LHC precision era*, The European Physical Journal C 75 (2015) [1412.7420].

[74] I. Scimemi, A. Vladimirov, *Analysis of vector boson production within TMD factorization*, Eur. Phys. J. C 78 (2018) 89 [1706.01473].

[75] Z.B. Kang, A. Prokudin, N. Sato, J. Terry, *Efficient Fourier Transforms for Transverse Momentum Dependent Distributions*, Comput. Phys. Commun. 258, 107611 (2021) [1906.05949].

[76] M.A. Ebert, J.K.L. Michel, I.W. Stewart, Z. Sun, *Disentangling Long and Short Distances in Momentum-Space TMDs*, J. of High Energy Physics, 129 (2022) [2201.07237].

[77] M. Mori, M. Sugihara, *The double-exponential transformation in numerical analysis*, Journal of Computational and Applied Mathematics 127 (2001) 287–296 doi:10.1016/S0377-0427(00)00501-X.

[78] H. Ogata, *A Numerical Integration Formula Based on the Bessel Functions*, Publications of the Research Institute for Mathematical Sciences, vol. 41, no. 4, pp. 949-970 (2005) doi:10.2977/prims/1145474602.

[79] N. Baddour, U. Chouinard, *Theory and operational rules for the discrete Hankel transform*, J. Opt. Soc. Am. A 32 (2015) 611 doi:10.1364/JOSAA.32.000611.

[80] N. Baddour, *The Discrete Hankel Transform, in Fourier Transforms – Century of Digitalization and Increasing Expectations*, IntechOpen, 2019. doi:10.5772/intechopen.84399.

[81] D. Levin, *Fast integration of rapidly oscillatory functions*, J. of Computational and Applied Mathematics (1996) 95-101 doi:10.1016/0377-0427(94)00118-9.

[82] M. Diehl, O. Grocholski, *BestLime: a C++ library for computing Fourier- Bessel transforms with Levin's integration method*, 2024. doi:10.5281/zenodo.11113672.

[83] T. Gehrmann, T. Luebbert, L.L. Yang, *Calculation of the transverse parton distribution functions at next-to-next-to-leading order*, JHEP 06 (2014) 155, [1403.6451].

[84] M.G. Echevarria, I. Scimemi, A. Vladimirov, *Unpolarized Transverse Momentum Dependent Parton Distribution and Fragmentation Functions at next-to-next-to-leading order*, JHEP 09 (2016) 004, [1604.07869].

[85] I. Scimemi, A. Tarasov, A. Vladimirov, *Collinear matching for Sivers function at next-to-leading order*, JHEP 05 (2019) 125, [1901.04519].

[86] I. Scimemi, A. Vladimirov, *Non-perturbative structure of semi-inclusive deep-inelastic and Drell-Yan scattering at small transverse momentum*, JHEP 06 (2020) 137, [1912.06532].

[87] MAP (Multi-dimensional Analyses of Partonic distributions) collaboration, *Unpolarized transverse momentum distributions from a global fit of Drell-Yan and semi-inclusive deep-inelastic scattering data*, JHEP 10 (2022) 127, [2206.07598].

[88] V. Moos, I. Scimemi, A. Vladimirov, P. Zurita, *Extraction of unpolarized transverse momentum distributions from fit of Drell-Yan data at N^4LL*, JHEP 36 (2024), [2305.07473].

[89] B. Dehnadi, P. Plößl, F.J. Tackmann, in preparation. [Indico talk].

[90] J.C. Collins, T. Rogers, *Understanding the large-distance behavior of transverse-momentum-dependent parton densities and the Collins-Soper evolution kernel*, Phys. Rev. D 91, 074020 (2015) [1412.3820].

[91] P. Pietrulewicz, D. Samitz, A. Spiering, F.J. Tackmann, *Factorization and Resummation for Massive Quark Effects in Exclusive Drell-Yan*, JHEP 114 (2017), [1703.09702].

[92] M. Diehl, J. R. Gaunt, D. M. Lang, P. Plößl, A. Schäfer, *Sum rule improved double parton distributions in position space*, Eur. Phys. J. C 80 (2020) 468, [2001.10428].

[93] J. R. Gaunt, W. J. Stirling, *Double Parton Distributions Incorporating Perturbative QCD Evolution and Momentum and Quark Number Sum Rules*, JHEP 03 (2010) 005, [0910.4347].

[94] G.S. Bali, M. Diehl, B. Gläßle, Andreas Schäfer, C. Zimmermann, *Double parton distributions in the nucleon from lattice QCD*, JHEP09 (2021) 106 [2106.03451].

[95] S. Bailey, T. Cridge, L.A. Harland-Lang, A.D. Martin, R.S. Thorne, *Parton distributions from LHC, HERA, Tevatron and fixed target data: MSHT20 PDFs*, Eur. Phys. J. C 81 (2021) 341 [2012.04684].

[96] R. von Kuk, J.K.L. Michel, Z. Sun, *Transverse Momentum Distributions of Heavy Hadrons and Polarized Heavy Quarks*, JHEP 205 (2023) [2305.15461].

[97] M. Diehl, J.R. Gaunt, P. Plößl, A. Schäfer, *Two-loop splitting in double parton distributions*, SciPost Phys. 7, 017 (2019), [1902.08019]

[98] M. Diehl, J. R. Gaunt, P. Plößl, *Two-loop splitting in double parton distributions: the colour non-singlet case*, JHEP 40 (2021) [2105.08425].

[99] R. Abbate, M. Fickinger, A.H. Hoang, V. Mateu, I.W. Stewart, *Thrust at N^3LL with Power Corrections and a Precision Global Fit for $\alpha_S(M_Z)$*, Phys. Rev. D 83 (2011) 074021 [1006.3080].

[100] C.F. Berger, C. Marcantonini, I.W. Stewart, F.J. Tackmann, W.J. Waalewijn, *Higgs Production with a Central Jet Veto at NNLL+NNLO*, JHEP 04 (2011) 092 [1012.4480].

[101] M.A. Ebert, *Analytic results for Sudakov form factors in QCD*, JHEP 02 (2022) 136 [2110.11360].

[102] A. Vladimirov, *Soft factors for double parton scattering at NNLO*, JHEP 38 (2016) [1608.04920].

[103] R.L. Workman et al. (Particle Data Group), Prog. Theor. Exp. Phys. 2022, 083C01 (2022).

[104] F. Hautmann, I. Scimemi, A. Vladimirov, *Non-perturbative contributions to vector-boson transverse momentum spectra in hadronic collisions*, Phys. Lett. B 806 (2020) 135478 [2002.12810].

[105] M. Schlemmer, A. Vladimirov, C. Zimmermann, M. Engelhardt, A. Schäfer, *Determination of the Collins-Soper Kernel from Lattice QCD*, JHEP 08 (2021) 004 [2103.16991].

[106] H.-T. Shu, M. Schlemmer, T. Sizmann, A. Vladimirov, L. Walter, M. Engelhardt et al., *Universality of the Collins-Soper kernel in lattice calculations*, Phys. Rev. D 108 (2023) 074519 [2302.06502].

[107] A. Avkhadiev, P. Shanahan, M. Wagman, Y. Zhao, *Collins-Soper kernel from lattice QCD at the physical pion mass*, Phys. Rev. D 108, 114505 (2023) [2307.12359].

[108] M.G. Echevarria, I. Scimemi, A. Vladimirov, *Unpolarized Transverse Momentum Dependent Parton Distribution and Fragmentation Functions at next-to-next-to-leading order*, JHEP 09 (2016) 004 [1604.07869].

[109] M. G. Echevarria, I. Scimemi, A. Vladimirov, *The Universal Transverse Momentum Dependent Soft Function at NNLO*, Phys. Rev. D 93 (2016) 5, 054004 [1511.05590].

[110] R.K. Ellis, W.J. Stirling, B.R. Webber, *QCD and collider physics*, Camb. Monogr. Part. Phys. Nucl. Phys. Cosmol. 8 (1996) 1-435 doi:10.1017/CBO9780511628788.

[111] C. Anastasiou, L. Dixon, K. Melnikov, F. Petriello, *High-precision QCD at hadron colliders: electroweak gauge boson rapidity distributions at NNLO*, Phys. Rev. D 69, 094008 (2004) [0312266].

[112] C. Duhr, F. Dulat, B. Mistlberger, *Charged Current Drell-Yan Production at N^3LO*, JHEP 11 (2020) 143 [2007.13313].

[113] M. Diehl, T. Kasemets, S. Keane, *Correlations in double parton distributions: effects of evolution*, JHEP 118, (2014) [1401.1233].